

AD-A120 081

TRANSPORTATION SYSTEMS CENTER CAMBRIDGE MA

F/G 20/4

CHICAGO MONOSTATIC ACOUSTIC VORTEX SENSING SYSTEM, VOLUME IV. W--ETC(U)

JUL 82 D C BURNHAM, J N HALLOCK

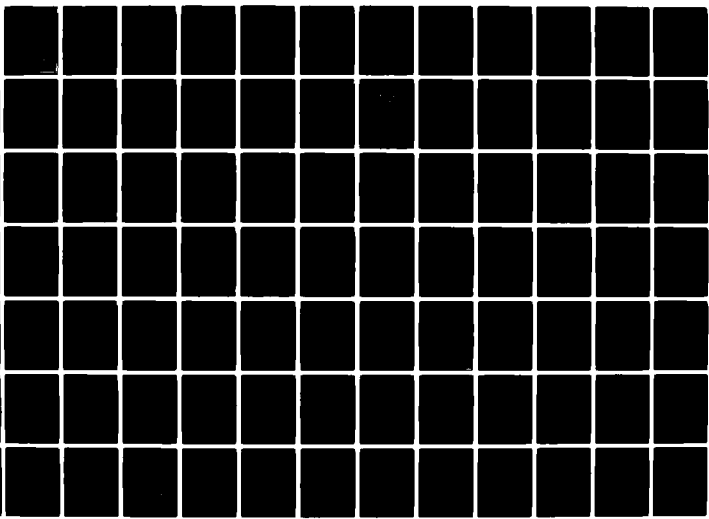
UNCLASSIFIED

DOT-TSC-FAA-79-18-4

DOT/FAA/RD-79-103-VOL-4

NL

1-3
AD
00000



DOT/FAA/RD-79-103, IV
DOT-TSC-FAA-79-18, IV

Chicago Monostatic Acoustic Vortex Sensing System

Volume IV: Wake Vortex Decay

D.C. Burnham
J.N. Hallock

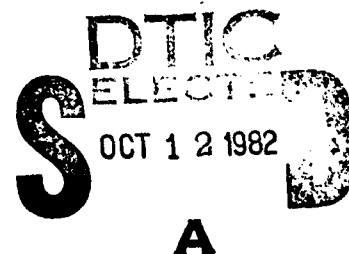
Transportation Systems Center
Cambridge MA 02142

July 1982
Final Report

This document is available to the public
through the National Technical Information
Service, Springfield, Virginia 22161.



U.S. Department of Transportation
Federal Aviation Administration



Systems Research and Development Service
Washington DC 20590

82 10 12 050

AD A120081

DTIC FILE COPY

7

NOTICE

This document is disseminated under the sponsorship of the Department of Transportation in the interest of information exchange. The United States Government assumes no liability for its contents or use thereof.

NOTICE

The United States Government does not endorse products or manufacturers. Trade or manufacturers' names appear herein solely because they are considered essential to the object of this report.

1. Report No. DOT/FAA/RD-79-103,IV	2. Government Accession No. AD-A120 081	3. Recipient's Catalog No.	
4. Title and Subtitle CHICAGO MONOSTATIC ACOUSTIC VORTEX SENSING SYSTEM Volume IV: Wake Vortex Decay		5. Report Date July 1982	
		6. Performing Organization Code	
7. Author(s) D.C. Burnham, J.N. Hallock		8. Performing Organization Report No. DOT-TSC-FAA-79-18, IV	
9. Performing Organization Name and Address U.S. Department of Transportation Research and Special Programs Administration Transportation Systems Center Cambridge, MA 02142		10. Work Unit No. (TRAIS) FA286/R2128	
		11. Contract or Grant No.	
12. Sponsoring Agency Name and Address U.S. Department of Transportation Federal Aviation Administration Systems Research and Development Service Washington, D.C. 20590		13. Type of Report and Period Covered Final Report Oct. 1976 - Dec. 1979	
14. Sponsoring Agency Code ARD-430		15. Supplementary Notes	
16. Abstract A Monostatic Acoustic Vortex Sensing System (MAVSS) was installed at Chicago's O'Hare International Airport to measure the strength and decay of aircraft wake vortices from landing aircraft. The MAVSS consists of an array of acoustic antennas which measure the vertical profile up to 60-m altitude of the vertical component of the wind. The decay in wake vortex strength is measured as the vortex passes over successive antennas in the array. Volume I (published in October 1979, 32 pages) described the MAVSS principles of operation, the hardware developed, and the data reduction methods employed. Volume II (published in September 1981, 162 pages) described the analysis of MAVSS data to examine whether landing B-707 and DC-8 aircraft need to remain divided into Heavy and Large categories on the basis of the wake vortex hazard. Volume III (published in January 1982, 25 pages) summarized the results of Volume II in terms of the safety implications of categorizing all landing B-707s and DC-8s as Large aircraft. In this volume, the statistical methods used to understand wake vortex decay are described and the data on all common jet transport aircraft are presented.			
17. Key Words Wake Vortices Wake Decay Acoustics Vortices		18. Distribution Statement DOCUMENT IS AVAILABLE TO THE PUBLIC THROUGH THE NATIONAL TECHNICAL INFORMATION SERVICE, SPRINGFIELD, VIRGINIA 22161	
19. Security Classif. (of this report) Unclassified	20. Security Classif. (of this page) Unclassified	21. No. of Pages 206	22. Price

PREFACE

An understanding of the statistical nature of aircraft wake vortex decay can lead to improved airport capacity. This report presents statistical data on the decay of wake vortex strength measured with the Monostatic Acoustic Vortex Sensing System (MAVSS). The data might be used to refine the wake vortex aircraft categories (Heavy, Large, and Small), which presently are predicated on gross certificated takeoff weight rather than directly on vortex behavior.

The authors would like to thank Myron Clark for reviewing early drafts of this report and for his many comments toward improving the clarity of an inherently complex analysis.



Accession For	
NTIS GRA&I	<input checked="" type="checkbox"/>
DTIC TAB	<input type="checkbox"/>
Unannounced	<input type="checkbox"/>
Justification	
Distribution/	
Availability Codes	
Avail and/or	
Dist	Special
A	

METRIC CONVERSION FACTORS

Approximate Conversions to Metric Measures				Approximate Conversions from Metric Measures			
Symbol	When You Know	Multiply by	To Find	Symbol	When You Know	Multiply by	To Find
LENGTH				LENGTH			
m	inches	2.5	centimeters	cm	millimeters	0.04	inches
ft	feet	30	centimeters	m	centimeters	0.4	inches
y	yards	0.9	meters	m	meters	2.2	feet
mi	miles	1.6	kilometers	m	kilometers	1.1	yards
AREA				AREA			
sq in	square inches	6.5	square centimeters	sq cm	square centimeters	0.16	square inches
sq ft	square feet	0.09	square meters	sq m	square meters	1.2	square yards
sq yd	square yards	0.8	square meters	sq km	square kilometers	0.4	square miles
ac	square miles	2.6	square kilometers	ha	hectares (10,000 m ²)	2.5	acres
MASS (weight)				MASS (weight)			
oz	ounces	28	grams	g	grams	0.005	ounces
lb	pounds	4.5	kilograms	kg	kilograms	2.2	pounds
sh	short tons (2000 lb)	0.9	tonnes	t	tonnes (1000 kg)	1.1	short tons
VOLUME				VOLUME			
fl oz	fluid ounces	30	milliliters	ml	milliliters	0.03	fluid ounces
cup	cups	240	milliliters	l	liters	2.1	pints
pt	pints	473	milliliters	l	liters	1.4	quarts
qt	quarts	946	milliliters	l	liters	0.26	gallons
gal	gallons	3.8	liters	m ³	cubic meters	26	cubic feet
cu ft	cubic feet	0.03	cubic meters	m ³	cubic meters	1.3	cubic yards
cu yd	cubic yards	0.76	cubic meters	TEMPERATURE (convert)			
TEMPERATURE (convert)				TEMPERATURE (convert)			
F	Fahrenheit temperature	5/9 (after subtracting 32)	Celsius temperature	C	Celsius temperature	9/5 (then add 32)	Fahrenheit temperature

* 1 in = 2.54 exactly. For other exact conversions and more detailed tables, see NIST Spec. Publ. 280, Units of Weight and Measure, NIST 82-35, SD Catalog No. C13.10-280.

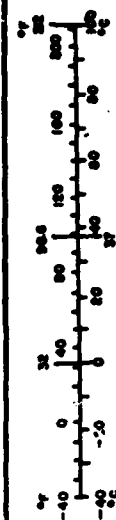


TABLE OF CONTENTS

<u>Section</u>	<u>Page</u>
1. INTRODUCTION AND SUMMARY.....	1-1
1.1 Introduction.....	1-1
1.2 Summary.....	1-2
2. MAVSS MEASUREMENTS.....	2-1
2.1 Vortex Strength.....	2-3
2.2 Vortex Strength History.....	2-8
2.3 Vortex Strength Errors.....	2-9
3. STATISTICS OF VORTEX DECAY.....	3-1
3.1 Vortex Hazard Probability.....	3-1
3.2 Hazard Probability Decay.....	3-2
3.3 Vortex Strength Distribution.....	3-6
4. HAZARD ANALYSIS.....	4-1
4.1 Rolling Moment Hazard Model.....	4-1
4.2 Hazard Decay.....	4-5
5. AIRCRAFT DEPENDENCE OF VORTEX CHARACTERISTICS....	5-1
5.1 Initial Vortex Strength.....	5-1
5.1.1 Theory.....	5-1
5.1.2 Measurements.....	5-5
5.2 Vortex Decay.....	5-14
5.2.1 Average Strength.....	5-14
5.2.2 Hazard Probability.....	5-17
5.2.3 Decay Modeling.....	5-23
5.2.3.1 Unsatisfactory Models.....	5-24
5.2.3.2 Simple Stochastic Model.....	5-26
6. RECATEGORIZATION.....	6-1
6.1 Current Exposure to Vortex Hazards.....	6-2
6.2 Evaluation of a Four-category System.....	6-12
6.3 Heavy-Large Boundary.....	6-15
6.4 Recommendations.....	6-17
6.4.1 Safety Analysis.....	6-17
6.4.2 Category Boundaries.....	6-17

TABLE OF CONTENTS (CONT.)

<u>Section</u>	<u>Page</u>
6.4.3 Operational Questions.....	6-17
6.4.4 United Kingdom Experience.....	6-18
APPENDIX A - MAVSS DETECTION THRESHOLD.....	A-1
APPENDIX B - VORTEX DECAY MODELS.....	B-1
APPENDIX C - VORTEX DECAY PLCTS.....	C-1
APPENDIX D - DECAY OF AVERAGE VORTEX STRENGTH.....	D-1
APPENDIX E - REFERENCES.....	E-1

LIST OF TABLES

<u>Table</u>	<u>Page</u>
1. AVERAGE CIRCULATION CORRECTIONS FOR ERRORS IN CORE RADIUS.....	2-8
2. NUMBER OF MEASURED VORTEX DEATHS.....	2-9
3. MOST PROBABLE INITIAL VORTEX STRENGTH (m^2/sec) FOR LANDING AIRCRAFT.....	3-10
4. INDUCED ROLLING MOMENT CORRECTION FACTORS.....	4-2
5. HAZARD THRESHOLD FOR $f=1$	4-4
6. AIRCRAFT MODEL PARAMETERS.....	5-2
7. AIRCRAFT TYPE PARAMETERS.....	5-3
8. INITIAL VORTEX STRENGTH.....	5-4
9. AVERAGE INITIAL VORTEX STRENGTH (m^2/sec): ALL LANDING VORTEX DETECTIONS BETWEEN 10 AND 15 SECONDS WITH TRANSPORT SPEEDS ABOVE 2 METERS/ SECOND.....	5-6
10. ANALYSIS OF INITIAL VORTEX STRENGTHS.....	5-11
11. VORTEX IFR SEPARATION STANDARDS AT RUNWAY THRESHOLD.....	6-3

LIST OF TABLES (CONT.)

<u>Table</u>	<u>Page</u>
12. HAZARD PROBABILITY AT CURRENT MINIMUM SEPARATION FOR $f=1.0$	6-4
13. HAZARD PROBABILITY AT CURRENT MINIMUM SEPARATION FOR $f=0.5$	6-5
14. SENSITIVITY ANALYSIS VARIATIONS.....	6-10
15. PROPOSED FOUR CATEGORY IFR RUNWAY THRESHOLD SEPARATION.....	6-13
16. COMPARISON OF SAFE SEPARATIONS FOR THE DC-8 AND THE B-707H.....	6-16
17. PARAMETERS FOR FIT TO DATA IN FIGURE 5.....	B-2

LIST OF FIGURES

<u>Figure</u>	<u>Page</u>
1. MAVSS DATA: (a) VORTEX TRAJECTORIES, (b) VELOCITY SIGNATURES.....	2-2
2. MODEL PROFILES: (a) VELOCITY, (b) CIRCULATION, (c) AVERAGE CIRCULATION.....	2-4
3. DEPENDENCE OF $\Gamma'(a)/\Gamma'(b)$ UPON r_c/a FOR TWO VALUES OF a/b . THE SCALE CHANGES FROM LINEAR TO LOGARITHMIC AT $r_c/a = 0.2$	2-7
4. HAZARD PROBABILITY VERSUS VORTEX AGE FOR ALL B-707 VORTICES FOR $\Gamma_T = 100 \text{ m}^2/\text{SEC}$ AND 10-m SEMISPAN.....	3-3
5. HAZARD PROBABILITY FOR 10-METER SEMISPAN VERSUS VORTEX AGE SQUARED FOR ALL B-707 VORTICES AND FIVE VALUES OF $\Gamma_T \text{ (m}^2/\text{sec)}$	3-4
6. DISTRIBUTION OF VORTEX STRENGTH $\Gamma'(10\text{m})$ FOR ALL B-707 LANDING VORTICES.....	3-8
7. PROBABILITY OF NONZERO VORTEX STRENGTH $\Gamma'(10\text{m})$ VERSUS AGE FOR ALL B-707 LANDING VORTICES.....	3-9
8. WINGSPAN DEPENDENCE OF VORTEX HAZARD.....	4-3

LIST OF FIGURES (CONT.)

<u>Figure</u>		<u>Page</u>
9.	COMPARISON OF VORTEX DECAY FOR VORTEX 1 AND VORTEX 2; B-707 AIRCRAFT, 10-m AVERAGING RADIUS.....	4-6
10.	COMPARISON OF VORTEX DECAY FOR VORTEX 1 AND VORTEX 2 FOR THE SAME PARAMETERS AS FIGURE 9, BUT EXCLUDING THE EXTRAPOLATION TO ZERO TIME BEFORE THE FIRST VORTEX DETECTION OCCURS.....	4-7
11.	DECAY OF AVERAGE VORTEX STRENGTH FOR ALL B-747 DETECTED VORTICES: AVERAGING RADIUS = 5 m (lower line), 10 m (middle line), AND 20 m (upper line).....	5-7
12.	DECAY OF AVERAGE VORTEX STRENGTH FOR ALL B-707 DETECTED VORTICES: AVERAGING RADIUS = 5 m (lower line), 10 m (middle line), and 20 m (upper line).....	5-8
13.	DECAY OF AVERAGE VORTEX STRENGTH FOR ALL DC-8 DETECTED VORTICES: AVERAGING RADIUS = 5 m (lower line), 10 m (middle line), and 20 m (upper line).....	5-9
14.	COMPARISON OF MEASURED TO CALCULATED VORTEX CIRCULATIONS.....	5-13
15.	DEPENDENCE OF MEASURED VORTEX CIRCULATION UPON AIRCRAFT WINGSPAN: (a) 10-15 SECOND AGE, (b) LINEAR DECAY INTERCEPT.....	5-15
16.	COMPARISON OF TWO CIRCULATION VALUES: LINEAR DECAY INTERCEPT VERSUS 10-15 SECOND AGE AVERAGE..	5-16
17.	TIME TO REACH A GIVEN HAZARD PROBABILITY VERSUS NORMALIZED HAZARD THRESHOLD Γ_T/Γ_0 : (a) VORTEX 1, (b) VORTEX 2. CURVES: 1) $F = 0.2$, 2) $F = 0.1$, 3) $F = 0.05$, 4) $F = 0.02$, 5) $F = 0.01$, AND 6) $F = 0.005$	5-19
18.	TIME TO REACH A GIVEN HAZARD PROBABILITY VERSUS NORMALIZED THRESHOLD Γ_T/Γ_0 FOR THREE AVERAGING RADII: 5 METERS (narrow/lines), 10 METERS (medium lines) AND 20 METERS (broad lines).....	5-20

LIST OF FIGURES (CONT.)

<u>Figure</u>		<u>Page</u>
19.	COMPARISONS OF NORMALIZED VORTEX HAZARD DECAY CURVES FOR ALL AIRCRAFT TYPES; $F = 0.05$, VORTEX 2, AVERAGING RADIUS = 5, 10, AND 20 METERS: (a) Γ_0 INITIAL VALUES, (b) Γ_0 ADJUSTED TO GIVE GOOD AGREEMENT FOR 10 METERS AVERAGING RADIUS.....	5-21
20.	EFFECTIVE VORTEX STRENGTH FOR DETERMINING THE DECAY OF THE WAKE VORTEX HAZARD.....	5-25
21.	FITTED PROBABILITY DECAY CURVES FOR THE DC-8 15-METER AVERAGING RADIUS, AND VORTEX 2. THE SIX CURVES REPRESENT Γ_T' VALUES OF 200, 150, 100, 75, 50, and 30 m^2/sec , RESPECTIVELY, FROM LEFT TO RIGHT. THE MEASURED DATA ARE PLOTTED WITH THICKER LINES THAN THE FITTED CURVES. THE NUMBERS BELOW THE CURVES ARE THE VALUES OF σ (sec) FOR EACH CURVE.....	5-28
22.	FITTED PROBABILITY DECAY CURVES USING TWO PARAMETERS, Γ_0' AND σ	5-29
23.	SAFE HAZARD PROBABILITY F_s VERSUS THE ASSUMED SAFE LIMIT f_s ON THE RATIO OF VORTEX INDUCED ROLL TO MAXIMUM ROLL CONTROL.....	6-7
24.	SAFE SEPARATION TIMES FOR AIRCRAFT CATEGORIES AS A FUNCTION OF FOLLOWING AIRCRAFT SEMISPAN: SOLID POINTS, $f/f_s = 1$; OPEN POINTS, VARIATION IN f/f_s GIVEN IN TABLE 14.....	6-11
25.	VORTEX STRENGTH VERSUS AVERAGE CORRELATION VELOCITY V_c FOR A SAMPLE OF B-707 AND DC-8 VORTICES.....	A-3
26.	DISTRIBUTION OF DETECTED VORTEX STRENGTHS FOR FOUR AIRCRAFT.....	A-4
27.	COMPARISONS OF MODEL HAZARD PROBABILITY (STRAIGHT LINES) WITH MEASUREMENTS (LINES WITH POINTS) FOR ALL B-707 VORTICES WITH 10-METER AVERAGING. THE VALUES OF Γ_T' (m^2/sec) ARE INDICATED.....	B-5
28.	COMPARISONS OF MODEL PROBABILITY DISTRIBUTIONS (STRAIGHT LINES) WITH MEASUREMENTS (LINES WITH POINTS) FOR ALL B-707 VORTICES WITH 10-METER AVERAGING. THE TIMES (sec) AT WHICH THE DISTRIBUTION IS EVALUATED ARE INDICATED.....	B-6

LIST OF FIGURES (CONT.)

<u>Figure</u>		<u>Page</u>
29.	VORTEX DECAY FOR THE STOCHASTIC MODEL WITH t_0 = 3σ AND $n = 2$	B-9
30.	DEPENDENCE OF THE TIME TO REACH A PARTICULAR HAZARD PROBABILITY UPON THE HAZARD STRENGTH THRESHOLD.....	B-11
31.	LEAST-SQUARE FIT TO VORTEX DECAY: ALL B-727 VORTICES.....	B-13
32.	LEAST-SQUARE FIT TO VORTEX DECAY: ALL B-747 VORTICES.....	B-14
33.	RMS ERRORS FOR ALL AIRCRAFT TYPES.....	B-16
34.	AIRCRAFT DEPENDENCE OF VORTEX HAZARD DURATION FOR $\Gamma_T'/\Gamma_0' = 1$	B-18
35.	LEAST-SQUARE FITS TO DISAGGREGATED B-707 AND B-727 DATA.....	B-19
36.	LEAST-SQUARE FITS WITH ONE FREE PARAMETER t_0 ($\sigma = 10$ SECONDS, $n = 2$).....	B-21
37.	DEPENDENCE OF THE TIME TO REACH A PARTICULAR HAZARD PROBABILITY UPON THE HAZARD STRENGTH THRESHOLD, INCLUDING THE EFFECTS OF THE INITIAL STRENGTH DISTRIBUTION.....	B-23
38.	FITTED PROBABILITY DECAY CURVES FOR THE B-707, 10-METER AVERAGING RADIUS, AND VORTEX 2.....	B-24
39.	FITTED PROBABILITY DECAY CURVES USING TWO PARAMETERS, Γ_T' AND σ	B-25
40.	VALUES OF SIGMA USED TO CHARACTERIZE THE VORTEX 1 AND 2 HAZARD DURATION.....	B-27
41.	PROBABILITY OF DECAY, B-747, VORTEX 1 AND 2, 5-m AVERAGING RADIUS.....	C-2
42.	PROBABILITY OF DECAY, B-747, WINDS LESS THAN 8 KNOTS, 5-m AVERAGING RADIUS.....	C-3
43.	PROBABILITY OF DECAY, B-747, VORTEX 1 AND 2, 10-m AVERAGING RADIUS.....	C-4

LIST OF FIGURES (CONT.)

<u>Figure</u>		<u>Page</u>
44.	PROBABILITY OF DECAY, B-747, WINDS LESS THAN 8 KNOTS, 10-m AVERAGING RADIUS.....	C-5
45.	PROBABILITY OF DECAY, B-747, VORTEX 1 AND 2, 15-m AVERAGING RADIUS.....	C-6
46.	PROBABILITY OF DECAY, B-747, WINDS LESS THAN 8 KNOTS, 15-m AVERAGING RADIUS.....	C-7
47.	PROBABILITY OF DECAY, B-747, VORTEX 1 AND 2, 20-m AVERAGING RADIUS.....	C-8
48.	PROBABILITY OF DECAY, B-747, WINDS LESS THAN 8 KNOTS, 20-m AVERAGING RADIUS.....	C-9
49.	PROBABILITY OF DECAY, DC-10, VORTEX 1 AND 2, 5-m AVERAGING RADIUS.....	C-10
50.	PROBABILITY OF DECAY, DC-10, WINDS LESS THAN 8 KNOTS, 5-m AVERAGING RADIUS.....	C-11
51.	PROBABILITY OF DECAY, DC-10, VORTEX 1 AND 2, 10-m AVERAGING RADIUS.....	C-12
52.	PROBABILITY OF DECAY, DC-10, WINDS LESS THAN 10 KNOTS, 10-m AVERAGING RADIUS.....	C-13
53.	PROBABILITY OF DECAY, DC-10, VORTEX 1 AND 2, 15-m AVERAGING RADIUS.....	C-14
54.	PROBABILITY OF DECAY, DC-10, WINDS LESS THAN 8 KNOTS, 15-m AVERAGING RADIUS.....	C-15
55.	PROBABILITY OF DECAY, DC-10, VORTEX 1 AND 2, 20-m AVERAGING RADIUS.....	C-16
56.	PROBABILITY OF DECAY, DC-10, WINDS LESS THAN 8 KNOTS, 20-m AVERAGING RADIUS.....	C-17
57.	PROBABILITY OF DECAY, L-1011, VORTEX 1 AND 2, 5-m AVERAGING RADIUS.....	C-18
58.	PROBABILITY OF DECAY, L-1011, WINDS LESS THAN 8 KNOTS, 5-m AVERAGING RADIUS.....	C-19

LIST OF FIGURES (CONT.)

<u>Figure</u>		<u>Page</u>
59.	PROBABILITY OF DECAY, L-1011, VORTEX 1 AND 2, 10-m AVERAGING RADIUS.....	C-20
60.	PROBABILITY OF DECAY, L-1011, WINDS LESS THAN 8 KNOTS, 10-m AVERAGING RADIUS.....	C-21
61.	PROBABILITY OF DECAY, L-1011, VORTEX 1 AND 2, 15-m AVERAGING RADIUS.....	C-22
62.	PROBABILITY OF DECAY, L-1011, WINDS LESS THAN 8 KNOTS, 15-m AVERAGING RADIUS.....	C-23
63.	PROBABILITY OF DECAY, L-1011, VORTEX 1 AND 2, 20-m AVERAGING RADIUS.....	C-24
64.	PROBABILITY OF DECAY, L-1011, WINDS LESS THAN 8 KNOTS, 20-m AVERAGING RADIUS.....	C-25
65.	PROBABILITY OF DECAY, DC-8 AND DC-8H, VORTEX 1 AND 2, 5-m AVERAGING RADIUS.....	C-26
66.	PROBABILITY OF DECAY, DC-8 AND DC-8H, WINDS LESS THAN 8 KNOTS, 5-m AVERAGING RADIUS.....	C-27
67.	PROBABILITY OF DECAY, DC-8 and DC-8H, VORTEX 1 AND 2, 10-m AVERAGING RADIUS.....	C-28
68.	PROBABILITY OF DECAY, DC-8 AND DC-8H, WINDS LESS THAN 8 KNOTS, 10-m AVERAGING RADIUS.....	C-29
69.	PROBABILITY OF DECAY, DC-8 AND DC-8H, VORTEX 1 AND 2, 15-m AVERAGING RADIUS.....	C-30
70.	PROBABILITY OF DECAY, DC-8 AND DC-8H, WINDS LESS THAN 8 KNOTS, 15-m AVERAGING RADIUS.....	C-31
71.	PROBABILITY OF DECAY, DC-8 AND DC-8H, VORTEX 1 AND 2, 20-m AVERAGING RADIUS.....	C-32
72.	PROBABILITY OF DECAY, DC-8 AND DC-8H, WINDS LESS THAN 8 KNOTS, 20-m AVERAGING RADIUS.....	C-33
73.	PROBABILITY OF DECAY, B-707 AND B-707H, VORTEX 1 AND 2, 5-m AVERAGING RADIUS.....	C-34

LIST OF FIGURES (CONT.)

<u>Figure</u>		<u>Page</u>
74.	PROBABILITY OF DECAY, B-707 AND B-707H, WINDS LESS THAN 8 KNOTS, 5-m AVERAGING RADIUS.....	C-35
75.	PROBABILITY OF DECAY, B-707 AND B-707H, VORTEX 1 AND 2, 10-m AVERAGING RADIUS.....	C-36
76.	PROBABILITY OF DECAY, B-707 AND B-707H, WINDS LESS THAN 8 KNOTS, 10-m AVERAGING RADIUS.....	C-37
77.	PROBABILITY OF DECAY, B-707 AND B-707H, VORTEX 1 AND 2, 15-m AVERAGING RADIUS.....	C-38
78.	PROBABILITY OF DECAY, B-707 AND B-707H, WINDS LESS THAN 8 KNOTS, 15-m AVERAGING RADIUS.....	C-39
79.	PROBABILITY OF DECAY, B-707 AND B-707H, VORTEX 1 AND 2, 20-m AVERAGING RADIUS.....	C-40
80.	PROBABILITY OF DECAY, B-707 AND B-707H, WINDS LESS THAN 8 KNOTS, 20-m AVERAGING RADIUS.....	C-41
81.	PROBABILITY OF DECAY, B-727, VORTEX 1 AND 2, 5-m AVERAGING RADIUS.....	C-42
82.	PROBABILITY OF DECAY, B-727, WINDS LESS THAN 8 KNOTS, 5-m AVERAGING RADIUS.....	C-43
83.	PROBABILITY OF DECAY, B-727, VORTEX 1 AND 2, 10-m AVERAGING RADIUS.....	C-44
84.	PROBABILITY OF DECAY, B-727, WINDS LESS THAN 8 KNOTS, 10-m AVERAGING RADIUS.....	C-45
85.	PROBABILITY OF DECAY, B-727, VORTEX 1 AND 2, 15-m AVERAGING RADIUS.....	C-46
86.	PROBABILITY OF DECAY, B-727, WINDS LESS THAN 8 KNOTS, 15-m AVERAGING RADIUS.....	C-47
87.	PROBABILITY OF DECAY, B-727, VORTEX 1 AND 2, 20-m AVERAGING RADIUS.....	C-48
88.	PROBABILITY OF DECAY, B-727, WINDS LESS THAN 8 KNOTS, 20-m AVERAGING RADIUS.....	C-49
89.	PROBABILITY OF DECAY, B-737, VORTEX 1 AND 2, 5-m AVERAGING RADIUS.....	C-50

LIST OF FIGURES (CONT.)

<u>Figure</u>		<u>Page</u>
90.	PROBABILITY OF DECAY, B-737, WINDS LESS THAN 8 KNOTS, 5-m AVERAGING RADIUS.....	C-51
91.	PROBABILITY OF DECAY, B-737, VORTEX 1 AND 2, 10-m AVERAGING RADIUS.....	C-52
92.	PROBABILITY OF DECAY, B-737, WINDS LESS THAN 8 KNOTS, 10-m AVERAGING RADIUS.....	C-53
93.	PROBABILITY OF DECAY, B-737, VORTEX 1 AND 2, 15-m AVERAGING RADIUS.....	C-54
94.	PROBABILITY OF DECAY, B-737, WINDS LESS THAN 8 KNOTS, 15-m AVERAGING RADIUS.....	C-55
95.	PROBABILITY OF DECAY, B-737, VORTEX 1 AND 2, 20-m AVERAGING RADIUS.....	C-56
96.	PROBABILITY OF DECAY, B-737, WINDS LESS THAN 8 KNOTS, 20-m AVERAGING RADIUS.....	C-57
97.	PROBABILITY OF DECAY, DC-9, VORTEX 1 AND 2, 5-m AVERAGING RADIUS.....	C-58
98.	PROBABILITY OF DECAY, DC-9, WINDS LESS THAN 8 KNOTS, 5-m AVERAGING RADIUS.....	C-59
99.	PROBABILITY OF DECAY, DC-9, VORTEX 1 AND 2, 10-m AVERAGING RADIUS.....	C-60
100.	PROBABILITY OF DECAY, DC-9, WINDS LESS THAN 8 KNOTS, 10-m AVERAGING RADIUS.....	C-61
101.	PROBABILITY OF DECAY, DC-9, VORTEX 1 AND 2, 15-m AVERAGING RADIUS.....	C-62
102.	PROBABILITY OF DECAY, DC-9, WINDS LESS THAN 8 KNOTS, 15-m AVERAGING RADIUS.....	C-63
103.	PROBABILITY OF DECAY, DC-9, VORTEX 1 AND 2, 20-m AVERAGING RADIUS.....	C-64
104.	PROBABILITY OF DECAY, DC-9, WINDS LESS THAN 8 KNOTS, 20-m AVERAGING RADIUS.....	C-65
105.	DECAY OF AVERAGE VORTEX STRENGTH FOR ALL DC-10 DETECTED VORTICES.....	D-2

LIST OF FIGURES (CONT.)

<u>Figure</u>		<u>Page</u>
106.	DECAY OF AVERAGE VORTEX STRENGTH FOR ALL L-1011 DETECTED VORTICES.....	D-3
107.	DECAY OF AVERAGE VORTEX STRENGTH FOR ALL DC-8H DETECTED VORTICES.....	D-4
108.	DECAY OF AVERAGE VORTEX STRENGTH FOR ALL B-707H DETECTED VORTICES.....	D-5
109.	DECAY OF AVERAGE VORTEX STRENGTH FOR ALL B-727 DETECTED VORTICES.....	D-6
110.	DECAY OF AVERAGE VORTEX STRENGTH FOR ALL B-737 DETECTED VORTICES.....	D-7
111.	DECAY OF AVERAGE VORTEX STRENGTH FOR ALL DC-9 DETECTED VORTICES.....	D-8

1. INTRODUCTION AND SUMMARY

1.1 INTRODUCTION

The operational hazard to air traffic posed by aircraft wake vortices is ultimately limited by the decay of the strength of the organized vortical motion. Experiments have shown that the decay can take several forms, generally occurs rapidly once it begins, and is a consequence of an instability in the vortex configuration.

Persistence of the wake vortex hazard depends upon aircraft parameters (wingspan, weight, configuration, engine location, etc.), meteorological parameters (wind velocity, wind shear, turbulence, atmospheric stability, pressure, etc.), and decay processes (vortex linking, bursting, and turbulent diffusion). Since the decay processes occur at random even when all the parameters are fixed, the persistence of a vortex can be defined only through a probability.

The current designation of wake vortex separation categories assigns the wake vortex hazard to a single aircraft parameter, the maximum certificated gross takeoff weight. Of necessity, this simplified procedure gives only a rough indication of the wake vortex hazard. The actual hazard persistence for a specified aircraft has a wide spread because of variations in the aircraft parameters, variation in the meteorological conditions, and the stochastic nature of vortex decay.

It is envisioned that eventually aircraft categories will be set based on an understanding of what aircraft parameters in addition to weight should be included. Wingspan must certainly play a role, and engine placement is also likely to be important. This report examines these issues. If vortex decay can be characterized by a few aircraft parameters, then one can hope to have a more rational system of dealing with the wake vortex hazard.

Between July 1976 and September 1977 TSC collected data at Chicago's O'Hare International Airport on the decay of wake vortex strength. The Monostatic Acoustic Vortex Sensing System (MAVSS), the remote sensing technique employed, makes use of sound energy scattered from temperature fluctuations to measure the velocity profile of a vortex. Volume I of this report (Ref. 1) described the hardware and data processing involved in these measurements. The data were collected during normal airport landing operations. Volume II (Ref. 2) described the analysis of whether landing B-707 and DC-8 aircraft need to be divided into Heavy and Large categories on the basis of their wake-vortex hazard. The results of the study indicate that all landing B-707 and DC-8 aircraft may be included in the Large wake-vortex category. Volume III (Ref. 3) summarized the results of Volume II in terms of safety implications of categorizing all landing B-707s and DC-8s as Large aircraft. This report (Volume IV in the four-volume series) describes the various statistical methods used to understand wake vortex decay and presents data on all common jet transport aircraft.

Section 2 outlines the data processing procedures and describes in detail the methods used to analyze the MAVSS data and their limitations. Section 3 introduces statistical models of vortex decay. Section 4 discusses a hazard model which is used to relate the MAVSS vortex strength measurements to an encounter hazard for a following aircraft. Section 5 relates the wake vortex characteristics of an aircraft to its physical parameters such as wingspan, weight, engine placement, etc. Empirical models of vortex decay are developed; two theoretical models extensively used in the literature are shown to be unrealistic. In Section 6 a preliminary look at recategorizing aircraft based on vortex behavior is presented.

1.2 SUMMARY

The maximum certificated gross weight is not a particularly good parameter for classifying aircraft as vortex generators or vortex encounterers. Wingspan is the best parameter for

characterizing a vortex encounterer. Wingspan with some corrections for engine placement can also be used to characterize jet transports as vortex generators. A combination of weight and wingspan is likely to be needed to characterize vortex-generating aircraft with wing loading significantly different from that of jet transports.

The decay of wake vortex strength can be represented by a simple model which contains a few aircraft-dependent parameters. The decay-time parameter is observed to depend much less upon aircraft size than has normally been assumed.

The modeled vortex decay was used to evaluate the safe separation vortexwise between pairs of aircraft under the assumption that the hazard probabilities for the current separation standards are acceptable for aircraft pairs which occur frequently. The resulting safe separations are then used to evaluate briefly a four-category separation system. This system appears to offer the possibility of improved safety while simultaneously relieving congestion at the major hub airports. Recommendations for further analysis are presented, if the four-category system is judged to have operational merit.

2. MAVSS MEASUREMENTS

The method of processing the Monostatic Acoustic Vortex Sensing System (MAVSS) data is described in detail in Volume I of this report (Ref. 1). Only a summary will be presented here. The methods used to analyze the MAVSS data and their limitations, however, will be examined in detail herein.

A single MAVSS antenna as used here is equivalent to a 60 (or 90-) meter tower with 16 evenly-spaced vertically-pointing single-axis anemometers. It measures the vertical component of the wind at 16 levels or range gates every 0.4 (or 0.6) seconds with a vertical resolution of 3.5 (or 5.2) meters and a horizontal resolution of about 2 meters. The 90-meter range (0.6-second sample rate) was used for aircraft taking off (Ref. 4). The remote sensing capability of the MAVSS provides two major advantages over the equivalent instrumented tower: 1) it does not protrude into the airspace so as to pose a safety hazard to aircraft, and 2) it does not influence the decay of the vortices being measured.

The actual MAVSS installation consists of an array of up to 10 antennas positioned along a baseline perpendicular to the aircraft flight path. A measurement of vortex strength is made whenever a vortex drifts over an antenna in the array. When the ambient wind is appropriate, a vortex will drift past many antennas and the measurements will show how the vortex decays with time. Figure 1a shows the MAVSS trajectories of the two counterrotating vortices generated by an aircraft taking off. The vertical velocity signatures of the vortices are shown in Figure 1b for each vortex detection at an antenna. The vortex height is determined by the range gate showing the highest velocities. The vortex arrival time is indicated by the change in sign of the velocity. The transport velocity of a vortex, measured by the arrival times at successive antennas, is used to convert the velocity time histories to the spatial velocity profiles in Figure 1b. One of the primary reasons for the success of the MAVSS is that it is insensitive to the ambient wind which is horizontal near the

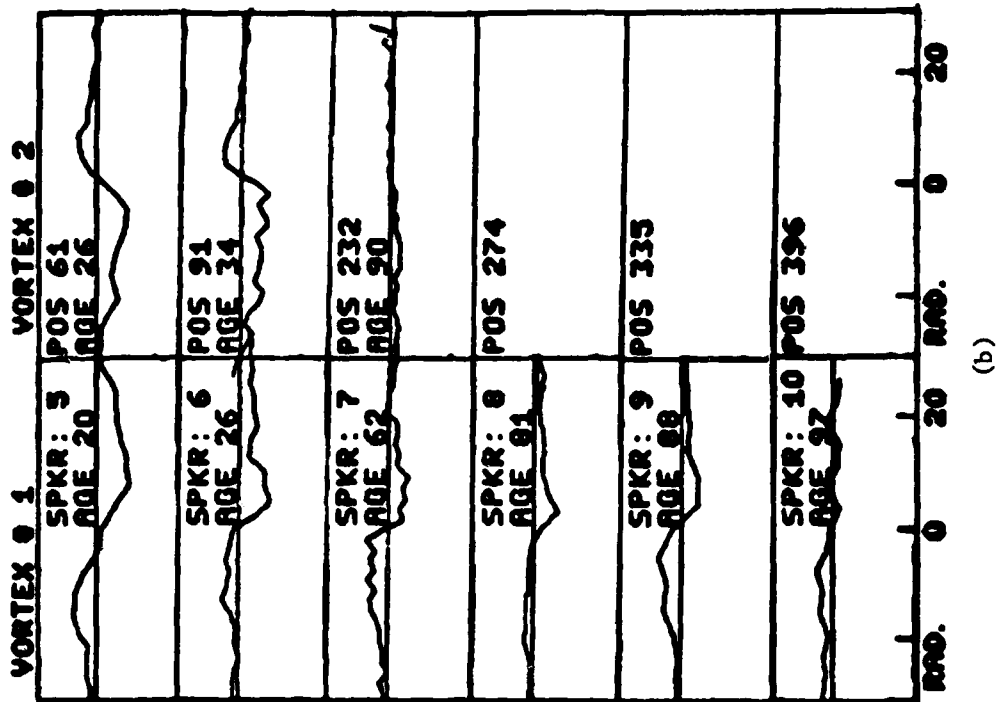
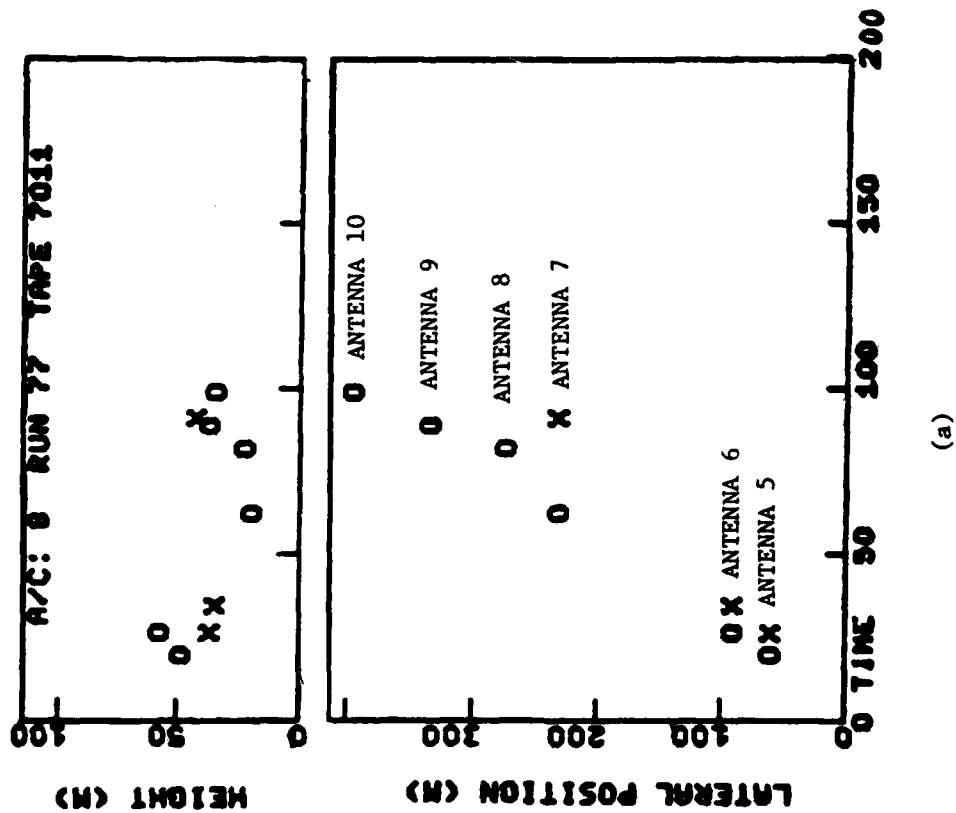


FIGURE 1. MAVSS DATA: (a) VORTEX TRAJECTORIES, (b) VELOCITY SIGNATURES

ground. Any departure of the vertical velocity from zero can be attributed to the aircraft wake. Moreover, the vertical velocity profile at the vortex height is a good measurement of the vortex tangential velocity profile under the assumption of axial symmetry.

Appendix A studies the detection threshold of the MAVSS which plays an important role in the analysis of vortex decay. Reference 1 contains background information on the MAVSS and Appendix C of Reference 5 addresses the error limitations of the MAVSS.

2.1 VORTEX STRENGTH

The velocity profile $V(r)$, where r is the vortex radius, measured by the MAVSS can be converted to the circulation or strength profile $\Gamma(r)$ by the relationship:

$$\Gamma(r) = 2\pi r V(r). \quad (1)$$

Figure 2 shows the relationship between $V(r)$ and $\Gamma(r)$ for an ideal vortex which is described by the following circulation profile:

$$\Gamma(r) = \Gamma_{\infty} / (1 + (r_c/r)^2), \quad (2)$$

where Γ_{∞} is the circulation at large radii and r_c is the core radius which represents the point where $V(r)$ is maximum and also where $\Gamma(r_c)$ is half of Γ_{∞} .

The parameter used to evaluate the vortex hazard is the average circulation,

$$\Gamma'(r) = \frac{1}{r} \int_0^r \Gamma(r') dr'. \quad (3)$$

The integral can be carried out for the form in Equation 2 to yield

$$\Gamma'(r) = \Gamma_{\infty} [1 - (r_c/r) \tan^{-1}(r/r_c)]. \quad (4)$$

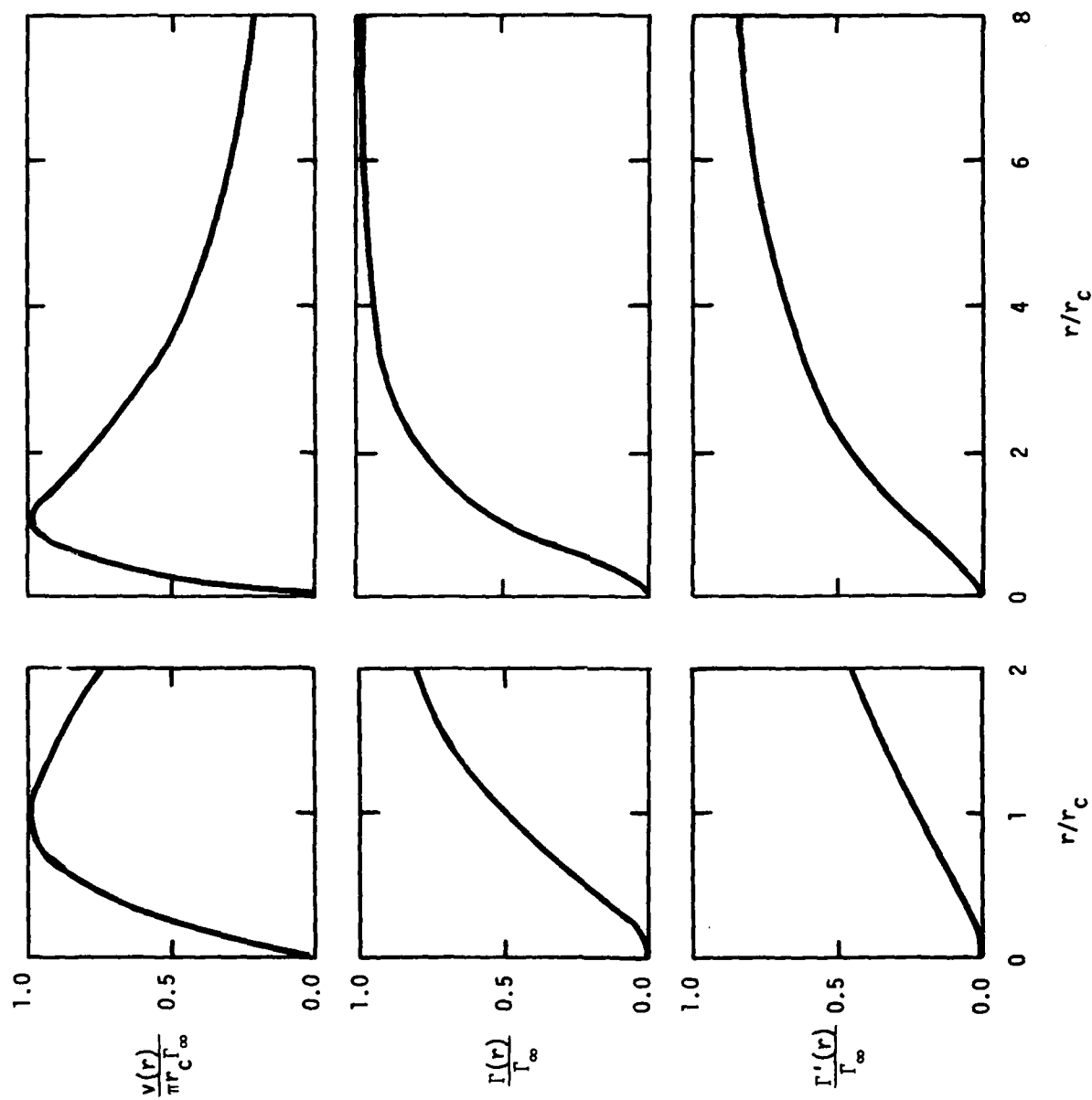


FIGURE 2. MODEL VORTEX PROFILES: (a) VELOCITY, (b) CIRCULATION, (c) AVERAGE CIRCULATION

Figure 2 also shows how $\Gamma'(r)$ compares to $V(r)$ and $\Gamma(r)$. $\Gamma'(r)$ approaches the limiting value Γ_∞ much more slowly than does $\Gamma(r)$. The average value is kept below Γ_∞ by the region of low $\Gamma(r)$ below about $2r_c$.

The MAVSS actually makes two measurements of $V(r)$, one on either side of the vortex core (see Figure 1b). To eliminate some systematic errors, values of Γ' are accepted only if the data from both sides can be averaged. The values of Γ' for four values of averaging radius (5, 10, 20, and 30 meters) are stored in a data base. Values for 15-meter averaging radius are subsequently obtained by interpolation.

The use of average circulation to characterize vortex strength has the advantage of giving a more stable value compared to other ways of processing the data, such as making a least-squares fit to a model such as Equation 2 (Ref. 13). The stored values of Γ' can be used, nevertheless, to estimate effective values of Γ_∞ and r_c . This process is particularly useful if $\Gamma'(r)$ is averaged over many cases before Γ_∞ and r_c are estimated. If $\Gamma'(r)$ is known for two values of r (a and b), then one can calculate the average of the circulation between radius a and radius b :

$$\begin{aligned}\Gamma'(a,b) &= \frac{1}{(b-a)} \int_a^b \Gamma(r) dr \\ &= (b\Gamma'(b) - a\Gamma'(a))/(b-a).\end{aligned}\tag{5}$$

If the core radius is 5 m or less, then the integral between 10 and 20 m gives a reasonable estimate of Γ_∞ . This estimate can be improved if the core radius is estimated. Equation 4 can be used to evaluate the ratio of the two average circulations:

$$\frac{\Gamma'(a)}{\Gamma'(b)} = \frac{1 - (r_c/a) \tan^{-1}(a/r_c)}{1 - (r_c/b) \tan^{-1}(b/r_c)}.\tag{6}$$

This equation can be solved graphically for r_c (see Figure 3). One can then use r_c in Equation 4 to estimate Γ_∞ . This method of analyzing the data depends primarily on the area of the circulation deficit for $r < 2r_c$ and is not sensitive to the actual shape of the vortex circulation profile.

This method of using r_c to represent the area of the $\Gamma(r)$ deficit for $r < 2r_c$ can also be used to correct for one of the MAVSS systematic errors, namely an underestimate of the vortex velocity for small vortex radii. Four effects contribute to this error: (1) The coarse spatial resolution of the MAVSS smears out the center of the vortex. (2) The very high velocities (up to 60 m/sec) present in some vortices cannot be detected because the MAVSS bandwidth and processing cut off any Doppler signals above approximately 13 m/sec. (3) The laminar flow in vortex cores tends to suppress the turbulence which is responsible for producing the MAVSS signals. (4) For rapidly moving vortices the sampling rate is too slow (0.4 or 0.6 seconds/sample) to accurately characterize the vortex core; for 10 m/sec, the highest transport velocity accepted for vortex analysis, the sample spacing is 4 or 6 meters. The loss in MAVSS signal at small radii will increase the area of the $\Gamma(r)$ deficit and lead to a larger r_c but with the same value of Γ_∞ . If r_{ca} is the actual core radius, then the actual average circulation $\Gamma'_a(r)$ is related to the measured values of $\Gamma'(r)$ and r_c by

$$\Gamma'_a(r) = \Gamma'(r) \frac{(1 - (r_{ca}/r) \tan^{-1}(r/r_{ca}))}{(1 - (r_c/r) \tan^{-1}(r/r_c))} . \quad (7)$$

Table 1 illustrates the sorts of errors which can arise for some estimates of core radius to be encountered in subsequent analysis. The corrections can be substantial especially for 5-meter average radius. The measured values of r_c (shown later in Table 10) are roughly 5.5 m for widebody aircraft and 4.0 m for other aircraft types. The core size for small aircraft with no wing-mounted engines, such as the DC-9 and the B-727, could be as small as 0.5 meters. Aircraft with four wing-mounted engines tend to have larger core sizes.

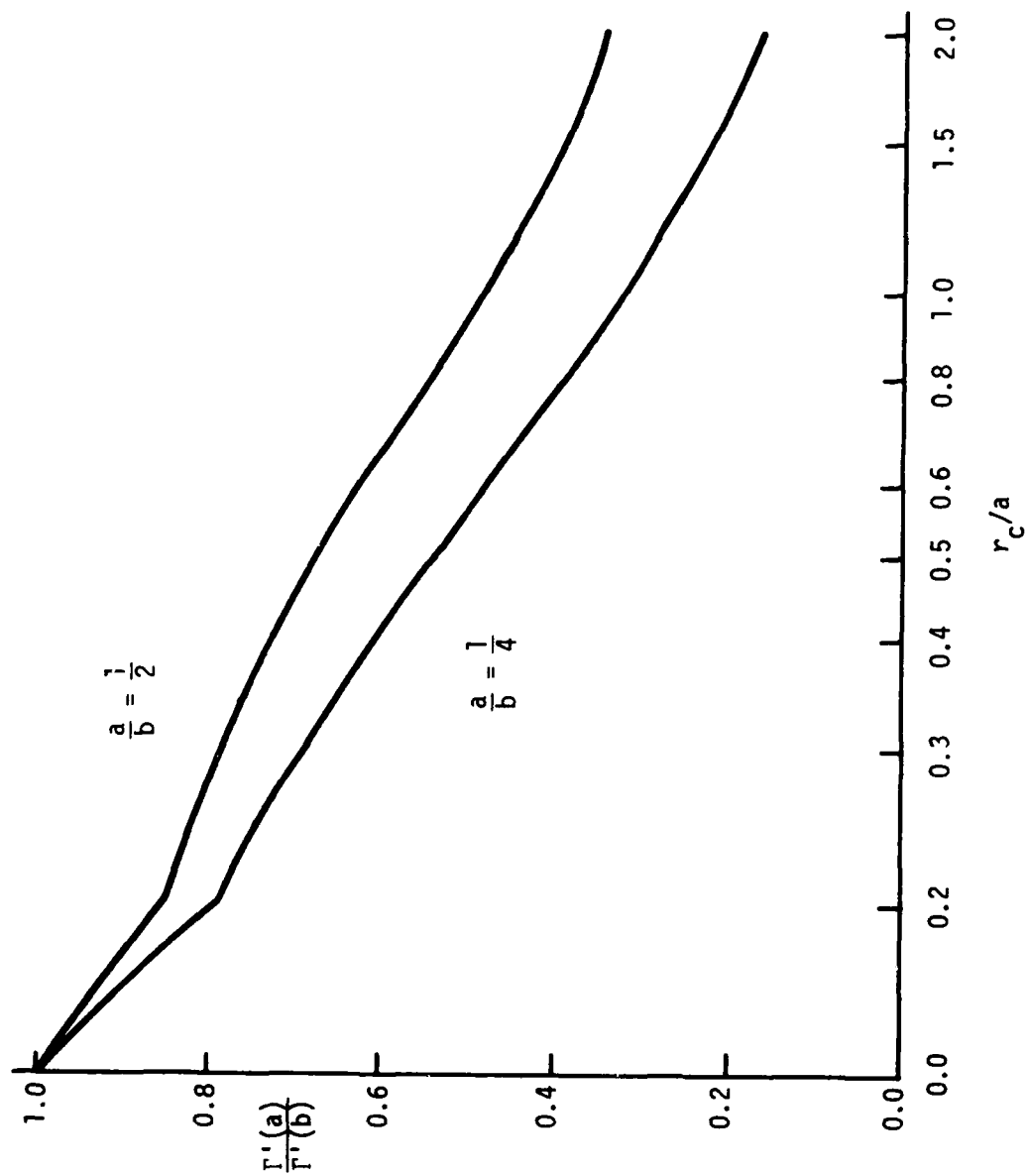


FIGURE 3. DEPENDENCE OF $\Gamma'(a)/\Gamma'(b)$ UPON r_c/a FOR TWO VALUES OF a/b . THE SCALE CHANGES FROM LINEAR TO LOGARITHMIC AT $r_c/a = 0.2$.

TABLE 1. AVERAGE CIRCULATION CORRECTIONS FOR ERRORS IN CORE RADIUS

r_{ca} (m)	r_c (m)	$\Gamma'_a(r)/\Gamma'(r)$			
		$r = 5$ m	$r = 10$ m	$r = 15$ m	$r = 20$ m
0.5	4.0	3.01	1.76	1.46	1.33
1.5	4.0	2.18	1.50	1.31	1.22
2.5	4.0	1.58	1.28	1.18	1.13
2.5	5.0	2.37	1.62	1.38	1.28

2.2 VORTEX STRENGTH HISTORY

The primary method selected for analyzing the MAVSS data requires that the time history of the vortex strength (i.e., average circulation) be known for each vortex measured. The MAVSS data base contains strength values only at times when a vortex passes over an antenna in the array. These values are processed by a combination of interpolation and extrapolation techniques to obtain a time history of the vortex strength. The following assumptions are made:

1. The vortex strength is constant until the vortex is first detected.
2. The vortex strength is obtained by interpolation between successive vortex detections.
3. The vortex strength is assumed to be zero if it cannot be detected at the next antenna after the last detection. The vortex strength is then extrapolated to zero at the time it would be expected to reach the next antenna, based on the latest value for transport velocity. This extrapolation is excluded if the last detection is in the last antenna in the array or if the expected arrival time is so close to the next aircraft landing that the next detection could be obscured by noise.

The death of a vortex in 3) is signaled by not being detected in an antenna over which it passes. The two exclusions on the extrapolation in 3) are designed to eliminate any causes for non-detection (e.g., aircraft noise) other than decay to a strength below the detection threshold. Appendix A evaluates the detection threshold. Section 2.1 of Volume II (Ref. 2) illustrates this vortex history procedure for actual data. Table 2 lists the number of vortex deaths measured for each aircraft type.

TABLE 2. NUMBER OF MEASURED VORTEX DEATHS

Aircraft Type	Vortex 1	Vortex 2
DC-9	318	171
B-737	89	50
B-727	848	464
B-707	249	162
DC-8	133	87
DC-8H	75	51
B-707H	31	17
DC-10	261	194
L-1011	62	39
B-747	135	69

2.3 VORTEX STRENGTH ERRORS

In the vortex history the two extrapolations 1) and 3) are more susceptible to error. In the case of a slowly moving vortex the first detection can occur after a significant amount of decay. In recent data analysis, assumption 1) has been modified to allow extrapolation to zero time only if the first detection occurs before a vortex age of 20 seconds. The assignment of zero strength to a missed detection in 3) is also a rather crude approximation in view of the finite detection threshold and the total uncertainty in the actual death position of a vortex. The errors associated

with these extrapolations are mitigated by the requirement that all vortices included in the data analysis are detected in at least two antennas. This requirement also assures reasonable accuracy since the vortex strength is proportional to the measured transport velocity which can be reliably estimated from two detections.

An other possible source of strength error can enter into the vortex strength at early times (e.g., less than 20 seconds) when the vortex is still descending toward the ground. The use of a single range gate for the tangential velocity profile can underestimate the vortex strength when the maximum velocities occur at different heights before and after the vortex passes. Readings as much as 25 percent low have been seen from this effect.

3. STATISTICS OF VORTEX DECAY

The decay of wake vortices must be described as a statistical process for two reasons. First, the condition of the atmosphere depends upon too many variables, (e.g., wind distribution, temperature distribution, etc.) to be specified exactly. Since the atmospheric conditions have a strong influence on vortex decay, a statistical description is needed to account for unknown variables. Second, many vortex decay mechanisms are themselves random processes which cannot be defined by the average properties of the atmosphere. A statistical description of vortex decay is therefore the best that can be expected.

Unfortunately, the average decay time of wake vortices is of little use in assessing the wake vortex hazard. Assured safe separation for a following aircraft requires a determination of the maximum duration of the wake vortex hazard. Such a determination immediately leads to the difficult problem of measuring small probabilities.

3.1 VORTEX HAZARD PROBABILITY

Section 4.1 describes a method for defining a vortex strength hazard threshold Γ_T^1 . For the present discussion it is sufficient to note that a wake vortex poses a potential hazard to a following aircraft separated by a time t if the vortex strength $\Gamma'(t)$ at age t is greater than Γ_T^1 and poses no hazard if $\Gamma'(t)$ is less than Γ_T^1 . The vortex hazard probability $F(\Gamma_T^1, t)$ predicts what fraction of the wake vortices generated will have a strength less than Γ_T^1 at age t . The dependence of $F(\Gamma_T^1, t)$ upon strength threshold and age characterizes the decay of the wake vortex hazard.

Probabilities can be measured in a simple way. The probability of a certain event is given by the ratio of the number of times the event occurs divided by the total number of times it could have occurred. Because of statistical fluctuations, an accurate measurement of probability requires a large number of events,

particularly if the probability is small. For example, if N events are expected in 1000 cases, the probability F is $N/1000$. For N much less than 1000, the root-mean-square (rms) variation in number of events for different selections of 1000 cases is N/\sqrt{N} . Thus, the rms variation in F becomes large for N less than 10. In the particular case of $F(\Gamma_T^1, t)$, the vortex hazard probability at a time t , F is given by the ratio of the number of cases with strength equal to or greater than Γ_T^1 at time t divided by the total number of cases with valid strength measurements at time t .

3.2 HAZARD PROBABILITY DECAY

Figure 4 shows an example of how the vortex hazard probability decays in time. The vortex time histories (Section 2.2) were evaluated for all B-707 vortices with a 10-meter averaging radius and a hazard threshold Γ_T^1 of 100 m^2/sec . The probability was calculated at 10-second intervals. The logarithm of the hazard probability is observed to decay more rapidly as the vortex age increases. In this plot the total number of vortices measured is about 500. A probability of 0.002 corresponds to one case above hazard threshold while a probability of 0.02 corresponds to 10 cases above the threshold. The earlier discussion of statistical fluctuations indicates that the measured probabilities below 0.02 can have large statistical errors (see Appendix D of Volume II, Ref. 2).

Early in the analysis of the hazard decay plots it was found that the decay in hazard probability F becomes approximately linear when plotted as $\log F$ vs. t^2 . Figure 5 shows $F(\Gamma_T^1, t)$ for strength thresholds of 150, 100, 75, 50, and 30 m^2/sec plotted against t^2 . The second curve from the left is the data of Figure 4. The probability decreases as the threshold increases. The format of Figure 5 has become the standard display used to analyze the vortex decay data. It shows in a single picture how the vortex hazard probability depends upon the vortex age and the assumed hazard threshold. Six hazard strength values (the five above and 200 m^2/sec) were used in the standard display of vortex decay.

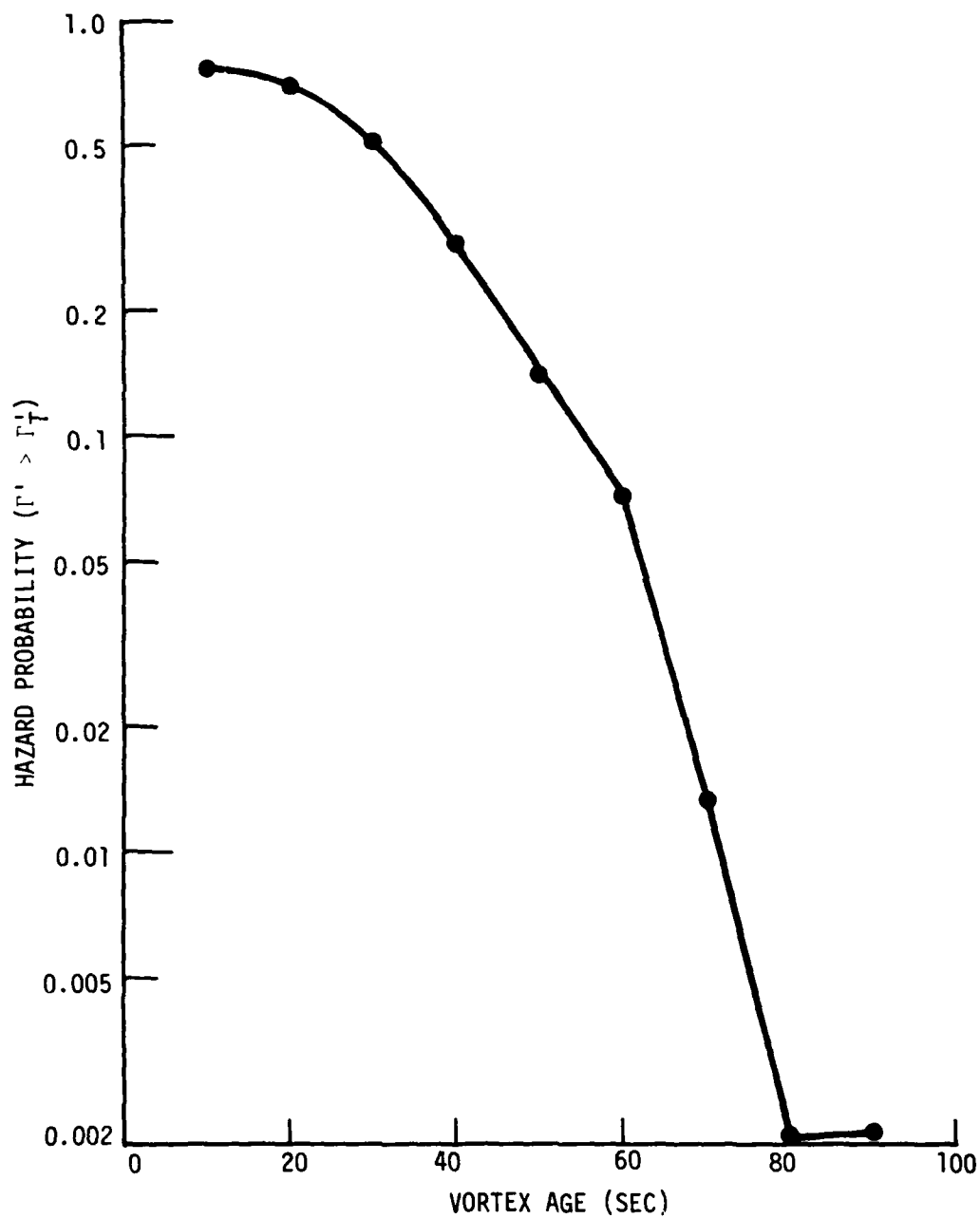


FIGURE 4. HAZARD PROBABILITY VERSUS VORTEX AGE FOR ALL B-707 VORTICES FOR $\Gamma'_T = 100 \text{ m}^2/\text{sec}$ AND 10-m SEMISPAN

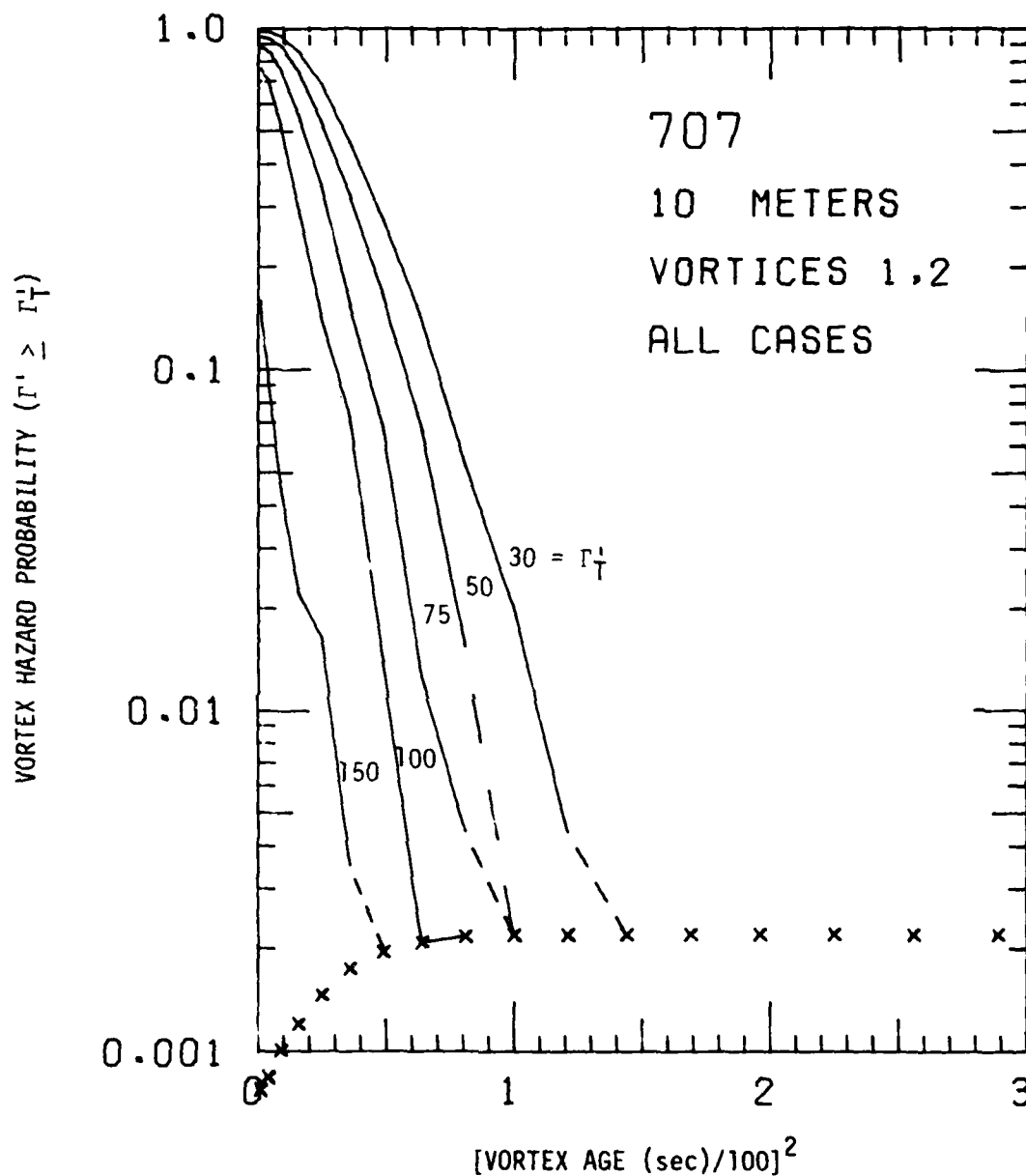


FIGURE 5. HAZARD PROBABILITY FOR 10-METER SEMISPAN VERSUS VORTEX AGE SQUARED FOR ALL B-707 VORTICES AND FIVE VALUES OF Γ_T^1 (m^2/sec)

Some of the details of Figure 5 require explanation. The x's plotted in Figure 5 correspond to the probability corresponding to one case. Since zero cannot be plotted on a logarithmic scale, the plots are terminated at the level of one case. If the probability drops to zero from a value higher than one case, a dashed line is drawn to the one-case value at the age where zero occurred. The age intervals are 10 seconds as in Figure 4. The single-case probability, marked by x's in Figure 5, rises with vortex age because the number of valid strength histories decreases with vortex age. Vortices are lost by passing the end of the antenna array or by interference from the noise of the following aircraft. The number of cases reaches a steady level after about 80 seconds, when most of the valid measurements are those of vortices which have been declared dead according to the restrictions of Section 2.2.

A straight-line fit to the curves of Figure 5 corresponds to the functional form

$$F(\Gamma_T^1, t) = \exp(-\alpha(t^2 - d)), \quad (8)$$

where α represents the slope and d the delay in t^2 to the point where $F = 1$. This functional dependence describes the vortex decay for more than three decades for the aircraft with the most data (notably, the B-727). This form also appears to give a reasonable asymptotic fit to the data no matter how the data are disaggregated according to meteorological conditions.

The functional dependence of equation 8 implies a decay probability that increases in time, which is plausible for the various modes of vortex decay. The probability of vortex linking and core bursting is observed to increase with time (Refs. 6 and 7). The vortex decay due to turbulent diffusion may also increase with time as vortex energy is converted to turbulent energy and as vorticity is diffused away from the vortex core to regions where it can annihilate with vorticity of opposite sign.

The fact that the vortex hazard decays as $\exp(-\alpha t^2)$ accounts for the observed safety of the air transportation system. If the decay were slower, for example, as $\exp(-t/\tau)$, the accident rate could not remain small except with inordinately large aircraft separations. Suppose the hazard probability decayed exponentially with a time constant τ as short as 30 seconds (which is much shorter than the e^{-1} decay for many of the aircraft at reasonable hazard strength levels; it would require 138 seconds for the hazard probability to drop to 1 percent and 207 seconds to drop to 0.1 percent.

3.3 VORTEX STRENGTH DISTRIBUTION

This section develops the mathematical formalism appropriate to a probabilistic description of vortex decay and then examines how the vortex strength distribution varies in time. Readers interested only in hazard decay should move ahead to Section 4.1.

At any given time the vortex strength Γ' can be described by the distribution function $P(\Gamma', t)$ which gives the probability $P d\Gamma'$ of the vortex strength lying in a small interval $d\Gamma'$. The normalization of P is given by:

$$\int_0^{\infty} P(\Gamma', t) d\Gamma' = 1. \quad (9)$$

A knowledge of $P(\Gamma', t)$ constitutes a complete description of vortex decay under the conditions specified for the distribution function (e.g., meteorological conditions, aircraft type, aircraft weights, etc.). For example, the average vortex strength $\bar{\Gamma}'$, is given by

$$\bar{\Gamma}'(t) = \int_0^{\infty} P(\Gamma', t) \Gamma' d\Gamma'. \quad (10)$$

The probability $F(\Gamma_T^i, t)$ that the vortex strength is above the hazard threshold Γ_T^i is given by

$$F(\Gamma_T^i, t) = \int_{\Gamma_T^i}^{\infty} P(\Gamma', t) d\Gamma'. \quad (11)$$

The evaluation of the vortex strength distribution function $P(\Gamma', t)$ is similar to that of the probability $F(\Gamma_T^i, t)$. The vortex history algorithms of Section 2.2 are used to get the strength of each vortex at age t . The vortices are then sorted into bins 20 m^2/sec wide. The strength distribution at the midpoint of the bin is then defined as the ratio of the number of vortices in the bin divided by the bin width and the total number of valid strength measurements at the time t . Figure 6 shows the resulting strength distribution for all B-707 landing vortices at a number of different ages. The initial distribution (10 sec) consists of a well-defined (40 percent full width at half maximum) peak with a tail extending to low strengths. Presumably the tail is due to vortices which have decayed before they were first detected. The peak in the distribution function P corresponds to the most probable vortex strength. The initial most probable strengths are listed in Table 3 for the major aircraft types using all the data collected.

The vortex decay in Figure 6 results in a steady decrease in the most probable vortex strength and an increase in the width of the distribution function. Eventually, a large portion of the distribution function drops below the detection threshold of 30 or 40 m^2/sec (Appendix A). Figure 7 shows the probability of the vortex strength remaining nonzero as a function of time. The long duration of nonzero strength compared to Figure 4, for example, is due to the nature of the extrapolation process by which a vortex is declared defunct (Section 2.2). The extrapolation procedure leads to the sizable vortex distribution below the detection threshold in Figure 6.

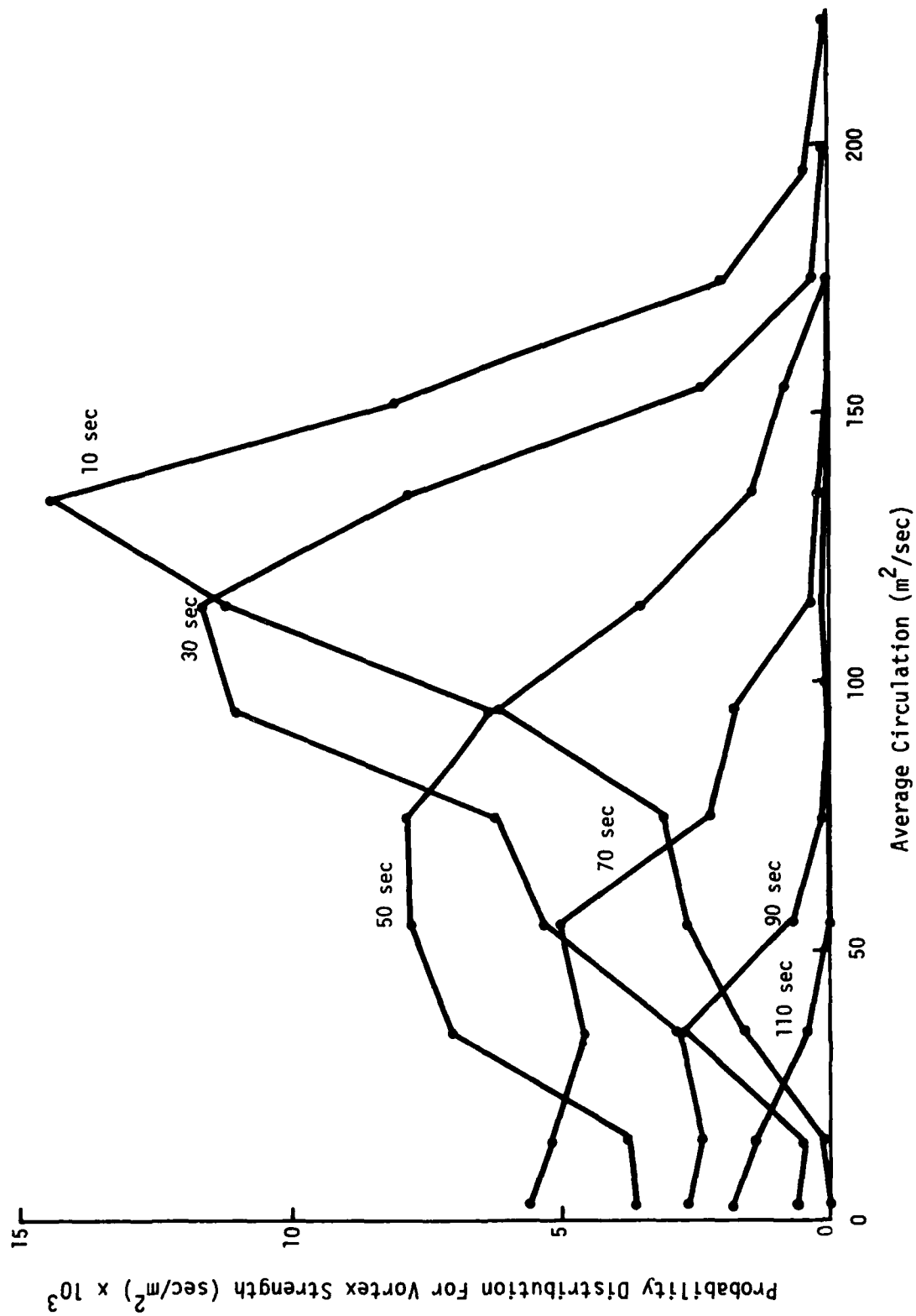


FIGURE 6. DISTRIBUTION OF VORTEX STRENGTH $\Gamma'(10 \text{ m})$ FOR ALL B-707 LANDING VORTICES

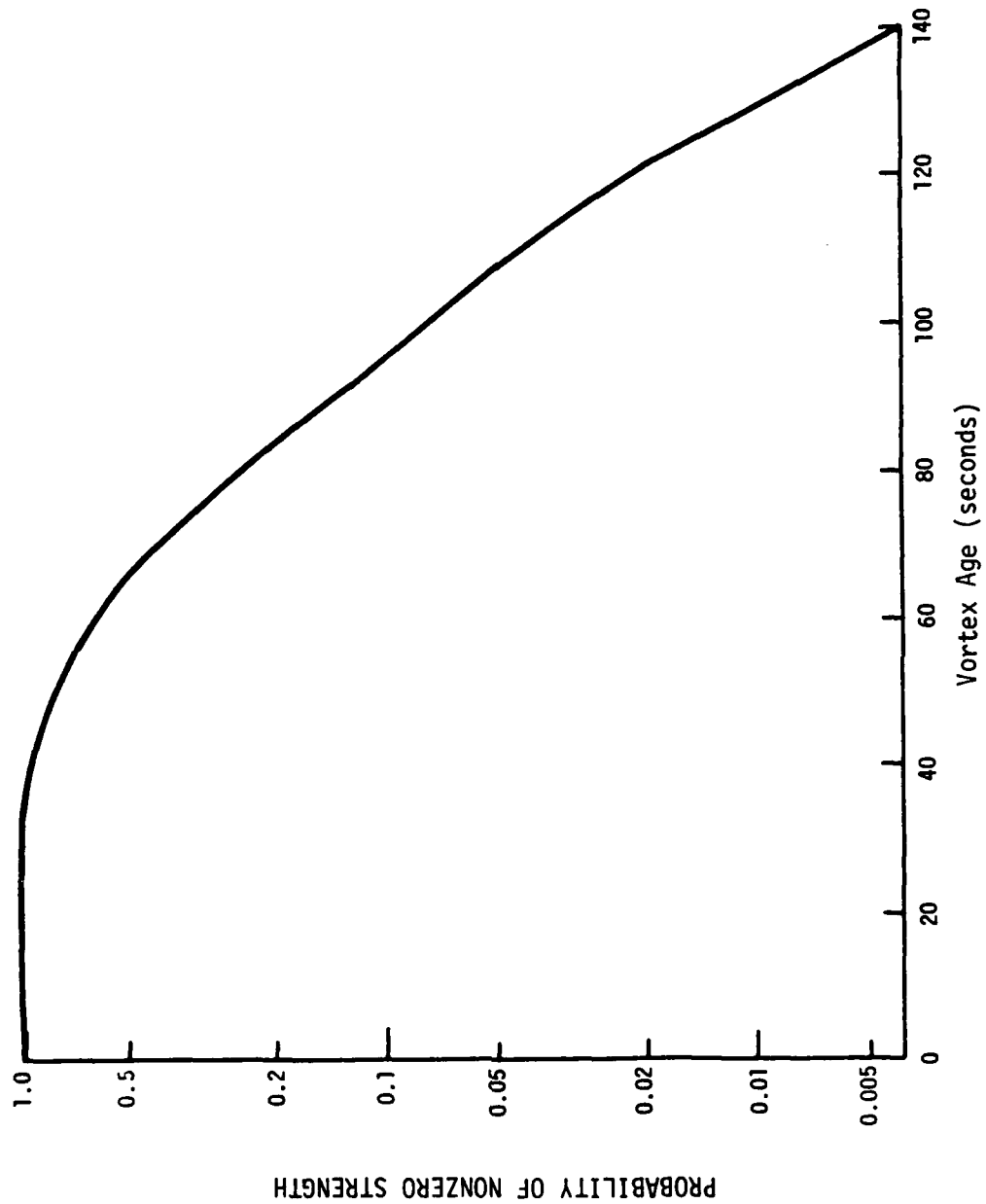


FIGURE 7. PROBABILITY OF NONZERO VORTEX STRENGTH Γ' (10 m) VERSUS AGE FOR ALL B-707 LANDING VORTICES

TABLE 3. MOST PROBABLE INITIAL VORTEX STRENGTH (m^2/sec)
FOR LANDING AIRCRAFT

Aircraft	Averaging Radius			
	5 m	10 m	15 m	20 m
DC-9	46	85	95	110
B-737	41	85	98	107
B-727	56	105	120	140
B-707	76	132	146	165
DC-8	76	135	155	185
DC-8H	72	135	145	170
B-707H	80	135	150	175
DC-10	60	135	165	195
L-1011	65	140	175	205
B-747	90	185	225	260

Consider how the features of Figure 5 are produced by the decay in the strength distribution of Figure 6. The initial probability is near one when the threshold is below the $135 \text{ m}^2/\text{sec}$ peak in the initial distribution. It is much reduced when the threshold is above the peak, as for $150 \text{ m}^2/\text{sec}$. Another feature of the decay is that a progressively increasing delay in the decay occurs when the threshold is dropped farther and farther below the initial strength. After the delay the $\log F$ versus t^2 curve again becomes roughly linear. This delay represents the time it takes for the peak in the distribution curve to drop below the threshold.

A number of different methods were developed to model the vortex decay of Figure 6. They are described in Appendix B. Some of them will be used in later sections of this report.

4. HAZARD ANALYSIS

A determination of the duration of the wake vortex hazard is a critical element in evaluating the safety of wake vortex separations. A hazard model is needed to relate the MAVSS strength measurements of Section 2 to the encounter hazard for a following aircraft. A number of improvements to the traditional hazard model will be presented. The amount of MAVSS data collected is sufficient to make estimates of the statistics of the hazard duration (as outlined in Section 3). In addition, the dependence of hazard duration upon the meteorological conditions will be discussed.

4.1 ROLLING MOMENT HAZARD MODEL

Volume II (Section 4.2.1) of this report (Ref. 2) derives the following expression for the vortex strength hazard threshold:

$$\Gamma_T'(b/2) = \frac{\pi}{3} KfbV\hat{p}, \quad (12)$$

where the parameters of the following aircraft are b = the wingspan, V = the airspeed, and \hat{p} = the maximum nondimensional roll rate. This hazard model assumes that a vortex poses a hazard if its induced rolling moment is greater than a fraction f of the maximum roll control of the aircraft. The derivation of Equation 12 assumes that the value of Γ' is independent of the shape of the vortex velocity profile. Equation 12 with $K = 1$ is correct for a velocity profile which increases linearly with radius. Appendix B of Reference 5 uses vortex-lattice theory to calculate the corrections for other velocity profiles. Table 4 lists the correction factors K for two aircraft types and several velocity profiles: 1) constant velocity and 2) Equations 1 and 2 with $r_c = 0, 2.5,$ and 5 meters. Deviations from $K = 1$ are larger for the DC-9 because of greater taper (and perhaps sweep) in the wing planform.

TABLE 4. INDUCED ROLLING MOMENT CORRECTION FACTORS

AIRCRAFT	WINGSPAN (m)	CORRECTION FACTOR K			
		Constant Velocity	$r_c=0$	$r_c=2.5$	$r_c=5$ m
T-37	10.3	.92	.82	.91	.95
DC-9 (flaps)	28.4	.87	.71	.78	.85

The basic equation (Equation 12) of the hazard model can be used to determine the wingspan dependence of the vortex hazard. Dividing Equation 12 by $b/2$ isolates the wingspan dependence:

$$2\Gamma_T'(b/2)/b = H_T = \frac{2\pi}{3} KfV\beta. \quad (13)$$

The vortex model (Equation 4) can be used to evaluate $\Gamma'(r)/r$ as a function of Γ_∞ and r_c . The results are plotted in Figure 8. The range of wingspans experiencing a hazard from a particular vortex is critically dependent on the value of H_T in Equation 12. The value H_{T1} in Figure 8 yields no hazardous wingspans. The value H_{T2} yields a hazard for wingspans between $2 r_c$ and $5.2 r_c$. Reducing H_{T2} by a factor of two to H_{T3} drastically increases the hazard wingspan range to $.69 r_c$ through $14.8 r_c$. For further reductions in H_T the lower hazard bound will decrease proportionally to H_T and the upper bound inversely with H_T .

The fact that a given vortex is safe for both small and large wingspans may be surprising at first glance, but it can be readily understood by careful examination. For large wingspans the vortex velocities are too small over much of the wingspan to present a hazard. For wingspans smaller than the core size the encountering aircraft experiences only the local velocity gradient in the core and not the full velocity variation of the vortex.

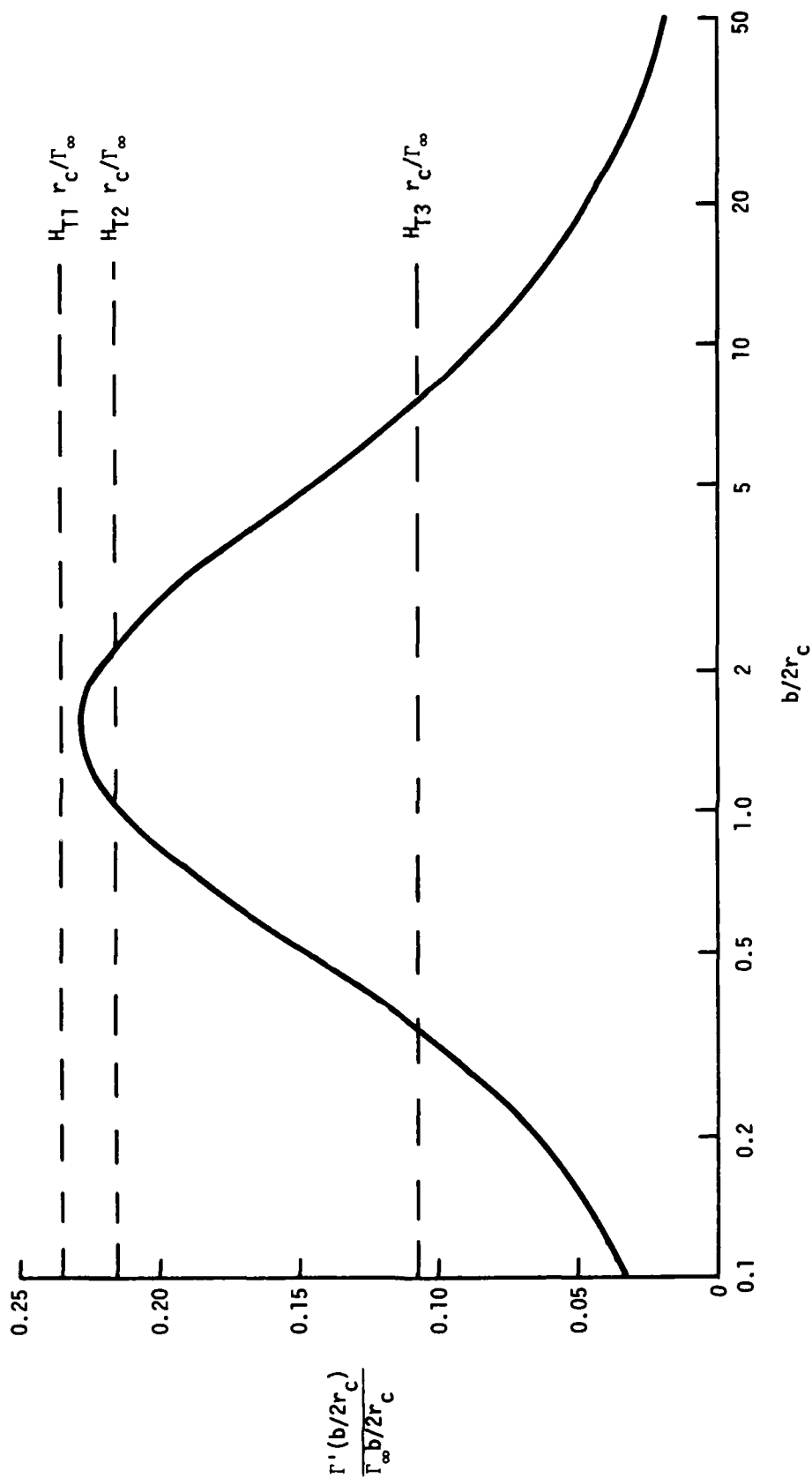


FIGURE 8. WINGSPAN DEPENDENCE OF VORTEX HAZARD

The hazard analysis of this report (also Volume II) assumes a hazard threshold of

$$H_T = 10 f \text{ (m}^2\text{/sec)}. \quad (14)$$

This value is consistent with the parameters $K = 1$, $V = 68 \text{ m/sec}$ (130 knots), and $\hat{p} = 0.07$. Table 5 shows the average circulation hazard threshold values from Equation 14 with $f = 1.0$. The sensitivity of the results to the parameter f will, in part, also serve to illustrate the effects of varying K , V , and \hat{p} . Variations in f can also account for the MAVSS errors estimated in Table 1. Possible variations in K are illustrated in Table 3. Conservative estimates for \hat{p} (Ref. 8) are 0.06 for jet transports and 0.08 for general aviation aircraft. These numbers refer to the roll control of ailerons alone. The use of spoilers for additional roll control can lead to $\hat{p} = 0.12$. Military aircraft generally have even larger values of \hat{p} (0.12 for the T-37 used in vortex encounter flight tests and 0.18 for the F-86). Because of pilot response times, the full roll-control capability of an aircraft cannot be used to compensate for a vortex encounter. Both flight encounters and simulator studies indicate that the actual hazard threshold for f is more like 0.4 than 1.0.

TABLE 5. HAZARD THRESHOLDS FOR $f = 1$

Aircraft Type	Semi Span	Strength Threshold
Small GA	5 m	50 m ² /sec
Large GA	10 m	100 m ² /sec
DC-9	15 m	150 m ² /sec
B-707	20 m	200 m ² /sec

The MAVSS detection thresholds discussed in Appendix A lead to a limit on the value of f in Equation 14 which can be examined experimentally. The approximate detection thresholds for 5, 10, and 20-meter averaging radii are, respectively, $f = 0.6$, 0.4, and 0.3.

4.2 HAZARD DECAY

The decay of the vortex hazard probability was investigated in Section 3.2 before the description of the hazard model was described in detail. The observations there can now be interpreted in terms of the hazard model parameter f . The choice of hazard threshold $\Gamma_T^i = 100 \text{ m}^2/\text{sec}$ for 10-m averaging radius in Figure 4 corresponds to $f = 1.0$ according to Equations 13 and 14. In Figure 5 the curves for $\Gamma_T^i = 150, 75, 50, \text{ and } 30 \text{ m}^2/\text{sec}$ correspond to $f = 1.5, 0.75, 0.50, \text{ and } 0.30$, respectively. The different Γ_T^i curves thus show how the selected value of f affects the hazard decay. As one would expect, the hazard lasts longer for the lower values of f .

Figure 5 was based on all the B-707 vortices measured. Information about meteorological effects on vortex decay can be obtained by disaggregating the measurements according to the ambient wind or some other meteorological parameter. The primary limit on disaggregating the data is the necessity of retaining enough cases to make statistically significant measurements.

The most significant parameter affecting vortex decay was found to be the vortex position relative to the ambient crosswind. The downwind vortex, which is the first to reach a MAVSS antenna (termed vortex 1), decays more rapidly than the upwind vortex, which is the second vortex to reach an antenna (termed vortex 2). Figure 9 shows the data of Figure 5 disaggregated into vortex 1 and vortex 2. The operational significance of this effect lies in the fact that vortex 2 is the one which could linger near the extended runway centerline and pose a hazard to an aircraft following on the same runway, while vortex 1 is more likely to drift toward any parallel runway. Most of the subsequent hazard analysis (e.g., Section 6) will deal with the decay of vortex 2 which determines the single runway vortex separation standards.

Figure 10 shows the data of Figure 9 analyzed with the recent algorithm which excludes extrapolation to zero time unless the first vortex detection is before 20 seconds. The result of this restriction is a significant reduction in the number of cases at

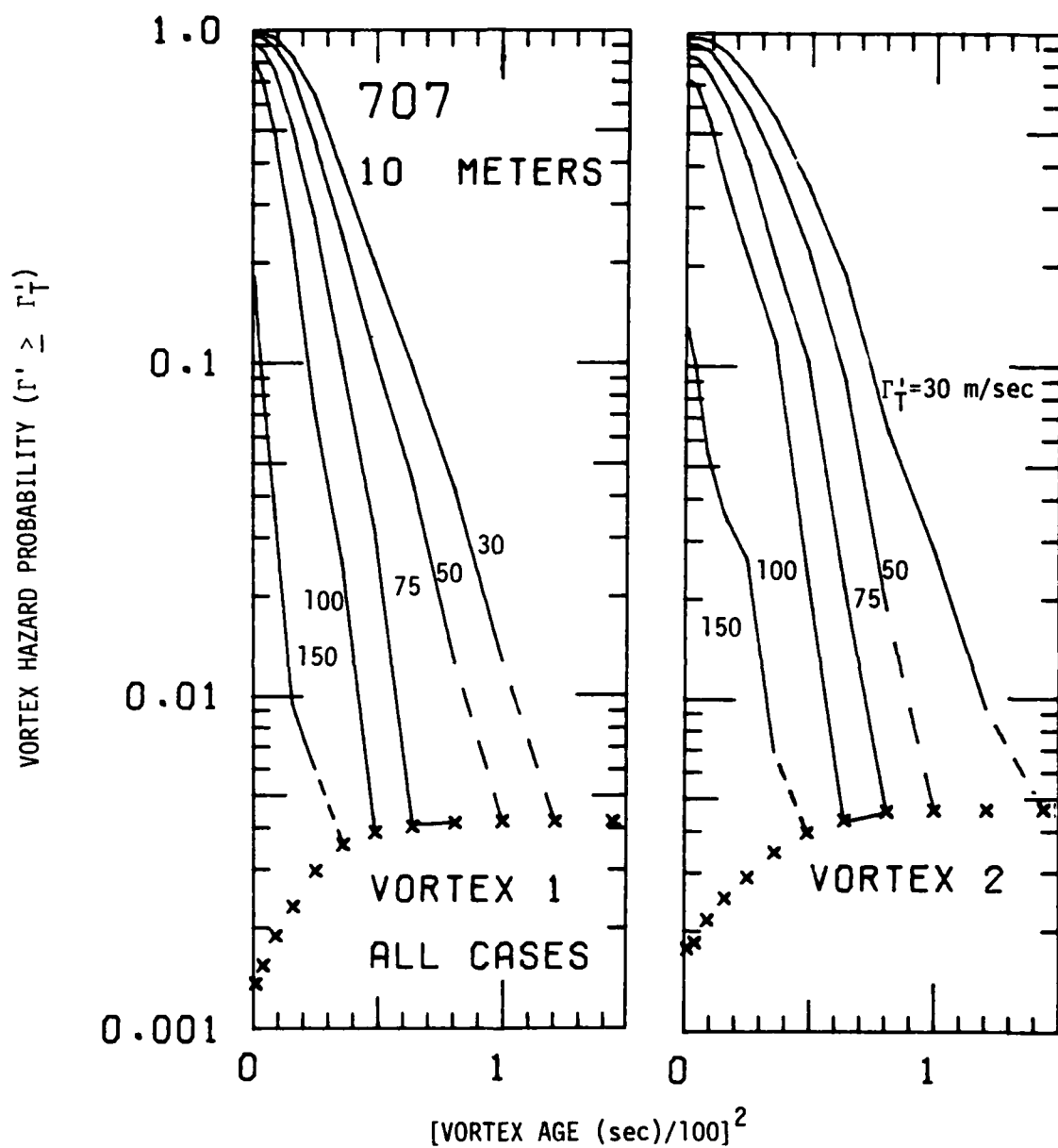


FIGURE 9. COMPARISON OF VORTEX DECAY FOR VORTEX 1 AND VORTEX 2;
B-707 AIRCRAFT, 10-m AVERAGING RADIUS

early times. In fact, the number of cases becomes relatively independent of vortex age. Appendix C presents plots like Figure 9 for all common jet transport aircraft and averaging radii.

High windspeeds are observed to increase the rate of vortex decay (see Appendix C). The functional dependence upon wind speed has not been determined, however, because the effect is not much greater than the statistical uncertainties.

5. AIRCRAFT DEPENDENCE OF VORTEX CHARACTERISTICS

This section relates the wake vortex characteristics of an aircraft to its physical parameters such as wingspan, weight, engine placement, etc. Vortex data are available for American-made commercial jet transports. Table 6 lists the relevant parameters (Ref. 9) for various models of these aircraft.

5.1 INITIAL VORTEX STRENGTH

5.1.1 Theory

The classical expression for the dependence of total wake vortex strength upon aircraft parameters (Ref. 10) is:

$$\Gamma_{\infty} = CW/\rho bV, \quad (15)$$

where C is a constant depending upon the wing loading distribution ($C = 4/\pi$ for elliptic loading, $C = 1$ for constant loading), W is the aircraft weight, ρ is the air density, b is the wingspan, and V is the airspeed. The total circulation Γ_{∞} increases with aircraft weight and decreases with airspeed and wingspan. Heavier aircraft tend to have larger wingspans.

The simple aircraft dependence of Equation 15 is in the three parameters W , b , and V . The wing-loading distribution factor C is much more difficult to address. The expression W/bV was evaluated for the maximum landing weight W_L in Table 6 for all the aircraft models. Two values were used for V : the listed landing speed and a fixed speed of 150 mph. Table 7 shows the values for W/bV assigned to each type as a mean value for the different models in use at the time of our data collection. A mean wingspan is also assigned. The spread in values for different models is shown in parentheses. The values of Table 7 are converted to estimates of Γ_{∞} in Table 8 through the use of Equation 15. The values are also converted to metric units in order to allow comparison with the

TABLE 6. AIRCRAFT MODEL PARAMETERS

MODEL	WINGSPAN (ft) b	MAXIMUM GROSS WEIGHT (klbs) W_T	MAXIMUM LANDING WEIGHT (klbs) W_L	LANDING SPEED (Mph) V_L	$\frac{(\text{lbs})}{(\text{Mph}, \text{ft})}$ $\frac{W_T}{V_L^2 b}$	$\frac{(\text{lbs})}{(\text{Mph}, \text{ft})}$ $\frac{W_L}{150b}$	NOMINAL WING LOADING (lbs) (ft ²) W_L/b^2
BOEING							
707-120	130.9	258	190	165	8.80	9.68	11.1
707-120B	130.9	258	190	158	9.19	9.68	11.1
707-320	142.4	316	207	161	9.03	9.69	10.2
707-320B/C	145.8	336	247	158	10.72	11.29	11.6
707/420	142.4	316	207	162	8.97	9.69	10.2
720	130.9	230	175	148	9.03	8.91	10.2
720B	130.9	235	175	152	8.80	8.91	10.2
727-100	108.0	170	142.5	140	9.42	8.80	12.2
727-200	108.0	191.5	154.5	145	9.87	9.54	13.2
737-100	93.0	111	101	134	8.10	7.24	11.7
737-200	93.0	117.5	105	134	8.43	7.52	12.1
747-100B	195.7	738	564	162	17.79	19.21	14.7
747SR	195.7	603	525	156	17.20	17.88	13.7
747-200B/C	195.7	788	564	162	17.79	19.21	14.7
747SP	195.7	696	450	158	14.55	15.33	11.7
MCDONNELL DOUGLAS							
DC-8-10	142.3	273	193	148	9.16	9.04	9.5
DC-8-20	142.3	276	199.5	151	9.28	9.35	9.9
DC-8-30/40	142.3	315	207	153	9.51	9.70	10.2
DC-8-50	142.3	325	207	145	10.63	9.70	10.2
DC-8-61	142.3	325	240	163	10.35	11.24	11.9
DC-8-62	148.4	335	240	143	11.31	10.78	10.9
DC-8-63	148.4	350	245	157	10.52	11.01	11.1
DC-9-10	89.4	90.7	81.7	145	6.30	6.09	10.2
DC-9-20	93.3	98	93.4	129	7.76	6.67	10.7
DC-9-30	93.3	121	110	137	8.61	7.86	12.6
DC-9-40	93.3	121	110	141	8.36	7.86	12.6
DC-9-50	93.3	122.2	110	142	8.30	7.86	12.6
DC-9-80	107.8	140	128	143	8.30	7.92	11.0
DC-10-10	155.3	455	363.5	148	15.82	15.60	15.1
DC-10-30	165.3	572	403	159	15.33	16.25	14.7
DC-10-40	165.3	572	403	161	15.14	16.25	14.7
LOCKHEAD-CALIFORNIA							
L-1011-1	155.3	430	358	164	14.06	15.37	14.8
L-1011-100/ 200	155.3	466	368	164	14.45	15.80	15.3
L-1011-250/ 500	155.3	496	368	164	14.45	15.80	15.3

TABLE 7. AIRCRAFT TYPE PARAMETERS

TYPE	<u>Wingspan (Range)</u> (ft)	<u>$W_L/V_L b$ (Range)</u> (lbs/Mph, ft)	<u>$W_L/150b$ (Range)</u> (lbs/Mph, ft)
DC-9	93.0 (89.4-93.3)	8.3 (6.3-8.6)	7.2 (6.1-7.9)
B-737	93.0	8.3 (8.1-8.4)	7.3 (7.2-7.5)
B-727	108.0	9.7 (9.4-9.9)	9.3 (8.8-9.5)
B-707	130.9	9.0 (8.8-9.2)	9.3 (8.9-9.7)
DC-8	142.3	9.2 (9.2-9.3)	9.2 (9.0-9.4)
DC-8H	145 (142.3-148.4)	10.4 (9.5-11.3)	10.5 (9.7-11.2)
B-707H	144 (142.4-145.8)	9.8 (9.0-10.7)	10.5 (9.7-11.3)
DC-10	160 (155.3-165.3)	15.5 (15.1-15.8)	15.9 (15.6-16.3)
L-1011	155.3	14.3 (14.1-14.5)	15.6 (15.4-15.8)
B-747	195.7	17.6 (17.2-17.8)	18.7 (17.9-19.2)

TABLE 8. INITIAL VORTEX STRENGTH

AIRCRAFT TYPE	WINGSPAN (m)	CALCULATED		MEASURED		
		Γ_{∞} (1), (2) (m ² /sec)	Γ_{∞} (1), (3) (m ² /sec)	Γ' (10-20 m) (4) (m ² /sec)	Γ_{∞} (4) (m ² /sec)	Γ_{∞} (5) (m ² /sec)
DC-9	28.3	270	234	179	200	161
B-737	28.3	270	237	182	203	179
B-727	32.9	315	302	223	249	230
B-707	39.9	293	302	240	259	278
DC-8	43.4	299	299	275	298	290
DC-8H	44.2	338	341	268	289	281
B-707H	43.9	319	341	238	249	286
DC-10	48.8	504	517	298	348	341
L-1011	47.3	465	507	307	354	377
B-747	59.6	572	608	417	497	499

- (1) At Maximum Landing Weight, Temperature = 0°C, Altitude = sea level, and Elliptic Wing Loading.
- (2) Published Landing Speed.
- (3) Constant Landing Speed (150 Mph).
- (4) Using Vortex Detections Between 10 and 15 seconds.
- (5) Linear Fit to Vortex Decay.

experimental measurements. The air density ρ was taken as 1.28 kg/m^3 which corresponds to sea level pressure and a temperature of 0°C . Elliptic loading ($C = 4/\pi$) was assumed.

5.1.2 Measurements

The conventional method of determining the initial vortex strength has been to average the measured vortex strengths for early vortex detections. Because of aircraft noise and the requirement that the vortex drift past the antenna to complete a measurement, vortex detections before 10 seconds produce unreliable strengths. Consequently, the average strength of vortices detected between 10 and 15 seconds age was selected as a reasonable indication of initial vortex strength. An additional requirement of reasonably high vortex transport velocity ($>2 \text{ m/sec}$) was imposed to reduce the influence of vortex decay during the measurement. For example, the measurement of a 20-meter average strength lasts for 20 seconds for a transport velocity of 2 m/sec . Table 9 shows the results of averaging the vortex strength over vortex detections between 10 and 15 seconds. The average strength, standard deviation, and ratio of standard deviation to average strength are listed for ten aircraft types and three averaging radii. One should note that most of the vortex detections (about 75 percent) used are first vortices because they are the first to reach a MAVSS antenna. Some difference was noted between the first and second vortex strengths, the latter being significantly greater for some aircraft types, especially for 5-m averaging radius. The average strengths $\Gamma'(10 \text{ m})$ and $\Gamma'(20 \text{ m})$ in Table 9 were used to calculate the values for $\Gamma'(10-20 \text{ m})$ in Table 8 by means of Equation 5.

Since the data in Section 2.1 show indications that the vortex decay can be significant even in 15 seconds, plots were generated showing the average strength of vortices detected at different ages. It was hoped that the strength values could be extrapolated back to zero time. Figures 11 through 13 are samples of these plots; the plots for the other aircraft types are shown in Appendix D. The 2nd, 4th, and 6th points in these plots are not

TABLE 9. AVERAGE INITIAL VORTEX STRENGTH (m^2/sec): All Landing Vortex Detections Between 10 and 15 Seconds With Transport Speeds Above 2 Meters/Second.

Averaging Radius

AIRCRAFT	5 METERS			10 METERS			20 METERS		
	$\bar{\Gamma}'$	σ_{Γ}	$\sigma_{\Gamma}/\bar{\Gamma}'$	$\bar{\Gamma}'$	σ_{Γ}	$\sigma_{\Gamma}/\bar{\Gamma}'$	$\bar{\Gamma}'$	σ_{Γ}	$\sigma_{\Gamma}/\bar{\Gamma}'$
DC-9	51	13	.25	93	18	.20	136	28	.20
B-737	47	15	.31	94	19	.20	138	31	.22
B-727	60	16	.26	115	22	.19	169	32	.19
B-707	79	14	.18	136	21	.15	188	30	.16
DC-8	85	18	.21	151	27	.18	213	34	.16
DC-8H	84	18	.21	152	29	.19	210	41	.19
B-707H	83	11	.14	148	21	.14	193	37	.19
DC-10	61	17	.27	138	30	.22	218	42	.19
L-1011	69	20	.28	147	32	.22	227	42	.18
B-747	87	21	.24	181	33	.18	299	41	.14

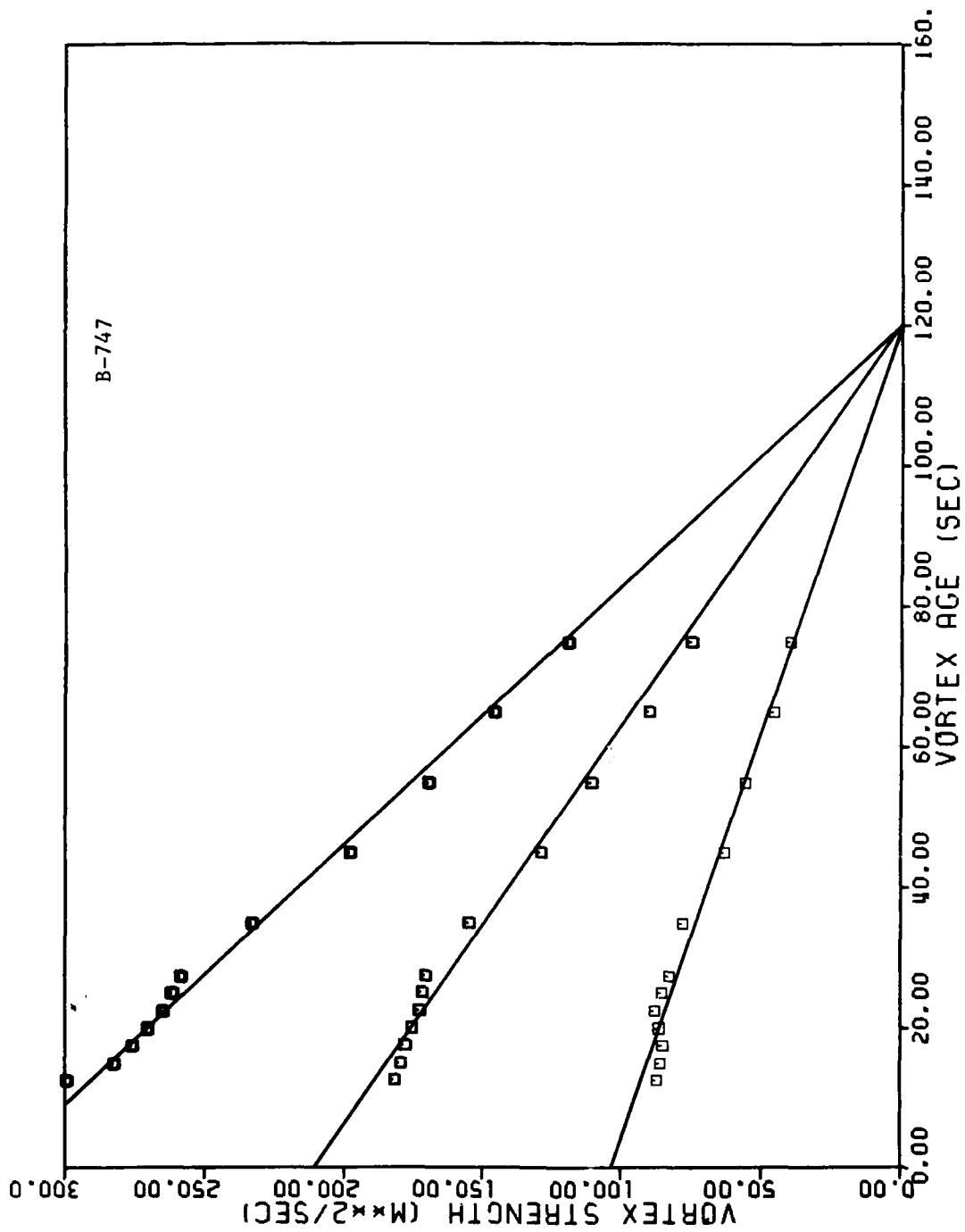


FIGURE 11. DECAY OF AVERAGE VORTEX STRENGTH FOR ALL B-747 DETECTED VORTICES: AVERAGING RADIUS = 5 m (lower line), 10 m (middle line), and 20 m (upper line).

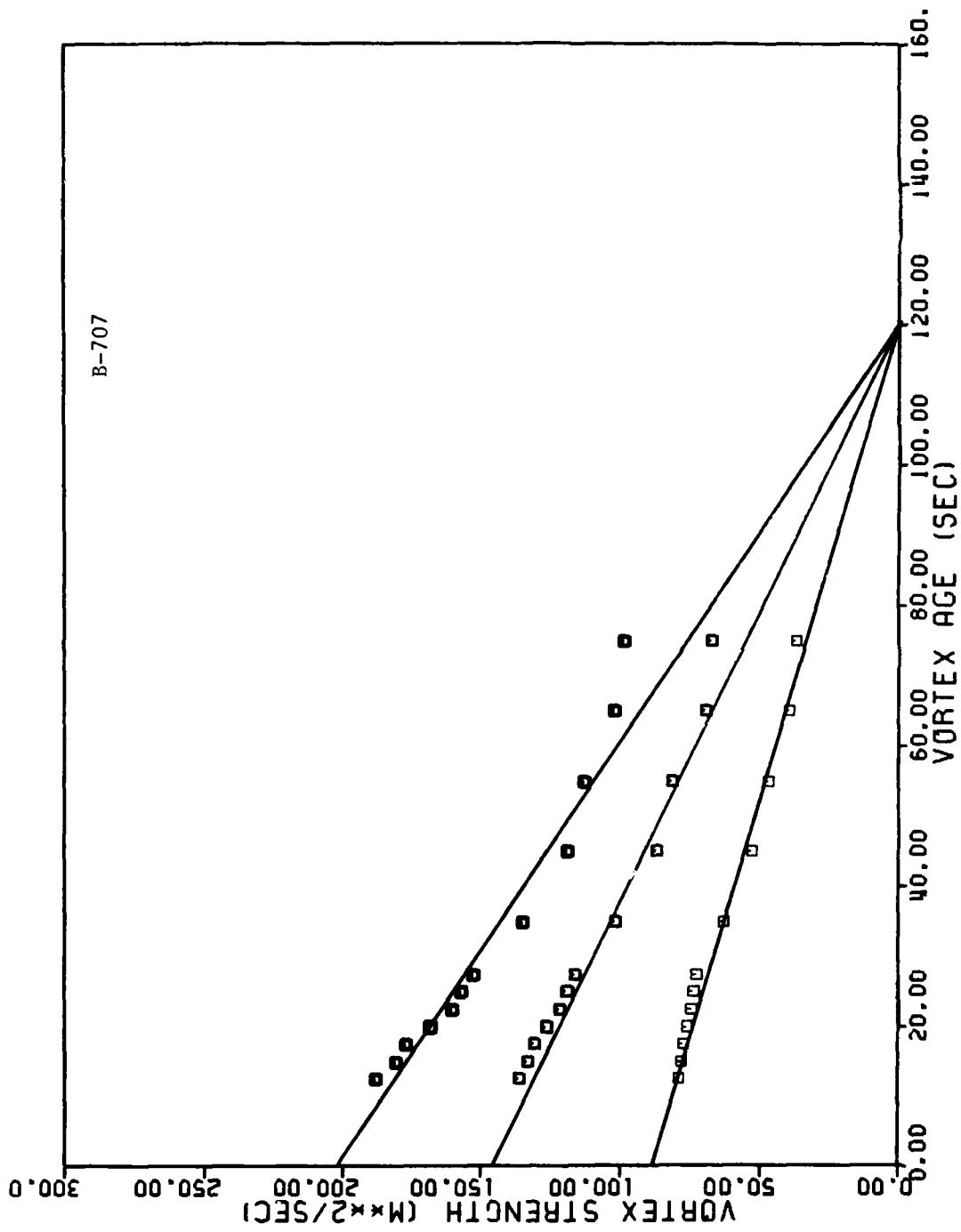


FIGURE 12. DECAY OF AVERAGE VORTEX STRENGTH FOR ALL B-707 DETECTED VORTICES: AVERAGING RADIUS = 5 m (lower line), 10 m (middle line), and 20 m (upper line).

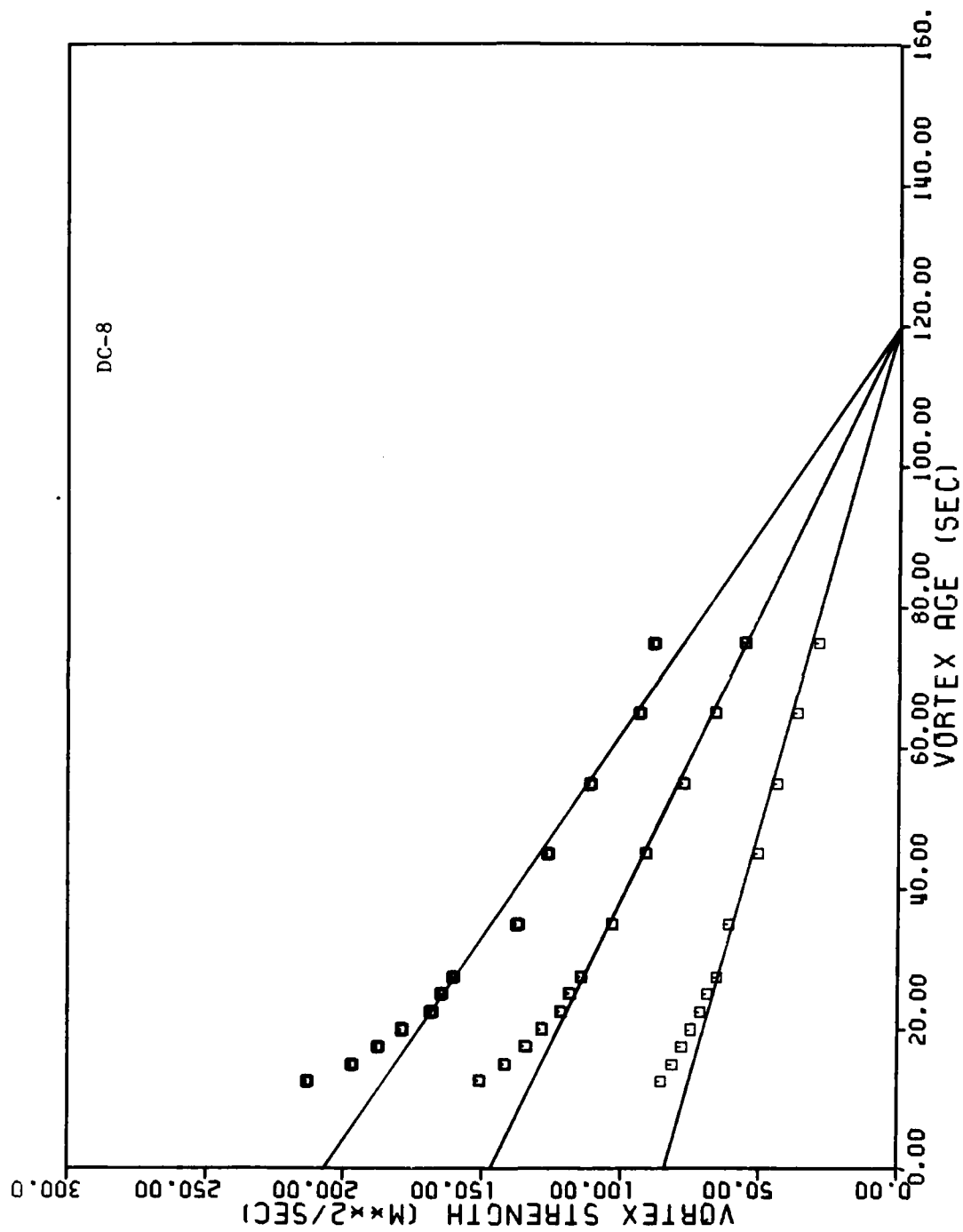


FIGURE 13. DECAY OF AVERAGE VORTEX STRENGTH FOR ALL DC-8 DETECTED VORTICES: AVERAGING RADIUS = 5 m (lower line), 10 m (middle line), and 20 m (upper line).

statistically independent, but are simply averages of the adjacent points. The results of these plots were surprising. It was found that the vortex strength decay could be approximated by a linear decay to zero at a particular time which turned out to be 120 seconds for aircraft with four wing-mounted engines and the B-727, and 140 seconds for other aircraft. For some aircraft types (see Figures 11 and 12) the linear decay curve fit reasonably well even back to zero age. For others (see Figure 13) the vortex initially decays more rapidly until it reaches the linear decay region. The vortex decay implications of these plots will be deferred to Section 5.2. The analysis here makes use only of the zero time intercepts of the linear decay curves. Table 10 lists these strength values and compares them with the average strength values of Table 9.

The vortex strength versus averaging radius data can be used to derive the core radius according to the procedure described in Section 2.1. Figure 3 (Equation 6) is used to obtain the core radius from the ratio of the strengths at two different averaging radii. The results of this analysis for three radius pairs are listed in Table 10. Using Equation 3, the vortex circulation Γ_{∞} is calculated from the core radius r_c and the strength Γ' at the larger radius. If the vortex model fits the data well, the core radius and circulation will be the same for all three radius pairs. If not, the best selection for evaluating Γ_{∞} is the 10/20-meter pair since it is least affected by what happens at the vortex core. The 10/20 values of Γ_{∞} are listed in Table 8. The calculated values of core radius range from 3.1 to 6.3 meters. The wide-body aircraft values, which range from 4.6 to 6.3 meters are significantly larger than the other aircraft whose values lie between 3.1 and 4.8 meters. Apart from this well-defined difference, there seems to be no consistent variation of core radius with aircraft size. One would suspect that the MAVSS itself is limiting the core size to perhaps a minimum of 3 meters because of the effects discussed in Section 2.2. Conventional estimates of core size are significantly smaller than those in Table 10, especially for the small aircraft with tail-mounted engines.

TABLE 10. ANALYSIS OF INITIAL VORTEX STRENGTHS

Aircraft Type	INPUT DATA			RADIUS-PAIR ANALYSIS				
	Averaging Radius (m)	$\Gamma'(1)$	$\Gamma'(2)$	Radius Pair	$r_c(1)$ (m)	$r_c(2)$ (m)	$\Gamma_\infty(1)$ (m ² /sec)	$\Gamma_\infty(2)$ (m ² /sec)
DC-9	5	51	51	5/10	4.0	3.1	178	139
	10	93	84	10/20	4.8	4.0	200	161
	20	136	117	5/20	4.2	3.4	191	155
B-737	5	47	52	5/10	4.6	4.4	198	204
	10	94	100	10/20	4.8	3.5	203	179
	20	138	135	5/20	4.7	4.0	201	186
B-727	5	60	67	5/20	4.3	3.8	230	222
	10	115	120	10/20	4.8	4.0	249	230
	20	169	167	5/20	4.4	3.8	241	228
B-707	5	79	86	5/10	3.5	3.4	239	251
	10	136	145	10/20	4.0	4.0	259	278
	20	188	202	5/20	3.6	3.5	251	270
DC-8	5	85	82	5/10	3.8	3.8	279	270
	10	151	146	10/20	4.2	4.2	298	290
	20	213	207	5/20	3.9	3.9	291	294
DC-8H	5	84	81	5/10	4.0	4.0	290	281
	10	152	147	10/20	4.0	4.0	289	281
	20	210	204	5/20	3.9	3.9	287	286
B-707H	5	83	94	5/10	3.8	3.5	274	283
	10	148	161	10/20	3.2	3.5	249	286
	20	193	216	5/20	3.5	3.4	255	286
DC-10	5	61	76	5/10	6.0	4.4	361	301
	10	138	148	10/20	5.8	5.2	348	341
	20	218	224	5/20	5.8	4.7	348	332
L-1011	5	69	77	5/10	4.6	4.9	309	359
	10	147	163	10/20	5.5	5.2	354	377
	20	227	248	5/20	5.4	5.2	351	374
B-747	5	87	102	5/10	5.0	5.0	405	473
	10	181	211	10/20	6.3	5.4	497	499
	20	299	323	5/20	5.7	5.0	473	487

(1) Average of Detections Between 10 and 15 Seconds.

(2) Linear Extrapolation to Zero Age.

Definitive laser Doppler velocimeter (LDV) data on the landing configuration velocity profile is available (Ref. 5) on the B-747. The maximum tangential velocity occurs at 2.5-meter radius. Because the circulation profile is significantly different from that (Equation 2) used in the core radius analysis here, the peak velocity core radius cannot be directly compared to the present results. If one applies the analysis of Table 10 to the LDV vortex strengths, one obtains a core radius of 3 to 3.5 meters at age 25 seconds. The core radius appears to decrease about 2.5 meters at age 60 seconds. Table 1 illustrates the factors which may be needed to correct the average circulation values in Table 9 for the error in measuring r_c . The value of $\Gamma'(5 \text{ m})$ is likely to be a factor of 2 too low for the B-747. This is a large error which will significantly affect the hazard duration estimate for small following aircraft. The errors for the other aircraft types cannot be estimated with any great confidence. Consequently, the sensitivity of the results to such errors must be considered in subsequent analyses. Any analysis of vortex decay which compares the strength of aged vortices to the initial measured strength is likely to be unaffected unless the core size changes significantly as the vortex decays. In any case, the value of Γ_∞ is not affected by the core radius error.

Figure 14 shows log-log plots comparing the measured (10-15 second age) values of Γ_∞ to the two calculated values in Table 8 which represent variable and fixed airspeed, respectively. The fixed airspeed values come somewhat closer to being proportional to the measured values, although the scatter is considerable. The measured values are generally lower than the calculated ones, as one might expect for a number of reasons, such as vortex decay and landing weights lower than the maximum value used to calculate Γ_∞ . The effects of airspeed, air density, and wing loading in Equation 15 are more difficult to assess. The line corresponding to constant wing loading is shown in Figure 14. The effect of landing flap deployment on Γ_∞ is likely to be relatively small since the flaps are roughly equivalent to a wing of constant loading but of shorter span. The net effect is probably a slight increase in Γ_∞ .

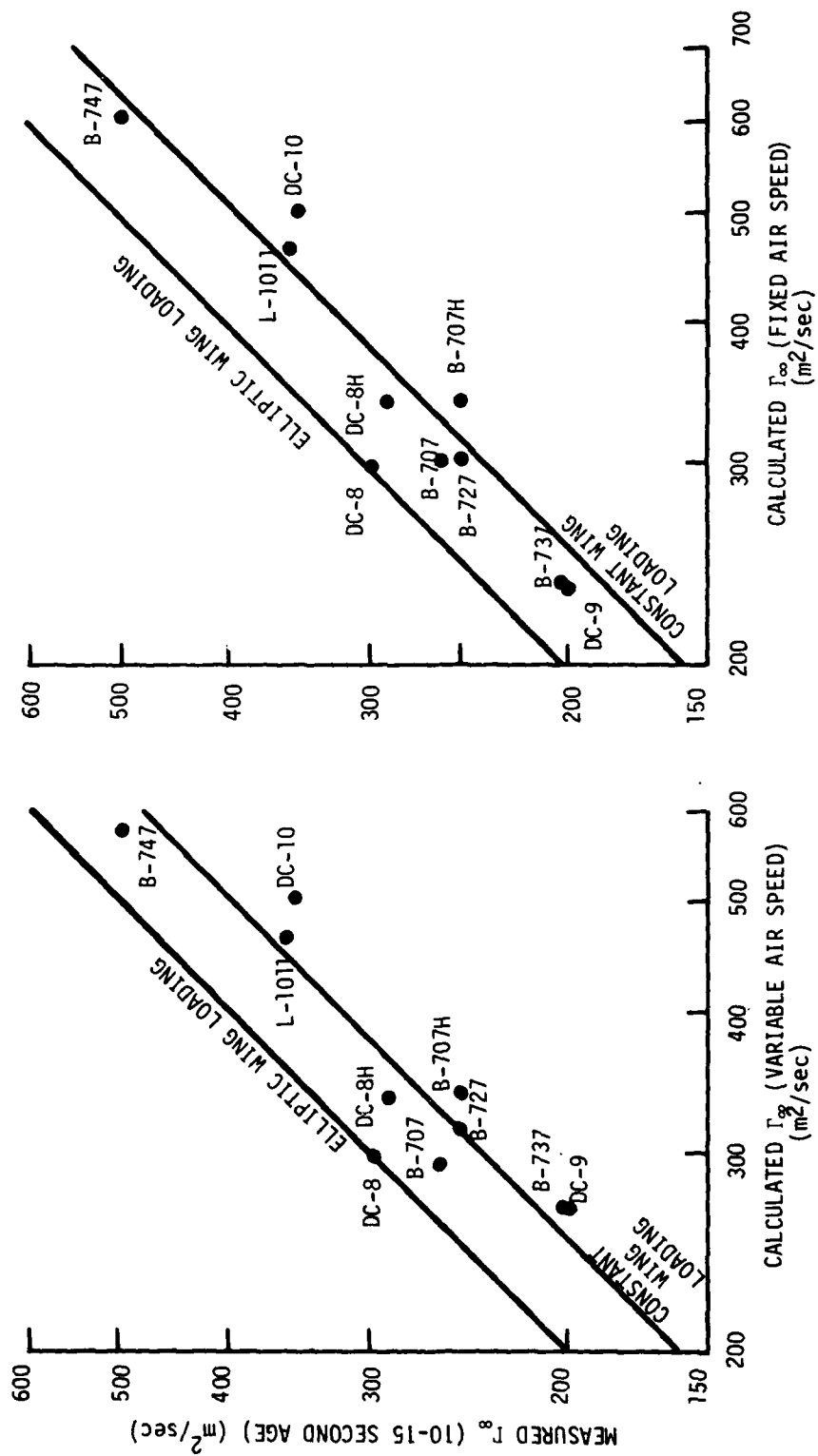


FIGURE 14. COMPARISON OF MEASURED TO CALCULATED VORTEX CIRCULATIONS

Another way of correlating the measured circulation values is shown in Figure 15 which shows log-log plots of circulation versus aircraft wingspan. The 10-15 second age circulations (Figure 15a) appear to correlate somewhat better with wingspan than with the calculated values in Figure 14. The straight line in Figure 15a corresponds to $\Gamma_{\infty} = 7.2b \text{ (m}^2\text{/sec)}$. Of particular interest for subsequent discussions is the abnormally low 10-15 second age value for the B-707H in all the comparisons. The B-707H had the fewest cases by a factor of two of all the aircraft types (see Table 2).

The linear decay intercept circulation appears to have a non-linear relationship with wingspan in Figure 15b where a line with a slope of 1.25 gives a better representation of the data than would be possible with a slope of 1.00. The same relationship appears to hold in Figure 16 where the linear decay intercept circulation is compared with the 10-15 second age circulation.

5.2 VORTEX DECAY

An understanding of wake vortex decay is needed to evaluate wake vortex separation criteria. The goal of the present effort has been to find a simple way of relating the decay of the wake vortex hazard to a small number of parameters of the generating and following aircraft. Sections 3.2 and 3.3 and Appendix B developed methods and models for describing the decay of vortices from a particular aircraft. This section will examine how the decay depends upon aircraft type.

5.2.1 Average Strength

Figures 11-13 and Appendix D show that the decay of the average strength of detectable vortices can be reasonably fitted by straight lines terminating with zero strength at times of 120 or 140 seconds. Although the selection of the exact termination time and initial strength is somewhat arbitrary, nevertheless the quality of the straight line fits is remarkable. A mathematical interpretation of these straight lines is not easy to define

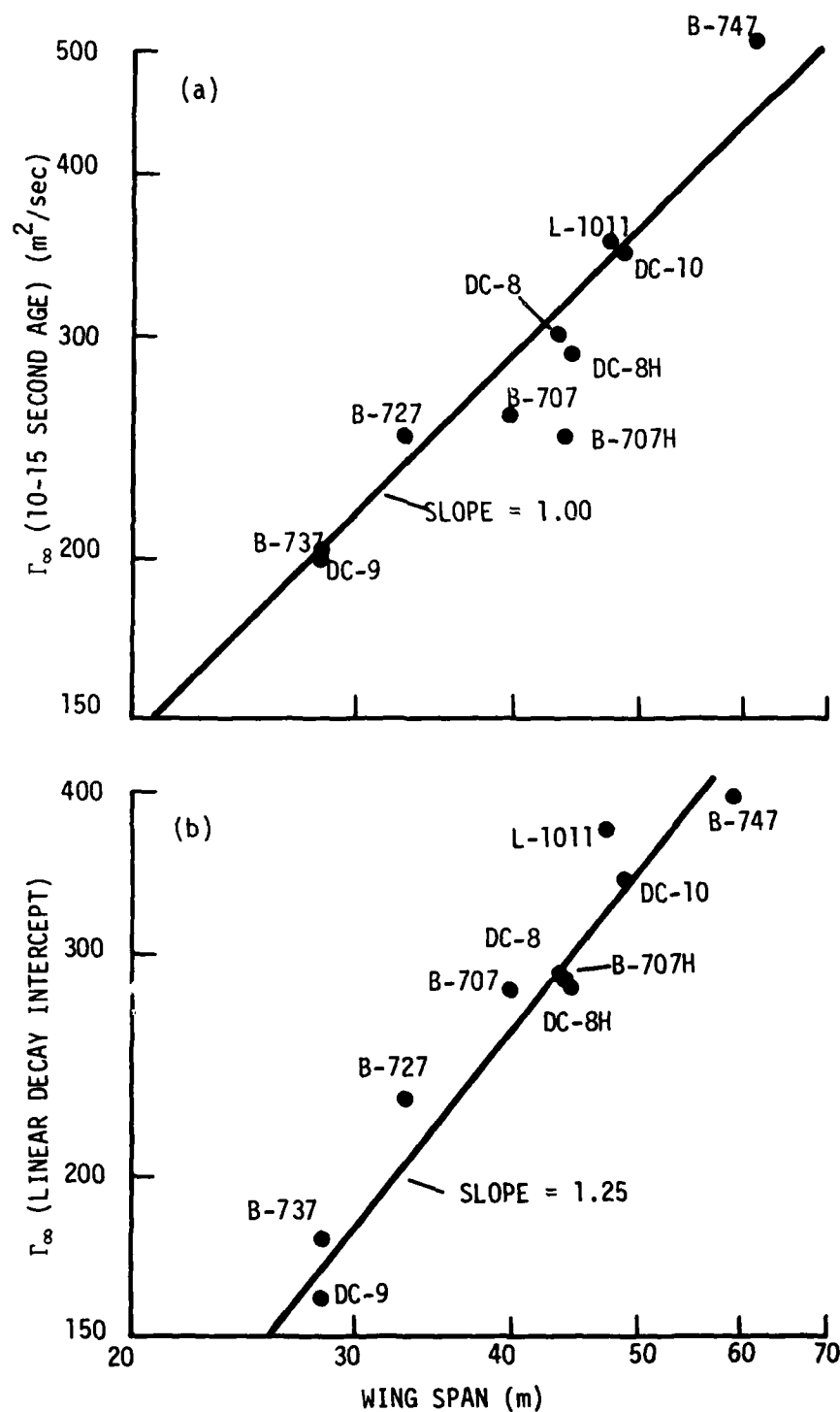


FIGURE 15. DEPENDENCE OF MEASURED VORTEX CIRCULATION UPON AIRCRAFT WINGSPAN: (a) 10-15 SECOND AGE, (b) LINEAR DECAY INTERCEPT

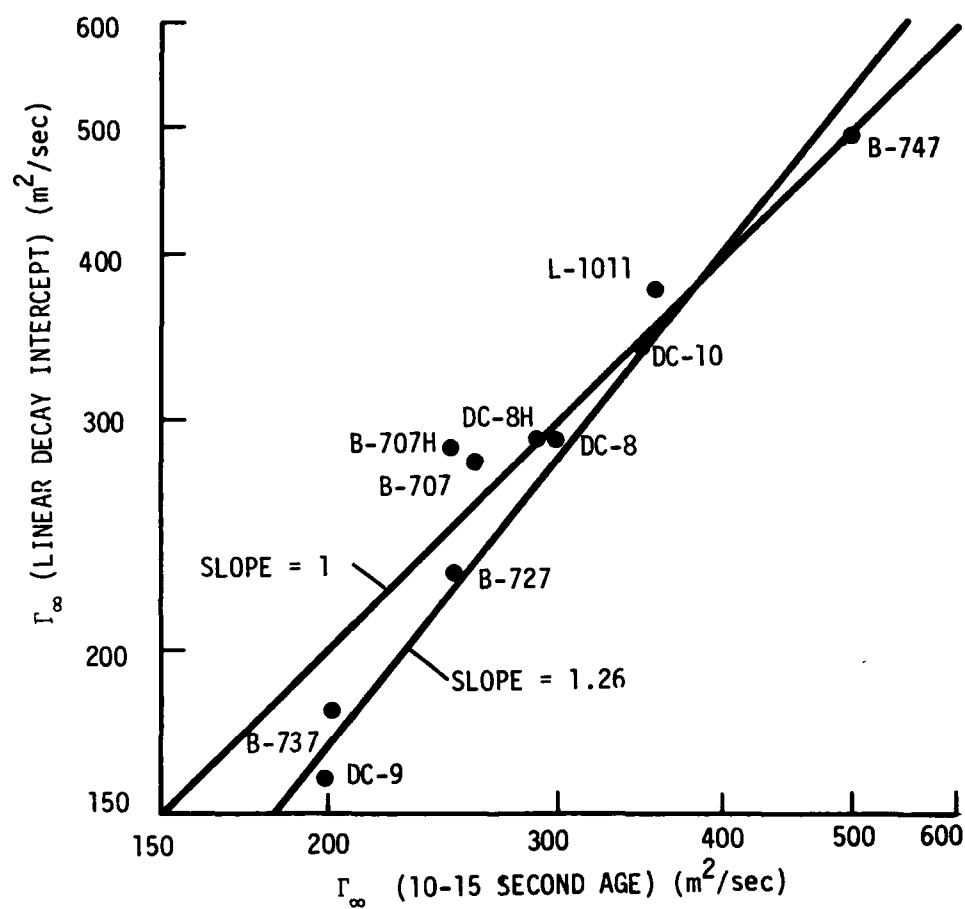


FIGURE 16. COMPARISON OF TWO CIRCULATION VALUES: LINEAR DECAY INTERCEPT VERSUS 10-15 SECOND AGE AVERAGE

since they represent only those vortices with strength above the MAVSS detection threshold, whose number is steadily diminishing. The following "picture" of vortex decay is a plausible explanation of how the straight lines might arise.

The straight line decay for all averaging radii corresponds to a vortex whose velocity profile is constant but whose strength is decreasing. Table 10 evaluates the core radii for the straight line decay. In some sense the straight-line-decay shape represents a vortex "equilibrium" decay state. For some cases (Figures 11 and 12), the "equilibrium" decay state is equivalent to the initial state. For others (Figure 13), the vortex undergoes a rapid transition from the initial state to the "equilibrium" state. Table 10 shows that, in general, the core radius is somewhat smaller for the "equilibrium" state than for the initial state. This change is consistent with the observation (Ref. 5) that the vorticity in the outer portion of the vortex tends to diffuse away more rapidly than that in the core. It is appealing to identify the linear vortex decay with turbulent diffusion which slowly eats away at a vortex. The loss of vortices below the detection threshold would then be identified as the result of instabilities which cause a vortex to rapidly lose strength and become undetectable. The inverse-time-squared decay in the models of Appendix B corresponds to this rapid decay. (Figures 7 and 8 of Volume II show how the detection rate of vortices decays in time).

5.2.2 Hazard Probability

In Section 5.1 of Volume II of this report it was found that the vortex hazard probabilities for different aircraft types could be characterized by assigning an effective vortex strength Γ'_{eff} to a generating aircraft such that the vortex hazard probability can be expressed as

$$F(\Gamma'_T, t) = Y(t, \Gamma'_T / \Gamma'_{eff}), \quad (16)$$

where Y is a universal decay function for all aircraft types. One would hope that the variation of Γ'_{eff} with averaging radius can be represented by an effective core radius r_{eff} which might be the same for all aircraft types. In this section an empirical quest for the universal function Y will be described. The next section will adopt a more analytical approach.

The first choice for Γ'_{eff} was simply the initial vortex strengths (10-15 second age) Γ'_0 given in Table 9. Figure 17 shows the data of Figure 10 plotted in a form where the hazard threshold Γ'_T is normalized to Γ'_0 . The points on a curve in Figure 17 correspond to the value of $(\text{vortex age}/100)^2$ where the curves in Figure 10 pass through a particular value of hazard probability F . A longer time is required to reach a lower value of F . Likewise, the time to reach a given hazard probability is longer if the hazard strength threshold is reduced.

Figure 18 shows how the averaging radius affects the plots of Figure 17. In general, the three averaging radii agree reasonably well in such normalized plots; changes in Γ'_0 of 20 percent or less would bring the curves into good agreement. The data in Figures 17 and 18 are subject to distortions below Γ'_T/Γ'_0 of about 0.4 because of the MAVSS detection threshold. The sharp break in the curves near $\Gamma'_T/\Gamma'_0 = 1$ occurs when Γ'_T becomes higher than some of the initial vortex strengths. The portion of the curves between these two limits can be represented as a straight line on these log-log plots. A slope of -1.00 is equivalent to the inverse time squared vortex decay which was used to generate the similar theoretical plots in Figure 37. The power law of the vortex decay is poorly defined in these plots because of the short range of the data validity.

Figure 19 compares the normalized decay curves for all the aircraft. The selected hazard probability $F = 0.05$ is low enough to give reasonable trends for safety considerations but is still high enough to have reasonable statistical accuracy for most aircraft types. (The B-707H is lost, however, because of too few cases). The left plots of Figure 19 show the curves where

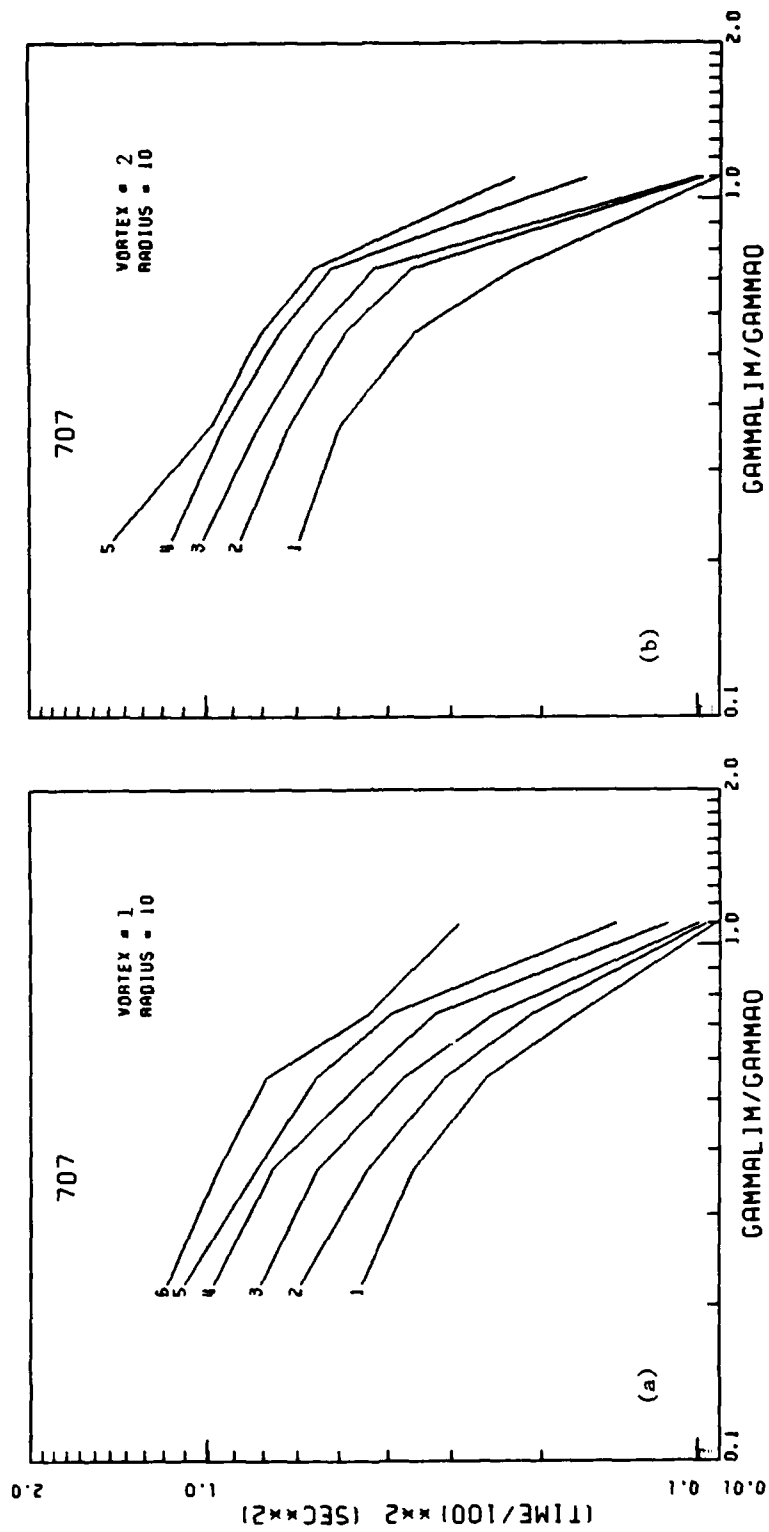


FIGURE 17. TIME TO REACH A GIVEN HAZARD PROBABILITY VERSUS NORMALIZED HAZARD THRESHOLD
 Γ_1/Γ_0 : (a) VORTEX 1, (b) VORTEX 2. CURVES: 1) $F = 0.2$, 2) $F = 0.1$, 3) $F = 0.05$,
 4) $F = 0.02$, 5) $F = 0.01$, AND 6) $F = 0.005$.

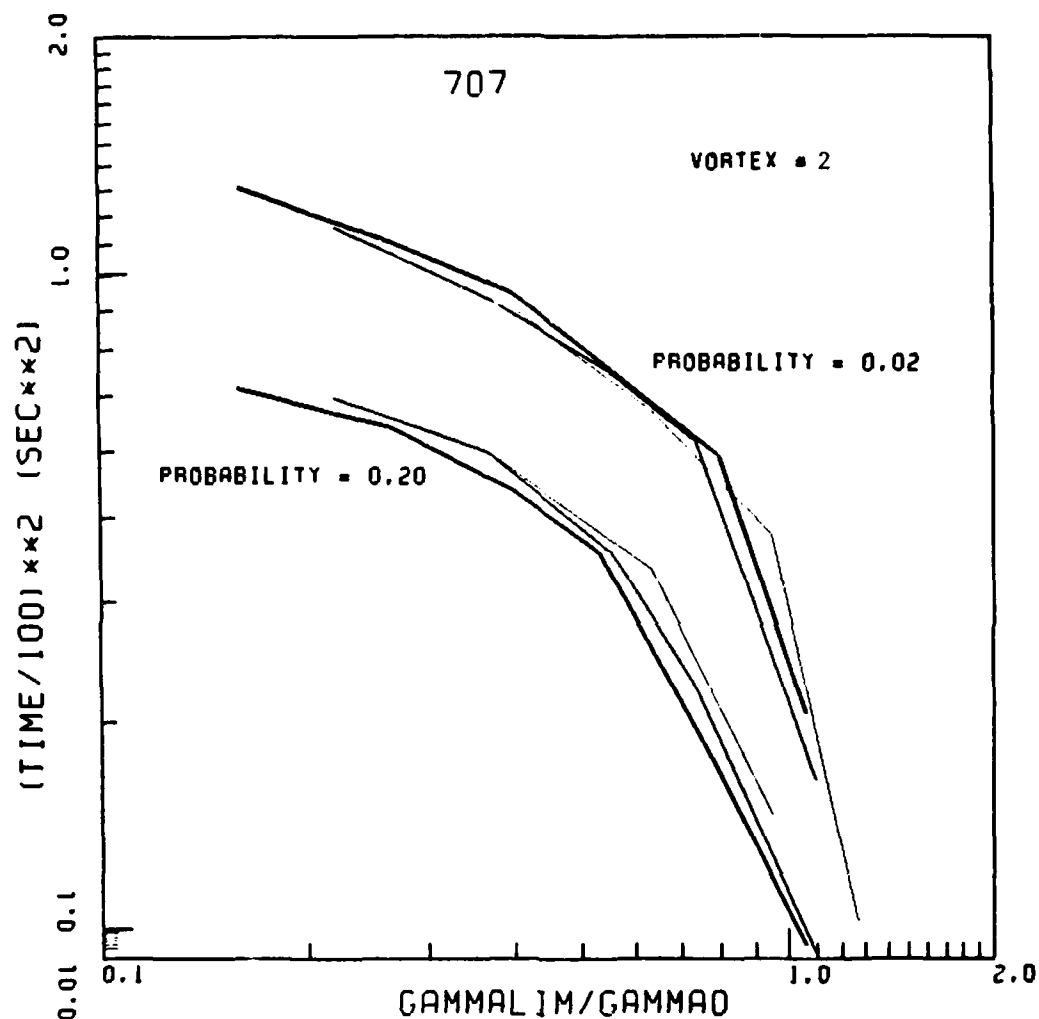


FIGURE 18. TIME TO REACH A GIVEN HAZARD PROBABILITY VERSUS NORMALIZED HAZARD THRESHOLD Γ_T/Γ_0 FOR THREE AVERAGING RADII: 5 METERS (NARROW LINES), 10 METERS (MEDIUM LINES) AND 20 METERS (BROAD LINES)

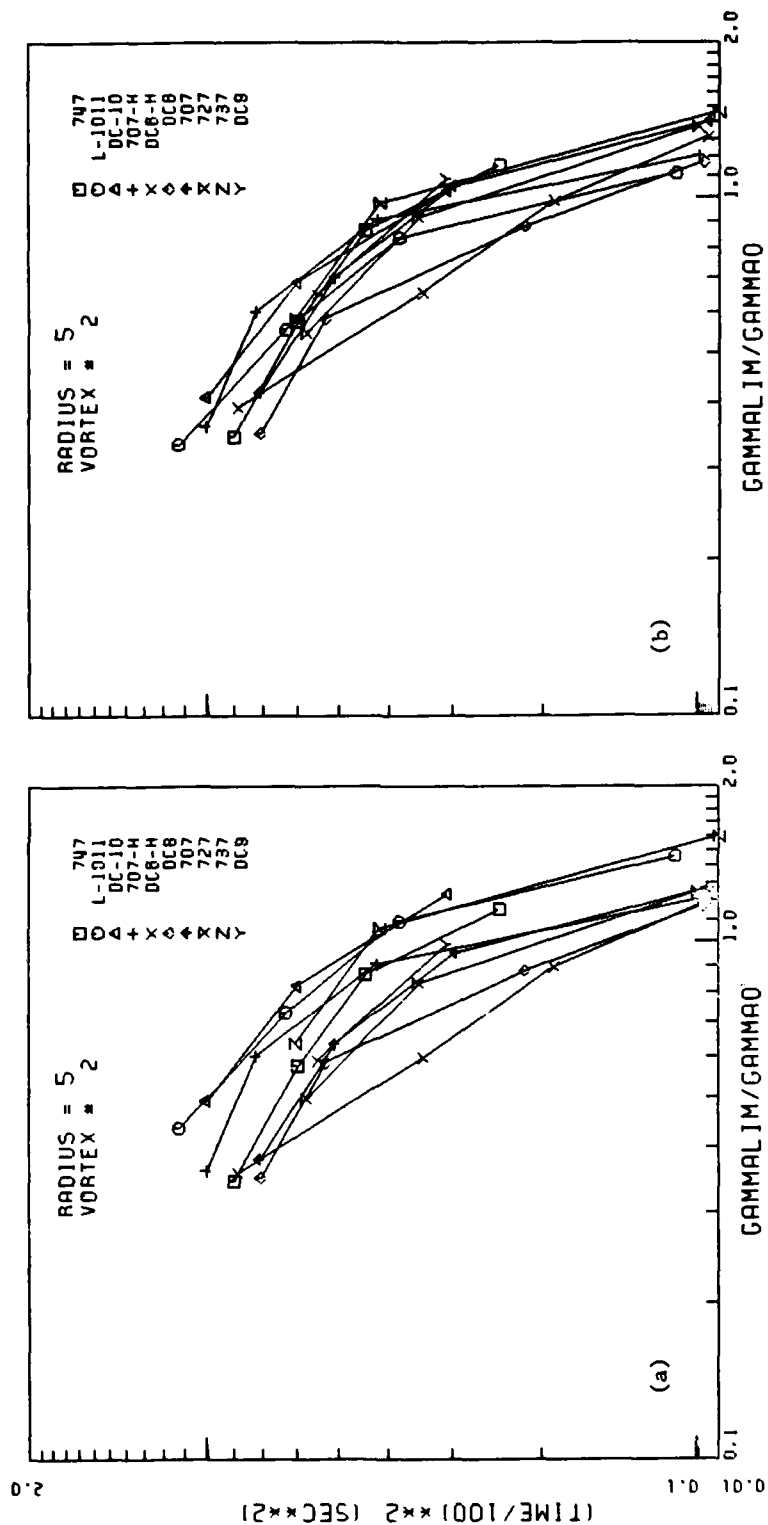


FIGURE 19. COMPARISONS OF NORMALIZED VORTEX HAZARD DECAY CURVES FOR ALL AIRCRAFT TYPES; $F = 0.05$, VORTEX 2, AVERAGING RADIUS = 5, 10, AND 20 METERS: (a) Γ_0 = INITIAL VALUES, (b) Γ_0 ADJUSTED TO GIVE GOOD AGREEMENT FOR 10 METER AVERAGING RADIUS (CONTINUED)

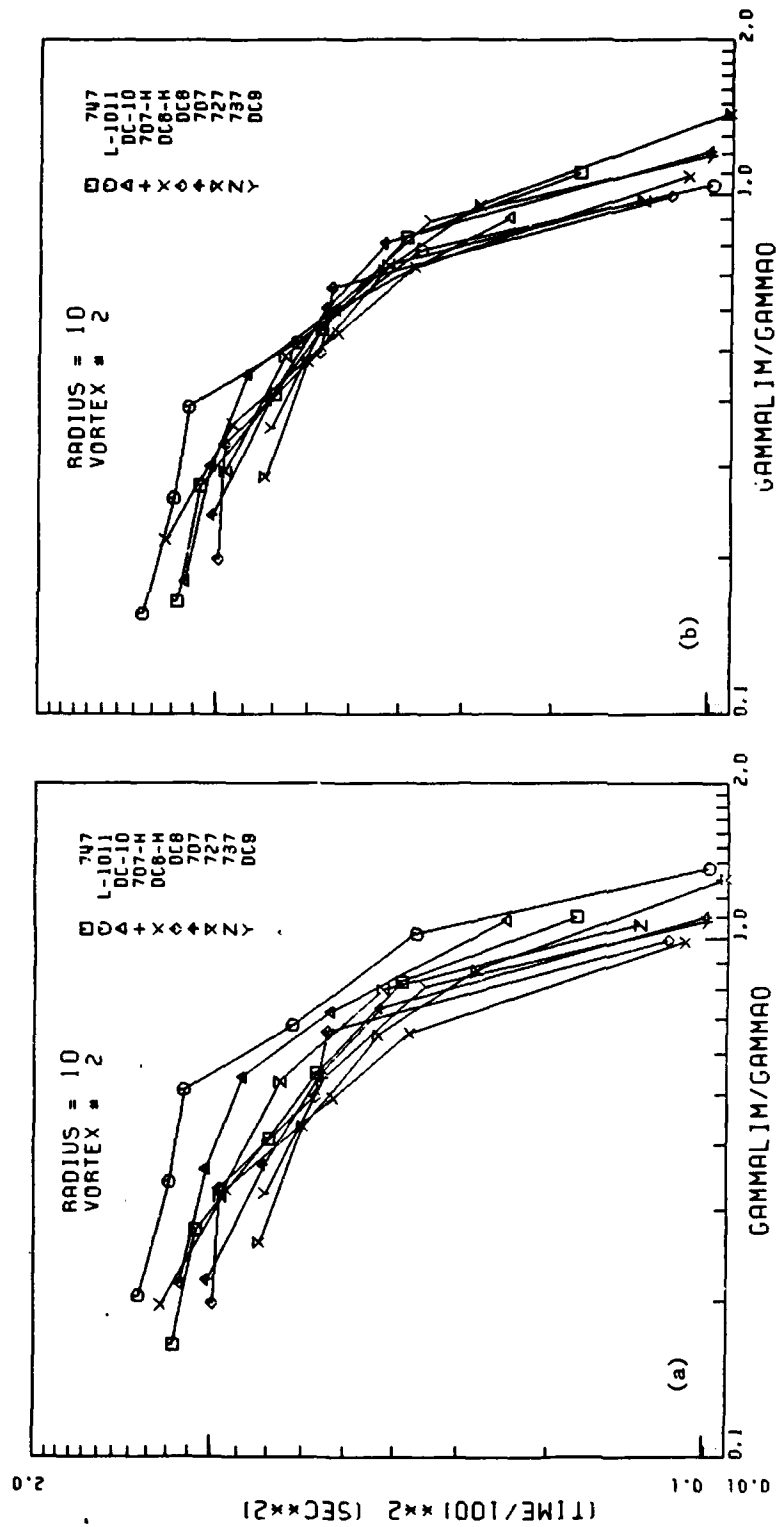


FIGURE 19. COMPARISONS OF NORMALIZED VORTEX HAZARD DECAY CURVES FOR ALL AIRCRAFT TYPES;
 $F = 0.05$, VORTEX 2, AVERAGING RADIUS = 5, 10, AND 20 METERS: (a) Γ_0 = INITIAL VALUES,
 (b) Γ_0 ADJUSTED TO GIVE GOOD AGREEMENT FOR 10 METER AVERAGING RADIUS (CONTINUED)

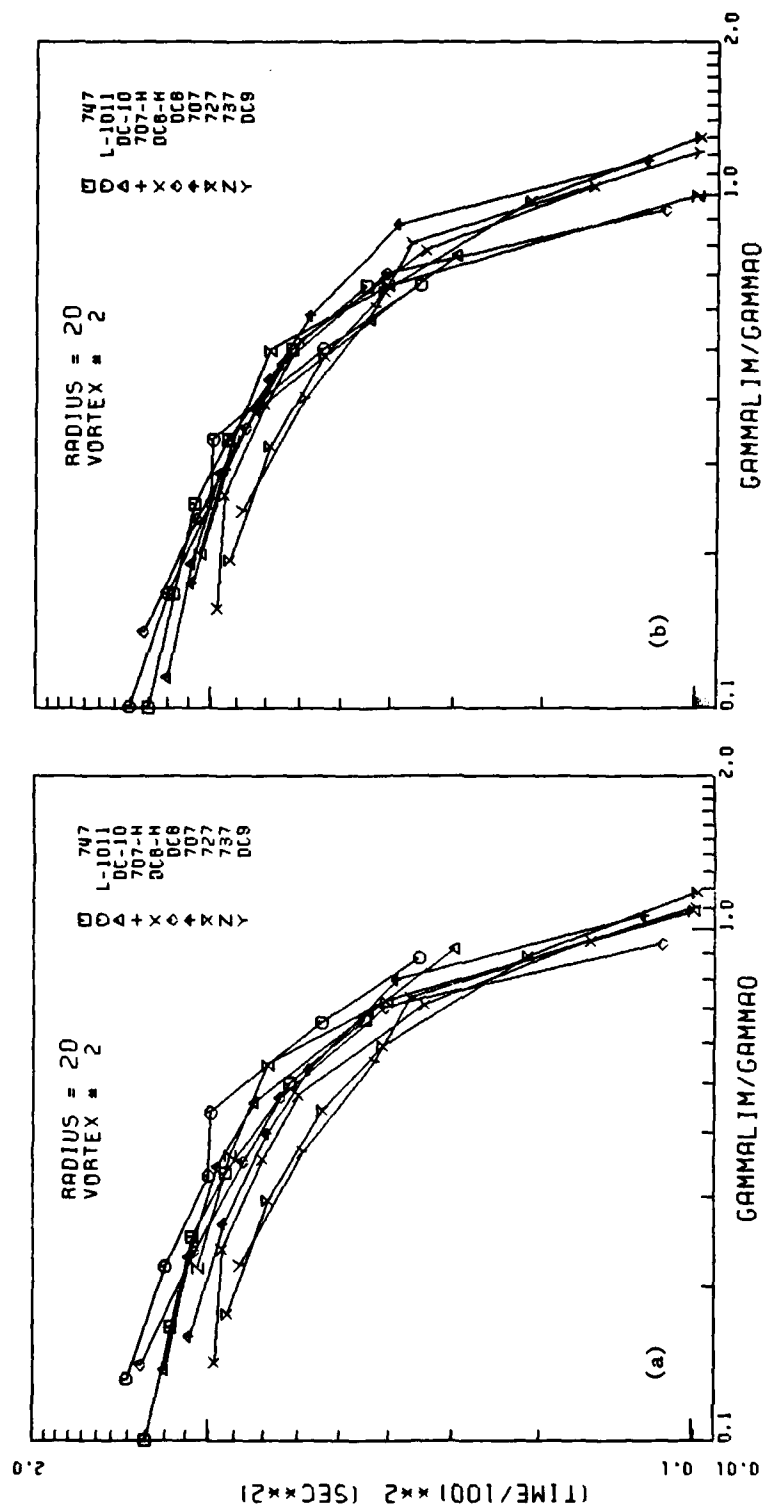


FIGURE 19. COMPARISONS OF NORMALIZED VORTEX HAZARD DECAY CURVES FOR ALL AIRCRAFT TYPES; $F = 0.05$, VORTEX 2, AVERAGING RADIUS = 5, 10, AND 20 METERS: (a) Γ_0 = INITIAL VALUES, (b) Γ_0 ADJUSTED TO GIVE GOOD AGREEMENT FOR 10 METER AVERAGING RADIUS

Γ'_0 was taken as the initial 10-15 second mean values. These values were adjusted to give excellent agreement in the middle of the -1.00 slope region for 10-meter averaging. The required changes in Γ'_0 were -9 percent for DC-9, B-727, B-707, and DC-8H; + 9 percent for B-737; + 20 percent for DC-10; and + 31 percent for L-1011. The same percentage changes were made for all radii. The resulting plots overlay fairly well for all radii. The only major deviations are the 5-meter DC-8 and DC-8H curves. Figure 20 plots these selected values of vortex strength as an effective Γ'_{eff} versus aircraft wingspan. Lines of slope 1.00 are drawn through the B-727 points as a guide for comparison.

This empirical method of searching for an effective vortex strength is not as fruitful as the analytical approach to be discussed in the next section. The concept of an effective strength to describe the vortex hazard is not completely satisfactory since the agreement of the curves in Figure 19 could probably be improved with displacements in the vertical time axis rather than the horizontal strength axis. In the vortex decay modeling these two are related by Equation 35 for a given hazard probability. Changing the time axis rather than the strength axis allows a more consistent treatment of the effects of the distribution of initial vortex strengths (see Section B.3).

5.2.3 Decay Modeling

Analytical models of vortex decay are more useful than the empirical fits of the last section because they can be extrapolated beyond the limits of the measurements to lower values of vortex strength and lower probabilities. Such an extrapolation is needed to reach the actual hazard probabilities encountered operationally and to explore the possible range of the fractional roll control parameter f .

5.2.3.1 Unsatisfactory Models - Before discussing the vortex models which can be used to represent vortex decay in a practical way, two unrealistic vortex models which are sometimes used to normalize vortex decay are examined. The first is the similarity

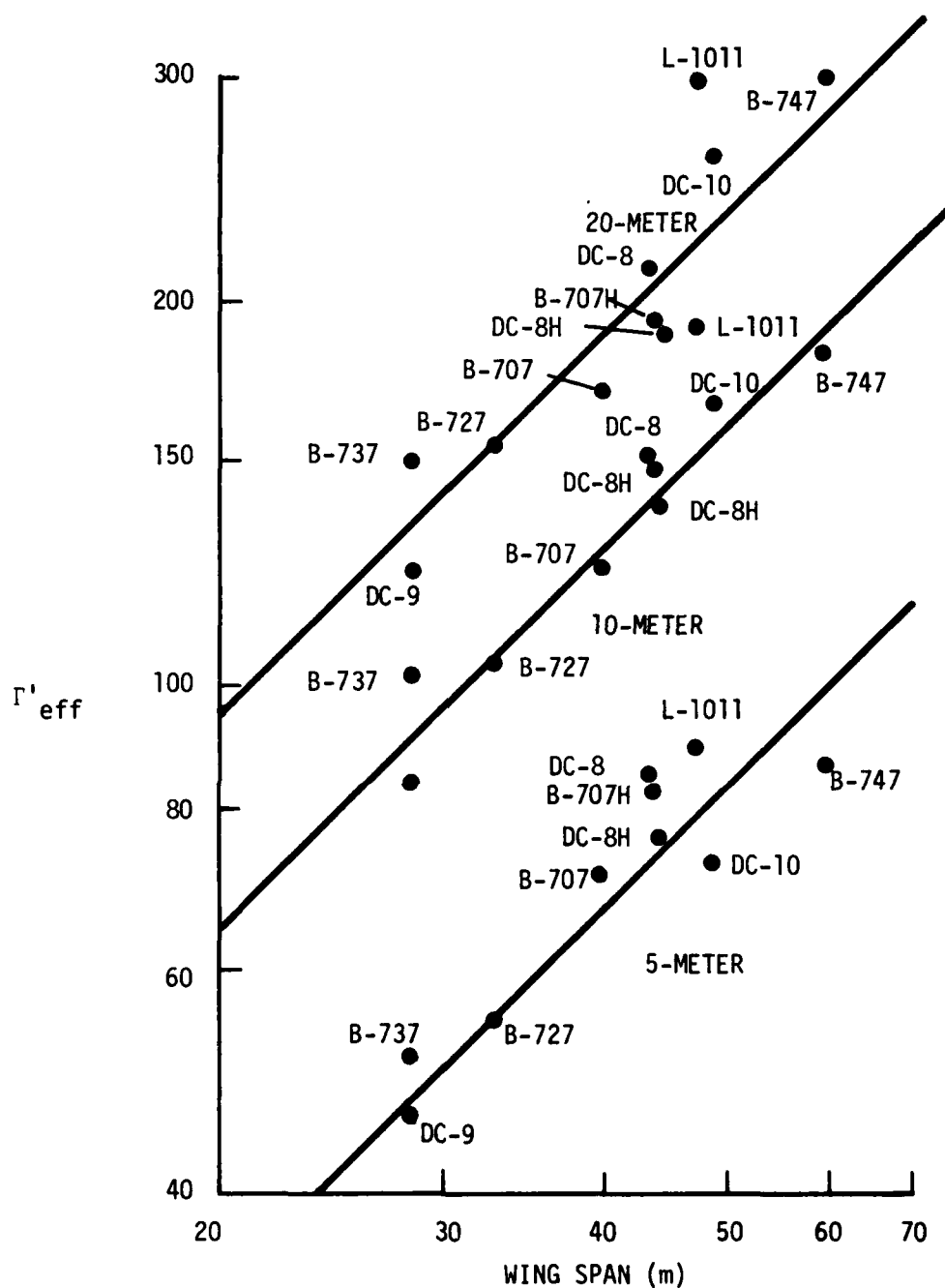


FIGURE 20. EFFECTIVE VORTEX STRENGTH FOR DETERMINING THE DECAY OF THE WAKE VORTEX HAZARD

model which is consistent with the eddy viscosity decay of vortices. This model assumes that the tangential velocity profile v of the vortex depends upon radius r and age t in the form $v(r^2/t)$. In this model the vortex core radius r_c slowly grows as $t^{1/2}$ and the value of Γ_∞ remains constant. In fact, real vortices tend to have constant or decreasing core radii with decreasing Γ_∞ .

The second model, which is used to normalize scale-model data, assumes that the decay of wake vortices can be normalized to the number of wingspans downstream multiplied by several correction factors:

$$\Gamma'(t)/\Gamma'_0 = Z(tVC_L/bA), \quad (17)$$

where V is the airspeed, C_L is the lift coefficient, b is the wingspan, A is the wing aspect ratio, and Z is a universal decay function. In Sections B.2 and B.3 the vortex decay time is found to have a much smaller dependence upon wingspan than given by Equation 17. The unsuitability of Equation 17 for describing vortex decay in the atmosphere may be at least partly due to the fact that the experimental data are related to the statistics of vortex decay under varying conditions while Equation 17 describes the deterministic decay of a single vortex.

5.2.3.2 Simple Stochastic Model - Appendix B develops a variety of analytic models which describe the decay of wake vortices. One of the models, the simple stochastic model (Section B.3) was selected to represent vortex decay in subsequent discussions (Section 6.0). The form of that model is outlined here. The example examined (DC-8) will be of particular interest in Section 6.0.

The vortex decay model used in this report serves the function of representing the vortex hazard decay data (as in Figures 8 to 10) in an analytical form. This analytical form is used to evaluate the vortex hazard duration for values of hazard probability F and hazard threshold Γ_T which lie outside the region where direct

measurement is possible. Only two free parameters, σ and $\bar{\Gamma}'$, are used to represent the vortex hazard decay for a particular aircraft type and averaging radius. Figures 21 and 22 (which correspond to Figures 38 and 39) illustrate this model for the case of DC-8 vortex 2 with 15-meter averaging radius, which will be important for the discussion in Section 6.1. Only vortex 2 is used since the results will be used to evaluate the wake vortex hazard for aircraft using the same runway. Figure 21 shows model fits to the vortex hazard decay using a separate value of σ for each hazard threshold Γ_T' and taking the 10-second value of hazard probability as the initial value. From Figure 21 a value of $\sigma = 12.2$ seconds was selected to fit the decay curves ($\Gamma_T' = 75$ and $100 \text{ m}^2/\text{sec}$) where the measurements are valid. This single value of σ is used to generate the model curves for all values of Γ_T' in Figure 22. The initial strength distribution assumes a 20 percent standard deviation in the initial vortex strength ($\bar{\Gamma}_0' = 182 \text{ m}^2/\text{sec}$). This method of fitting the data gives hazard duration times that are longer than measured for low threshold Γ_T' values. The fitted form is thus conservative in estimating the vortex hazard. It is also likely to be a better estimate of vortex decay than the actual data since the MAVSS cannot detect weak vortices. (Note: the fitted curves also overestimate the duration of the vortex hazard for $\Gamma_T' > \Gamma_0'$, a region of little practical consequence.)

The simple stochastic model thus is a realistic representation of the decay of the wake vortex hazard for the purposes of the analysis of Section 6.0. For aircraft types and averaging radii other than the case considered here, the value of Γ_0' comes from Table 9 and the value of σ from Figure 40.

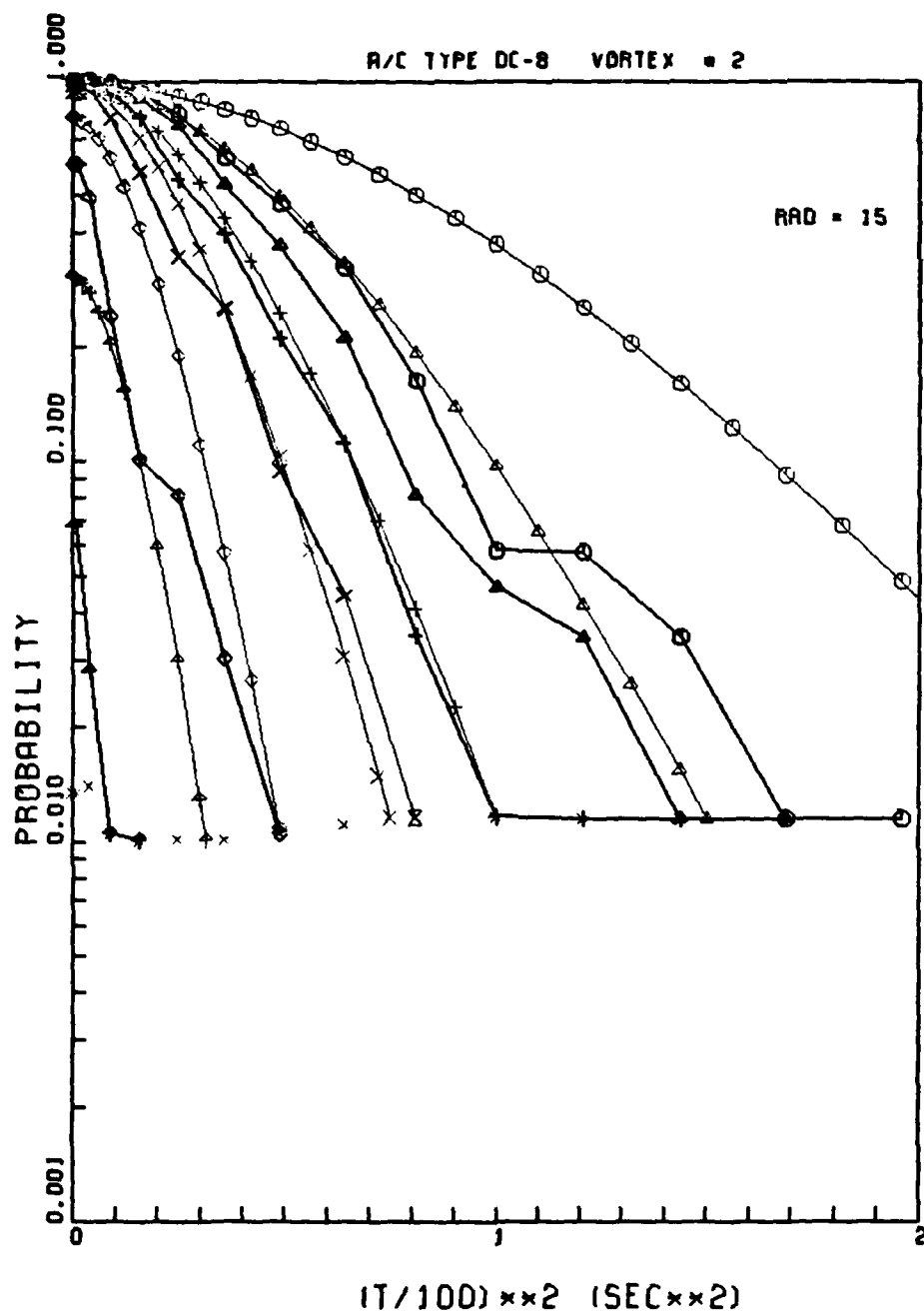


FIGURE 21. FITTED PROBABILITY DECAY CURVES FOR THE DC-8, 15-METER AVERAGING RADIUS, AND VORTEX 2. THE SIX CURVES REPRESENT Γ VALUES OF 200, 150, 100, 75, 50, AND 30 m^2/sec , RESPECTIVELY, FROM LEFT TO RIGHT. THE MEASURED DATA ARE PLOTTED WITH THICKER LINES THAN THE FITTED CURVES. THE NUMBERS BELOW THE CURVES ARE THE VALUES OF σ (sec) FOR EACH CURVE.

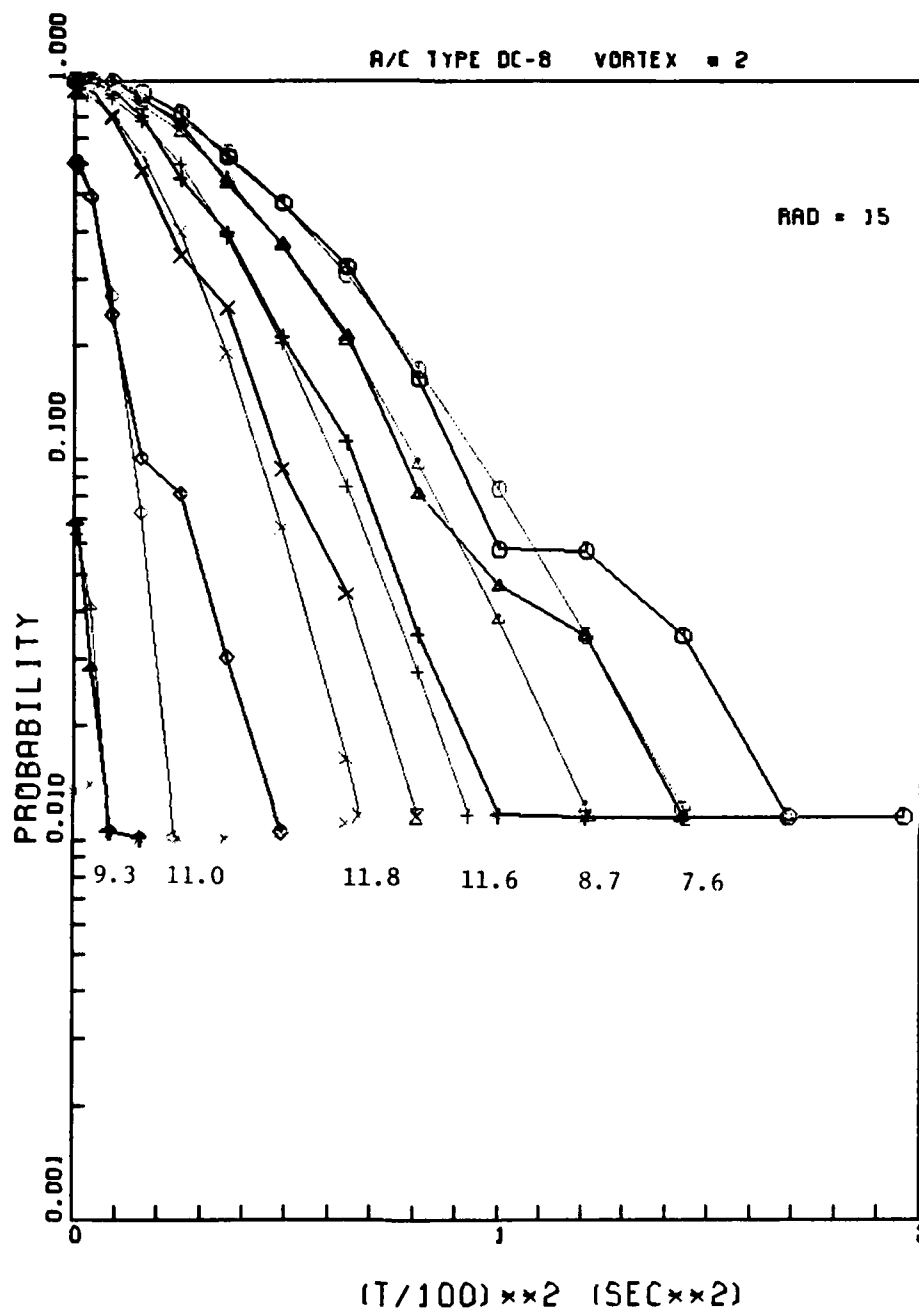


FIGURE 22. FITTED PROBABILITY DECAY CURVES USING TWO PARAMETERS, Γ'_0 AND σ

5-29/5-30

6. RECATEGORIZATION

In this section a preliminary look at recategorizing aircraft based on vortex behavior is presented. Resources did not permit a comprehensive analysis; however, the method of analysis is described through the development of a four-category system. Recommendations for further work are proffered.

The philosophy to be followed in examining the safety of aircraft separation standards is similar to that used in previous vortex safety analysis (Ref. 11). The present separation standards are assumed to be safe for those pairs of generator/follower aircraft which occur frequently in normal airport operations. The vortex hazard probability F found acceptable in current operations will be assumed to be acceptable under revised vortex categorization. The hazardous vortex encountered rate R_{hve} is given by

$$R_{hve} = R_{op} H F \quad (18)$$

where R_{op} is the rate of operations, H is the probability of encountering a vortex, and F is the probability that the vortex is hazardous. The acceptable level for F can be surprisingly large for several reasons. First, the probability H of encountering a vortex is very small because of the normal motion of vortices. Second, a large fraction of the aircraft operations occur at separations larger than the minimum. Since F decreases rapidly with separation distance, these operations contribute little to the hazardous encounter rate. In fact, there is probably a correlation between the vortex hazard duration and aircraft separation which further reduces R_{hve} . The operations rate R_{op} tends to be low under conditions such as early morning when the vortex lifetime is longest. The considerations in this report will be limited to vortex encounters occurring on final approach inside the middle marker. This location, where the MAVSS landing data

were collected, is most hazardous for vortex encounters for two reasons: (1) The normal descent of wake vortices is arrested by the ground so that a vortex (vortex 2) can remain stalled in the normal approach path. (2) The low aircraft altitude leaves little room for recovery from a vortex encounter. Reference 11 examined the wake vortex hazard both here and at higher altitudes.

6.1 CURRENT EXPOSURE TO VORTEX HAZARDS

The current IFR runway-threshold wake-vortex separation standards are listed in Table 11. Aircraft are separated by certificated maximum gross take-off weight W into three categories: Small ($W \leq 12,500$ lbs), Large ($12,500 < W < 300,000$ lbs), and Heavy ($W \geq 300,000$ lbs). The spacings of 3, 4, 5, and 6 nautical miles translate into time separations of 80, 107, 133, and 160 seconds, respectively, assuming a nominal approach speed of 135 knots. The most notable feature of the current separation standards is the extremely large range of aircraft sizes within the Large category.

The procedure for fitting the vortex decay data described in Section 5.2.3 is used to evaluate the vortex hazard probability F at the times (80, 107, 133, or 160 seconds) corresponding to the minimum separations in Table 11. Table 12 shows the results for $f = 1.0$ (Equation 13 and Table 4), and Table 13 the results for $f = 0.5$. Different averaging radii equal to the following aircraft semispan are used as appropriate to the size of the aircraft. The hazard probability results in Tables 12 and 13 show some departures from the expectation that larger aircraft should generate more hazardous vortices. The B-737 and the L-1011 show vortex hazards similar, respectively, to the larger B-727 and B-747. It is tempting to ascribe this increased hazard to the greater persistence (see Section B.2) of vortices from aircraft with two wing-mounted engines (e.g., DC-10, L-1011, B-737).

The highest probabilities in Tables 12 and 13 occur for 10-meter semispan Large (e.g., Gulfstream II) aircraft behind the

TABLE 11. VORTEX IFR SEPARATION STANDARDS AT RUNWAY THRESHOLD

(SEPARATIONS IN NAUTICAL MILES)

LEADING AIRCRAFT	FOLLOWING AIRCRAFT		
	HEAVY	LARGE	SMALL
HEAVY	4	5	6
LARGE	3	3	4
SMALL	3	3	3

TABLE 12. HAZARD PROBABILITY AT CURRENT MINIMUM SEPARATION FOR f=1.0

SEMISPAN	FOLLOWING AIRCRAFT					
	HEAVY	LARGE			SMALL	
	20m	20m	15m	10m	10m	5m
LEADING AIRCRAFT						
HEAVY						
B-747	2.2×10^{-4}					
L-1011	9.9×10^{-6}			1.8×10^{-6}		
DC-10						
B-707H						
DC-8H						
LARGE						
DC-8	2.4×10^{-4}	2.4×10^{-4}	1.3×10^{-3}	1.0×10^{-2}	2.0×10^{-5}	2.3×10^{-4}
B-707	2.3×10^{-5}	2.3×10^{-5}	1.6×10^{-4}	5.1×10^{-3}	3.3×10^{-6}	7.8×10^{-5}
B-727			4.2×10^{-6}	4.8×10^{-4}		
B-737			1.2×10^{-6}	2.9×10^{-4}		8.9×10^{-8}
DC-9			7.8×10^{-8}	7.2×10^{-5}		

Those combinations with no entry have a probability less than 10^{-11} .

TABLE 13. HAZARD PROBABILITY AT CURRENT MINIMUM SEPARATION FOR $f=0.5^*$

	FOLLOWING AIRCRAFT					
	HEAVY	LARGE			SMALL	
SEMISPAN	20m	20m	15m	10m	10m	5m
LEADING AIRCRAFT						
HEAVY						
B-747	2.3×10^{-2}	6.9×10^{-4}	1.4×10^{-3}	7.1×10^{-3}	1.8×10^{-4}	6.4×10^{-4}
L-1011	1.9×10^{-2}	4.8×10^{-4}	1.3×10^{-3}	1.1×10^{-2}	3.9×10^{-4}	2.3×10^{-5}
DC-10	5.6×10^{-3}	5.0×10^{-5}	2.0×10^{-4}	4.3×10^{-3}	7.9×10^{-5}	9.2×10^{-5}
B-707H	2.3×10^{-3}	9.1×10^{-6}	2.0×10^{-4}	2.8×10^{-3}	3.8×10^{-5}	1.6×10^{-4}
DC-8H	3.2×10^{-4}			4.0×10^{-5}		
LARGE						
DC-8	6.7×10^{-2}	6.7×10^{-2}	1.1×10^{-1}	2.3×10^{-1}	2.2×10^{-2}	2.1×10^{-2}
B-707	3.3×10^{-2}	3.3×10^{-2}	5.7×10^{-2}	1.8×10^{-1}	1.3×10^{-2}	1.2×10^{-2}
B-727	7.1×10^{-3}	7.1×10^{-3}	1.8×10^{-2}	8.1×10^{-2}	2.0×10^{-3}	9.6×10^{-4}
B-737	7.3×10^{-3}	7.3×10^{-3}	2.0×10^{-2}	8.6×10^{-2}	2.3×10^{-3}	1.8×10^{-3}
DC-9	1.1×10^{-3}	1.1×10^{-3}	9.7×10^{-3}	5.3×10^{-2}	7.7×10^{-4}	4.2×10^{-4}

Those combinations with no entry have a probability less than 10^{-11} .

* $f=0.6$ for 5-m averaging radius.

Large DC-8 and B-707 aircraft. This combination occurs too infrequently in normal operations to constitute a satisfactory choice for a safe vortex hazard probability. The next highest probability in the tables occurs for a 15-meter semispan aircraft following a Large DC-8. Since this size follower represents the DC-9 and the B-737, this combination occurs often enough in normal operations to represent a safe level of hazard probability. With the increase in commuter traffic since deregulation, the number of aircraft operations in the 10-meter semispan Large category has increased considerably. This higher hazard probability for such aircraft following the biggest Large aircraft raises possible questions concerning the safety of the current separation standards.

The DC-8 with a 15-meter semispan following aircraft represents the highest vortex hazard probability F_s which is known to be safe. Figure 23 shows how the hazard probability for this case depends upon the selected value of f_s , which is the ratio of the maximum safe vortex-induced rolling moment to the nominal maximum control-induced rolling moment. This ratio is given by $f = \Gamma_T' / 5b$ according to Equations 13 and 14. The values for $f = 1.0$ and 0.5 were included in Tables 12 and 13, respectively.

The shape of the F_s versus f_s curve is virtually identical to the F versus t^2 plots such as Figure 9. This similarity stems from the fact that f_s is proportional to Γ_T' and the model used gives F as a function of $\Gamma_T' t^2$ as long as Γ_T' is less than 70 percent of Γ_C' (which is true for all the hazard cases to be evaluated in the following discussion).

The relationship between F_s and f_s in Figure 23 can be used to investigate the sensitivity of the safe vortex separation time to the assumed value of f_s . (Here the subscript s refers to the value of f for the known safe case.) For example, if a 10-meter semispan aircraft has the same hazard model parameters (\hat{p} and K in Equation 12) as the DC-9 and the B-737, then the hazard duration can be calculated as the time for the 10-meter hazard probability

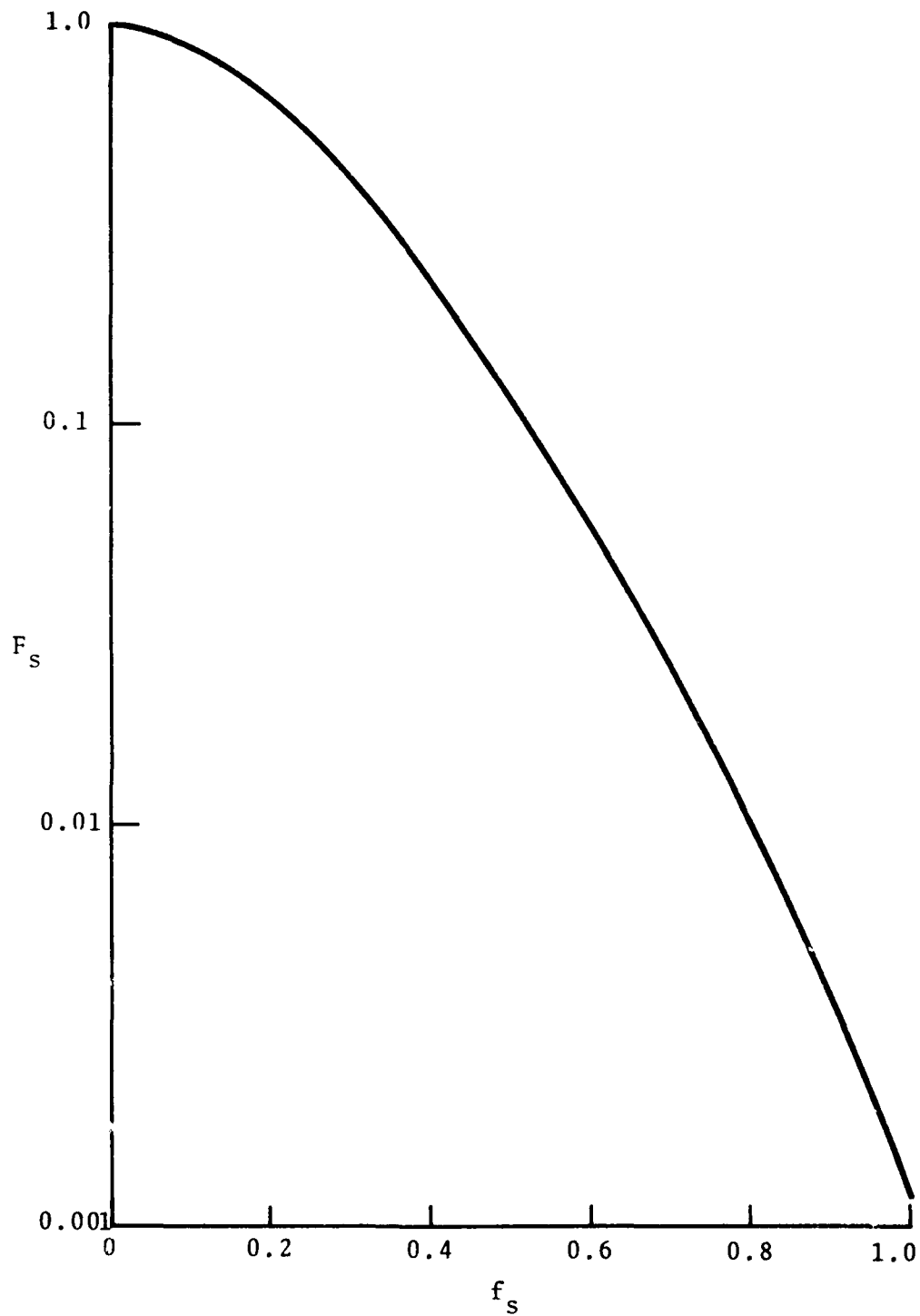


FIGURE 23. SAFE HAZARD PROBABILITY F_s VERSUS THE ASSUMED SAFE LIMIT f_s ON THE RATIO OF VORTEX-INDUCED ROLL TO MAXIMUM ROLL CONTROL^s

to reach the value F_s using the same value of $f = f_s$ ($\Gamma_T' = f5b$). The resulting safe time t_s behind a DC-8 is 90.0 seconds for f_s equal to 0.7 or less. The value of t_s increases to 90.8 seconds at $f_s = 1.0$. This small dependence upon f_s is a consequence of Γ_T' being less than for Γ_O' for this range of f values. The similar functional form for all the decay curves leads to very little dependence of t_s upon f_s . In all cases to be presented here, the variation in t_s for f_s between 0.1 and 1.0 is less than 2 seconds. The values plotted will be for $f_s = 0.5$. The value of $t_s = 90.0$ seconds for a 10-meter semispan aircraft following a DC-8 is larger than the defined safe time of 80 seconds for a 15-meter semispan aircraft following a DC-8, as one would expect. Tables 12 and 13 show a higher hazard probability at 80 seconds for the smaller semispan. A longer time must elapse before the 10-meter hazard probability drops to the 80-second value for 15-meter semispan.

It is possible that the values of \hat{p} and K for the 10-meter semispan aircraft may be significantly different from those for the 15-meter semispan aircraft. For example, the value of \hat{p} for the DC-9 with spoilers is known (Ref. 12) to be 0.11 rather than the 0.06 and 0.08 \hat{p} values assigned to jet transport and general aviation aircraft, respectively.

Another effect which affects the value of the safe time t_s in the same way as differences in \hat{p} and K is the error introduced by the MAVSS overestimate of the core radius. According to Table 1, if the DC-8 core radius is actually 1.5 m instead of the measured value of about 4.0 m, the 10-m strength will read a factor of $1.31/1.50 = 0.87$ low relative to the 15-meter reference value. The value of f used to evaluate the safety time for a different semispan should be reduced by this same factor. A similar reduction in f is needed if the actual value of \hat{p} is lower than the 0.11 DC-9 value with spoilers; a reduction factor of $0.08/.11 = .73$ might be required for a general aviation aircraft. Because of the possible existence of these correction factors, an additional safe time $t_s = 116.2$ seconds for

$f = 0.6 f_s$ is calculated to evaluate the sensitivity of the results to these two types of effects. The time is significantly increased since these effects are equivalent to reducing the effective hazard threshold. The actual hazard duration probably lies between the $f = f_s$ and $f = 0.6 f_s$ values of 90.0 and 116.2 seconds.

Table 14 shows a similar selection of variations in f/f_s which are needed to estimate the sensitivity of the vortex hazard duration to \hat{p} and K variations and to core size errors for three aircraft types which will be important to the subsequent discussion. The assumed values of the core radii are the values contained in Table 1.

Since the DC-8 has the most persistent vortex hazard of any of the Large aircraft, it can be used to represent the safe separation required behind the Large category. The dependence of the safe separation behind Large aircraft upon the semispan of the following aircraft is plotted as circles in Figure 24. The solid points are for $f/f_s = 1$ and the open points are for the values of f/f_s given in Table 14. The B-747 similarly has the most persistent vortex hazard of the Heavy aircraft (except for a 10-meter semispan follower where the L-1011 hazard has greater persistence). The B-747 safe separations (L-1011 for 10-meter semispan) are plotted as squares in Figure 24 to represent the Heavy category. Data for the DC-9 are also included in Figure 24 to illustrate the hazard associated with the middle of the current Large category. The selection of the DC-8 and B-747 to represent the worst wake generators of the Large and Heavy categories could be in error for small averaging radii if the Γ' core correction of another aircraft type is enough larger to offset the apparent slower decay of these largest aircraft types.

The results of Figure 24 are in reasonable agreement with the current separation standards of Table 11, particularly for the Heavy category. The 5-nautical-mile separation for Large aircraft behind Heavies is satisfactory for all semispans for $f/f_s = 1$ and for semispans above 10.5 meters when considering the

TABLE 14. SENSITIVITY ANALYSIS VARIATIONS

LEADING AIRCRAFT	FOLLOWING AIRCRAFT SEMISPAN (m)	CORRECTION	f/f_s^{**}
DC-8	15	0	1.00***
B-747	10	0.87	0.60
DC-9	5	0.60	0.40
B-747	20	1.02	0.70
	15	0.95	0.70
	10	0.81	0.60
	5	0.55	0.40
DC-9	15	0.90	0.70
	10	0.74	0.60
	5	0.44	0.40

* Relative to 15-meter DC-8 case.

ASSUMED CORE RADII:

	MEASURED	ACTUAL
DC-8	4.0	1.5
B-747	5.5	2.5
DC-9	4.0	0.5

** Incorporating Γ' core corrections and 0.73 factor for \hat{p} and K.

*** Defined as safe.

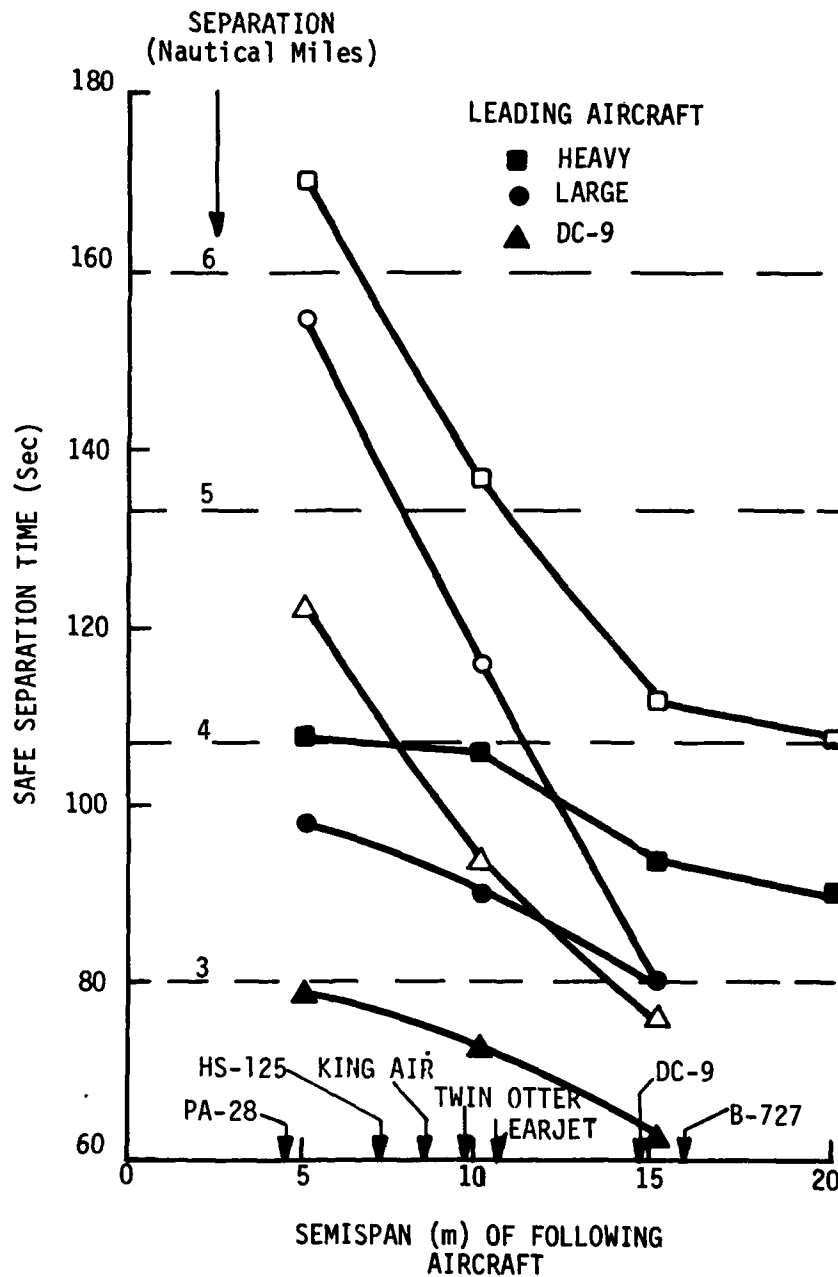


FIGURE 24. SAFE SEPARATION TIMES FOR AIRCRAFT CATEGORIES AS A FUNCTION OF FOLLOWING AIRCRAFT SEMISPAN: SOLID POINTS, $f/f_s = 1$; OPEN POINTS, VARIATION IN f/f_s GIVEN IN TABLE 14

sensitivity analysis variations. The 6-nautical-mile separation for Small aircraft behind Heavies is very conservative for all semispans for $f/f_s = 1$, and is satisfactory for semispans above 6.5 meters when considering the sensitivity analysis variation. The spacings behind the Large category are less conservative for the assumed variations of Table 14. The 4-nautical-mile separation for Small aircraft is satisfactory for all semispans for $f/f_s = 1$ and only for semispans above 11 meters when considering the variations of Table 14. These observations set the stage for a proposed four-category separation standard to be examined in the next section

6.2 EVALUATION OF A FOUR-CATEGORY SYSTEM

This report will restrict its examination of possible wake vortex recategorization to a single scheme, namely dividing the Large category into two categories termed Large and Medium. The break between Large and Medium is set just below the DC-9 and B-737 so that all commercial jet transports will be either Heavy or Large. Such a split is in use in the United Kingdom. This split can simultaneously improve safety and reduce traffic delays because it more accurately reflects the actual wake vortex hazards. A glance at Table 11 shows that the current separations are extremely conservative for most pairs of aircraft and that only a few pairs experience any significant hazard. The use of four categories rather than three allows a more uniform hazard probability.

Table 15 shows proposed separation standards for a four-category system. Only three pairs show changes from current standards. The spacing of a Large behind a Heavy is reduced from 5 to 4 nautical miles. The spacing of a Medium and a Small behind a Large is increased from 3 to 4 and from 4 to 5 nautical miles, respectively. The net effect of these changes is likely to be an increase in capacity at the major hub airports where the traffic is predominately a mix of the Large and Heavy aircraft of the four-category system. At some airports the Medium and Small aircraft are assigned to a separate shorter runway.

TABLE 15. PROPOSED FOUR-CATEGORY IFR RUNWAY THRESHOLD SEPARATION

(SEPARATIONS IN NAUTICAL MILES)

LEADING AIRCRAFT	FOLLOWING AIRCRAFT			
	HEAVY	LARGE	MEDIUM	SMALL
HEAVY	4	4**	5	6
LARGE	3	3	4*	5*
MEDIUM	3	3	3	4
SMALL	3	3	3	3

* An increase from current separations.

** A decrease from current separations.

The reduction of the Large behind Heavy spacing from 5 to 4 nautical miles is well justified by the data in Figure 24. The points for reduced f/f_s lie only slightly above the 4-nautical-mile line for the appropriate 15- and 20-meter semispans. Most of the reduction in f/f_s is intended to account for \hat{p} values less than those of the DC-9 and B-737. Since those are exactly the aircraft most at hazard behind a Heavy aircraft, such a reduction is unnecessarily large; the actual hazard duration is therefore comfortably below the 4-nautical mile line.

The proper safe separation of Medium and Small aircraft behind Large aircraft is less easily determined because of the uncertainties associated with the MAVSS core-size errors. A strict requirement that the separations remain below the open-circle line in Figure 24 leads to separations which seem too conservative in comparison to the current standards. The 4-nautical-mile Medium-behind-Large separation is strictly valid only for following-aircraft semispans greater than 11 meters. Similarly, the 5-nautical-mile Small-behind-Large separation is strictly valid only for semispans greater than 7.5 meters. It is apparent that the hazard model of Section 3.1 related the vortex hazard for a following aircraft to the wingspan rather than the weight which is used to define the current categories. For the purposes of the present discussion it therefore makes sense to define the boundaries dividing Large, Medium, and Small on the basis of wingspan. The Medium-Large division is set at a 25-meter wingspan (12.5-m semispan) which is just below the DC-9 and B-737. The Small-Medium division is more arbitrary and is set at a 15-meter wingspan (7.5-m semispan).

The proper separation of a Small behind a Medium is difficult to define for two reasons. First, we have little vortex data on Medium aircraft. Second, the aircraft wingspan, which properly classifies an aircraft as a follower, may not properly classify an aircraft as a generator. The effective vortex strength, shown in Figure 20, is roughly proportional to wingspan for jet transport aircraft which have similar wing loading. However, the

vortex hazard is likely to be much less for an aircraft such as the DC-3 which has much lower wing loading. The vortex hazard from the DC-9, which is just above the Medium category, can give some clue to the hazard from Medium leading aircraft. The DC-9 data in Figure 24 show that 4-nautical-mile spacing is strictly safe for aircraft with semispans above 7.5 meters. In accord with the philosophy used with Large leading aircraft, the Small-behind-Medium safe separation was set a 4 nautical miles.

6.3 HEAVY-LARGE BOUNDARY

The data in this report have some bearing on current questions regarding the division between the Heavy and Large categories. This division becomes somewhat less important in the four-category system of Section 6.2 than in the current system since the Large and Heavy categories have the same separations as follows.

Volume II of this report (Ref. 2) examined the feasibility of including the B-707H and DC-8H in the Large category. The impact of this change on the Large separations in Figure 24 is shown in Table 16. The DC-8H actually has a less persistent vortex hazard than the DC-8 and is not included. The B-707H, however, shows a more persistent hazard. Because of the small number of cases, the B-707H results have relatively poor statistical accuracy.

A number of new jet-transport aircraft (e.g., A-300, A-310, B-757, B-767) have been and are being added to the jet transport fleet since the MAVSS data were collected. They all have weights near the break point between the Large and Heavy categories and they all have two wing-mounted engines. In the light of the observed abnormally high persistence of vortices from aircraft with two wing-mounted engines, it may be advisable to assign such aircraft to the Heavy category. Such has been the practice in the UK where the A-300 has been designated a Heavy on the basis of vortex encounter reports.

TABLE 16. COMPARISON OF SAFE SEPARATIONS FOR THE
DC-8 AND THE B-707H

SEMISPAN OF FOLLOWING AIRCRAFT (m)	f/f_s	DC-8 t_s (sec)	B-707H t_s (sec)
15	1.0	80.0	85.7
10	1.0	90.0	97.0
10	0.6	116.2	125.3
5	1.0	98.1	112.0
5	0.4	155.0	177.1

6.4 RECOMMENDATIONS

This preliminary analysis indicates that a four-category system might have merit. If the system does indeed have operational utility, a host of questions needs to be examined before proceeding to implementation. The following paragraphs outline recommended tasks.

6.4.1 Safety Analysis

The safety analysis herein should be refined by:

- 1) Investigating the adequacy of the hazard model for wide variations in aircraft size. (Should a pilot response time be included?)
- 2) Examining the adequacy for the MAVSS measurements (particularly the core corrections).
- 3) Combining the hazard probabilities for each aircraft pair with the frequency of occurrence for each pair to derive an estimate of the total hazardous encounter rate for the current and proposed systems.
- 4) Considering encounters at locations other than between the middle marker and touchdown (including takeoffs).

6.4.2 Category Boundaries

The selection of category boundaries (Heavy, Large, Medium, and Small) must be based on a detailed evaluation of the exact characteristics (e.g., \hat{p} , b , and W) of the aircraft which lie near the boundary. The selection of boundaries and separations must also include the effect on capacity at different types of airports, such as commercial hubs and busy GA fields.

6.4.3 Operational Questions

The air traffic implications of increasing the number of categories must be examined. It may be feasible to retain a three-by-three separation matrix but with different leader and follower

categories (e.g., an A-300, say, be classified as a Heavy when it is the leading aircraft but classified as a Large when it is the following aircraft); would such a differentiation be useful?

6.4.4 United Kingdom Experience

The UK has considerable experience with both operational and safety aspects of possible recategorization. Closer cooperation with the UK would be advantageous to answering questions and also would expedite the ICAO acceptance of a new categorization system.

APPENDIX A

MAVSS DETECTION THRESHOLD

The detection of wake vortices as they pass over successive MAVSS antennas is accomplished by correlating the vertical velocity profile with a function which is similar to a vortex signature (see Volume I, Section 5.2). For vortices from landing aircraft the correlator sums vertical velocities over a region 18 m high (5 range gates) and 20 m wide. The threshold assigned to the correlator corresponds to a uniform absolute velocity, $V_c = 2.5$ m/sec over the correlation region. Of course, the vertical velocity signature of a vortex is not uniform (see Figure 1); it is zero along a vertical line through the vortex center, reaches a maximum on either side of the vortex core, and then decreases for both horizontal and vertical displacements from the vortex center (Reference 13 shows many such profiles). Some indication of the vertical variation in average velocity can be obtained by comparing the average velocity V_c (absolute value) over five range gates from the correlator with the average velocity V_r along the single range gate nearest the vortex height. The ratio of V_r to V_c varied between 1.1 and 2.0 with a typical value of 1.5 for B-707 and DC-8 data.

One estimate of the vortex strength detection threshold can be obtained by calculating the average circulation of a vortex with a constant tangential velocity v_0 . According to equation 3, the value of $\Gamma'(r)$ is proportional to the averaging radius r :

$$\Gamma'(r) = \pi v_0 r. \quad (19)$$

If we take $v_0 = 2.5$ m/sec, the average velocity V_c of the correlator threshold, we obtain a vortex strength threshold estimate of

$$\Gamma'(r) = 7.9 r. \quad (\text{m}^2/\text{sec}) \quad (20)$$

For consistency this value should be reduced by the ratio V_r/V_c since V_r is the average tangential velocity. Taking $V_r/V_c = 1.5$ leads to a threshold estimate of

$$\Gamma'(r) = 5.2 \text{ r.} \quad (\text{m}^2/\text{sec}) \quad (21)$$

This value corresponds to the hazard fraction value $f = 0.52$ in Equation 13.

A more direct determination of the effective MAVSS detection threshold can be obtained by comparing the measured strength with the value of the detection correlation. Figure 25 shows such a comparison for 10-m averaging radius for a sample of B-707 and DC-8 data. To increase the number of low value points, data for parts of the sample were plotted only if the correlator was less than 60 or the strength less than $80 \text{ m}^2/\text{sec}$. According to this set of data, vortices of strength less than $50 \text{ m}^2/\text{sec}$ start to be undetected. The strength for a 50 percent detection probability appears to be about $30 \text{ m}^2/\text{sec}$. Note that the 10-m averaging radius was used in Figure 25 because the correlator and strength are averaged over the same distance and therefore might be expected to show the best correlation.

Another way of estimating the detection threshold is to examine the distribution of the detected vortex strengths, which is shown in Figure 26 for four different sizes of aircraft. One would expect a break in the distribution curve below the detection threshold. In fact, a well-defined break is observed in most cases. The dashed lines indicate possible continuations of the actual vortex-strength distribution. The detection thresholds appear to be about $30 \text{ m}^2/\text{sec}$ for 5-m averaging radius, $40 \text{ m}^2/\text{sec}$ for 10-m radius, and 50 to $60 \text{ m}^2/\text{sec}$ for 20-m radius. These numbers were used ($60 \text{ m}^2/\text{sec}$ for 20-m radius) to calculate the limiting values of f in Section 4.1.

AD-A120 081

TRANSPORTATION SYSTEMS CENTER CAMBRIDGE MA
CHICAGO MONOSTATIC ACOUSTIC VORTEX SENSING SYSTEM. VOLUME IV. W--ETC(U)

F/G 20/4

JUL 82 D C BURNHAM, J N HALLOCK

UNCLASSIFIED

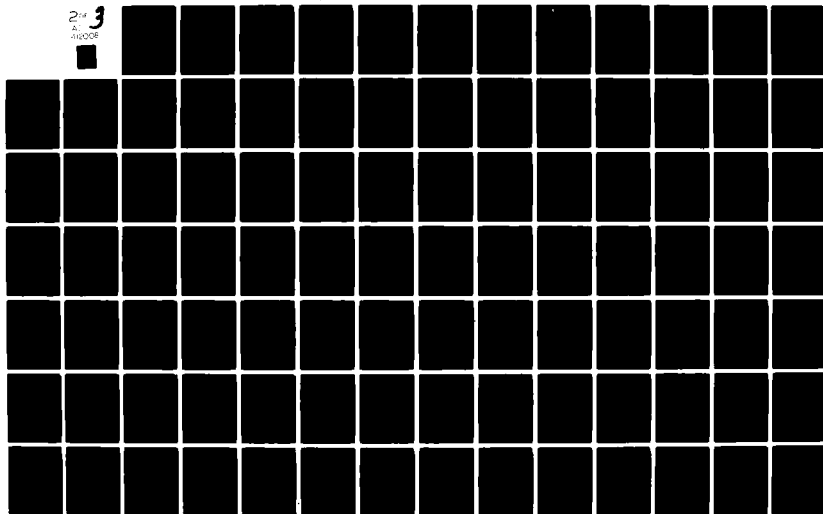
DOT-TSC-FAA-79-18-4

DOT/FAA/RD-79-103-VOL-4

NL

2nd
A.
JUL 82

3



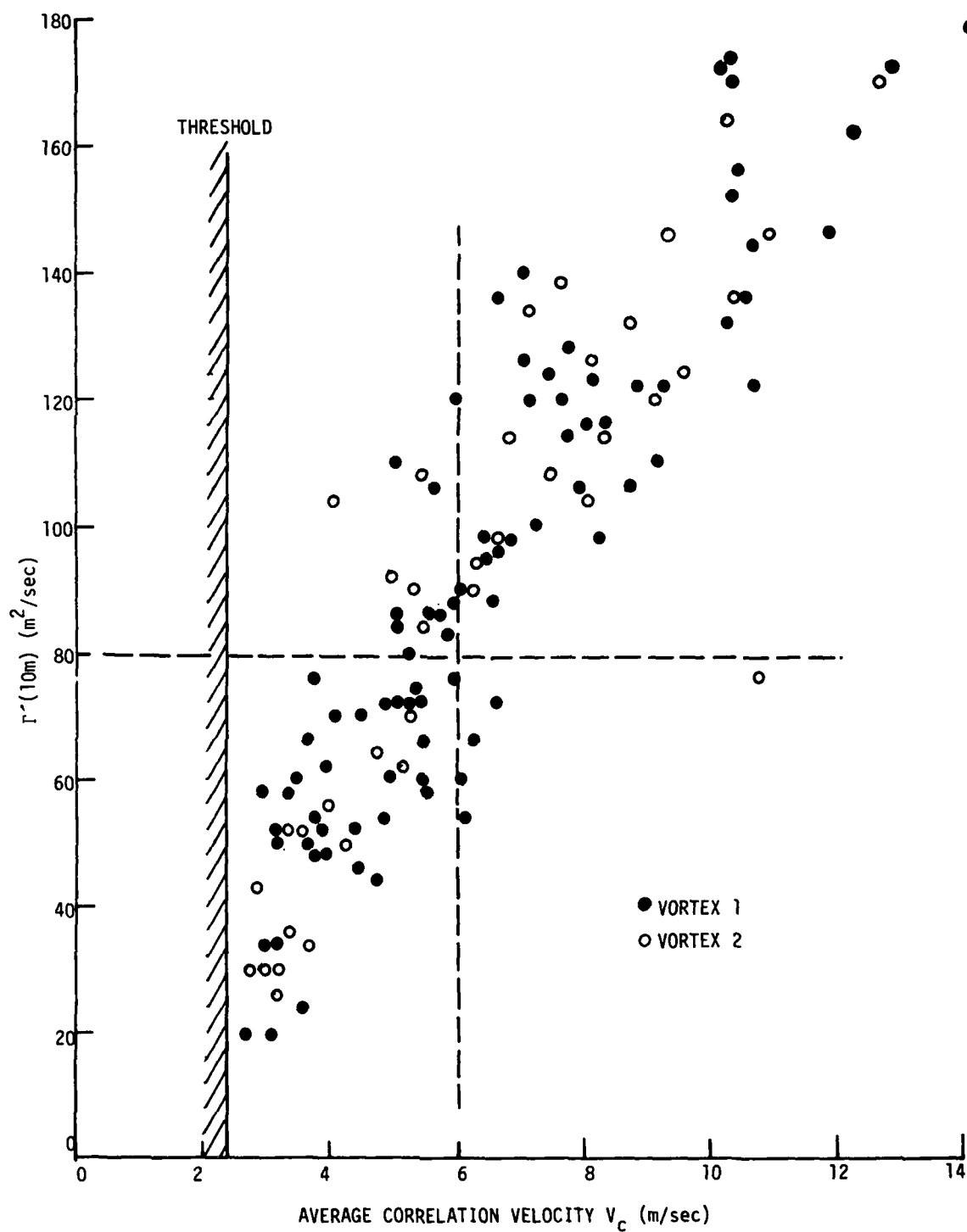


FIGURE 25. VORTEX STRENGTH VERSUS AVERAGE CORRELATION VELOCITY V_c FOR A SAMPLE OF B-707 AND DC-8 VORTICES

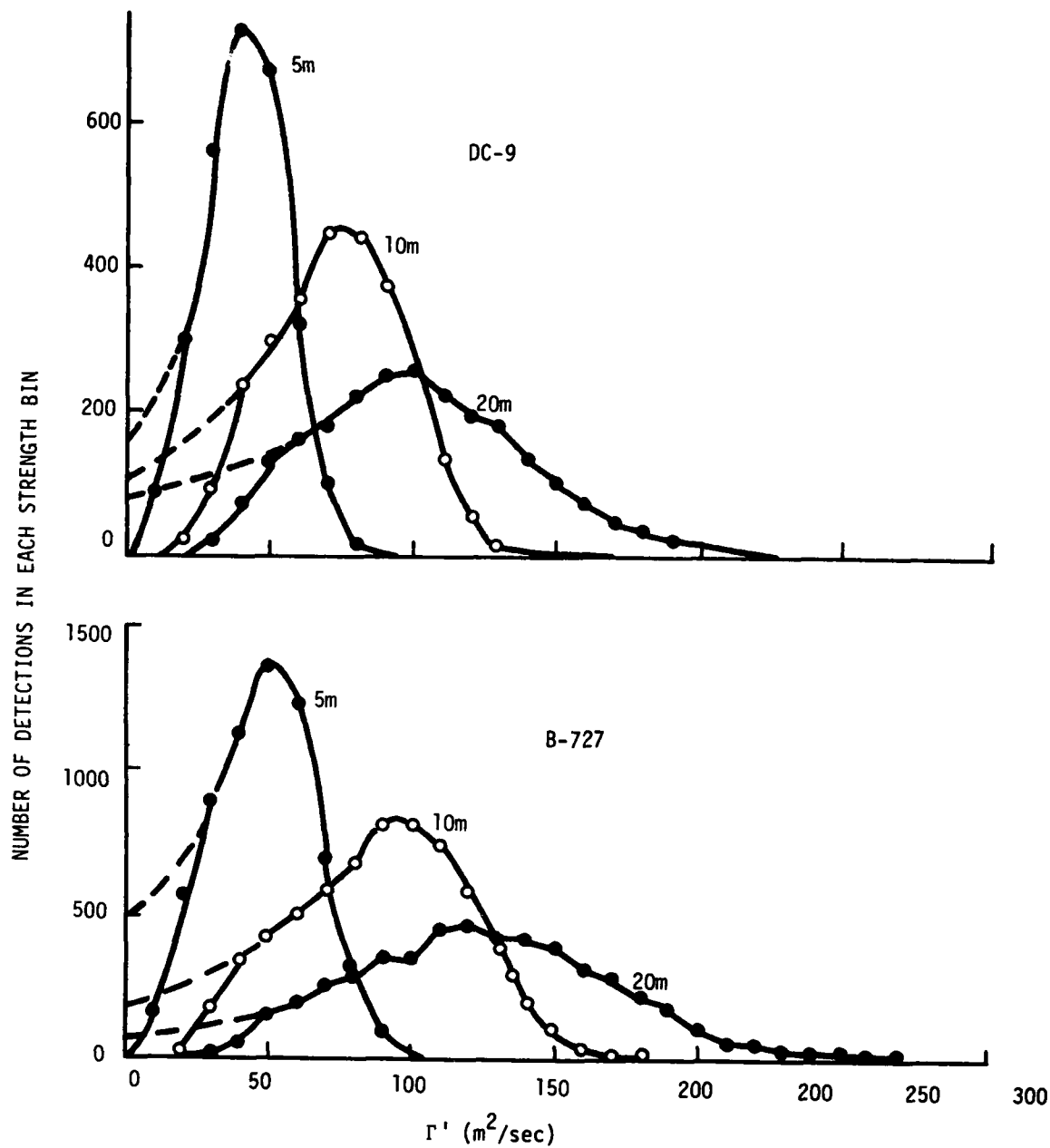


FIGURE 26. DISTRIBUTION OF DETECTED VORTEX STRENGTHS FOR FOUR AIRCRAFT (CONTINUED)

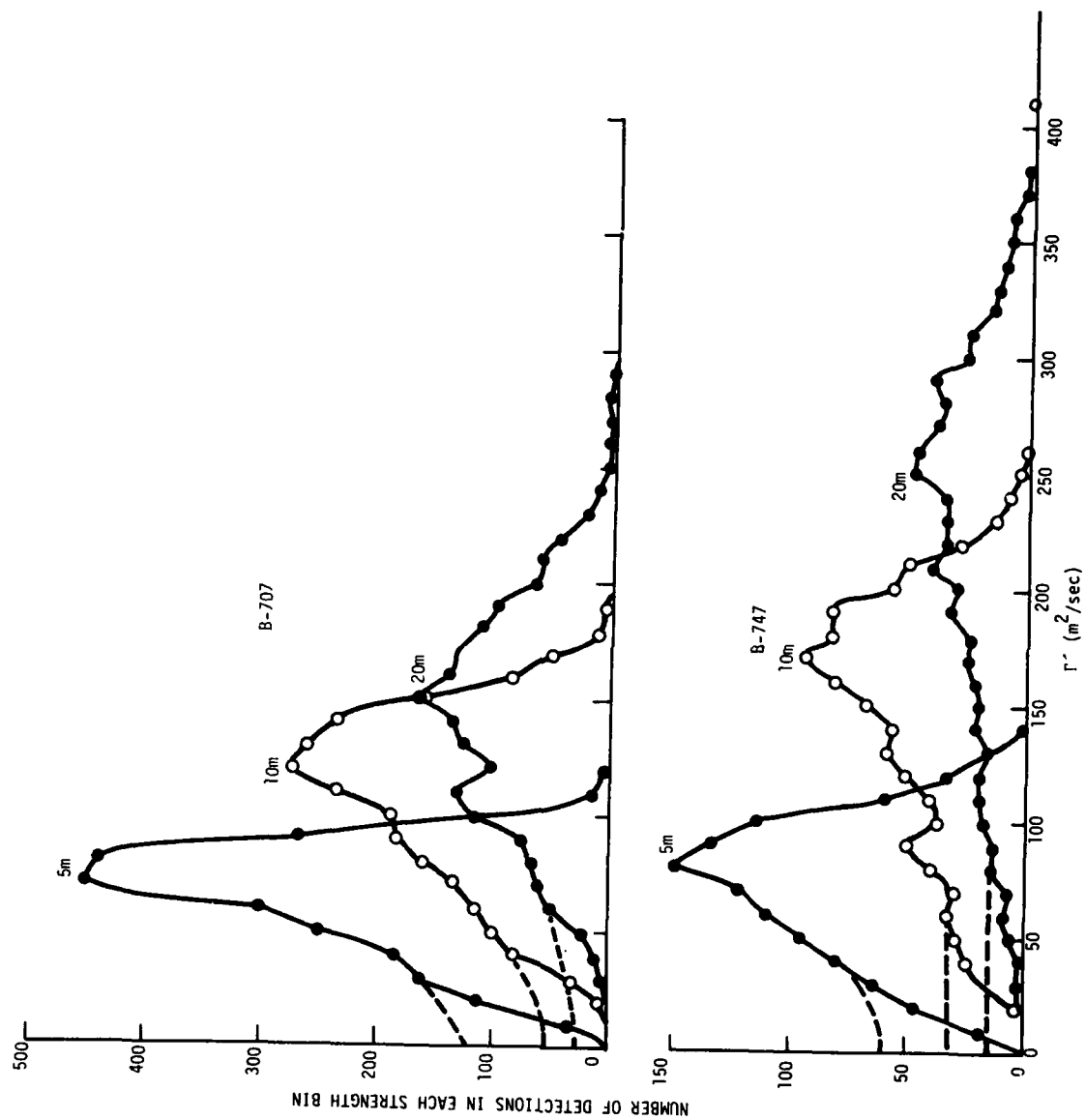


FIGURE 26. DISTRIBUTION OF DETECTED VORTEX STRENGTHS FOR FOUR AIRCRAFT (Concluded)

APPENDIX B

VORTEX DECAY MODELS

An accurate model for vortex decay can serve a number of useful purposes. First, it would allow the extrapolation of decay properties beyond the experimental limits of the measurements. Two limits are of particular importance: (1) the finite number of measurements precludes the direct measurement of very small probabilities. (2) The finite MAVSS detection threshold distorts the vortex decay measurements at low strength. A second purpose for a decay model is to characterize the decay by a small number of parameters whose variation with the cases selected can be used to determine the dependence of vortex decay upon weather conditions and aircraft type.

B.1 SIMPLE ANALYTICAL MODEL

Equation 8 in Section 3.2 can be used to describe the long-time asymptotic decay of the wake vortex hazard. The two parameters of the model α and d represent, respectively, the asymptotic slope and the delay of the decay. The delay d is close to zero when the hazard threshold Γ_T' is near the most probable initial strength Γ_0' . The value of d becomes increasingly positive as Γ_T' decreases below Γ_0' and increasingly negative as Γ_T' increases above Γ_0' . The value of α increases as Γ_T' decreases for $\Gamma_T' < \Gamma_0'$ but tends to remain constant for $\Gamma_T' > \Gamma_0'$. Early in the analysis of the data a simple dependence of α upon Γ_T' was found, namely that the slope α is proportioned to Γ_T' for $\Gamma_T' < \Gamma_0'$ and greater than the detection threshold:

$$\Gamma = G \Gamma_T'. \quad (22)$$

The analysis leading to this result for the data in Figure 5 is presented in Table 17. The values of $(t/100)^2$ which correspond to a probability $F(\Gamma_T', t)$ of 5 percent will be used. This value of

TABLE 17. PARAMETERS FOR FIT TO DATA IN FIGURE 5

Γ'_0 (m ² /sec)	$(T/100)^2$ for F=0.05	$\Gamma'_T(T/100)^2$ for F=0.05
30	0.81	24
50	0.68	34
75	0.51	38
100	0.39	39
150	0.09	14

F is small enough that the delay d can be ignored since most of the variation in $(t/100)^2$ is due to α for $\Gamma_T' \leq \Gamma_0'$. It is also large enough to be above the statistical fluctuations near the single-case level. Use Equation 8 with d = 0 to relate F = 5 percent and α by taking the natural logarithm of both sides:

$$-3.00 = -\alpha t^2. \quad (23)$$

Combining Equations 22 and 23 yields

$$G = 3.00/(\Gamma_T' t^2). \quad (24)$$

Table 17 shows the values of $\Gamma_T'(t/100)^2$ for Figure 5. These values are roughly constant in the region between the detection threshold of 40 m²/sec and the most probable initial strength Γ_0' of 135 m²/sec. The corresponding value of G is 7.9×10^{-6} m⁻² sec⁻¹.

Although the assumption of d = 0 in the analysis of Equations 22 to 24 is not strictly applicable when Γ_T' is significantly different from Γ_0' , it can deal with many of the cases of interest. Specifically, the values of Γ_0' in Table 3 are generally close to the f = 1.0 hazard thresholds of Table 5. The ratio of Γ_0' to Γ_T' lies in the range of 0.8 to 1.85.

The assumption d = 0 in Equation 8 combined with Equation 22 leads to a very simple analytical expression for the distribution function P(Γ' , t) in Equation 11:

$$F(\Gamma_T', t) = \exp[-G\Gamma_T' t^2] = \int_{\Gamma_T'}^{\infty} P(\Gamma', t) d\Gamma'. \quad (25)$$

Differentiation with respect to Γ_T' leads to

$$P(\Gamma', t) = G t^2 \exp[-G\Gamma_T' t^2]. \quad (26)$$

The decay of average strength from Equation 10 becomes:

$$\bar{\Gamma}'(t) = [G t^2]^{-1}. \quad (27)$$

The ensemble mean strength decays inversely with vortex age squared. One should note that this model describes the decay of wake vortices with a single parameter G which depends upon aircraft type, meteorological conditions, and strength averaging radius.

Figures 27 and 28, respectively, show a comparison of the predictions of Equations 25 and 26 with the measured values for all B-707 vortices and a 10-m averaging radius. In Figure 27 the exponential decay lines of Equation 25 agree exactly at $F = 5$ percent for $\Gamma'_T = 75$ and $100 \text{ m}^2/\text{sec}$ because those points were used to calculate the value of G . The straight-line fit to the $100 \text{ m}^2/\text{sec}$ curve (the $f = 1.0$ hazard threshold) agrees very well for $F > 5$ percent but agrees less well for lower probabilities because of statistical fluctuations. The agreement is poorer for $\Gamma'_T = 75$ and 50 because the assumption of $d = 0$ is less reasonable. Figure 28 is a logarithmic plot of Figure 6. The model line agrees reasonably well at 70 seconds between Γ'_0 of $135 \text{ m}^2/\text{sec}$ and the detection threshold of $40 \text{ m}^2/\text{sec}$, as anticipated in the evaluation of G . For earlier times (e.g., 50 seconds) where the probability distribution has a well-defined peak the fit is less good. This peak in the probability distribution is closely related to the need for nonzero d for the 75 and $50 \text{ m}^2/\text{sec}$ curves in Figure 27. The shape of the model curves is suitable for times of 90 and 110 seconds, but the levels are low because of statistical fluctuations and the loss of cases below the detection threshold of $40 \text{ m}^2/\text{sec}$.

B.2 STOCHASTIC MODEL

The simple analytical model of Section B.1 suffers from a number of deficiencies, the most important of which is the lack of dealing adequately with the delay in the vortex decay. A

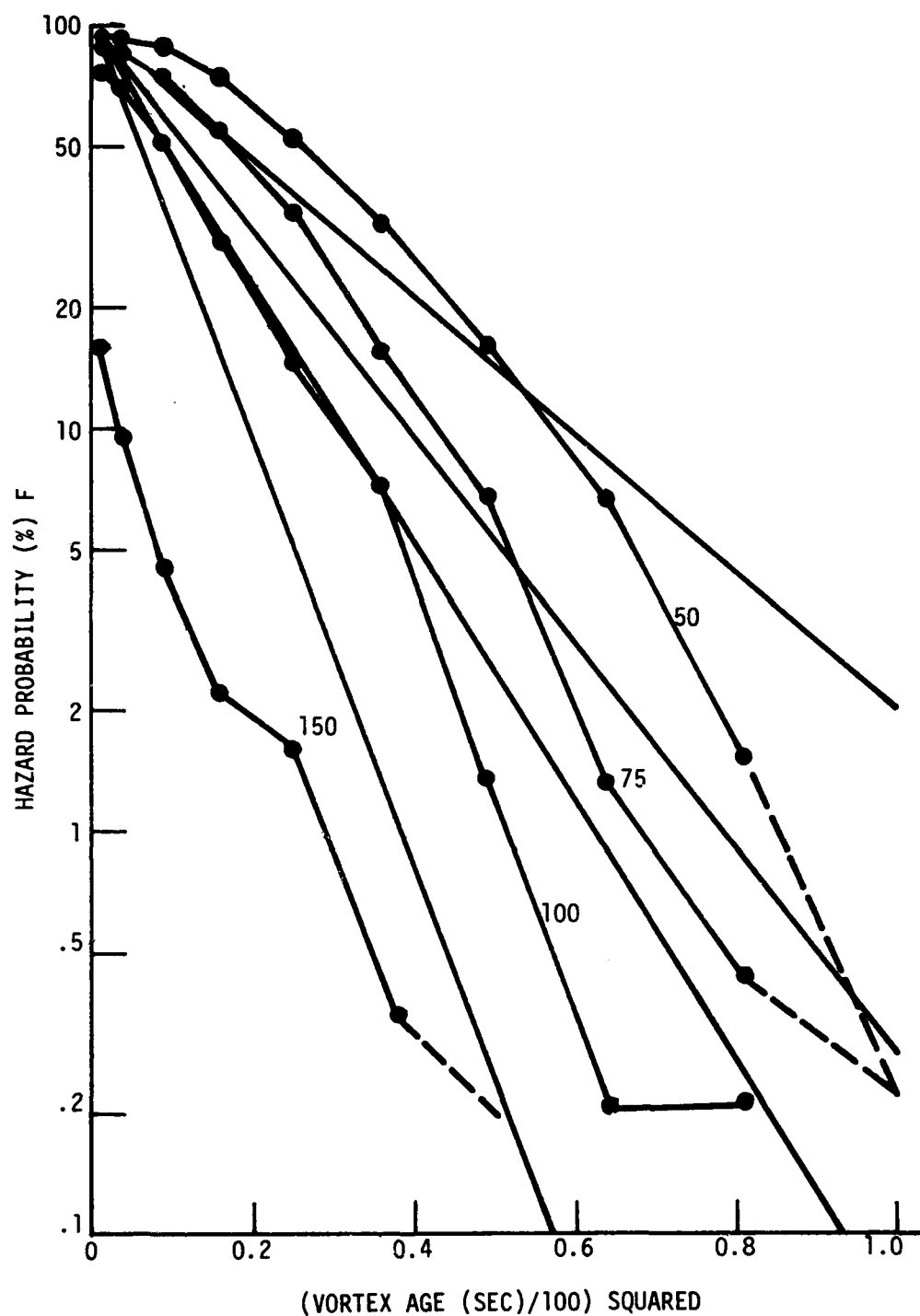


FIGURE 27. COMPARISONS OF MODEL HAZARD PROBABILITY (STRAIGHT LINES) WITH MEASUREMENTS (LINES WITH POINTS) FOR ALL B-707 VORTICES WITH 10-METER AVERAGING. THE VALUES OF Γ_T' (m^2/SEC) ARE INDICATED.

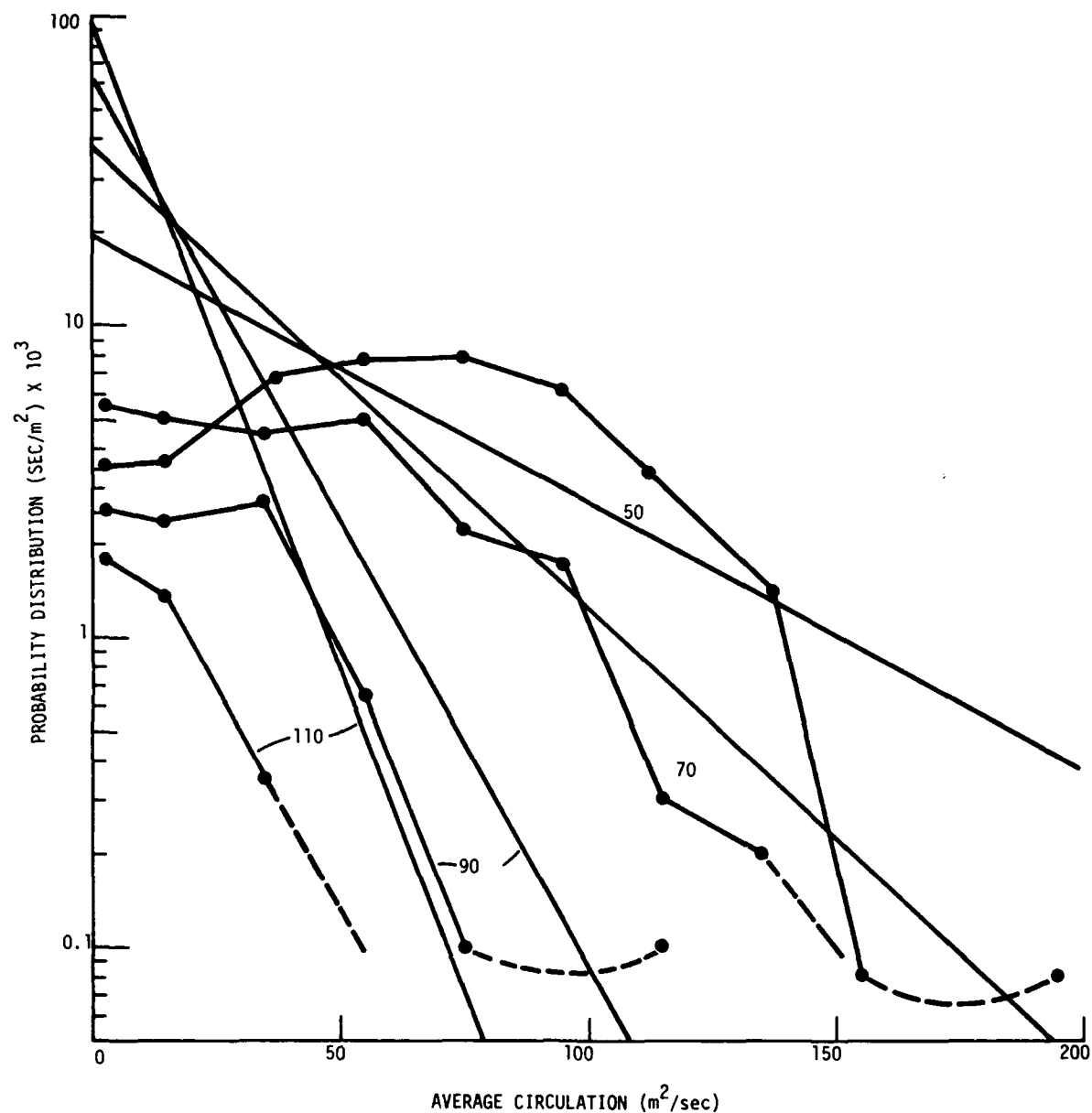


FIGURE 28. COMPARISONS OF MODEL PROBABILITY DISTRIBUTIONS (STRAIGHT LINES) WITH MEASUREMENTS (LINES WITH POINTS) FOR ALL B-707 VORTICES WITH 10-METER AVERAGING. THE TIMES (SEC) AT WHICH THE DISTRIBUTION IS EVALUATED ARE INDICATED.

secondary problem is the lack of any systematic consideration of the initial vortex strength distribution. The stochastic model described in this section deals directly with these questions.

The basic concept of the stochastic model is based on the observation that vortices often decay in two stages. During the first stage the vortex strength remains roughly constant. During the second stage the strength decays rapidly. This type of decay can be modeled mathematically by

$$\begin{aligned}\Gamma' &= \Gamma'_0 (t_1/t)^n & t > t_1 \\ \Gamma' &= \Gamma'_0 & t < t_1\end{aligned}\tag{28}$$

where Γ' is the average circulation for a particular aircraft and averaging radius, Γ'_0 is the initial value of Γ' , and t_1 is the time t when the strong vortex decay begins. The vortex decay in time is governed by the power n . The model in Section B.1 corresponds to $n = 2$ (see Equation 27). The stochastic feature of the model is introduced by assuming that the time the decay starts (t_1) is distributed in a normal distribution with mean value t_0 and standard deviation σ :

$$P(t_1) = \frac{1}{\sqrt{2\pi} \sigma} \exp\left[-(t_1 - t_0)^2 / 2\sigma^2\right].\tag{29}$$

The three parameters of the model are thus n , t_0 , and σ .

If the distribution in initial vortex strengths is ignored, the hazard probability $F(\Gamma'_T, t)$ can be calculated explicitly in terms of the error function. The limiting value of initial decay time t_{1T} is when the initial strength Γ'_0 is reduced to Γ'_T according to Equation 28:

$$t_{1T} = t(\Gamma'_T/\Gamma'_0)^{1/n}.\tag{30}$$

The hazard probability is given by the integral of $P(t_1)$ for all times greater than t_{1T} :

$$F(\Gamma'_T, t) = \int_{-t_{1T}}^{\infty} P(t_1) dt_1 . \quad (31)$$

This integral is related to the error function erf which satisfies the relationship:

$$1 - \text{erf}(z) = \frac{2}{\sqrt{\pi}} \int_z^{\infty} e^{-t^2} dt. \quad (32)$$

Combining Equations 29 through 32 leads to the expression

$$F(\Gamma'_T, t) = \frac{1}{2} \left[1 - \text{erf}((t_{1T} - t_o)/\sqrt{2} \sigma) \right] . \quad (33)$$

The results of this model assuming $n = 2$ and $t_o = 3\sigma$ are shown in Figure 29. The values selected for Γ'_T/Γ'_o correspond to the B-707 10-m results plotted in Figures 5 and 27. The curves corresponding to $\Gamma'_T = 50, 75$, and $100 \text{ m}^2/\text{sec}$ are in reasonable correspondence with the measurements for low probabilities. The $30\text{-m}^2/\text{sec}$ curve, however, is off, perhaps because it is below the MAVSS detection threshold or perhaps because of the wrong value for n .

Several features of Equation 33 and Figure 29 are worth noting. First, the shapes of the curves are similar and correspond simply to scaling the horizontal axis for different values of Γ'_T/Γ'_o . One way of looking at the dependence of F upon Γ'_T/Γ'_o is to note that a given value of F corresponds to a particular value of the argument z of erf in Equation 33:

$$z = \left[t(\Gamma'_T/\Gamma'_o)^{1/n} - t_o \right] / \sqrt{2} \sigma. \quad (34)$$

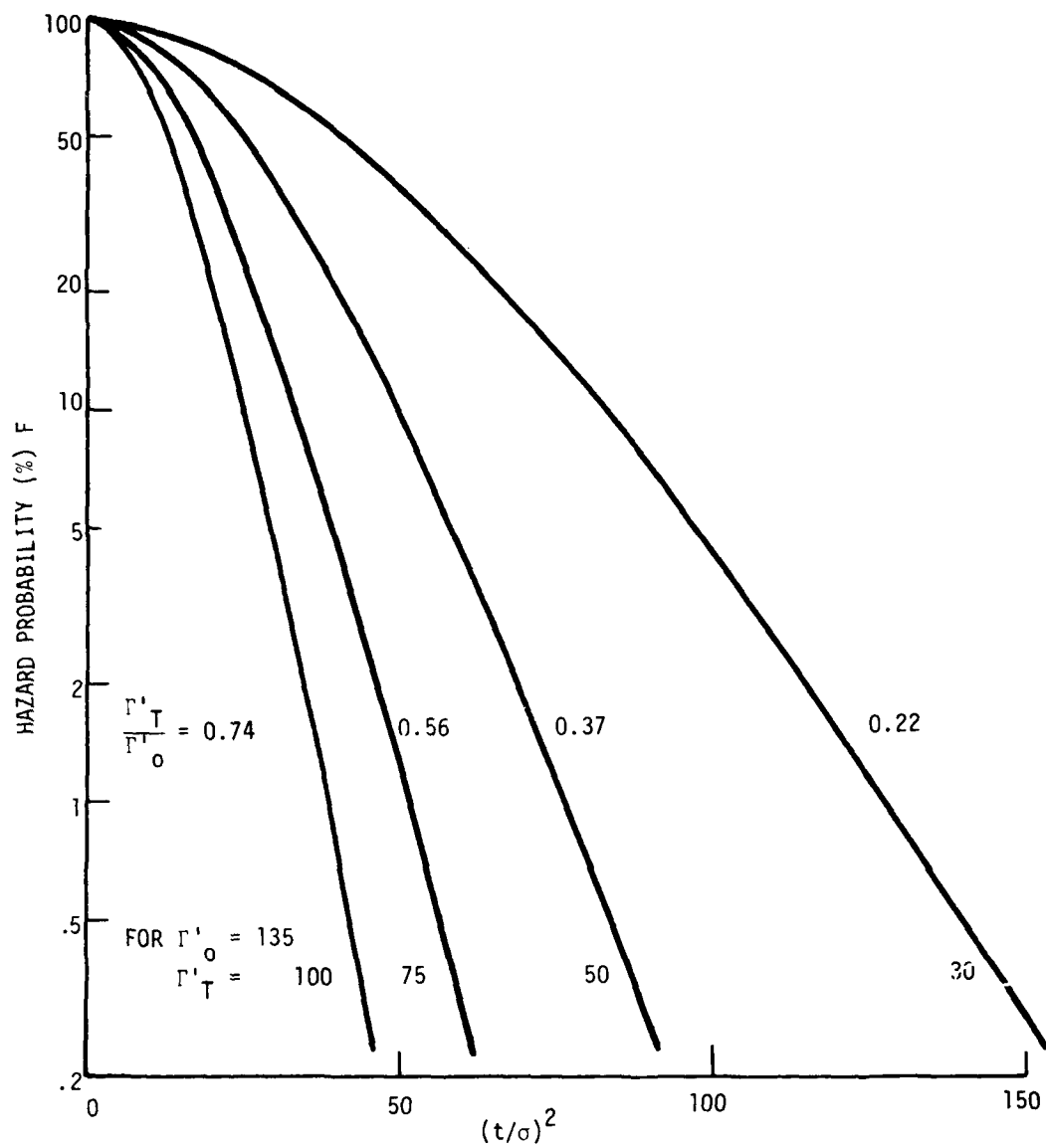


FIGURE 29. VORTEX DECAY FOR THE STOCHASTIC MODEL WITH $t_0 = 3\sigma$ AND $n = 2$

Equation 34 can be rearranged to give:

$$t/\sigma = (t_0/\sigma + \sqrt{2} z) (\Gamma'_T/\Gamma'_0)^{-\frac{1}{n}}. \quad (35)$$

A second feature of the curves in Figure 29 is that the asymptotic line for low probabilities is not straight but in fact is slightly curved. This curvature is consistent with the asymptotic expression for the error function:

$$(1 - \text{erf}(z)) \sim \frac{1}{\sqrt{\pi} z} e^{-z^2} \quad (36)$$

The inverse z dependence in Equation 36 causes the curvature.

Equation 35 can be used to calculate the time t_F required to reach a certain hazard probability. Listed below are the error-function argument z values leading to specified hazard probabilities, F :

F	z
0.2	0.59
0.1	0.91
0.05	1.16
0.02	1.45
0.01	1.65
0.005	1.82
0.002	2.03

Figure 30 shows a log-log plot of the dependence of $(t_F/\sigma)^2$ upon Γ'_T/Γ'_0 for three F values for the choice of parameters $t_0/\sigma = 3$ and $n = 2$. For $n = 2$ the lines have a slope of -1 . Changing the value of n simply changes the slope of the lines passing through the point where $\Gamma'_T/\Gamma'_0 = 1$. Changing the value of t_0/σ moves the lines up or down.

The stochastic model was fitted to the measured data on vortex decay. A weighted least-squares fit was designed to find parameters which would produce reliable predictions of the vortex hazard probabilities at long times. The vortex strength

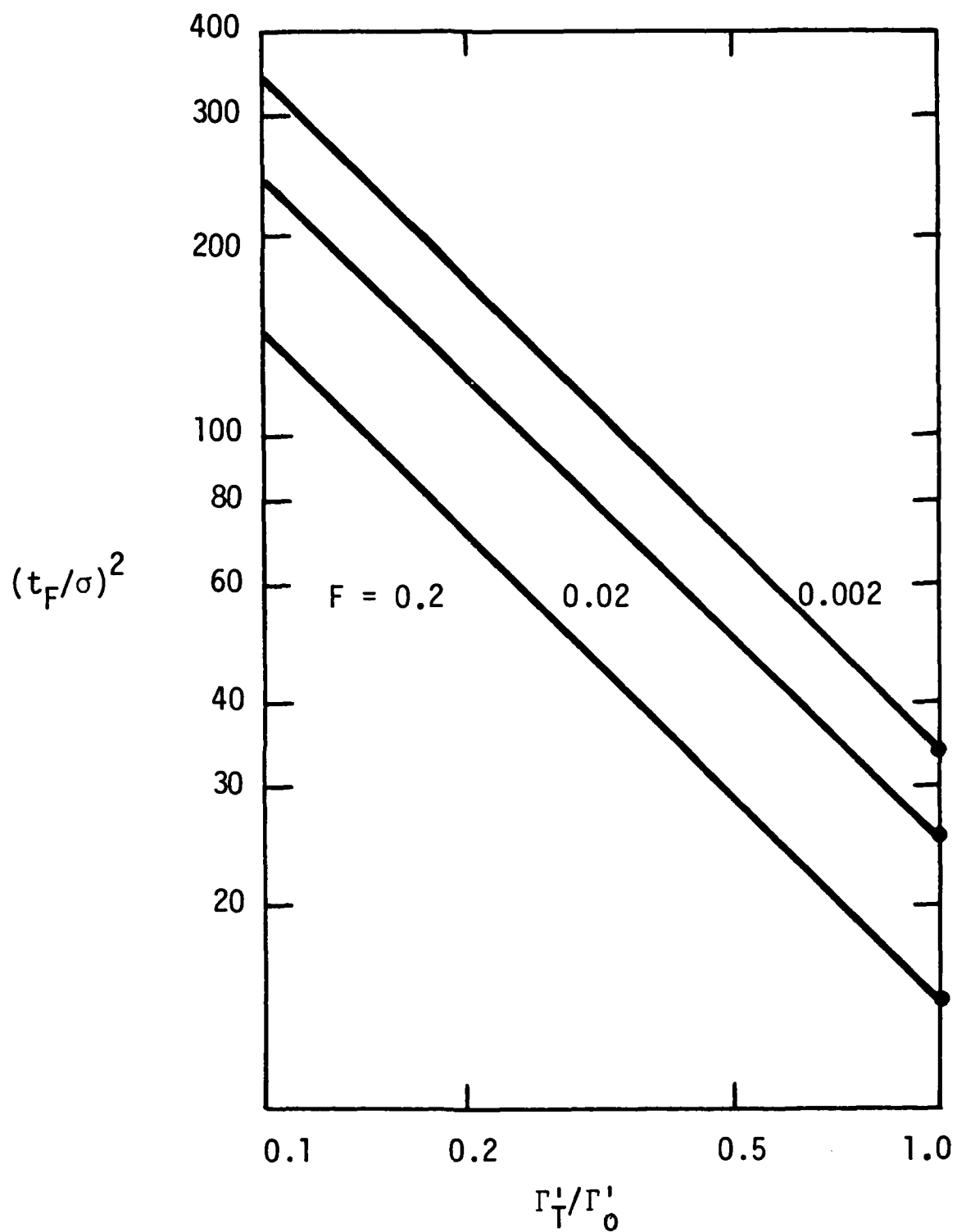


FIGURE 30. DEPENDENCE OF THE TIME TO REACH A PARTICULAR HAZARD PROBABILITY UPON THE HAZARD STRENGTH THRESHOLD

distribution is evaluated in bins of width $20 \text{ m}^2/\text{sec}$ (as in Figure 6). The initial strength Γ'_0 distribution is taken as the 10-second distribution. The stochastic model (parameters σ , t_0 , n) is used to calculate the probability of going from an initial strength bin i to another strength bin j at a time t later. The total strength distribution at time t is obtained by summing over the initial strength distribution $P(i,10)$. The calculated strength distribution $P_c(j,t)$ was compared to the measured distribution $P_m(j,t)$ by evaluating the weighted sum:

$$S = \sum_{t=t_1}^{t_m} \sum_{j=1}^N (\ln P_c(j,t) - \ln P_m(j,t))^2 N_m(j) \quad (37)$$

where the sum is taken over both time (even multiples of 10 seconds) and strength bins. The sum S is minimized to yield the least-square fit. The use of logarithms in Equation 37 gives equal weight to fractional errors in the distribution at both high and low values. The sum is weighted by the number of measured points $N_m(j)$ in a bin to account for the expected statistical fluctuations. Some limitations on the sum are placed to achieve the goal of reliable long-time predictions. First, the lowest strength bin is set to be above the MAVSS detection threshold. The lowest bin used is 26 to $45 \text{ m}^2/\text{sec}$ for 5-meter averages, 46 to $65 \text{ m}^2/\text{sec}$ for 10-meter averages, and 66 to $85 \text{ m}^2/\text{sec}$ for 15- and 20-meter averages. Second, the first time used is 40 seconds. The procedure for minimizing S is to select the value for n (1.0, 1.5, 2.0 or 2.5) and vary σ and t_0 until the smallest S is found. The smallest increment on σ and t_0 is $1/4$ second.

Figures 31 and 32 show sample results of the least-square fit for two aircraft types, B-727 and the B-747. The rms error in the figures is the root-mean-square of the logarithm difference in Equation 37. It is obtained by normalizing S to the sum where the quantity squared is set equal to 1, and then taking the

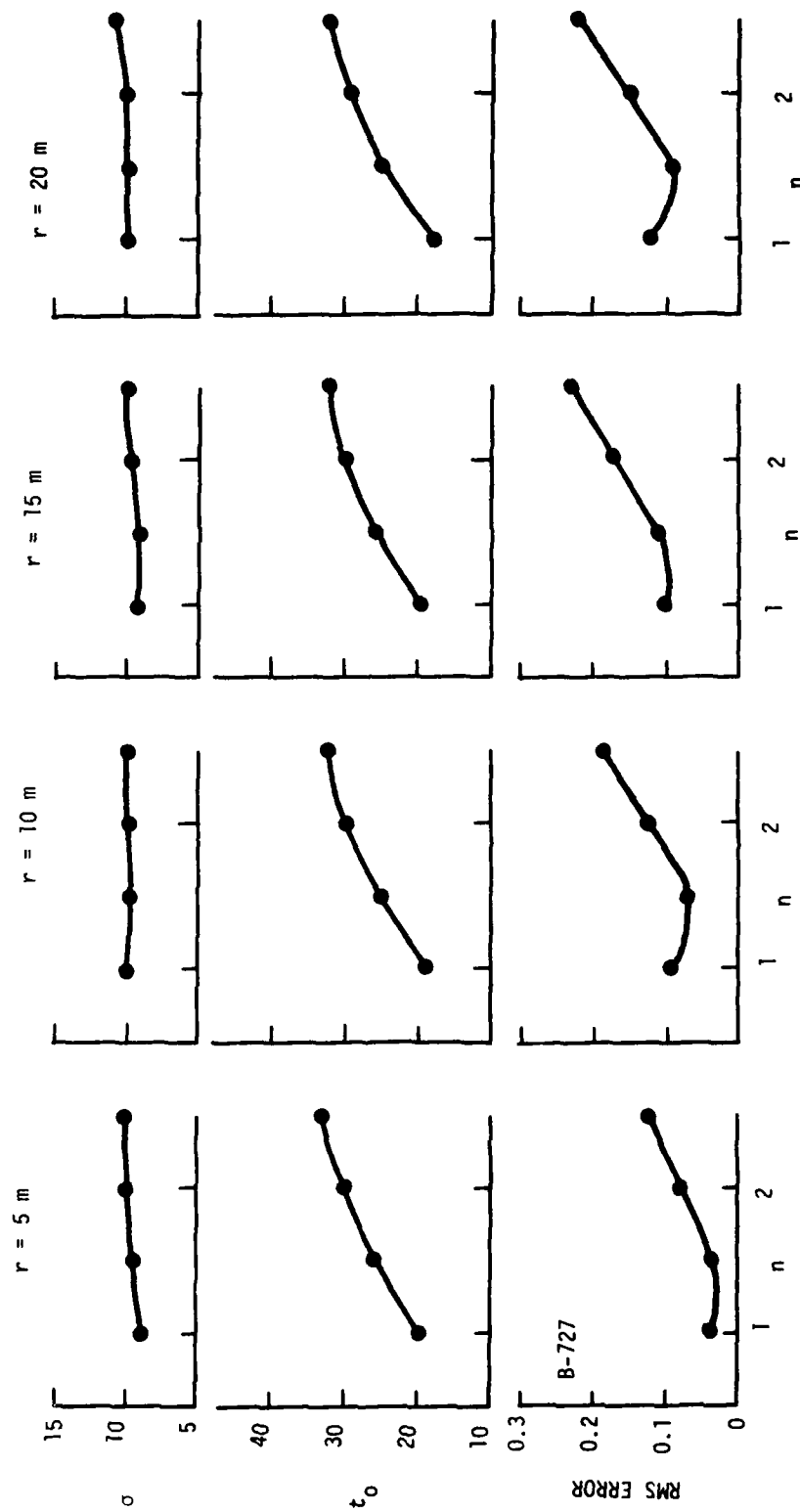


FIGURE 31. LEAST-SQUARE FIT TO VORTEX DECAY: ALL B-727 VORTICES

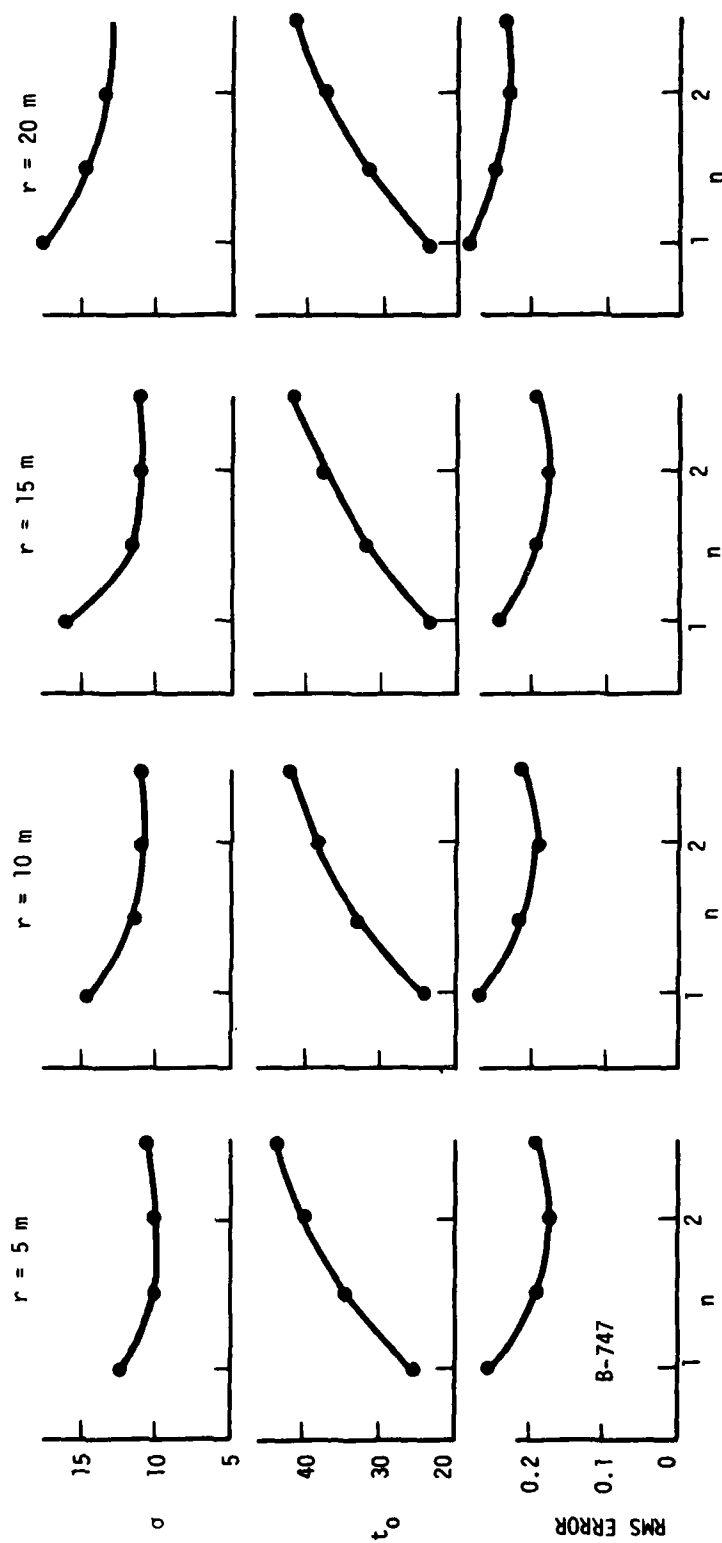


FIGURE 32. LEAST-SQUARE FIT TO VORTEX DECAY: ALL B-747 VORTICES

square root. An rms error of 0.1 corresponds to an rms 11 percent error in the fit to the strength distribution at various times.

Figures 31 and 32 show that the parameters σ and t_0 change as the power n of the decay is varied. The variation in t_0 is always consistent, increasing with increasing n . This variation is caused by the requirement for the distribution to reach a particular low level at late times. If the assumed decay rate is faster (higher n), a longer delay t_0 is called for in order to match the experimental data. The variation in σ with n shows no consistent trends and seems to be related to the particular set of data; similar variations in σ are seen as the averaging radius is changed.

Perhaps the most interesting parameter to examine is how the rms error depends upon the decay power n . One would expect the best fit, i.e., the lowest rms error, to indicate the actual power law of the vortex decay. Figure 33 compares the power n dependence of the rms error for all ten aircraft types. The data show a consistent trend with aircraft size. The power $n = 2$ gives a minimum value for the largest aircraft types (B-747, L-1011, and DC-10). The B-707s and DC-8s show a somewhat slower decay between $n = 1.5$ and $n = 2.0$. The B-727 data indicate n between 1.0 and 1.5, while the B-737 and DC-9 data show no minimum. The values of n for the largest aircraft are likely to be the most accurate representation of the actual vortex decay; consequently, the value $n = 2$ will be used in subsequent analysis. A determination of the value of n depends upon making measurements at different strength levels on the same vortex. The most accurate decay rate measurements occur for the largest aircraft where the initial strength may be four times the MAVSS detection threshold (see Table 3). The smallest aircraft (B-737 and DC-9) may have an initial strength only twice the detection threshold. The lack of a well-defined value of n for the smallest aircraft is a result of the small number of strength bins and times involved in the least-square fit.

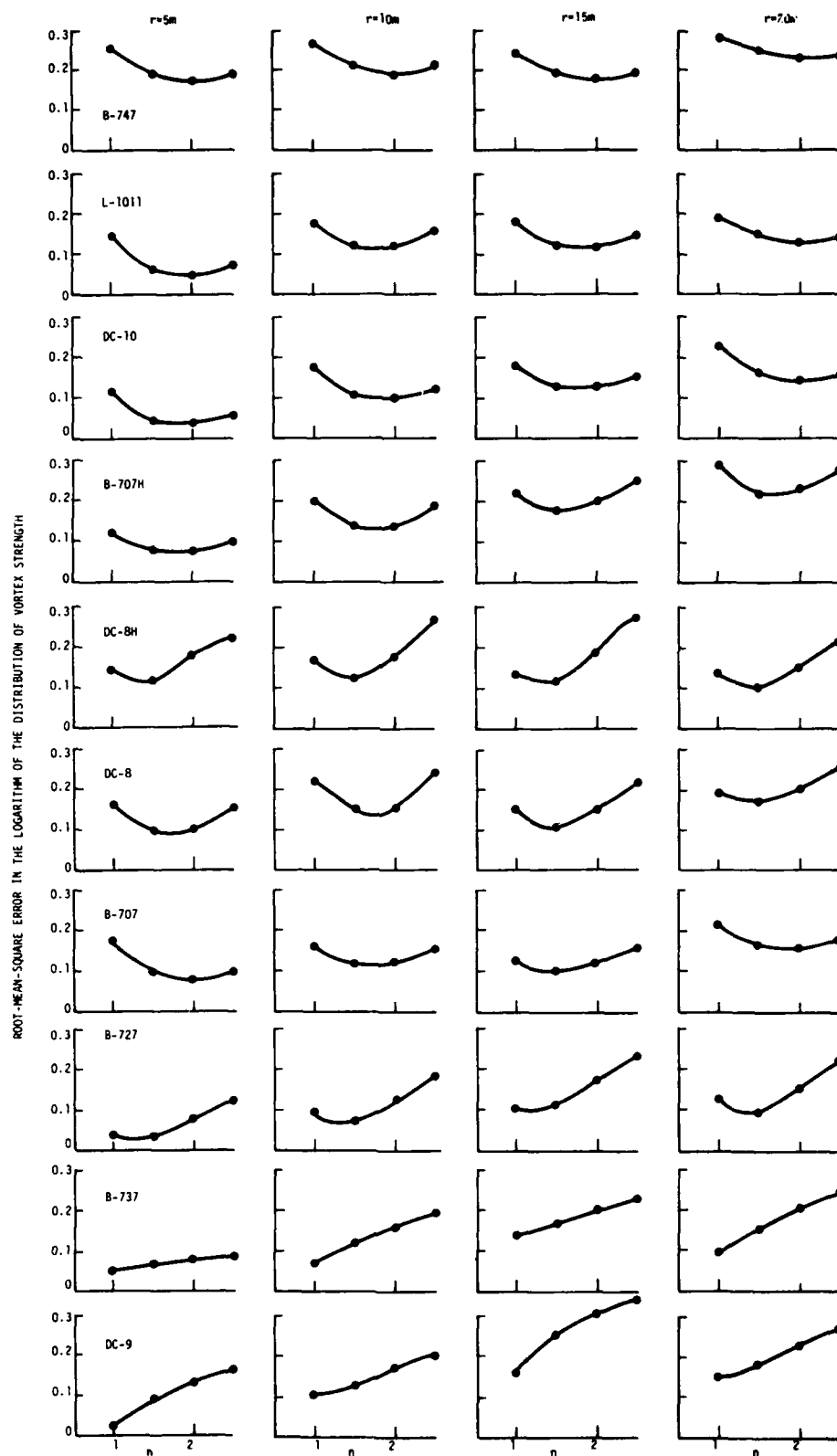


FIGURE 33. RMS ERRORS FOR ALL AIRCRAFT TYPES

The data on least-square fits for all vortices can be used to assess the aircraft dependence of vortex decay. In order to include the effects of both t_0 and σ , Equation 35 is used to calculate the times t_F leading to the same hazard probability $F = 0.2, 0.02$, and 0.002 used in Figure 30. The t_0 and σ values for $n = 2$ and 10-meter averaging radius were selected. Changing the averaging radius has little effect on the results. The strength threshold Γ_T' is set equal to the initial strength Γ_0' . Reducing Γ_T' by a factor of two would increase t_F by $\sqrt{2}$ because of the $n = 2$ decay. The dependence of t_F on aircraft wingspan b is shown as a log-log plot in Figure 34. The points for the aircraft with the greatest amount of data lie neatly on a straight line with slope .32 for $F = 0.02$. The points lying above this line are for the three aircraft types with two wing-mounted engines and the B-707H which has the fewest cases of all the types plotted. The presence of two engines on the wings may contribute to abnormal vortex persistence.

One should note that these results are inconsistent with the conventional way of normalizing vortex decay to the time bA/VC_L where A is the aspect ratio, V is the airspeed, and C_L is the lift coefficient. The parameters A and C_L vary little with aircraft type. The landing airspeed V may be at most 20 percent higher for the largest jet transports compared to the smallest. Correcting for V would increase the slope in Figure 34, but it would still be less than half the unity slope expected from the conventional normalization.

In principle, the parameters of the least-square fit can be used to examine the dependence of vortex decay upon meteorological parameters. In practice, the use of two free parameters t_0 and σ ($n = 2$ is fixed) leads to a poor determination of each. Figure 35 shows the results of fitting B-707 and B-727 data disaggregated by vortex number and wind speed. The wind speed bins were selected to have approximately equal numbers of cases (equal areas in the x and y wind velocity component plane). The results show that the parameter t_0 generally decreases with increasing

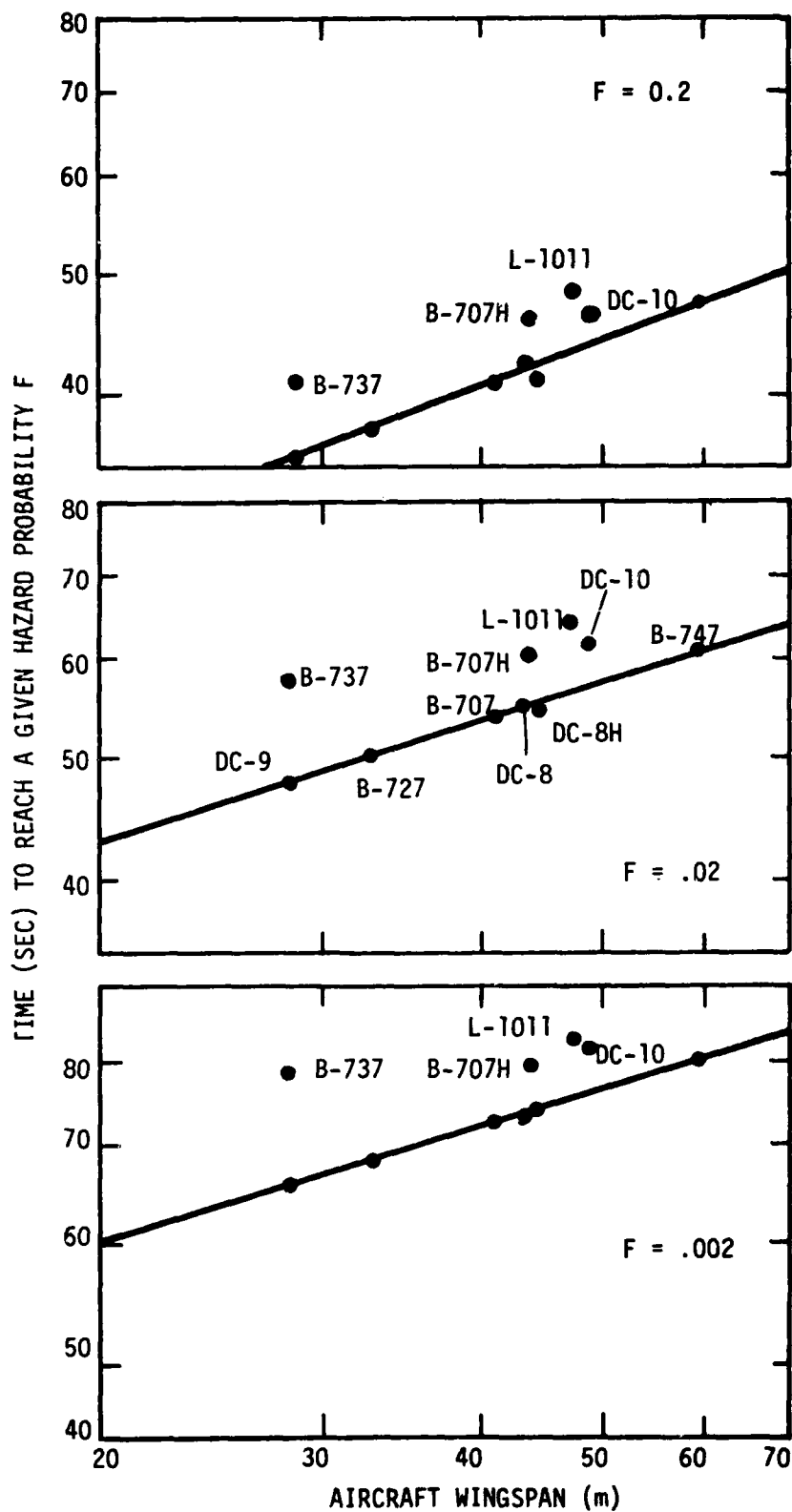


FIGURE 34. AIRCRAFT DEPENDENCE OF VORTEX HAZARD DURATION
FOR $\Gamma'_T/\Gamma'_O = 1$

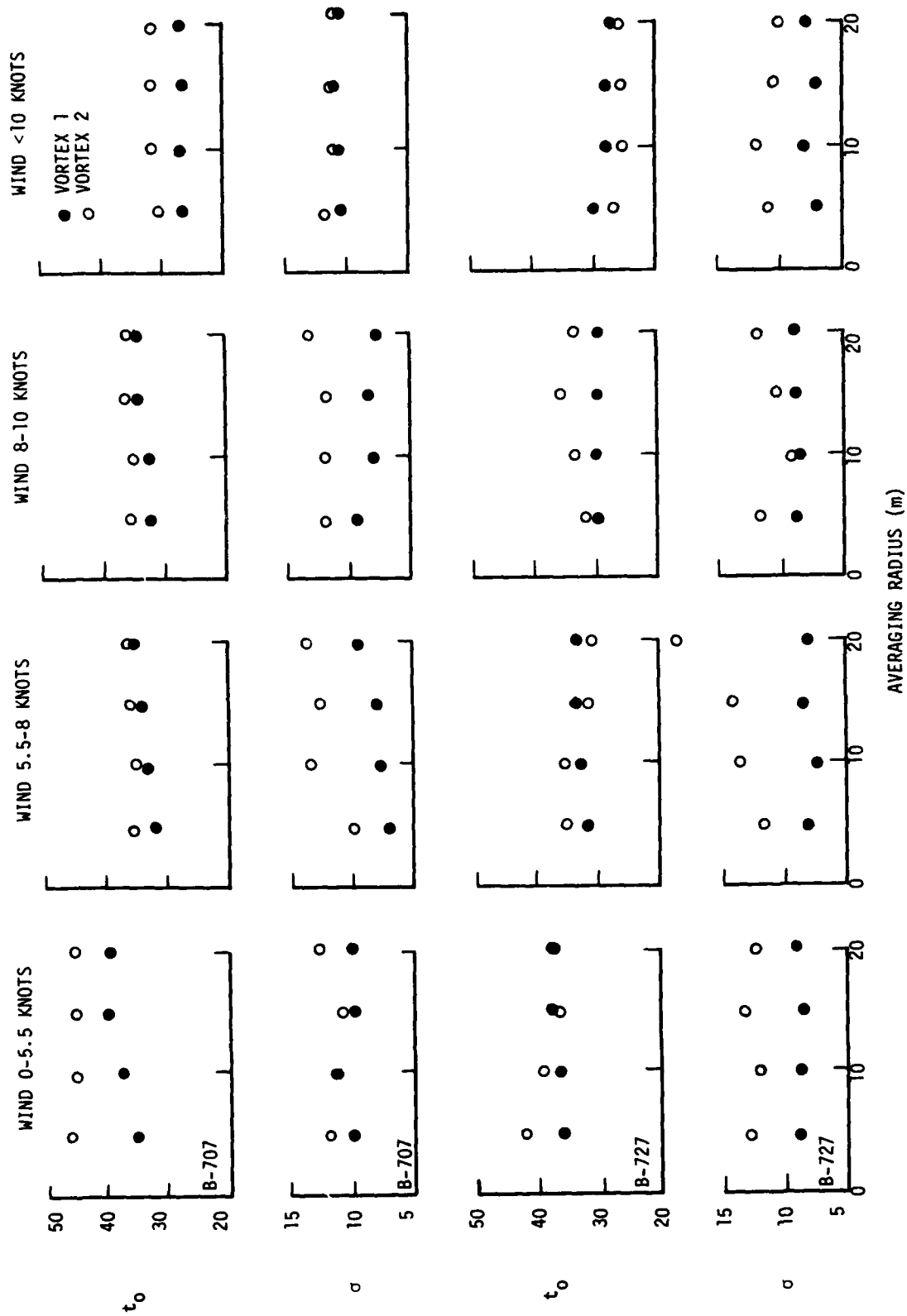


FIGURE 35. LEAST-SQUARE FITS TO DISAGGREGATED B-707 AND B-727 DATA

total wind while the value of σ varies haphazardly. The slower decay of vortex 2 is sometimes reflected in t_0 differences and other times reflected in σ differences. The way in which the least-square values of t_0 and σ were found started out by finding the best value of t_0 for an initial value $\sigma = 10$ seconds. The values of t_0 for $\sigma = 10$ are shown in Figure 36 for two wind speed ranges and 5 aircraft types. As would be expected, a single parameter fit yields values that are more consistent in representing the differences between vortex 1 and 2 and the effect of wind on vortex decay.

B.3 SIMPLE STOCHASTIC MODEL

The least-square fit stochastic model of Section B.2 is inconvenient to use for predicting hazard decay curves since it uses a measured distribution function for initial strengths and has too many free parameters (t_0 and σ) to allow an unambiguous fit to the data. The simple stochastic model assumes a Gaussian distribution of initial vortex strengths with a standard deviation equal to 20 percent of the mean value Γ'_0 (see Table 3). The two parameters t_0 and σ are reduced to one by assuming $t_0 = 3\sigma$ which is in the middle of the fitted values. The value of n is still assumed to be two. Rather than conducting a complicated integral over the initial strength distribution, the approximation is made that the hazard probability is simply reduced by the fraction of the initial strengths lying above the hazard threshold. Since the primary purpose of the model is to extrapolate the data to long times, this approximation should introduce no serious errors. The resulting hazard probability is a modification of Equation 33:

$$F(\Gamma'_T, t) = \frac{1}{2} \left[1 - \operatorname{erf} \left((\Gamma'_T - \Gamma'_0) / \sqrt{2} \sigma_T \right) \right] \\ \times \frac{1}{2} \left[1 - \operatorname{erf} \left((t_{1T} - 3\sigma) / \sqrt{2} \sigma \right) \right] \quad (38)$$

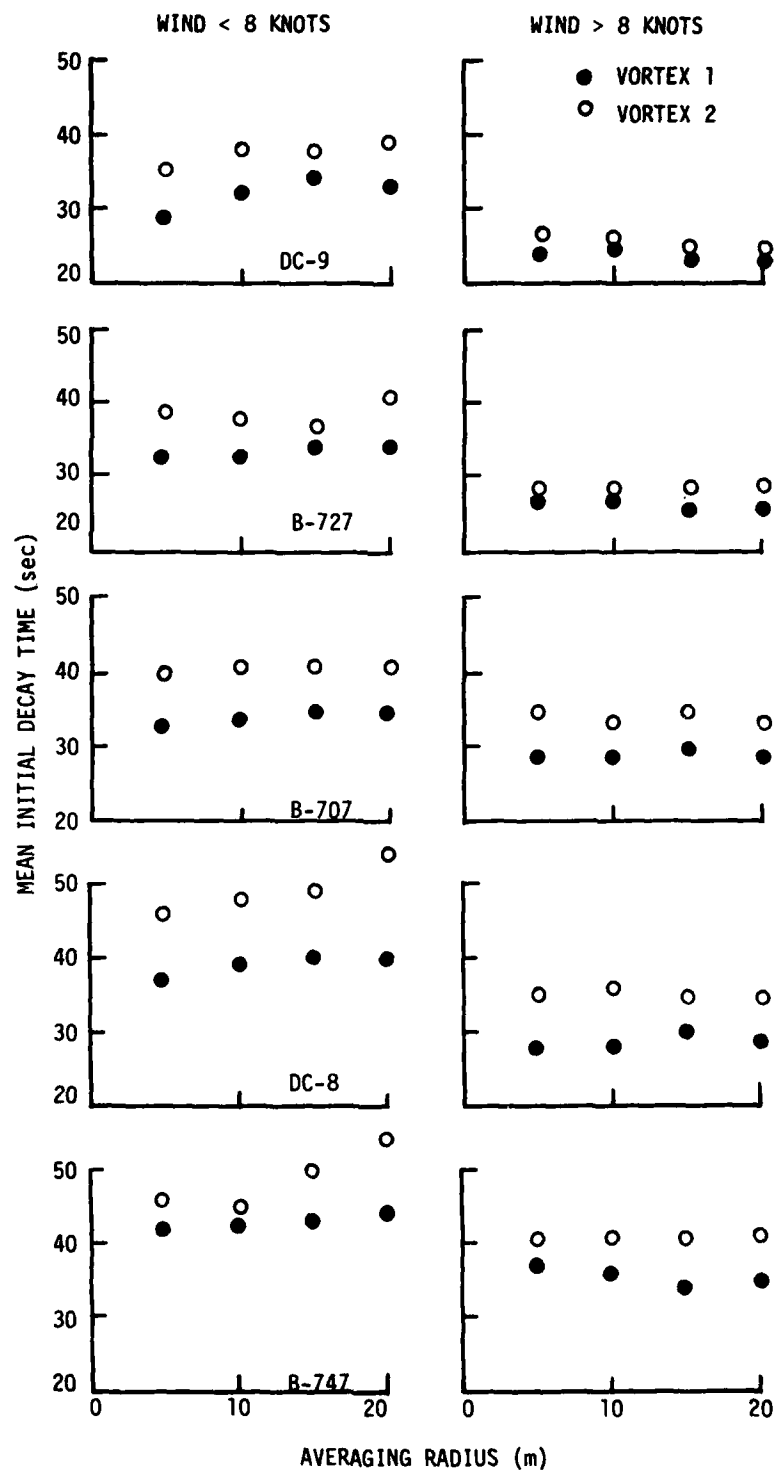


FIGURE 36. LEAST-SQUARE FITS WITH ONE FREE PARAMETER t_0
 ($\sigma = 10$ SECONDS, $n = 2$)

Figure 37 shows how the factor describing the initial strength distribution affects the results of Figure 30. The straight lines turn downward when Γ_T' is near Γ_0' .

Figure 38 shows one hazard probability decay curve fitted to the form of Equation 38 by a steepest-descent least-square method which minimized the deviation in F (rather than $\ln F$ as in Section B.2). An optimum value for α was found for each of the six Γ_T' curves; the σ values are listed on the graph. Only measured points for $F < 0.5$ were used in the fit in order to emphasize the decaying part of the curves. In addition, the value of F at zero time was taken from the data rather than using the first factor in Equation 38, since the resulting fit was poor for the cases where the calculated initial value disagreed significantly with the measured value. The variation in σ shown in Figure 38 is typical. The values are roughly constant for Γ_T' between the detection threshold (about $50 \text{ m}^2/\text{sec}$) and the initial value (about $150 \text{ m}^2/\text{sec}$). Lower values are obtained for Γ_T' outside this range. One should note that the use of $\Gamma_T' > \Gamma_0'$ in Equations 38 and 30 is not strictly consistent with the original model since the vortex strength was supposed to be constant at value Γ_0' before it starts to decay.

The results of fitting the decay curves in Figure 38 were used to assign a single value of σ to describe the complete vortex decay. The values in the middle of the constant σ range (e.g., $\Gamma_T' = 75$ and $100 \text{ m}^2/\text{sec}$ in Figure 38) were averaged. Since the purpose of the selected value is to characterize the low probability decay region, the fitted curves were adjusted slightly to give a better fit to the lower part of the decay curve. This change generally required an increase in σ . The final value selected for Figure 38 was $\sigma = 12.4$. Figure 39 shows how the calculated curves (using both factors in Equation 38) agree with the measured curves. For values of Γ_T' at or below the MAVSS detection threshold the measured decay is more rapid than the calculated decay. This difference could be the result of threshold effects on the measurements or it could mean that

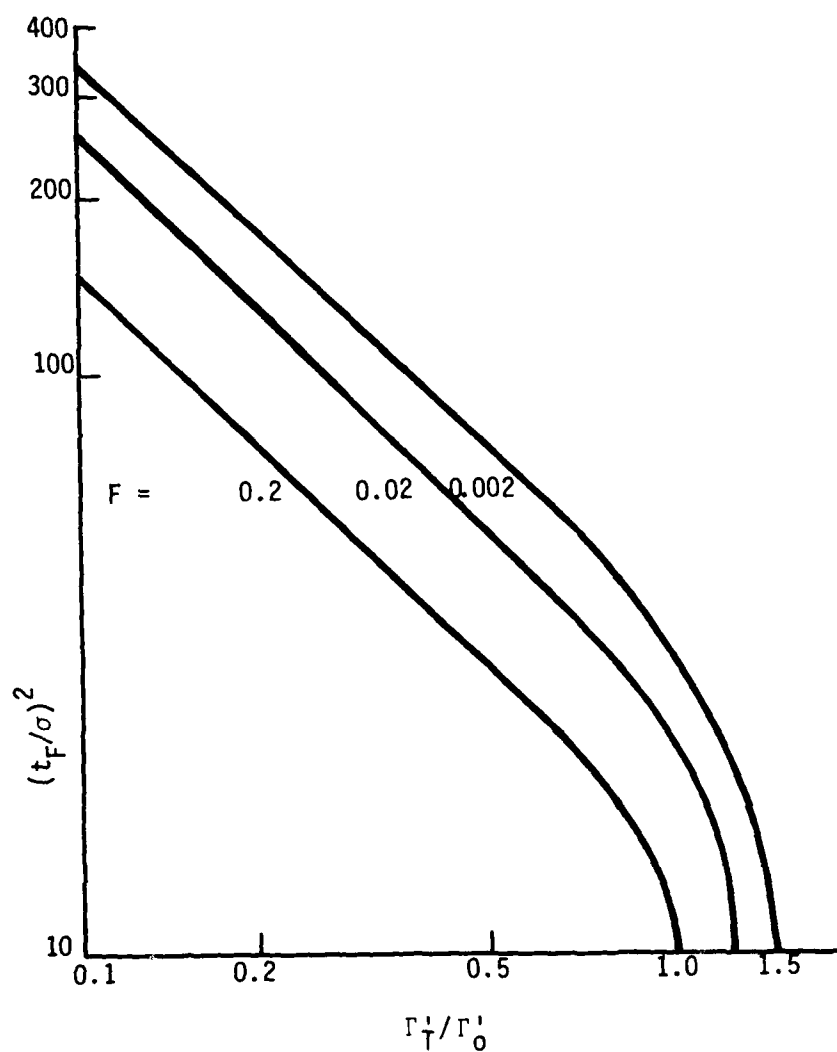
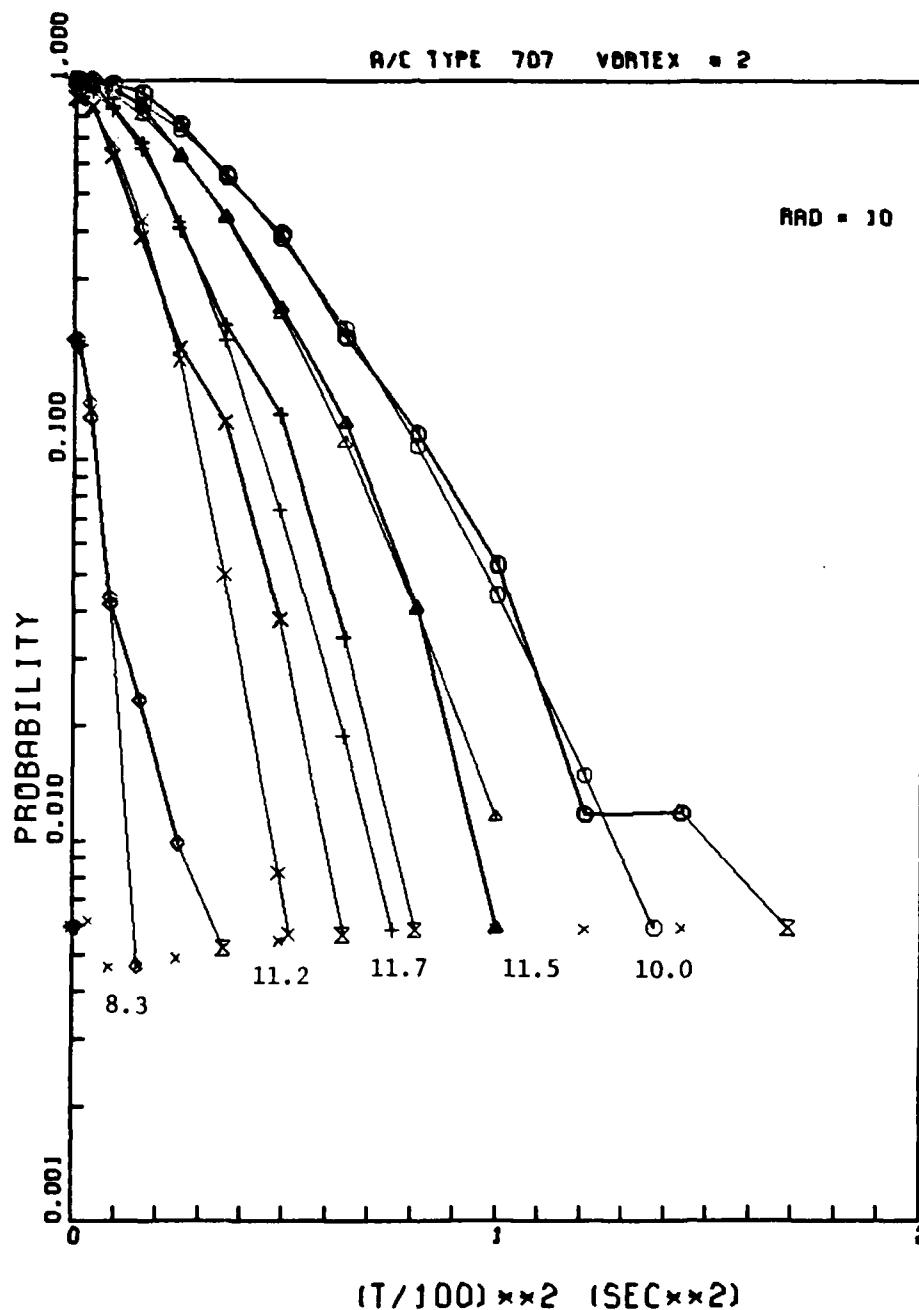


FIGURE 37. DEPENDENCE OF THE TIME TO REACH A PARTICULAR HAZARD PROBABILITY UPON THE HAZARD STRENGTH THRESHOLD, INCLUDING THE EFFECTS OF THE INITIAL STRENGTH DISTRIBUTION



Note: The five curves represent Γ_T^i values of 150, 100, 75, 50, and 30 m^2/sec respectively from left to right. The measured data are plotted with thicker lines than the fitted curves, the numbers below the curves are the values of σ for each curve.

FIGURE 38. FITTED PROBABILITY DECAY CURVES FOR THE B-707, 10-METER AVERAGING RADIUS, AND VORTEX 2

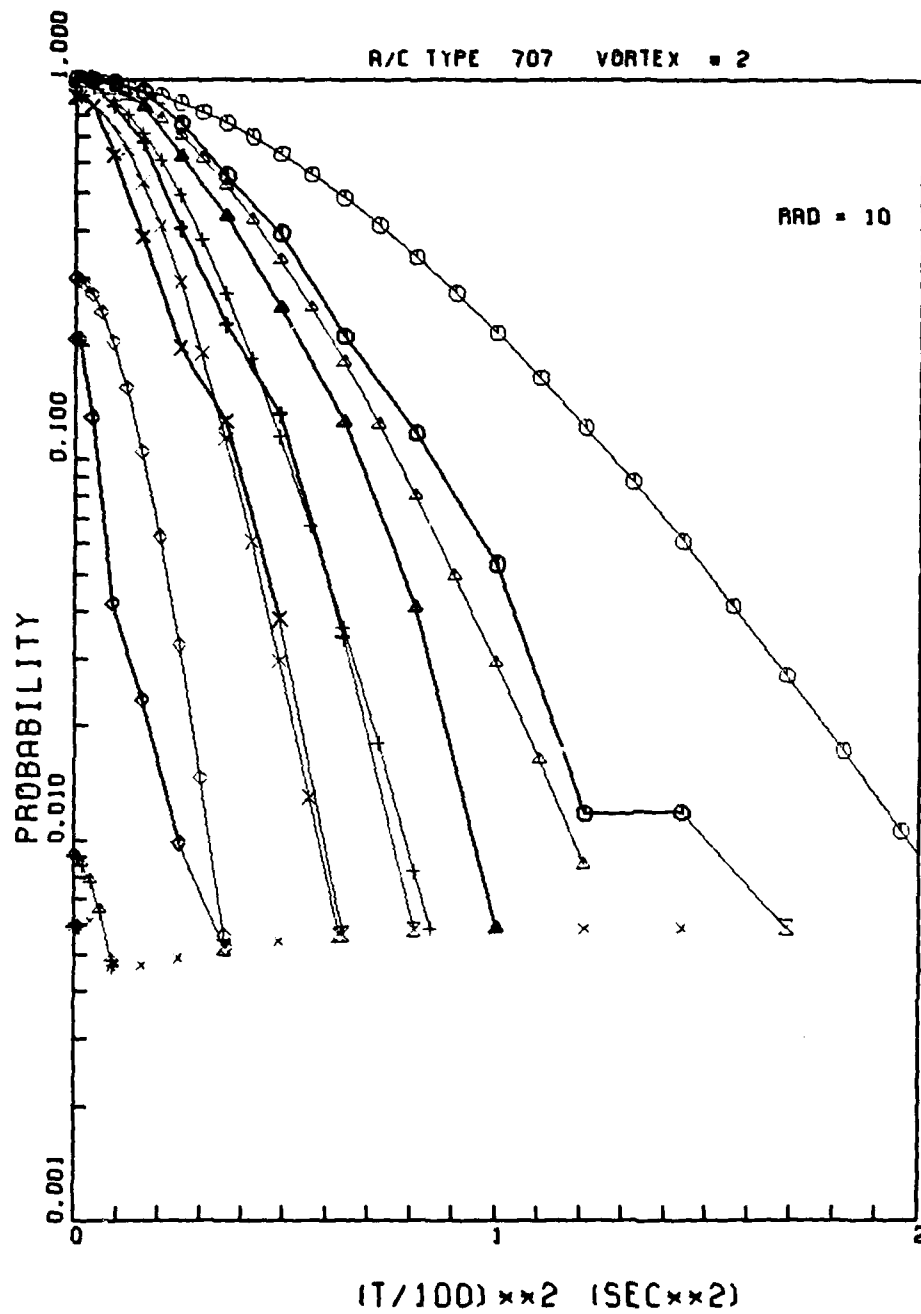


FIGURE 39. FITTED PROBABILITY DECAY CURVES USING TWO PARAMETERS, Γ'_0 AND σ

the vortices decay more rapidly when weakened. In any case, the calculated values are a conservative estimate of the duration of low strength vortices.

Figure 40 shows the values of σ selected to characterize the vortex hazard decay for both vortex 1 and vortex 2 for all ten aircraft types and four averaging radii. The value of $t_0/\sigma = 3$ used in the model gave satisfactory curve shapes for all aircraft except the DC-9, which would have fit better with a smaller value, and the B-747 and L-1011 which would have fit better with a larger value. The ratio of t_0 to σ appears to increase with aircraft size. In some ways the variations in Figure 40 are less consistent than those obtained with the least-square fits of Section B.2. Considerable variation with averaging radius is seen here, particularly for vortex 2, while little was noted before. The difference may be due to the fact that, vortex 1 dominated most of the results in Section B.2. Figure 36 also indicates more drastic variations with radius for vortex 2 than for vortex 1. The general trend in Figure 40 is for the smaller radii to decay more slowly (larger σ) although there are obvious exceptions such as the DC-8H. The differences between the DC-8 and the DC-8H must certainly reflect statistical variations since there are no physical differences which could affect dependence on averaging radius. The results in Figure 40 show too much variation to give the well defined size dependence of Figure 34. However, the generally slower vortex 2 decay for the B-737, B-707H, DC-10, and L-1011 are again evident.

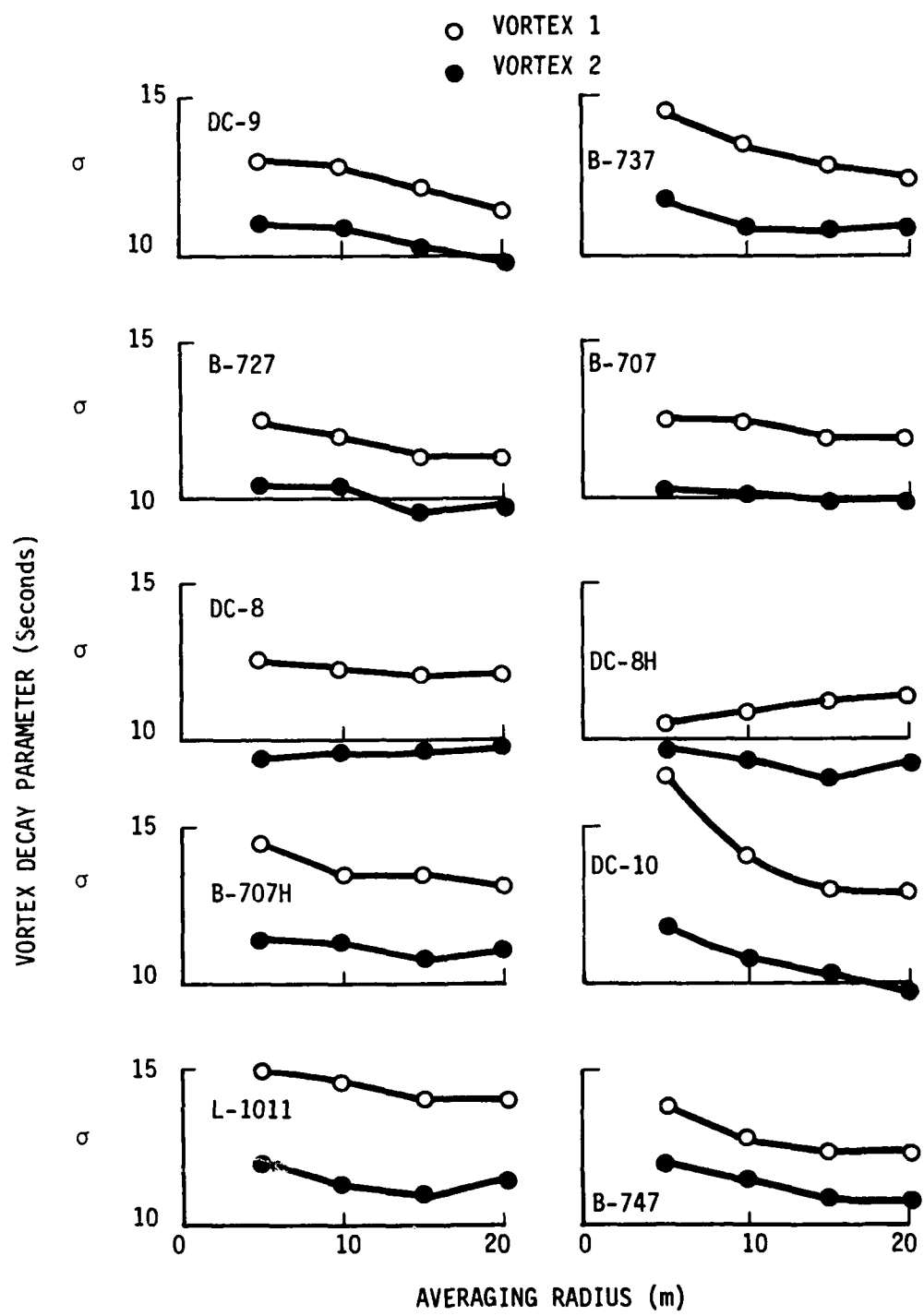


FIGURE 40. VALUES OF SIGMA USED TO CHARACTERIZE THE VORTEX 1 AND 2 HAZARD DURATION

APPENDIX C

VORTEX DECAY PLOTS

This appendix contains the vortex decay probability plots for the B-747 (Figs. 41 to 48), DC-10 (Figs. 49 to 56), L-1011 (Figs. 57 to 64), DC-8H and DC-8 (Figs. 65 to 72), B-707H and B-707 (Figs. 73 to 80), B-727 (Figs. 81 to 88), B-737 (Figs. 89 to 96), and DC-9 (Figs. 97 to 104). Figures 65 through 80 are from Volume II of this report (Ref. 2), but are repeated here to permit comparisons among the various common jet transport aircraft. Recall that vortex 1 is the first vortex to be detected by the MAVSS sensors and is the downwind vortex (the vortex that might translate to a neighboring parallel runway, for instance). Vortex 2 is the second vortex to be detected and is from the upwind side of the flight path (the vortex that might stall near the extended runway centerline). The plots are disaggregated into vortices 1 and 2 and winds less than 8 knots.

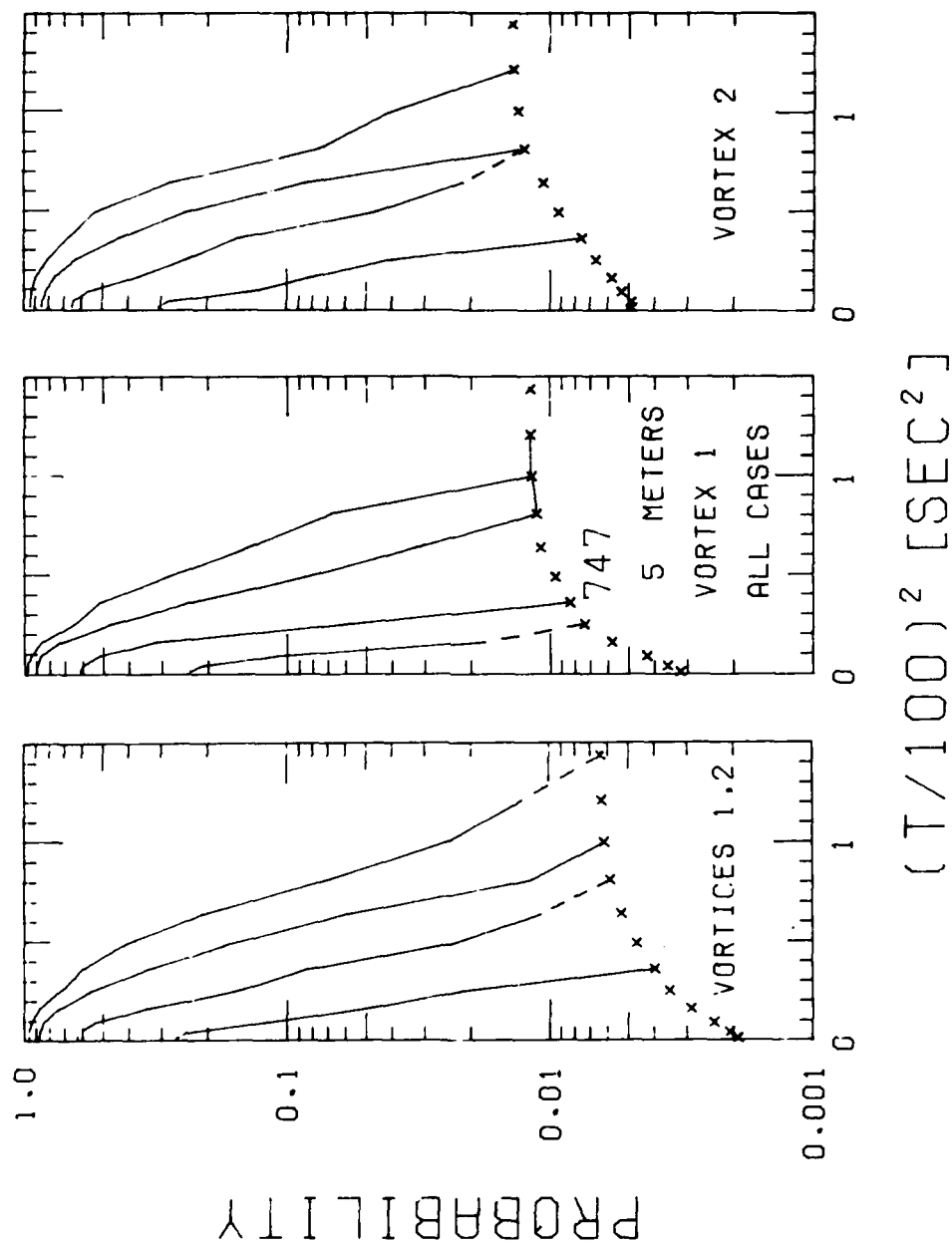


FIGURE 41. PROBABILITY OF DECAY, B-747, VORTEX 1 AND 2, 5-m AVERAGING RADIUS

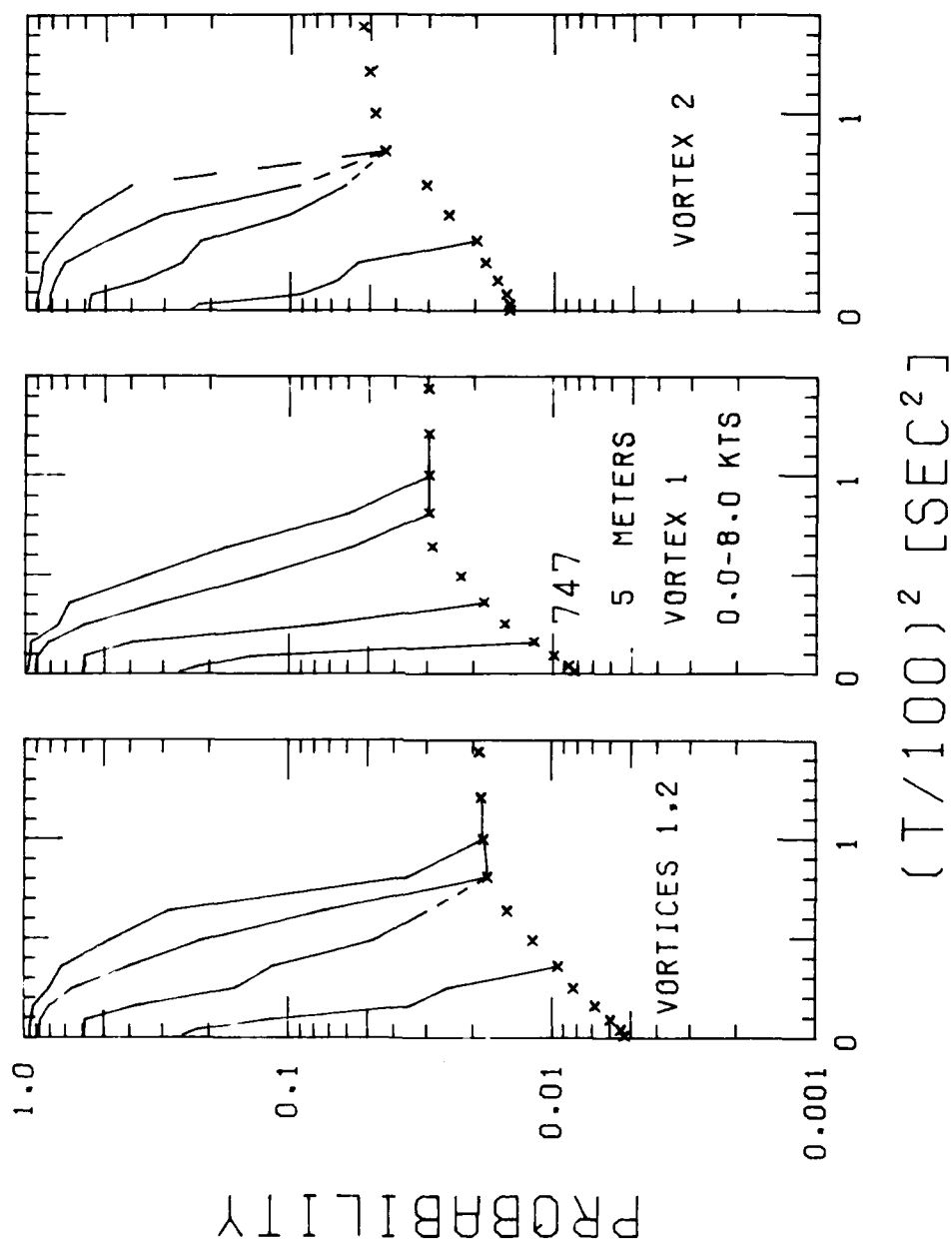


FIGURE 42. PROBABILITY OF DECAY, B-747, WINDS LESS THAN 8 KNOTS, 5-m AVERAGING RADIUS

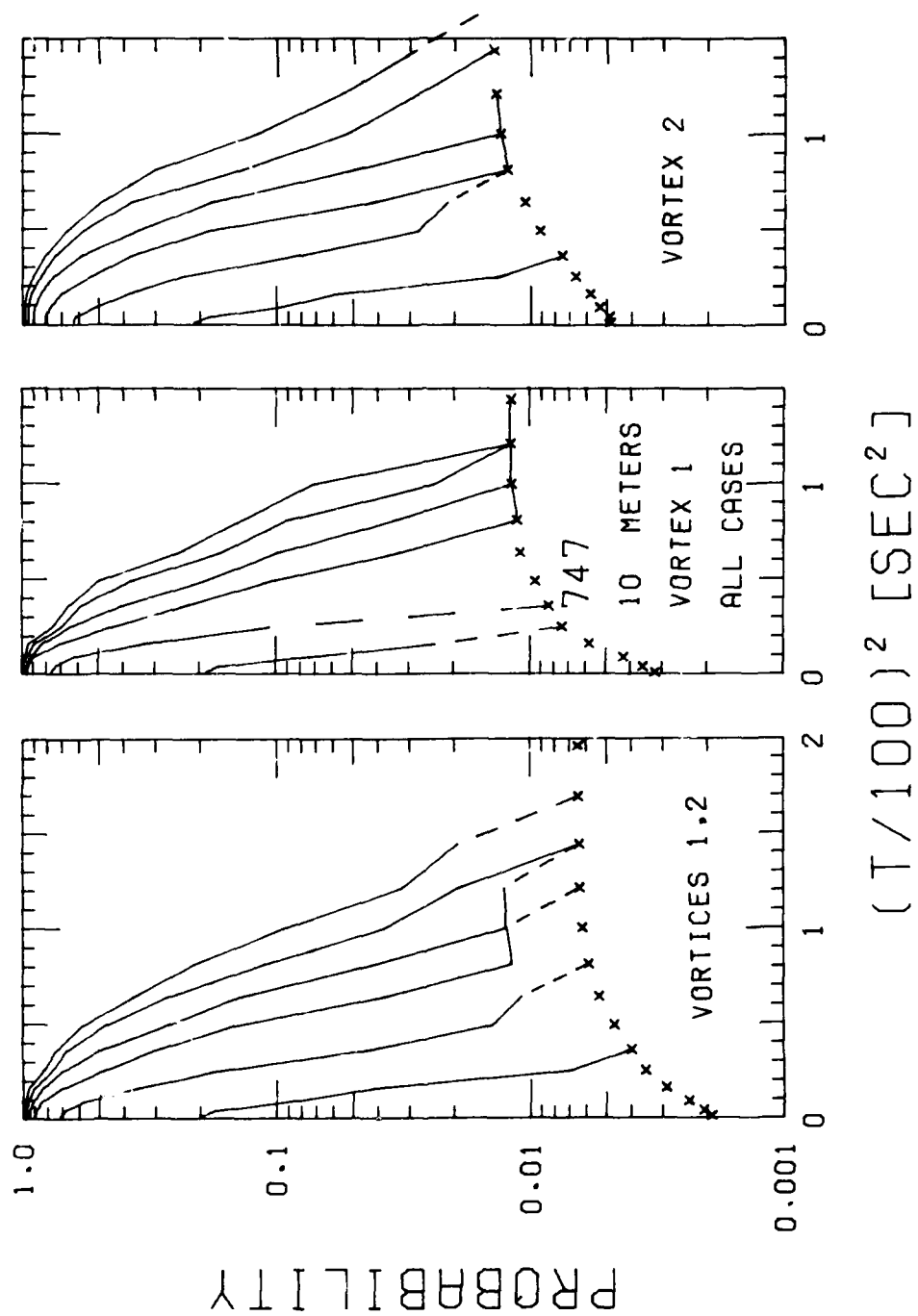


FIGURE 43. PROBABILITY OF DECAY, B-747, VORTEX 1 AND 2, 10-m AVERAGING RADIUS

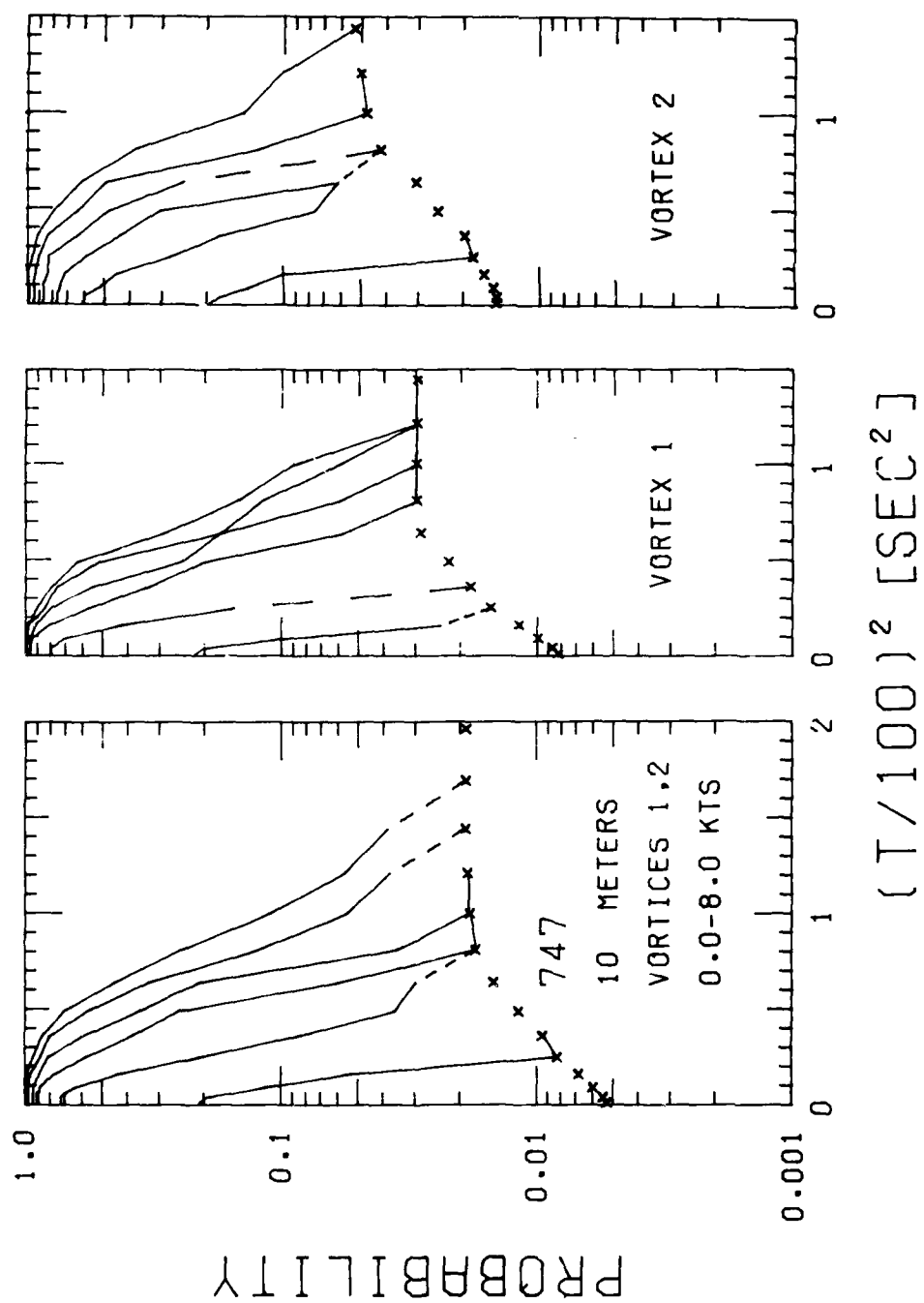


FIGURE 44. PROBABILITY OF DECAY, B-747, WINDS LESS THAN 8 KNOTS, 10-m AVERAGING RADIUS

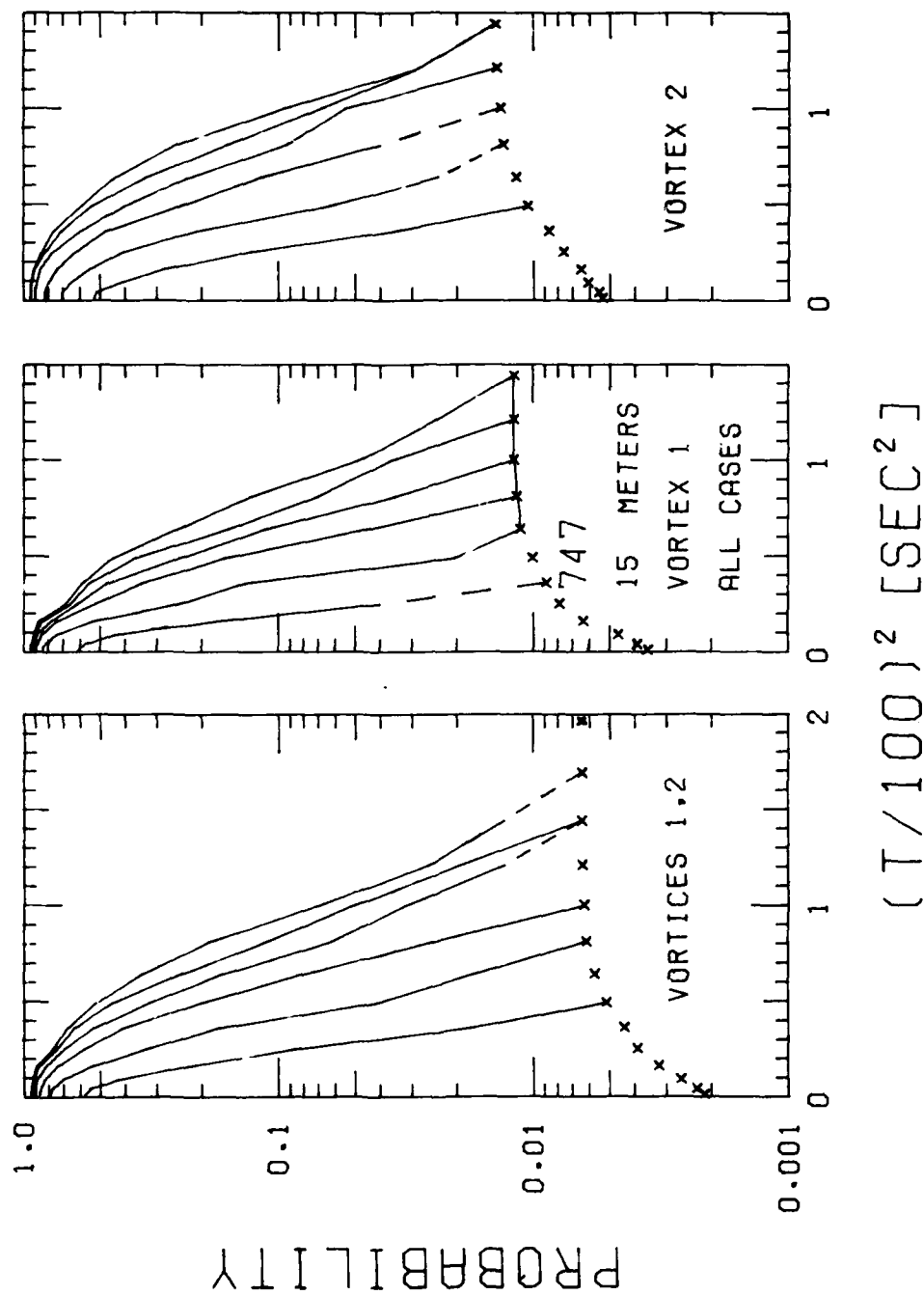


FIGURE 45. PROBABILITY OF DECAY, B-747, VORTEX 1 AND 2, 15-m AVERAGING RADIUS

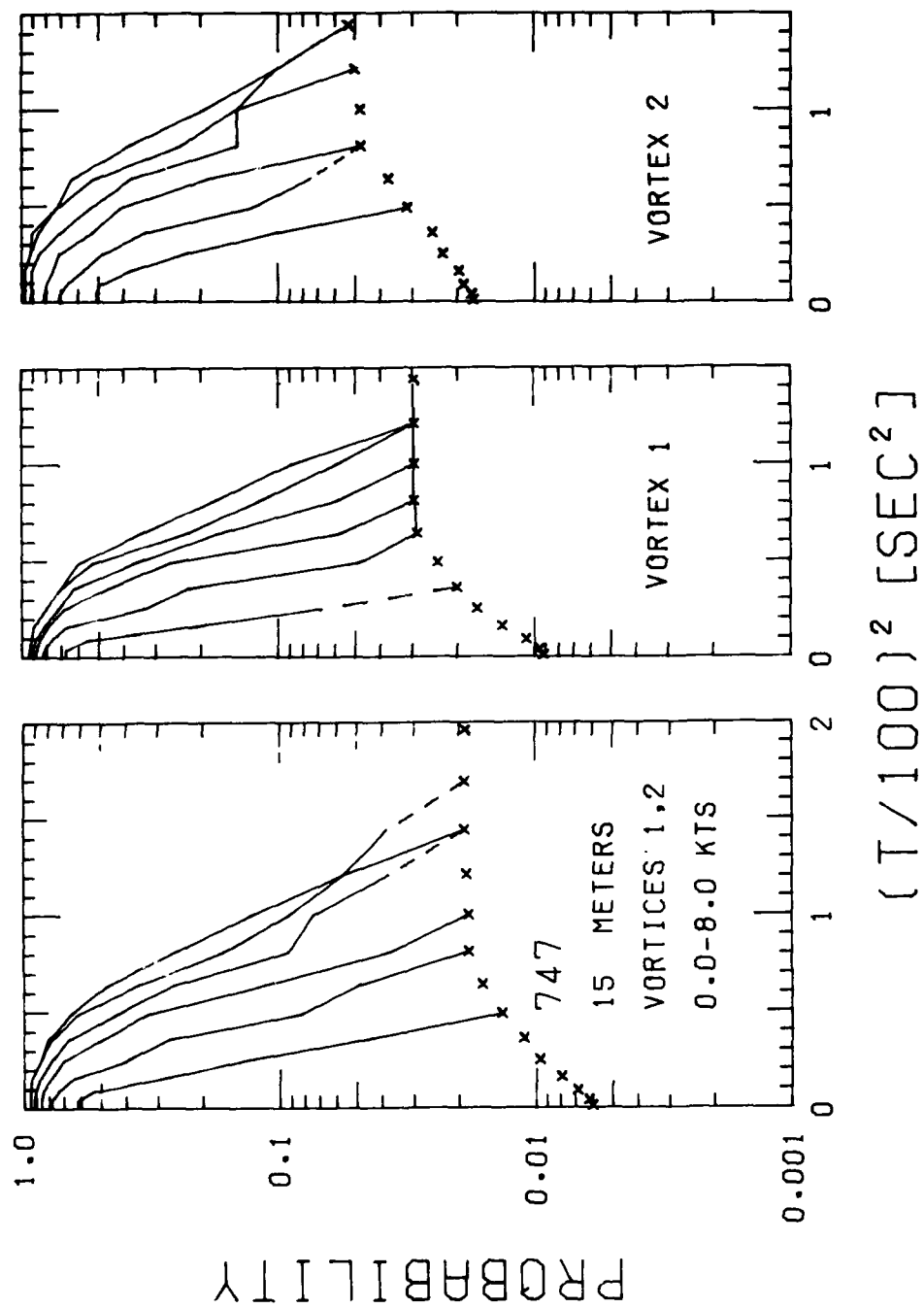


FIGURE 46. PROBABILITY OF DECAY, B-747, WINDS LESS THAN 8 KNOTS, 15-m AVERAGING RADIUS

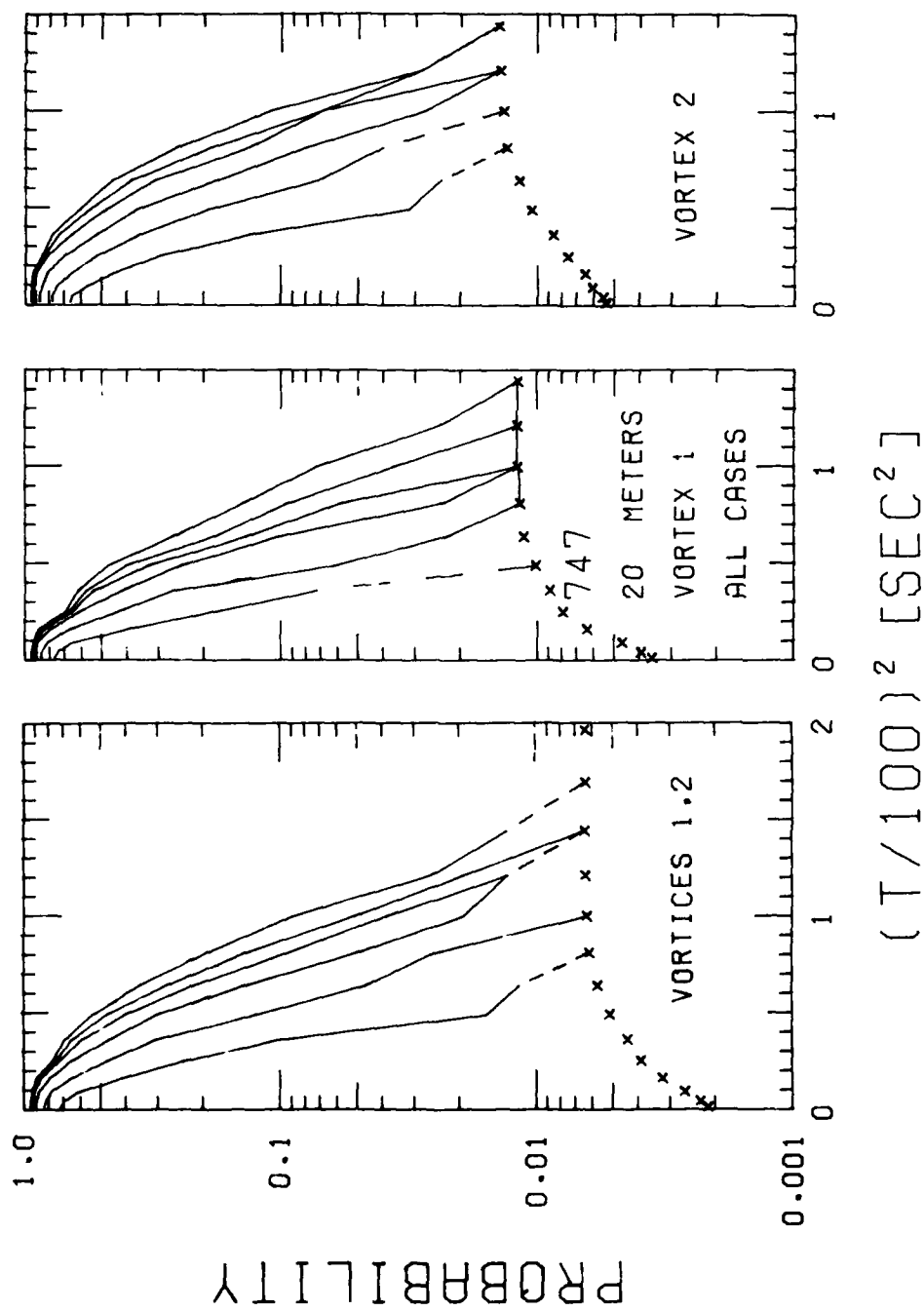


FIGURE 47. PROBABILITY OF DECAY, B-747, VORTEX 1 AND 2, 20-m AVERAGING RADIUS

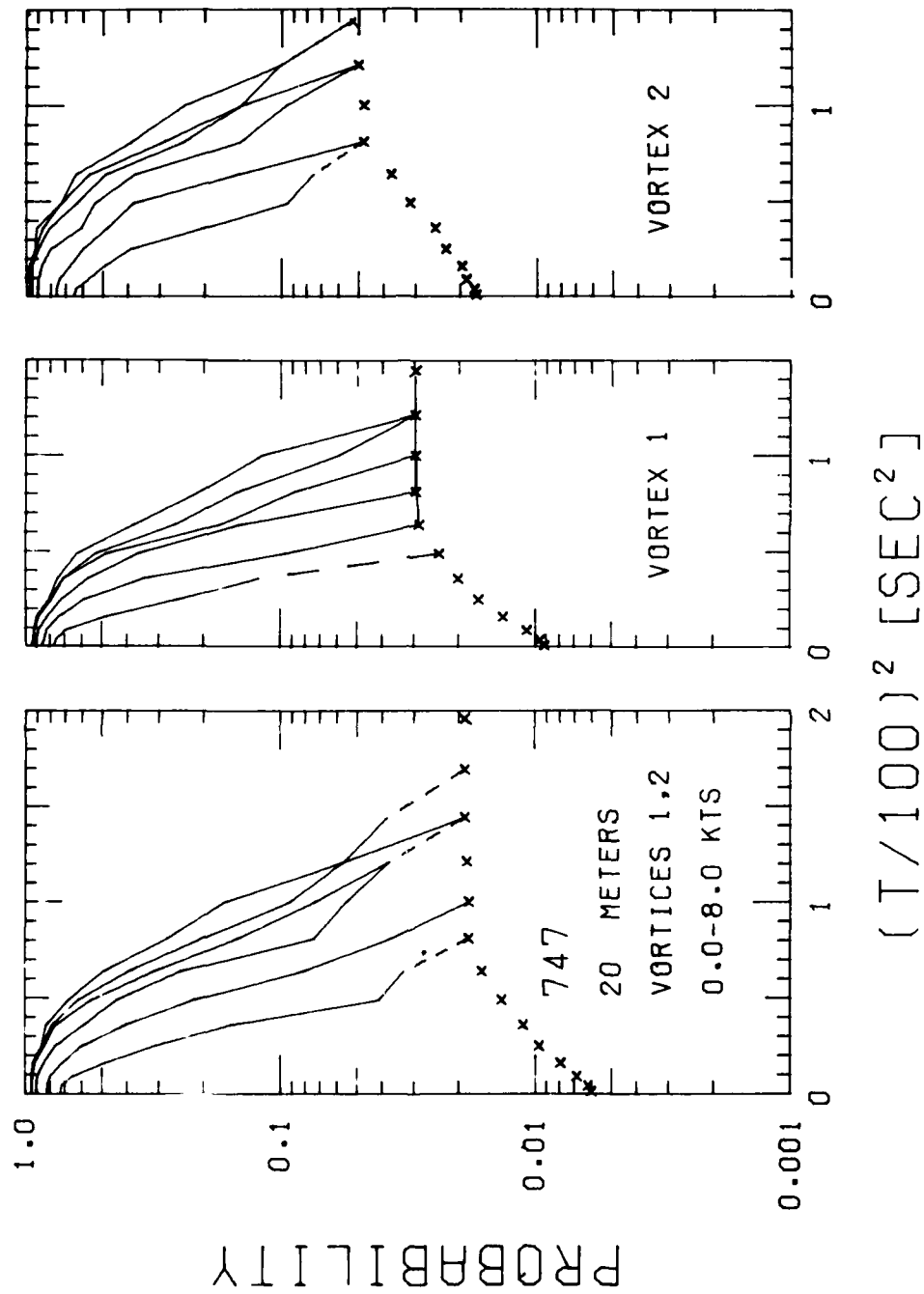


FIGURE 48. PROBABILITY OF DECAY, B-747, WINDS LESS THAN 8 KNOTS, 20-m AVERAGING RADIUS

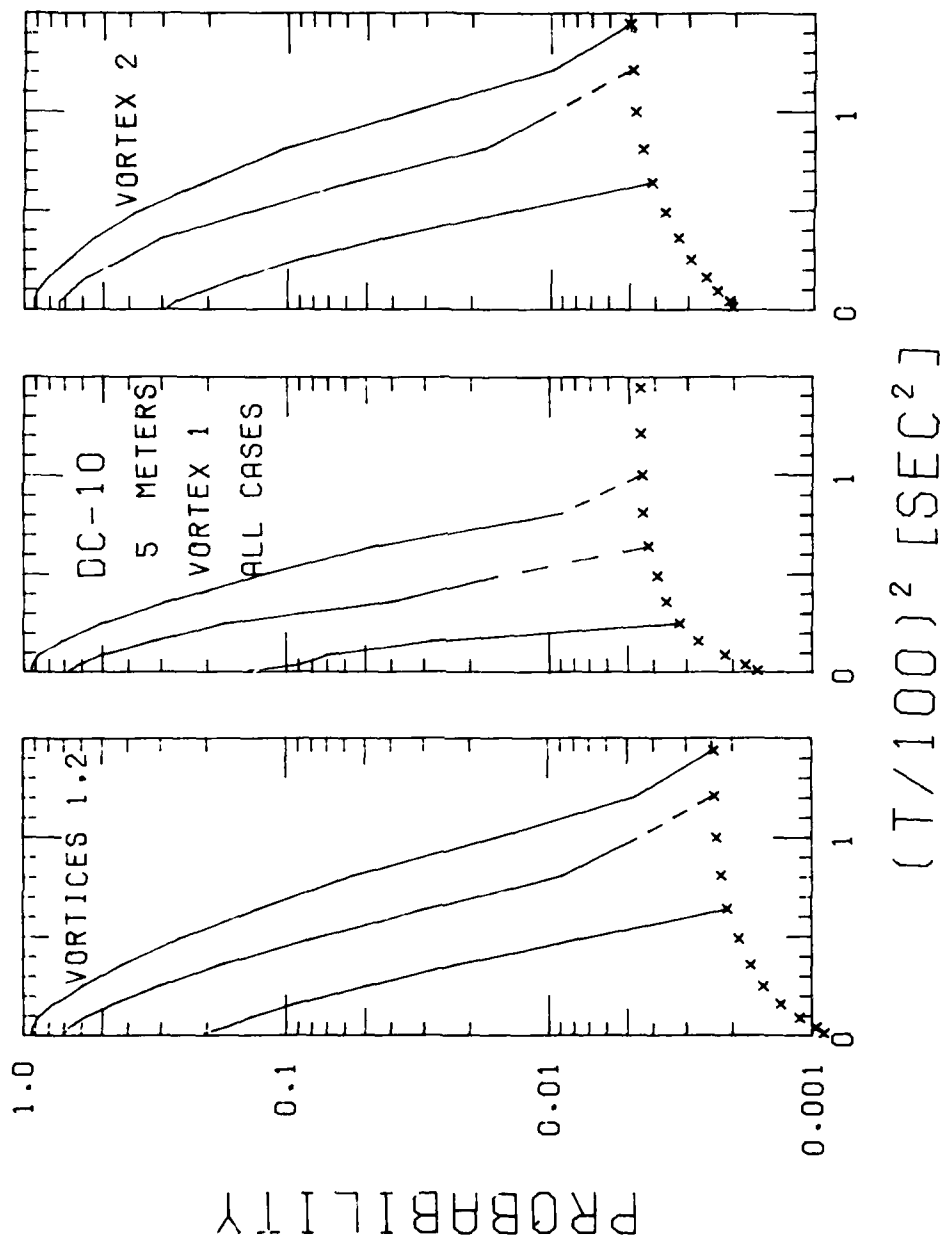


FIGURE 49. PROBABILITY OF DECAY, DC-10, VORTEX 1 AND 2, 5-m AVERAGING RADIUS

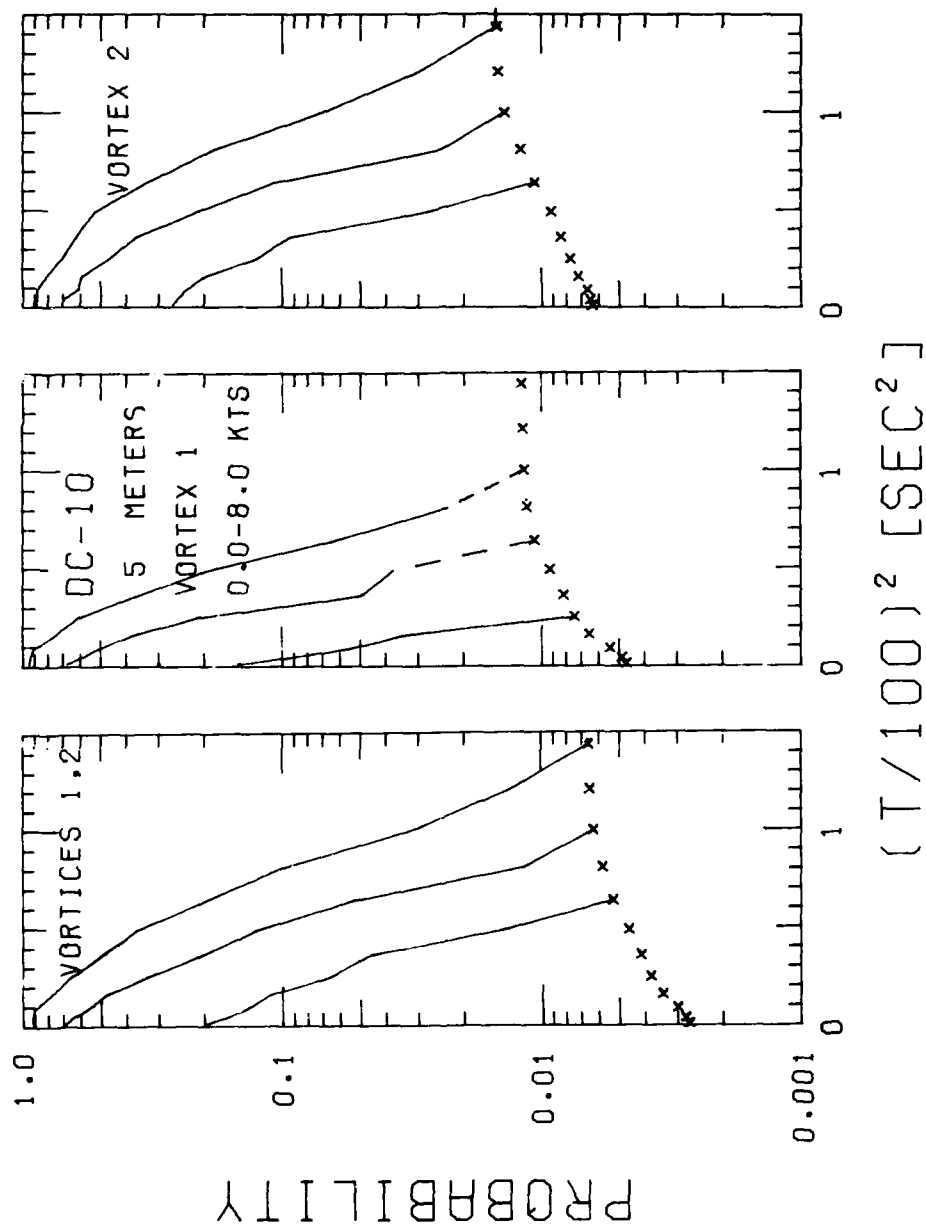


FIGURE 50. PROBABILITY OF DECAY, DC-10, WINDS LESS THAN 8 KNOTS, 5-m AVERAGING RADIUS

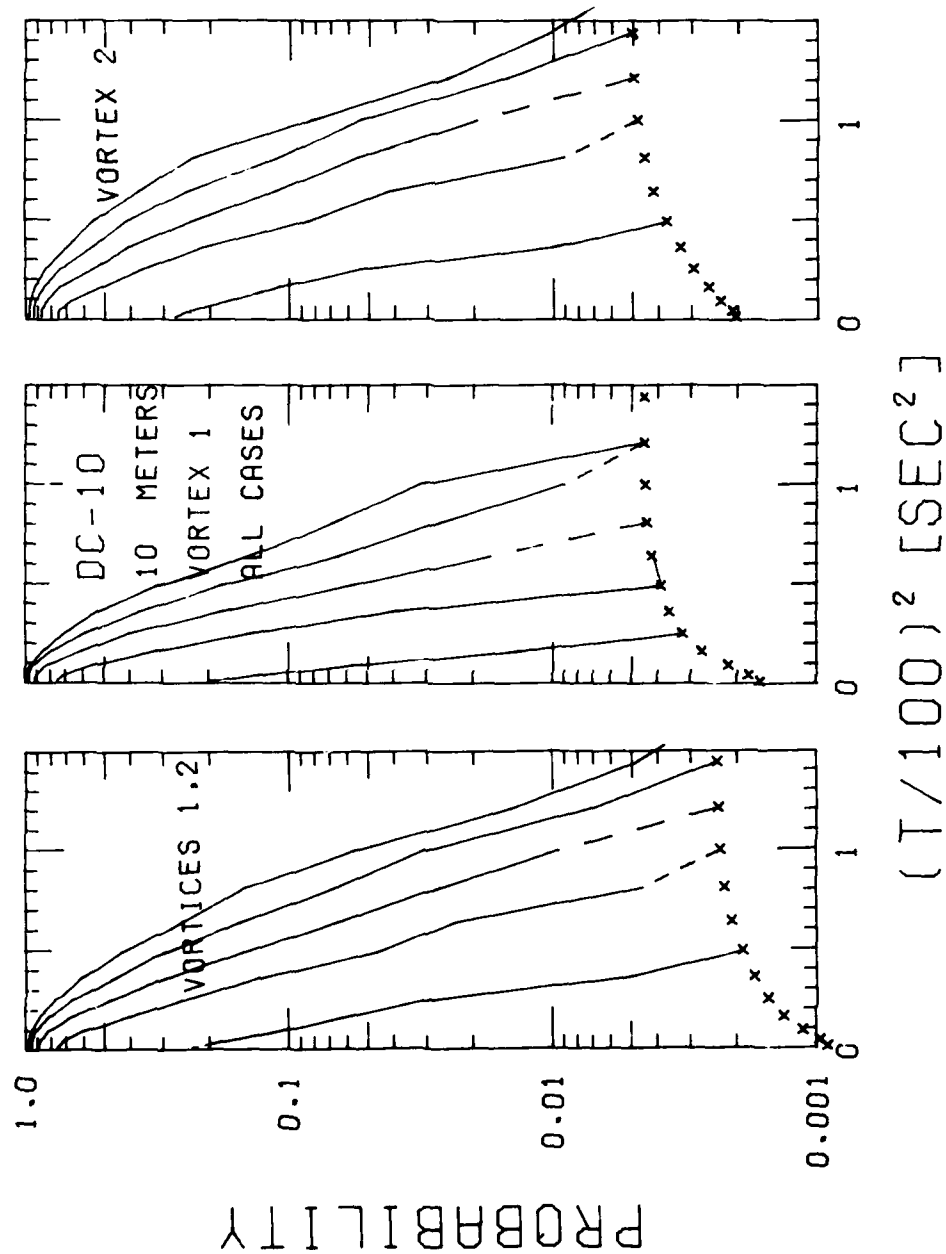


FIGURE 51. PROBABILITY OF DECAY, DC-10, VORTEX 1 AND 2, 10-m AVERAGING RADIUS

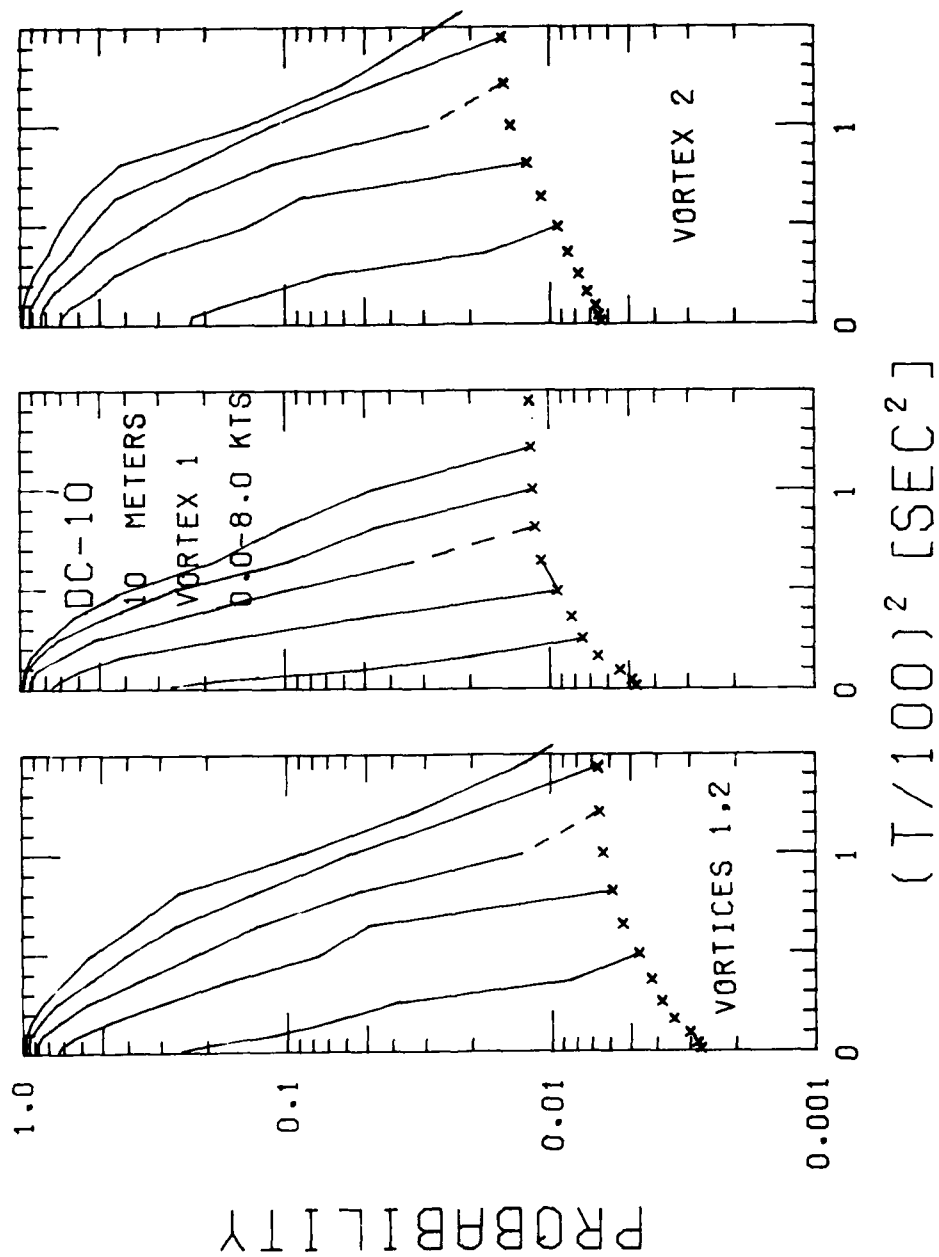


FIGURE 52. PROBABILITY OF DECAY, DC-10, WINDS LESS THAN 10 KNOTS, 10-m AVERAGING RADIUS

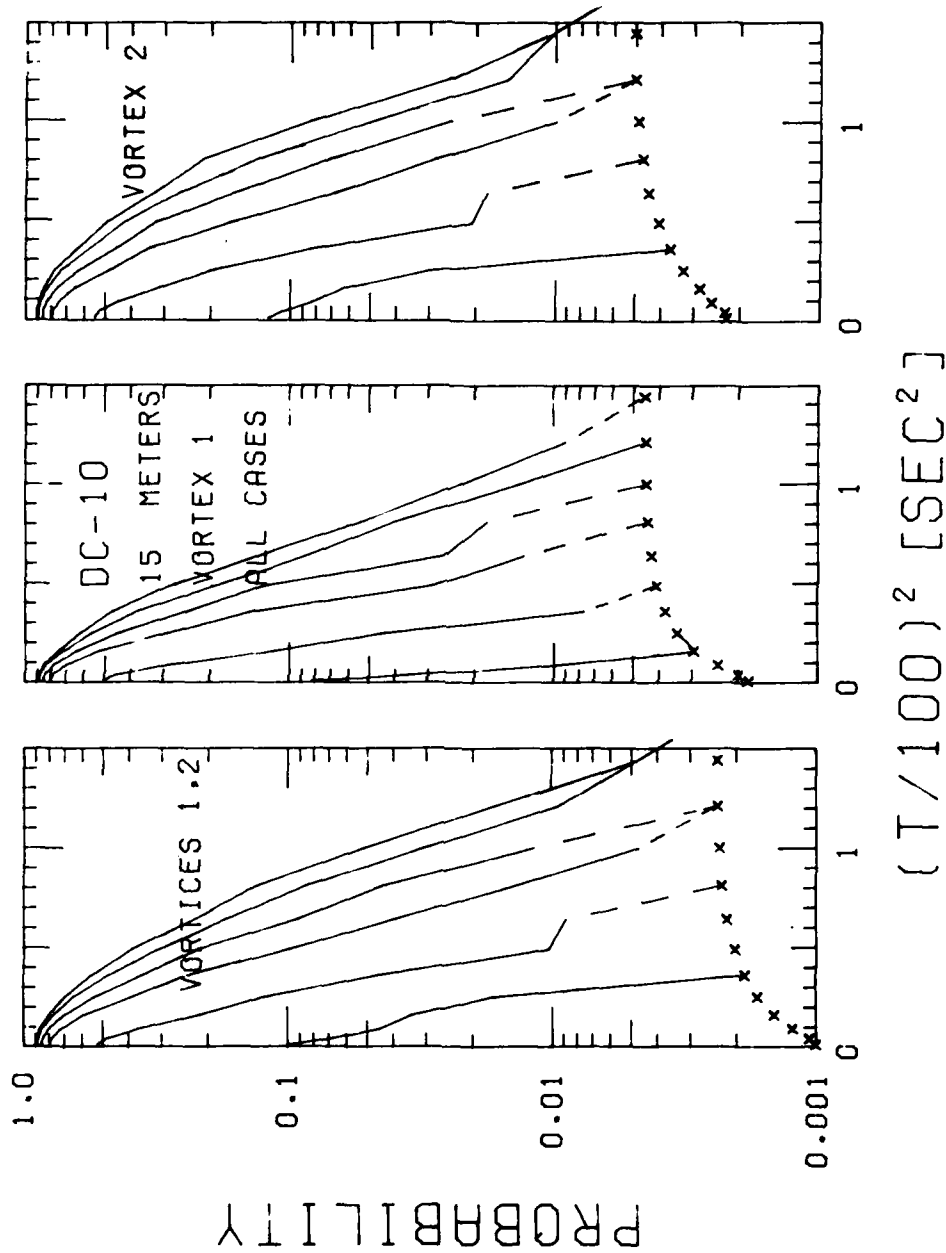


FIGURE 53. PROBABILITY OF DECAY, DC-10, VORTEX 1 AND 2, 15-m AVERAGING RADIUS

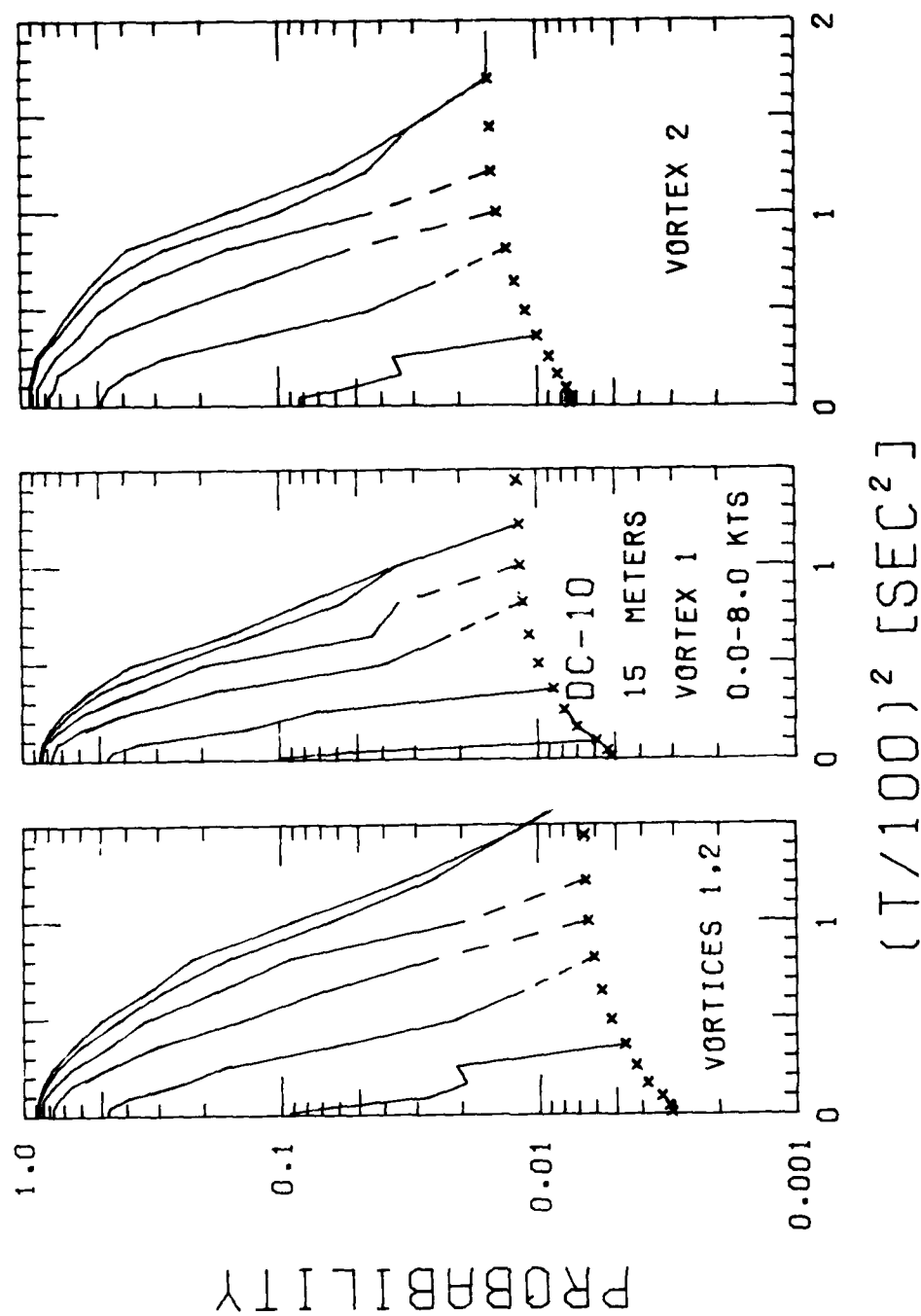


FIGURE 54. PROBABILITY OF DECAY, DC-10, WINDS LESS THAN 8 KNOTS, 15-m AVERAGING RADIUS

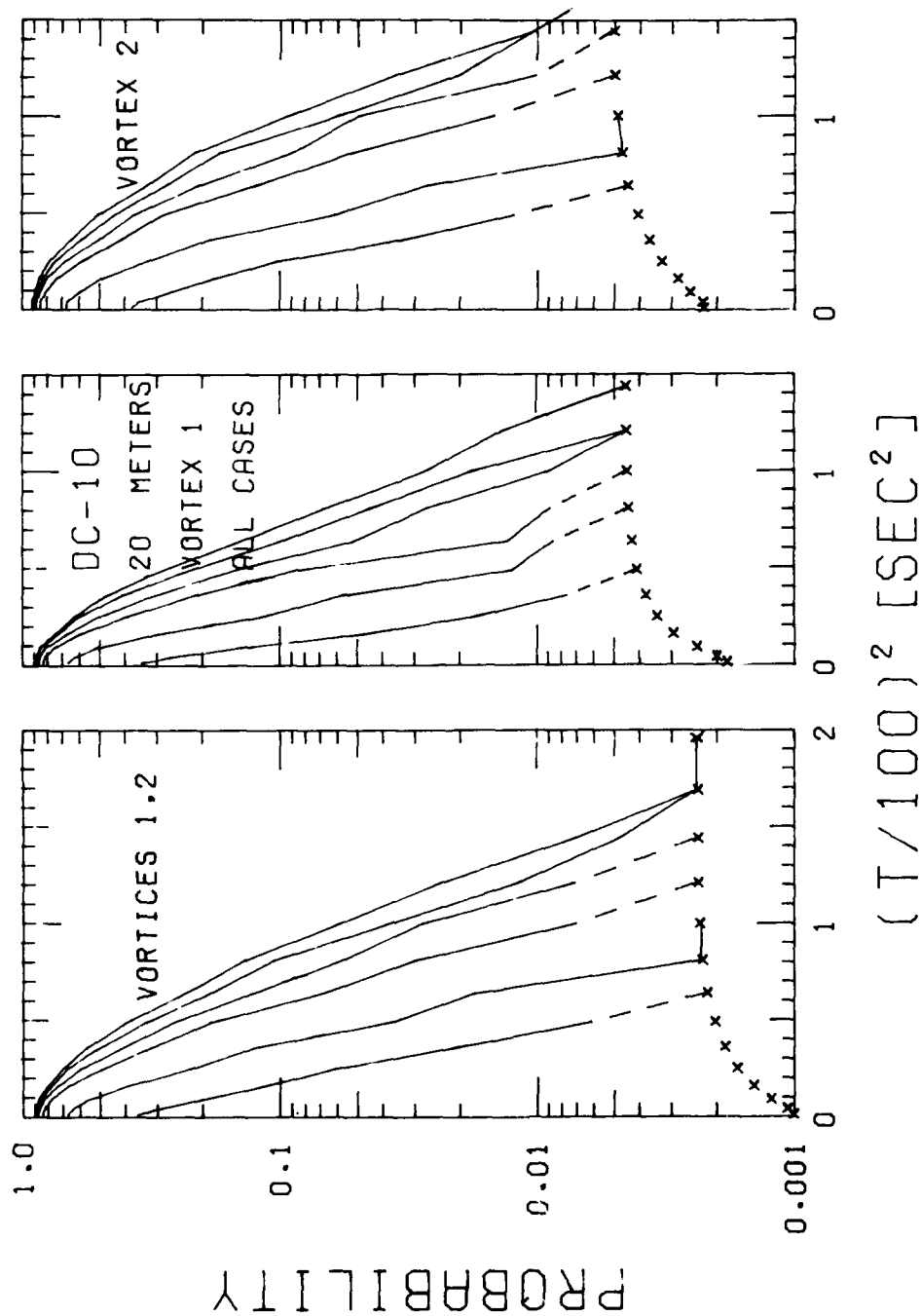


FIGURE 55. PROBABILITY OF DECAY, DC-10, VORTEX 1 AND 2, 20-m AVERAGING RADIUS

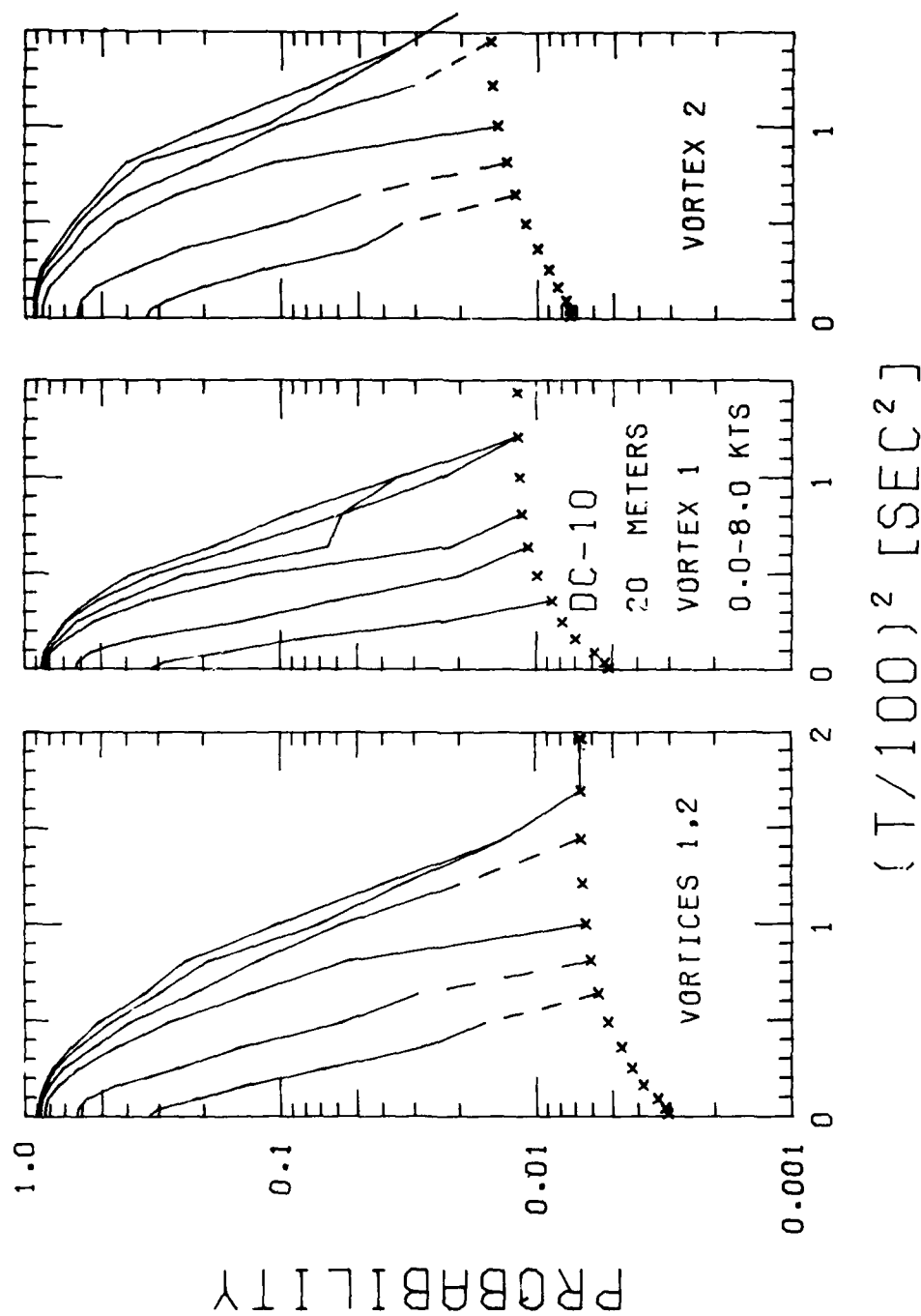


FIGURE 56. PROBABILITY OF DECAY, DC-10, WINDS LESS THAN 8 KNOTS, 20-m AVERAGING RADIUS

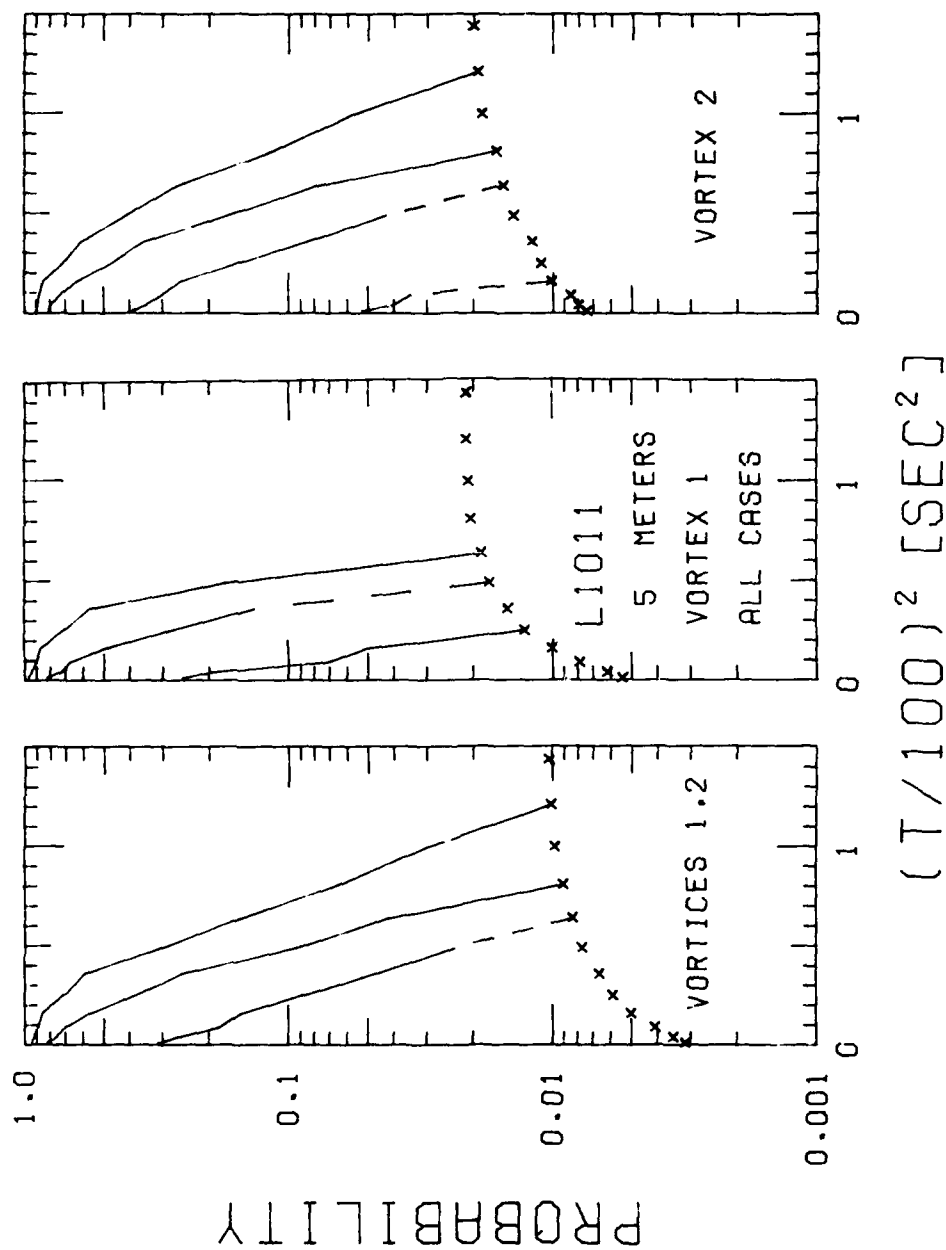


FIGURE 57. PROBABILITY OF DECAY, L-1011, VORTEX 1 AND 2, 5-m AVERAGING RADIUS

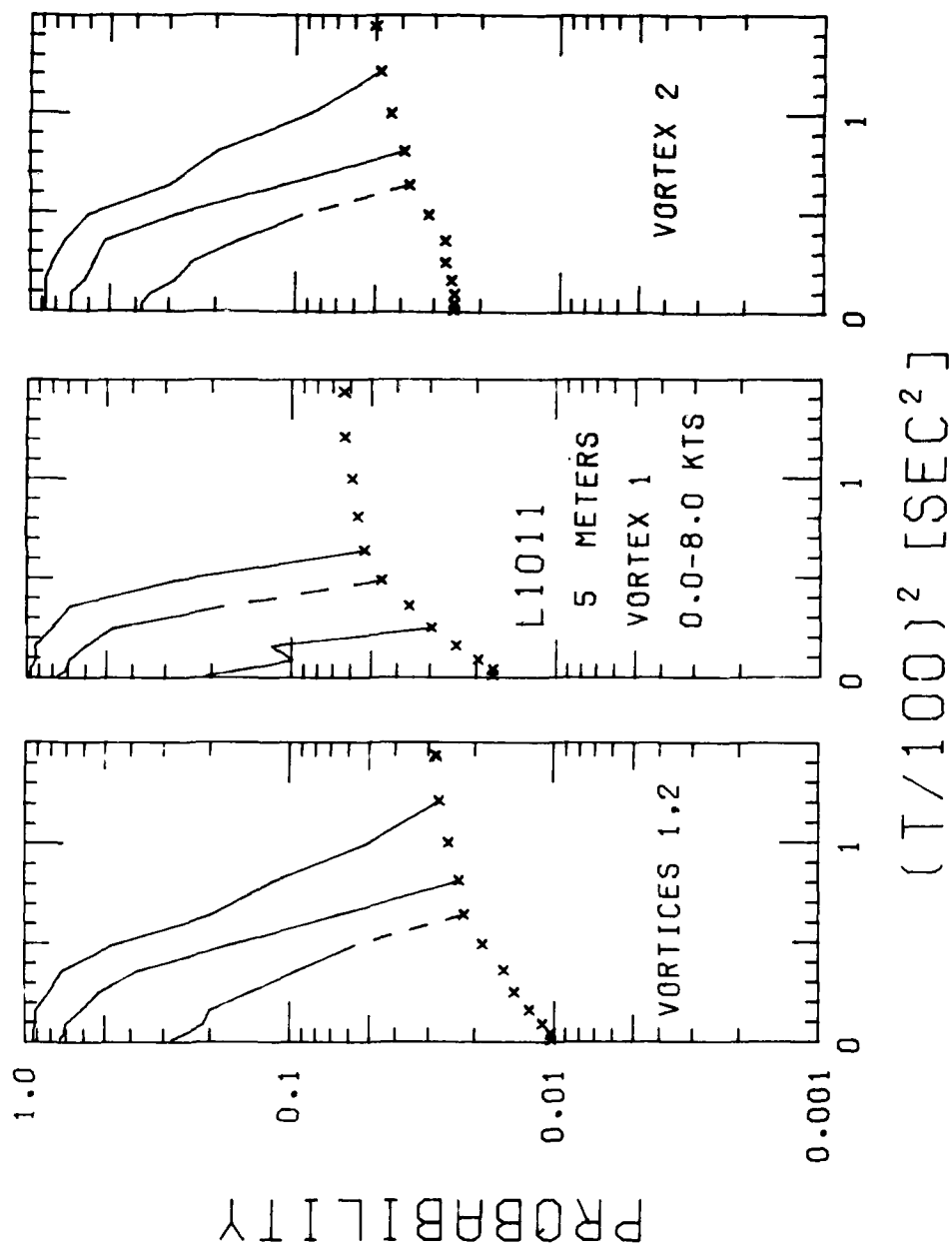


FIGURE 58. PROBABILITY OF DECAY, L-1011, WINDS LESS THAN 8 KNOTS, 5-m AVERAGING RADIUS

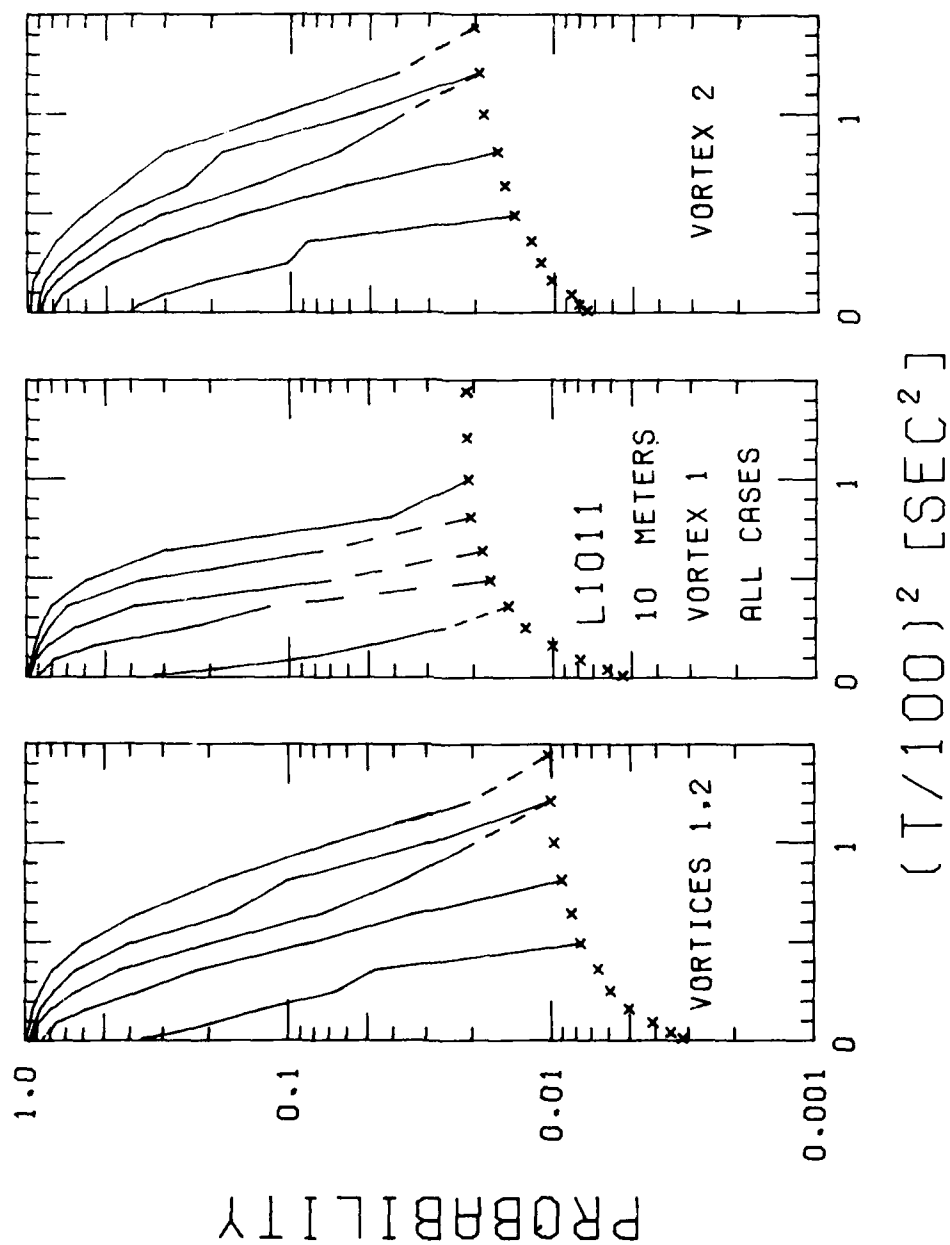


FIGURE 59. PROBABILITY OF DECAY, L-1011, VORTEX 1 AND 2, 10-m AVERAGING RADIUS

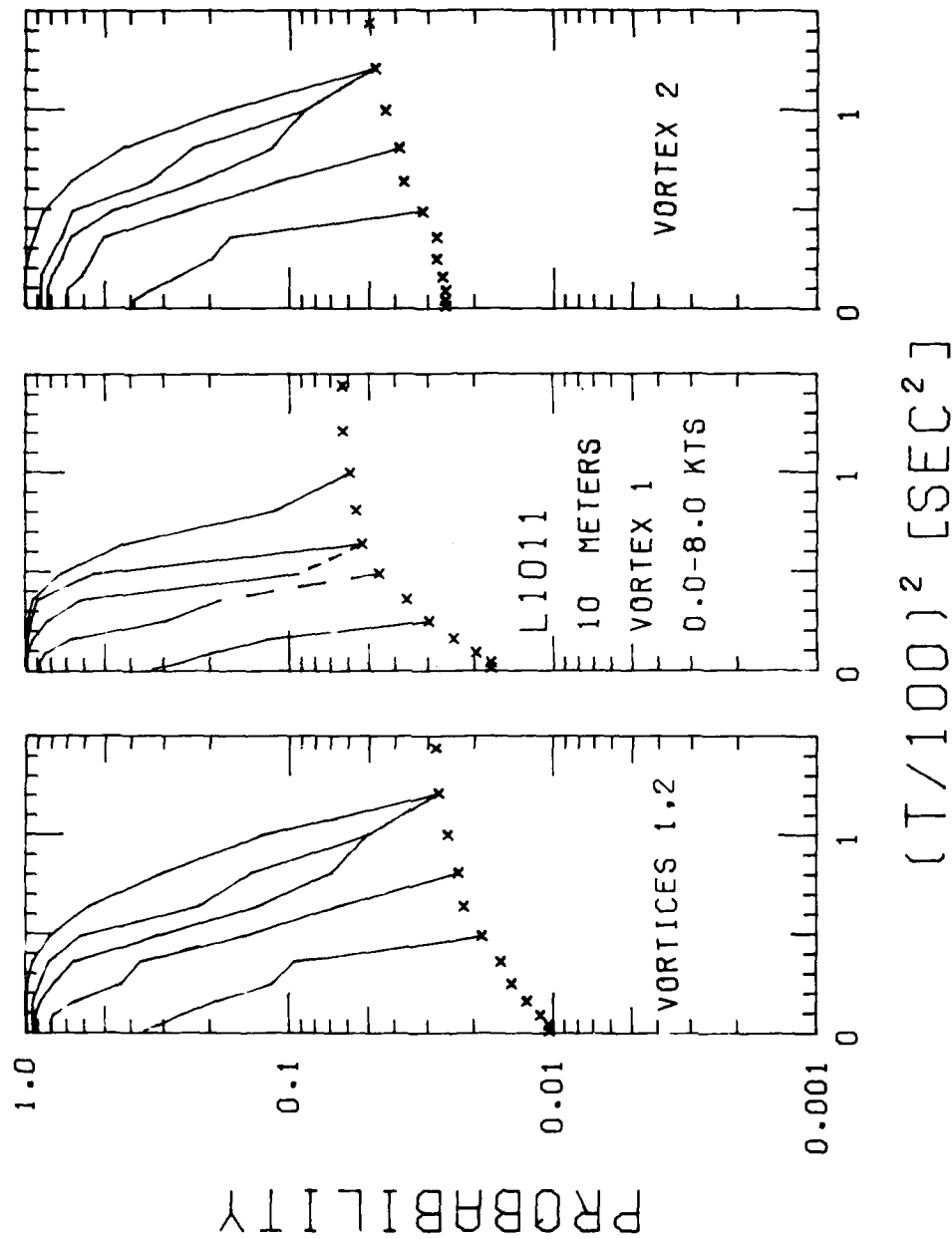


FIGURE 60. PROBABILITY OF DECAY, L-1011, WINDS LESS THAN 8 KNOTS, 10-m AVERAGING RADIUS

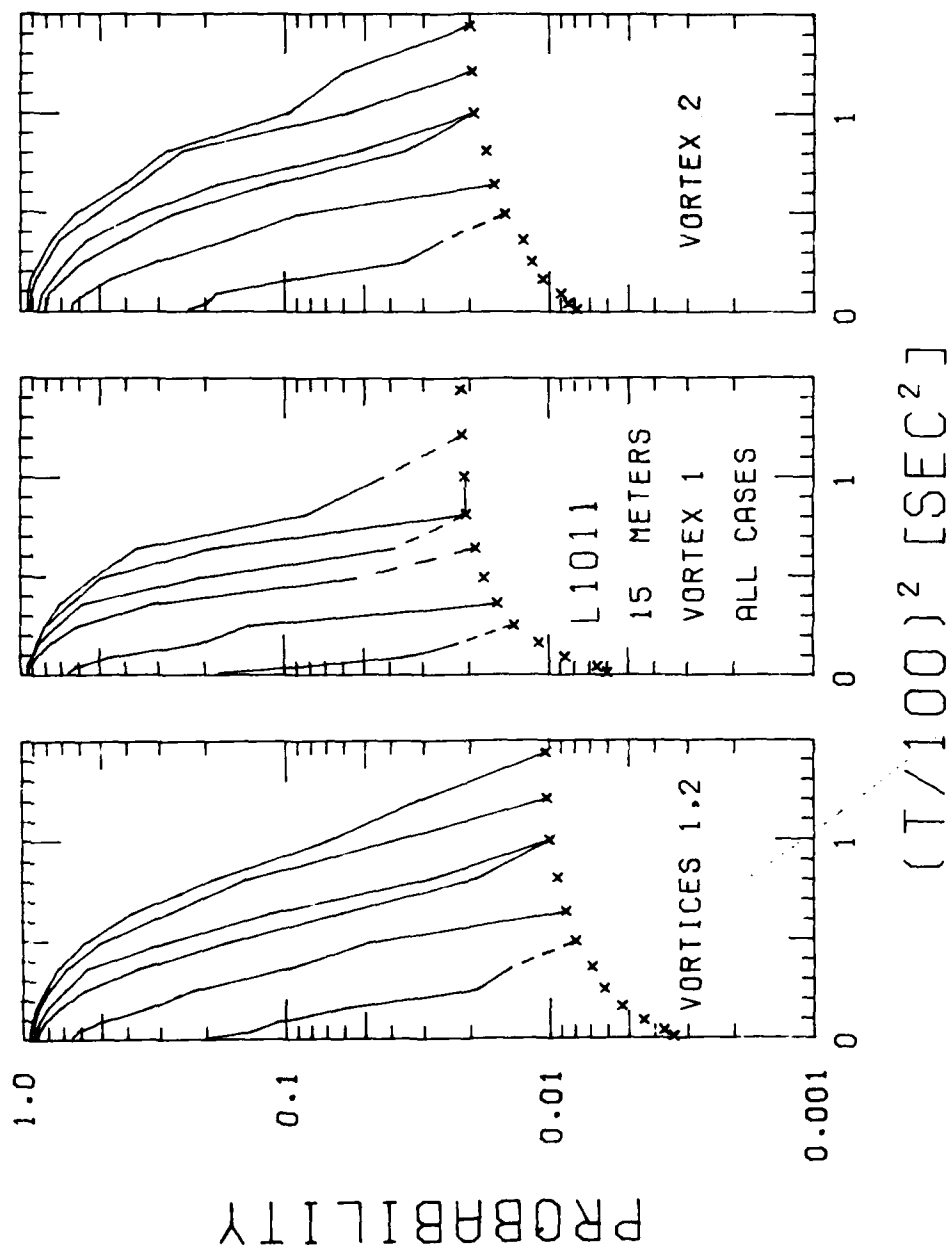


FIGURE 61. PROBABILITY OF DECAY, L-1011, VORTEX 1 AND 2, 15-m AVERAGING RADIUS

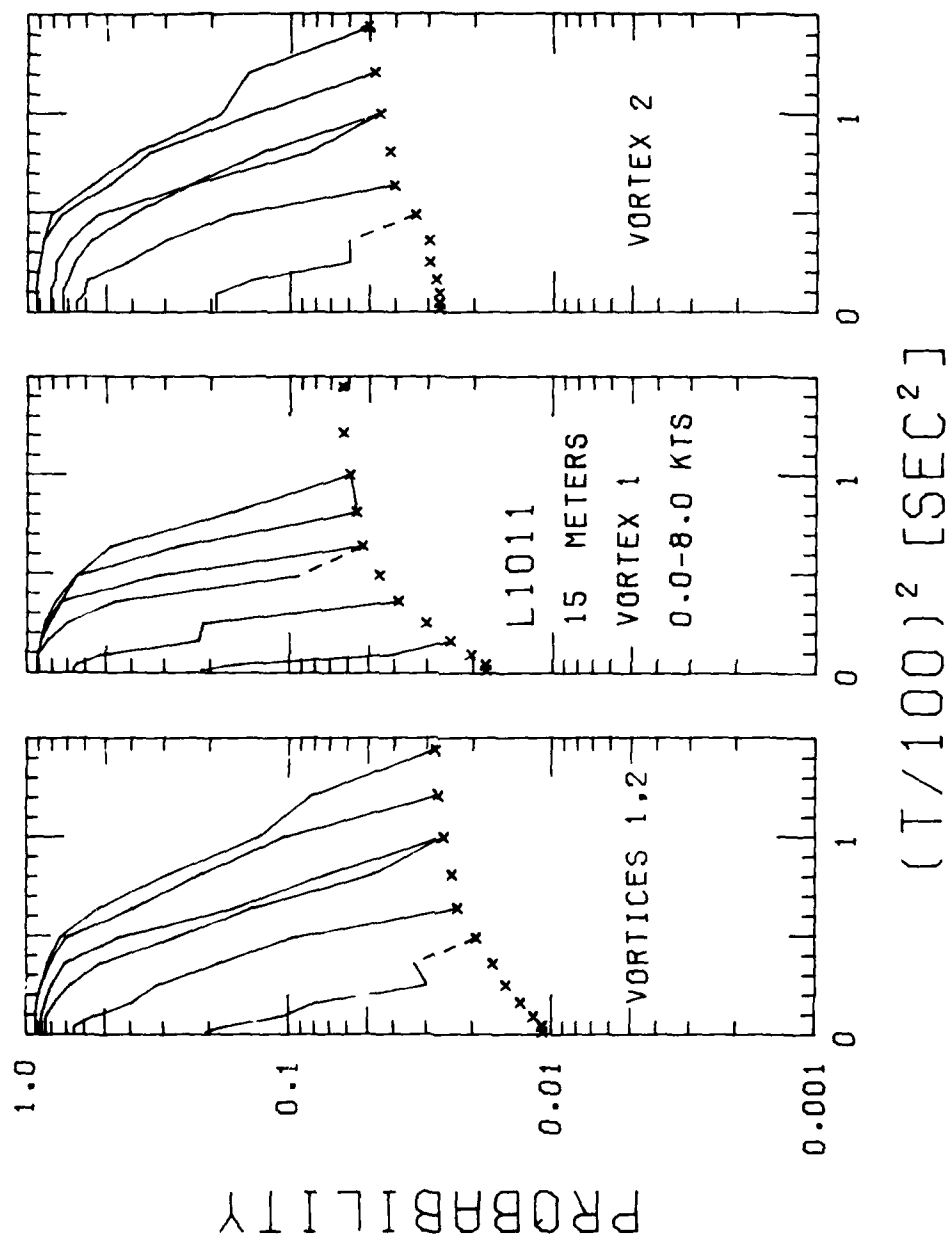


FIGURE 62. PROBABILITY OF DECAY, L-1011, WINDS LESS THAN 8 KNOTS, 15-m AVERAGING RADIUS

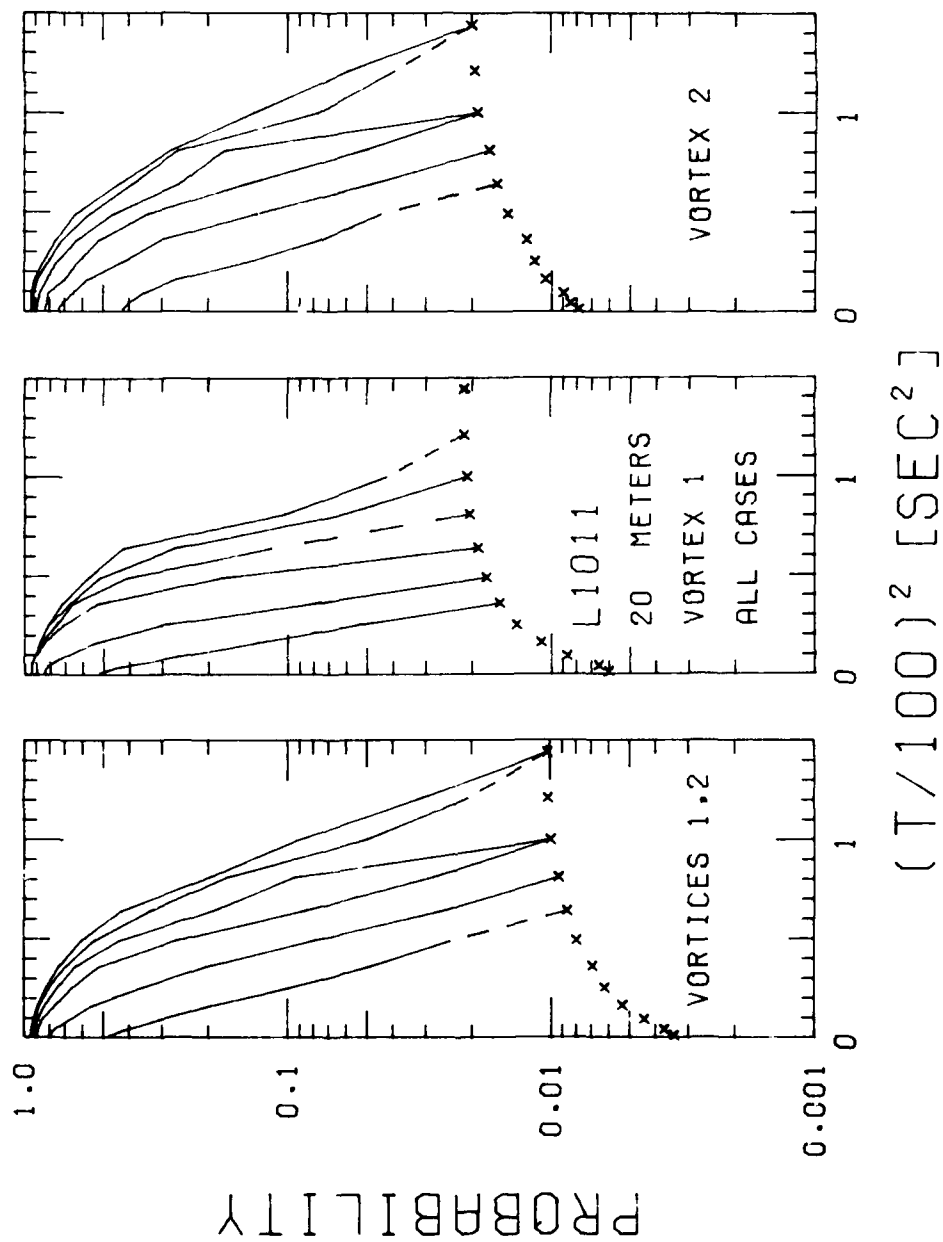


FIGURE 63. PROBABILITY OF DECAY, L-1011, VORTEX 1 AND 2, 20-m AVERAGING RADIUS

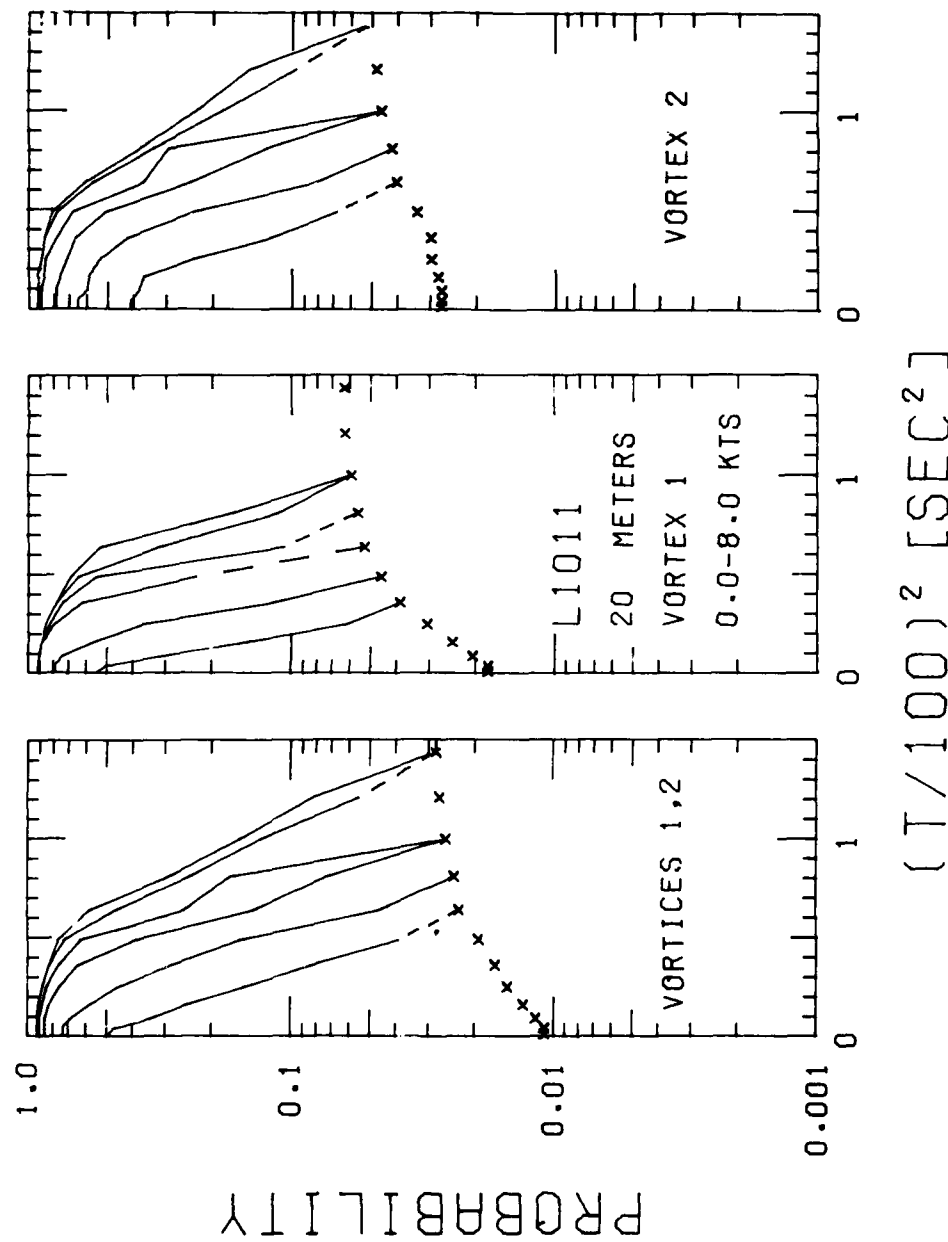


FIGURE 64. PROBABILITY OF DECAY, L-1011, WINDS LESS THAN 8 KNOTS, 20-m AVERAGING RADIUS

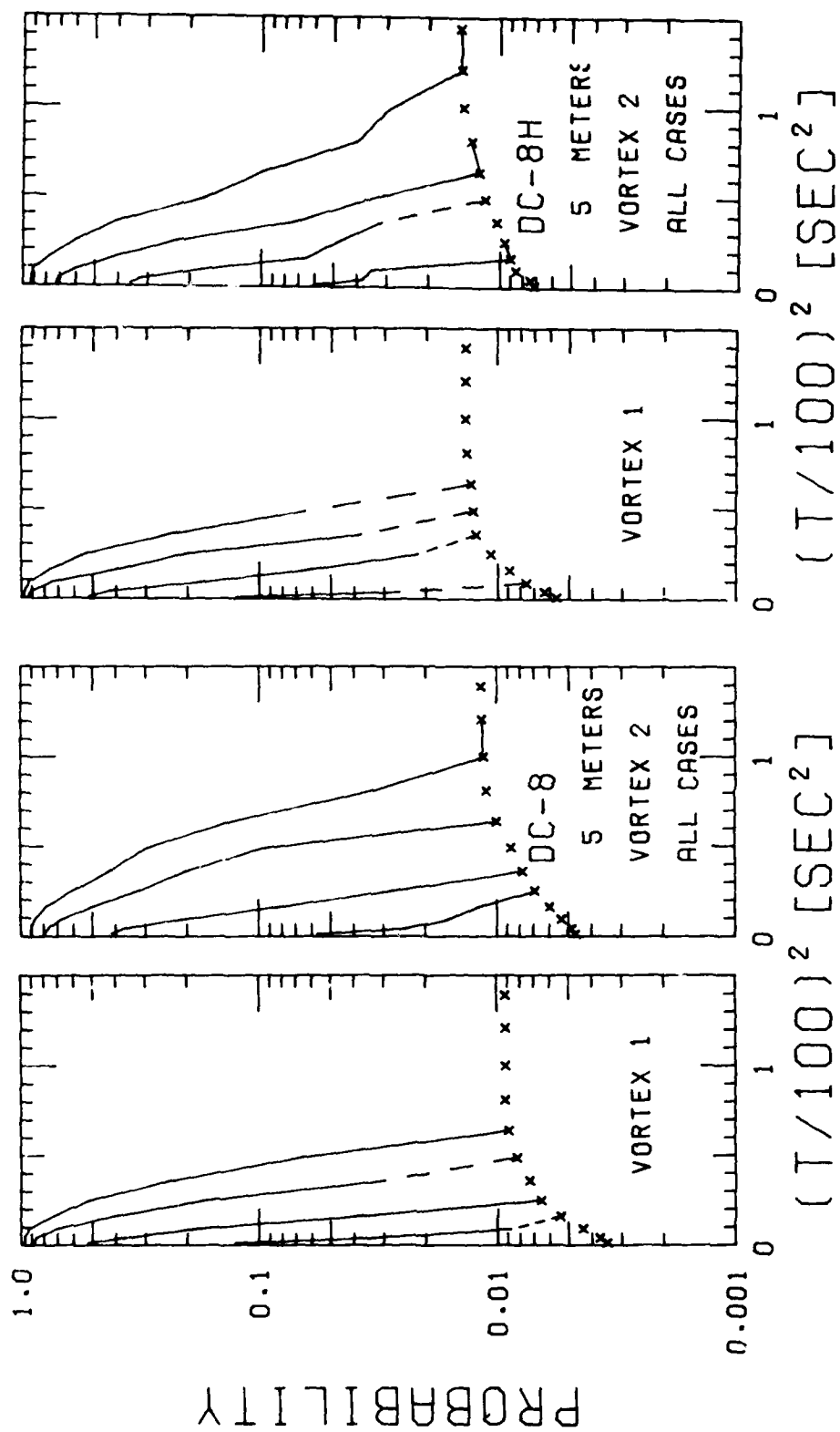


FIGURE 65. PROBABILITY OF DECAY, DC-8 AND DC-8H, VORTEX 1 AND 2, 5-m AVERAGING RADIUS

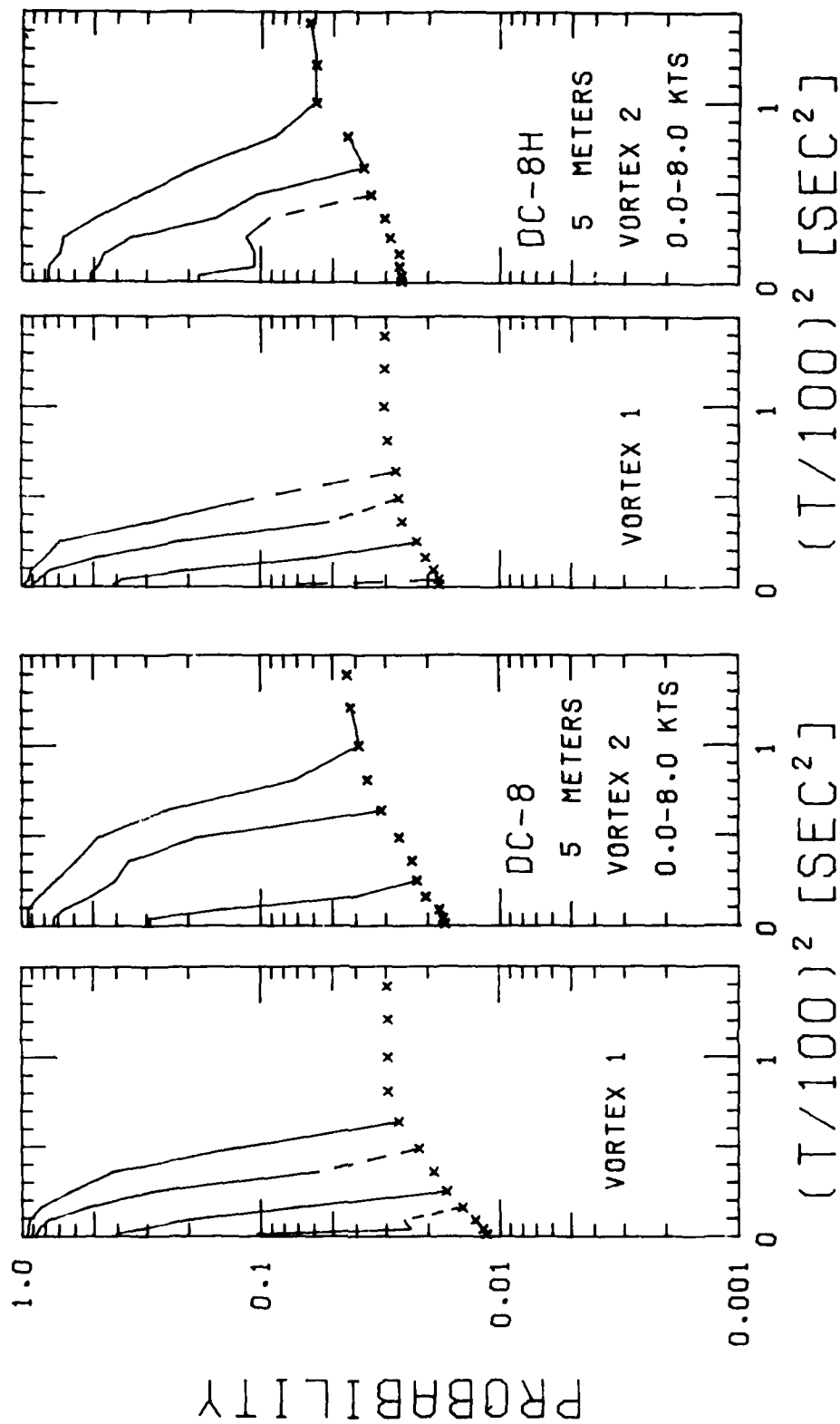


FIGURE 66. PROBABILITY OF DECAY, DC-8 AND DC-8H, WINDS LESS THAN 8 KNOTS, 5-m AVERAGING RADIUS

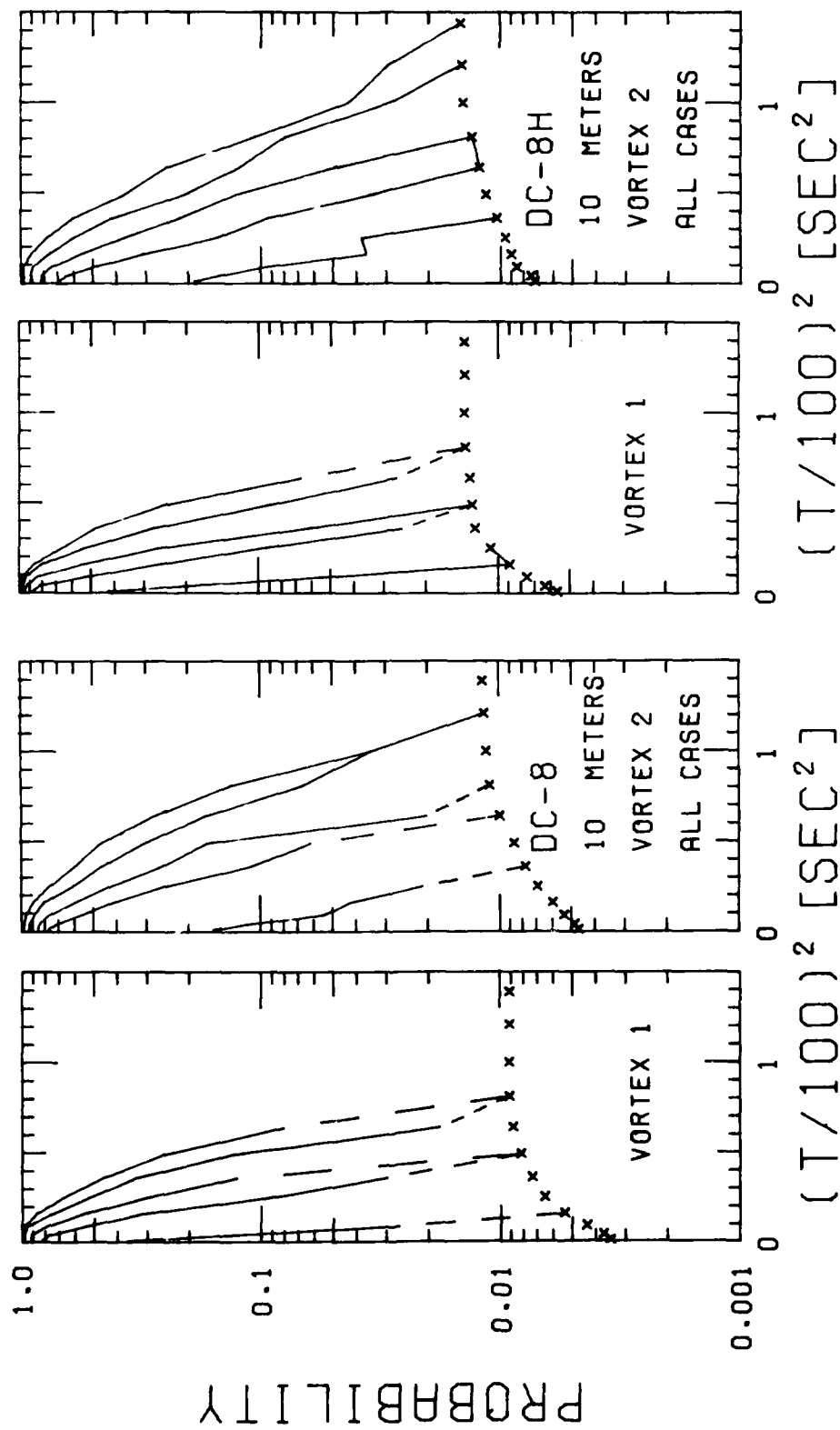


FIGURE 67. PROBABILITY OF DECAY, DC-8 AND DC-8H, VORTEX 1 AND 2, 10-m AVERAGING RADIUS

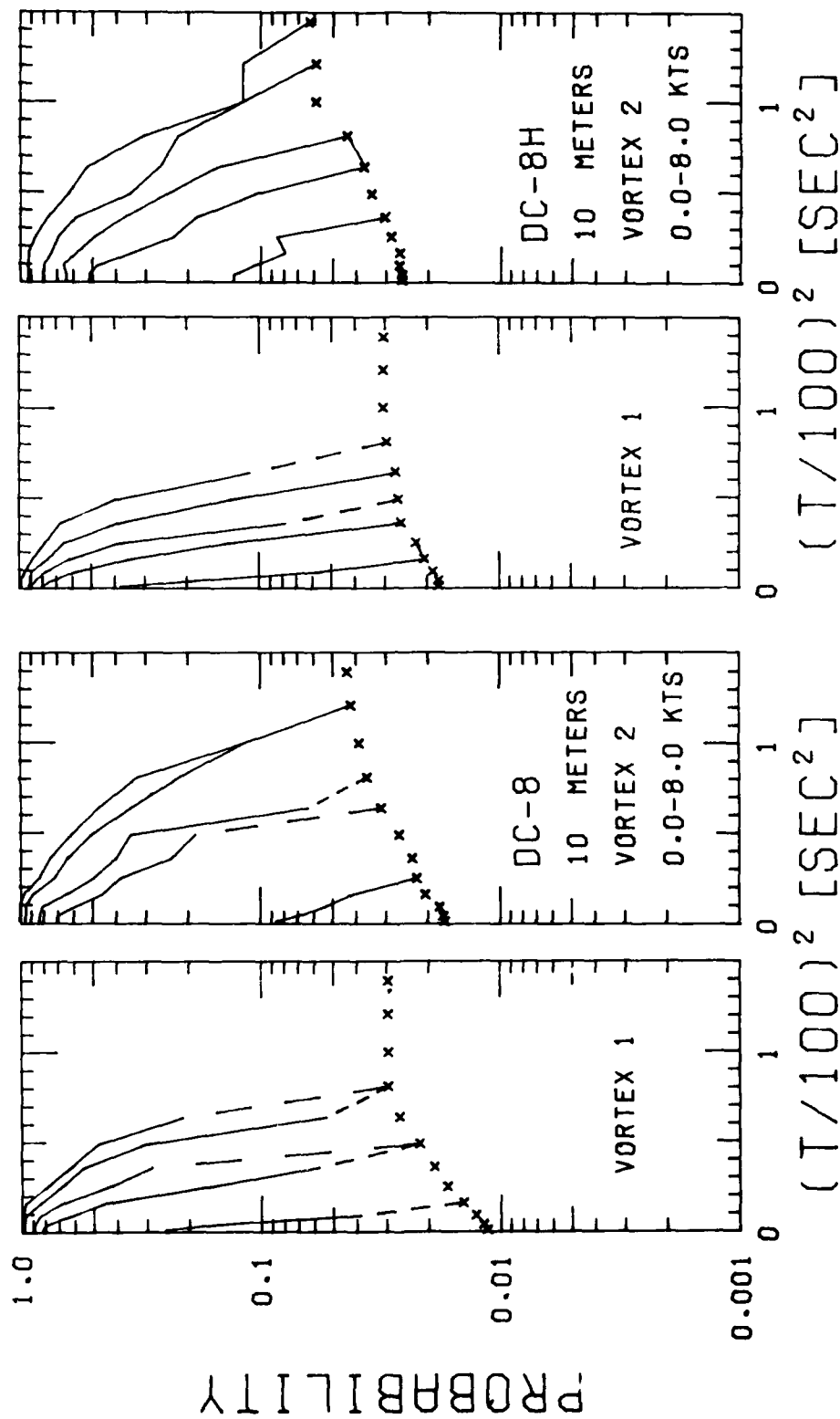


FIGURE 68. PROBABILITY OF DECAY, DC-8 AND DC-8H, WINDS LESS THAN 8 KNOTS, 10-m AVERAGING RADIUS

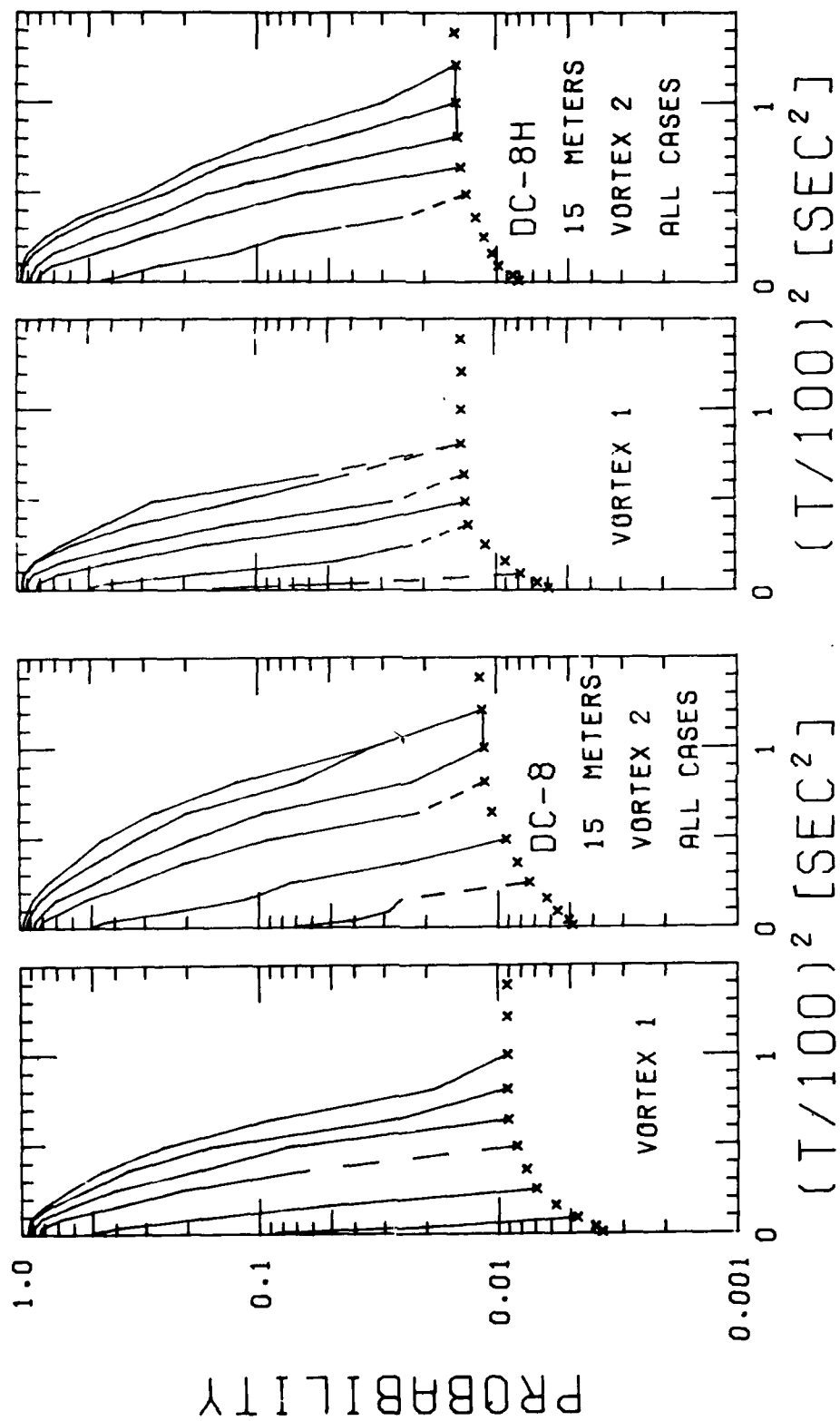


FIGURE 69. PROBABILITY OF DECAY, DC-8 AND DC-8H, VORTEX 1 AND 2, 15-m AVERAGING RADIUS

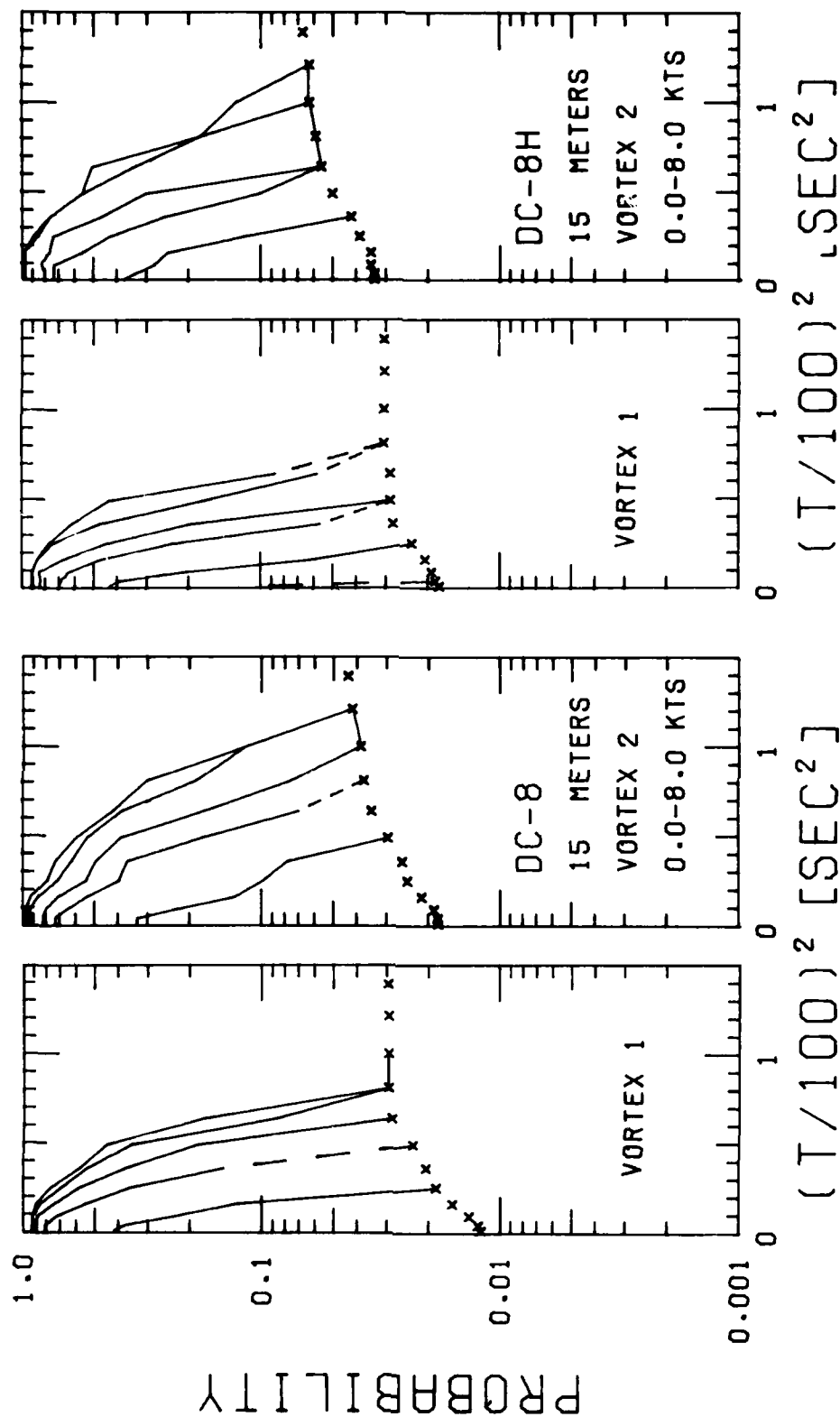


FIGURE 70. PROBABILITY OF DECAY, DC-8 AND DC-8H, WINDS LESS THAN 8 KNOTS, 15-m AVERAGING RADIUS

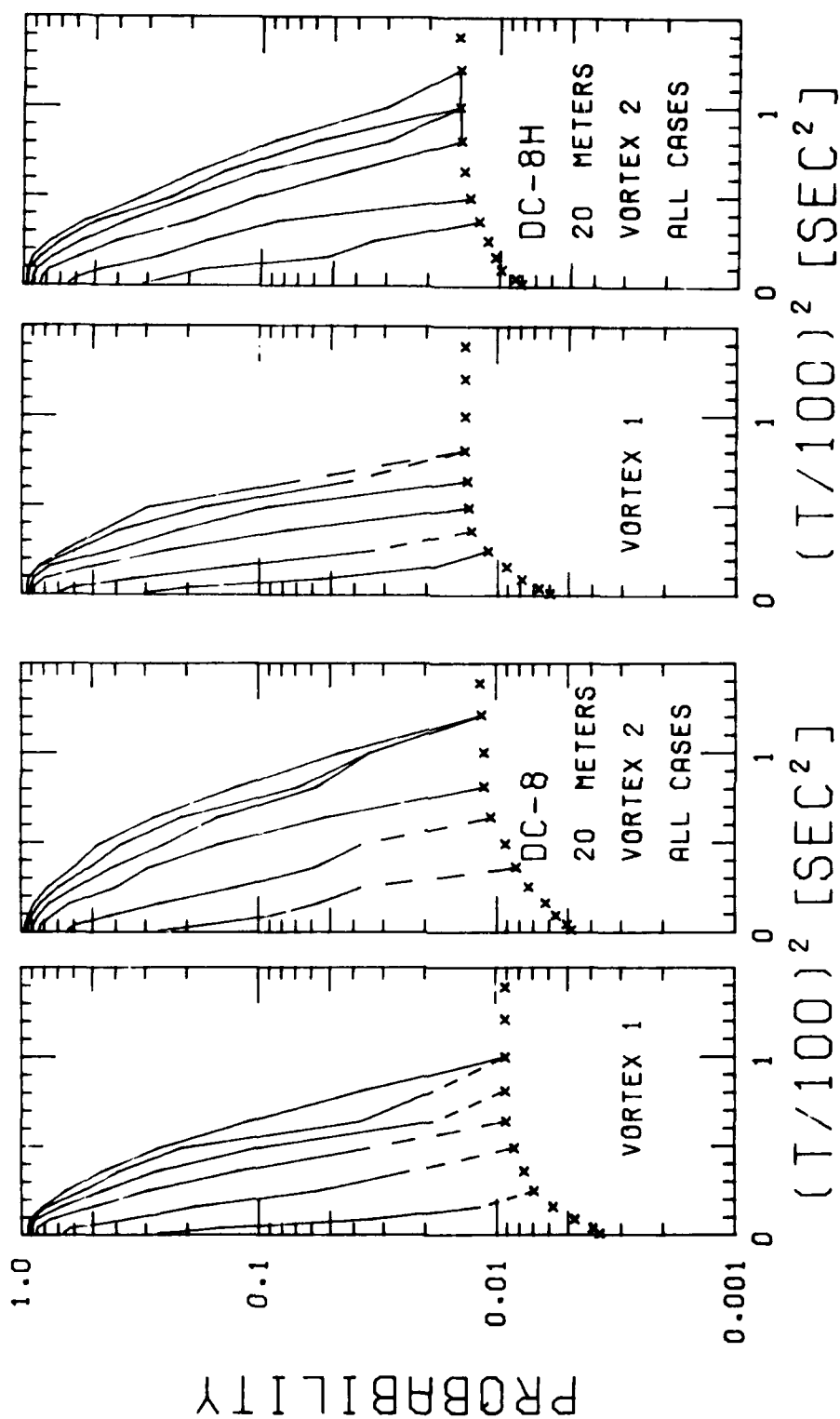


FIGURE 71. PROBABILITY OF DECAY, DC-8 AND DC-8H, VORTEX 1 AND 2, 20-m AVERAGING RADIUS

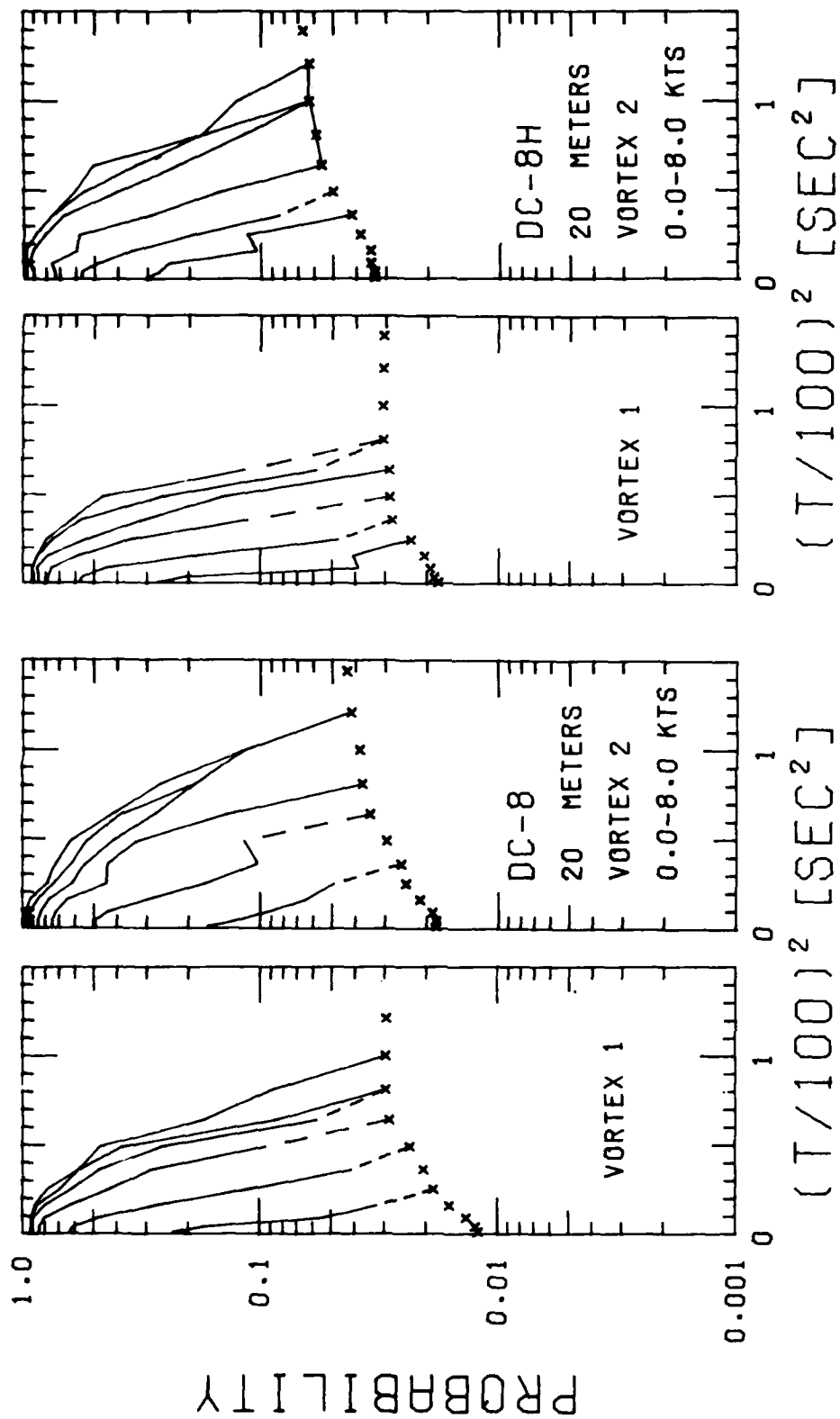


FIGURE 72. PROBABILITY OF DECAY, DC-8 AND DC-8H, WINDS LESS THAN 8 KNOTS, 20-m AVERAGING RADIUS

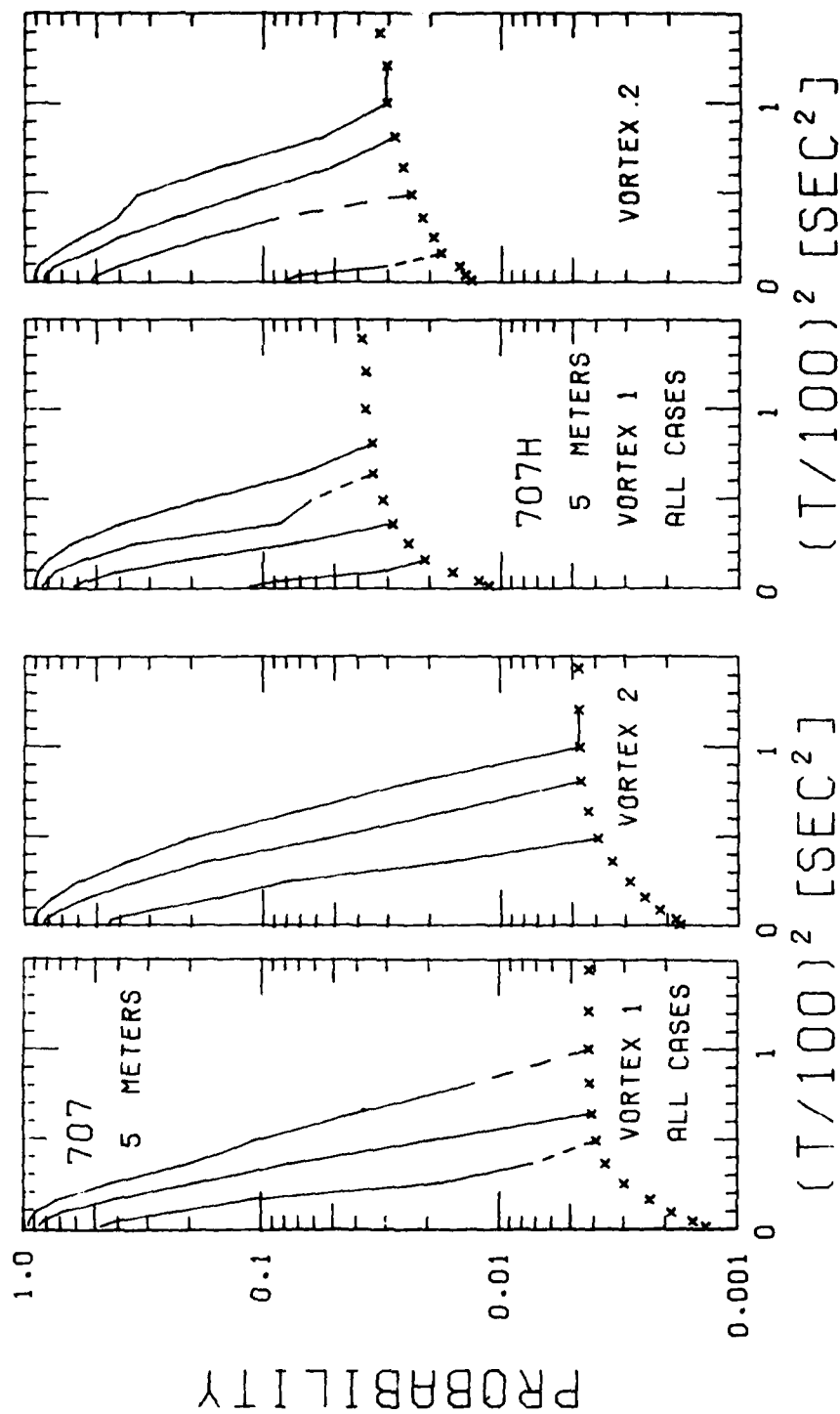


FIGURE 73. PROBABILITY OF DECAY, B-707 AND B-707H, VORTEX 1 AND 2, 5-m AVERAGING RADIUS

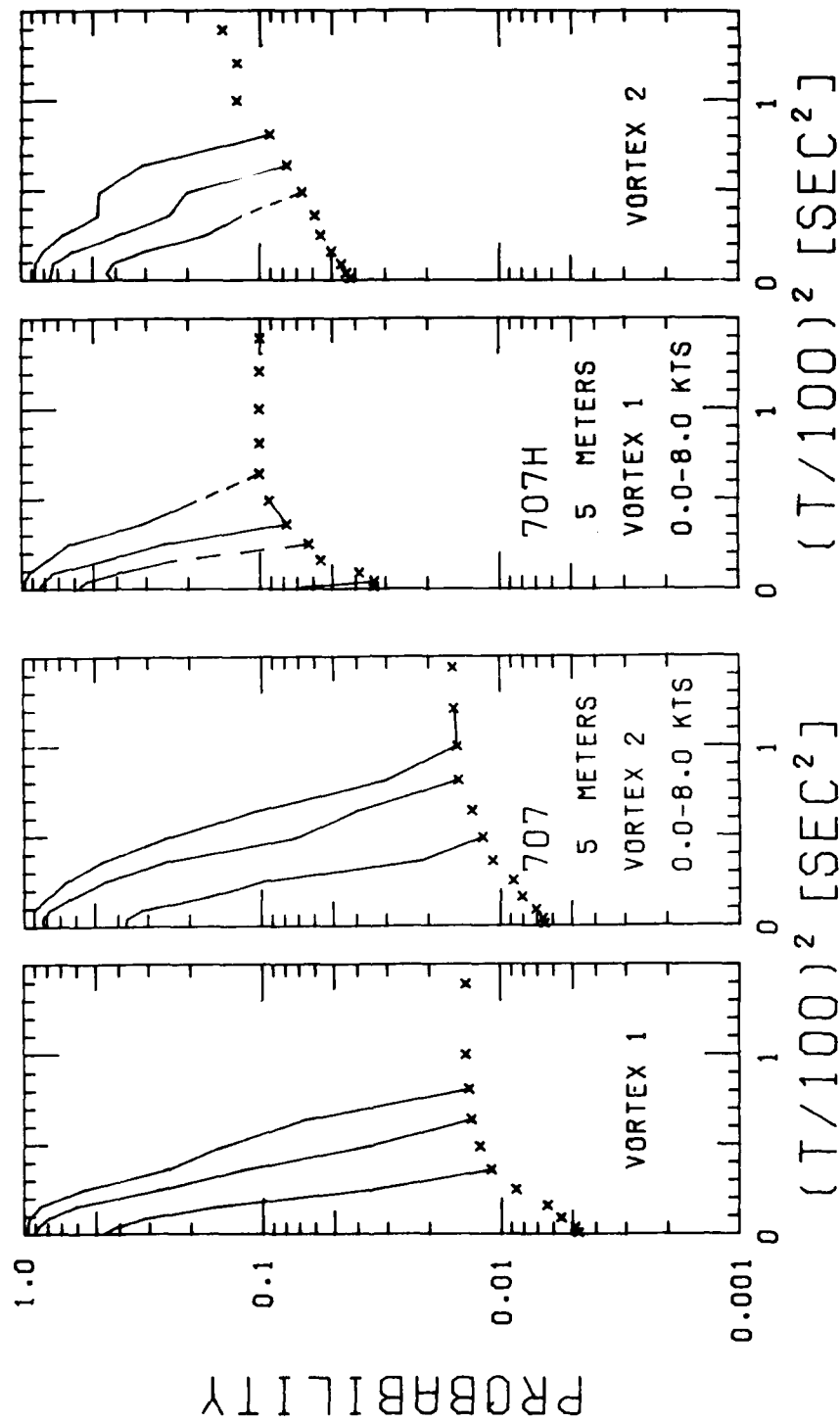


FIGURE 74. PROBABILITY OF DECAY, B-707 AND B-707H, WINDS LESS THAN 8 KNOTS, 5-m AVERAGING RADIUS

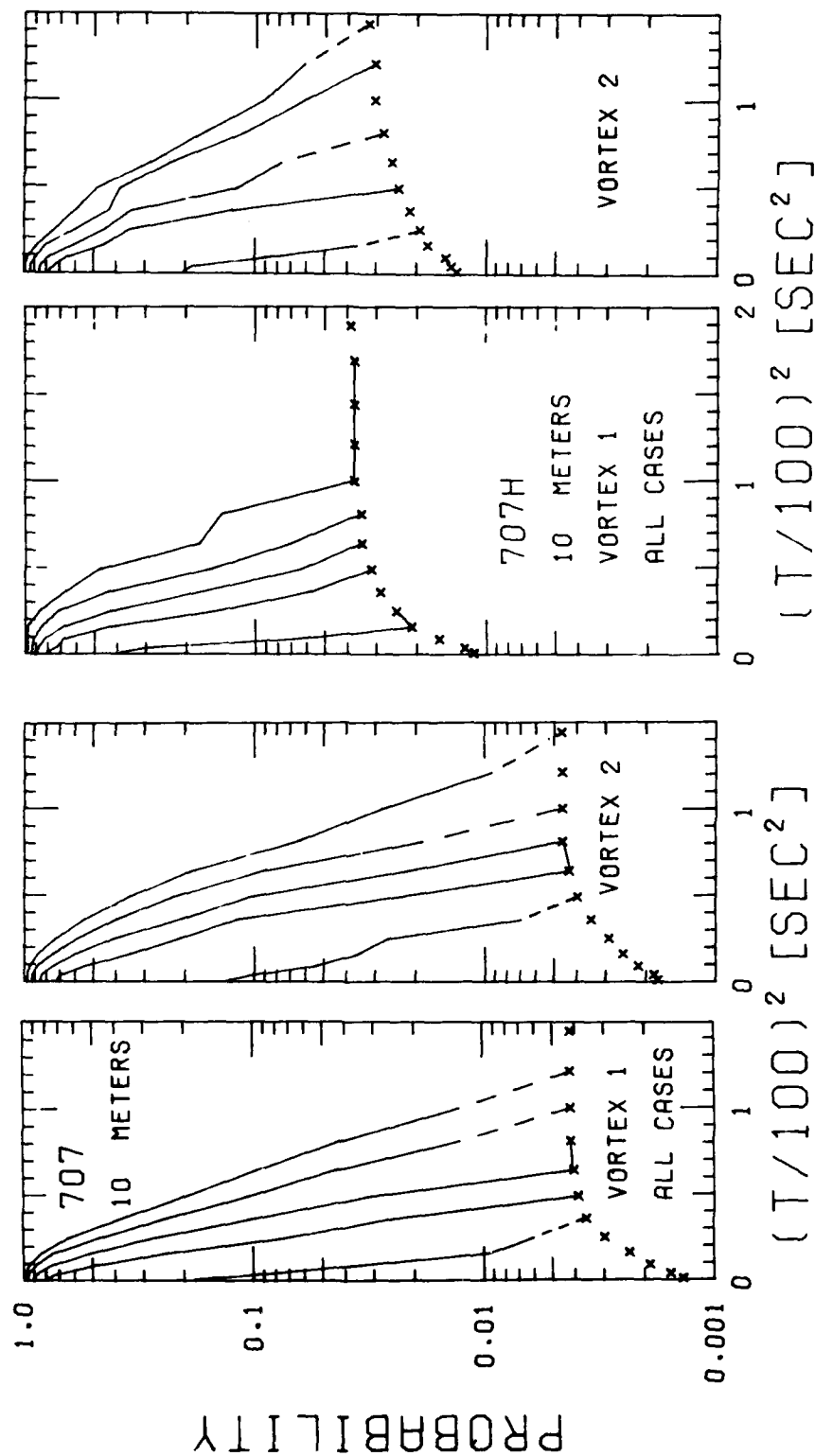


FIGURE 75. PROBABILITY OF DECAY, B-707 AND B-707H, VORTEX 1 AND 2, 10-m AVERAGING RADIUS

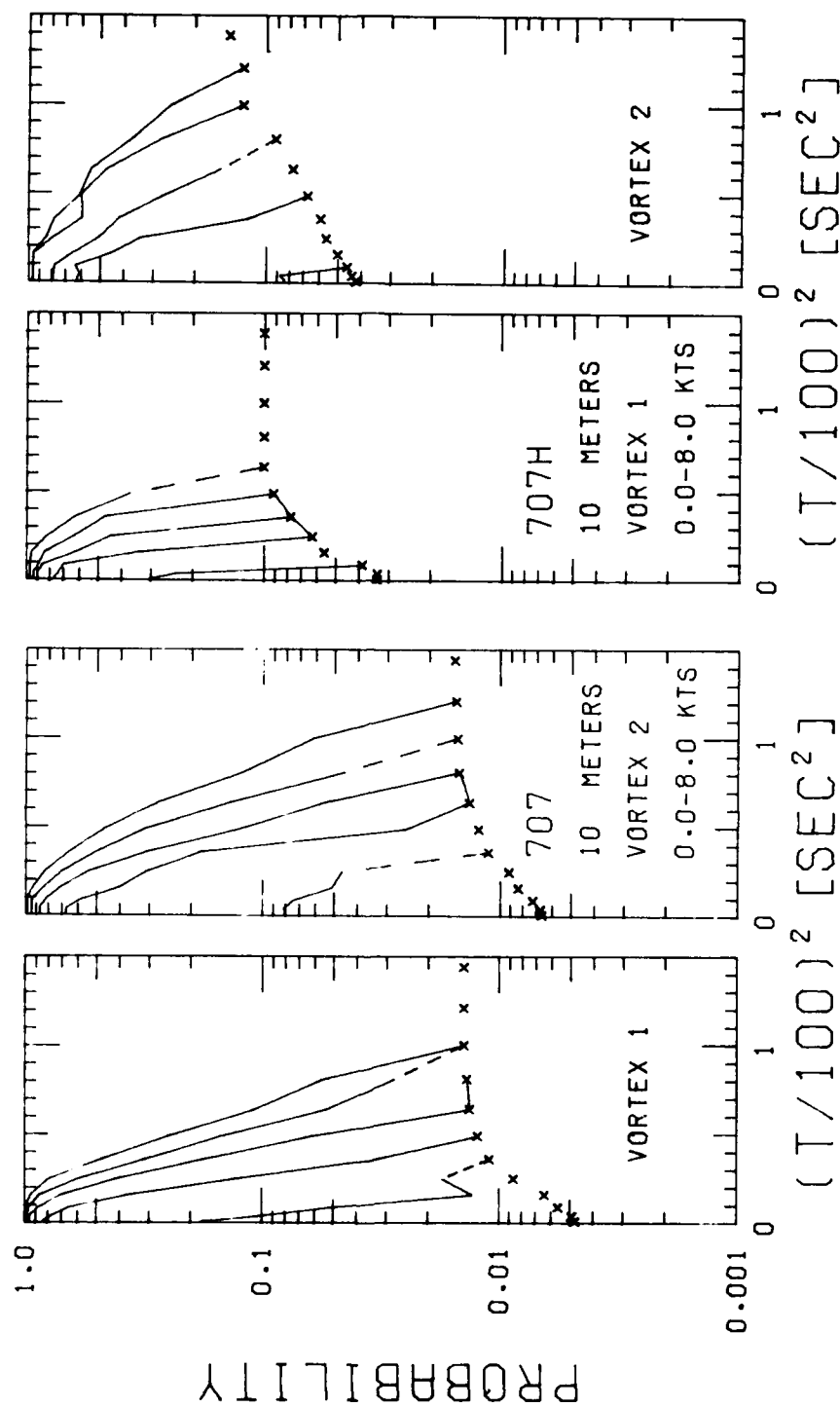


FIGURE 76. PROBABILITY OF DECAY, B-707 AND B-707H, WINDS LESS THAN 8 KNOTS, 10-m AVERAGING RADIUS

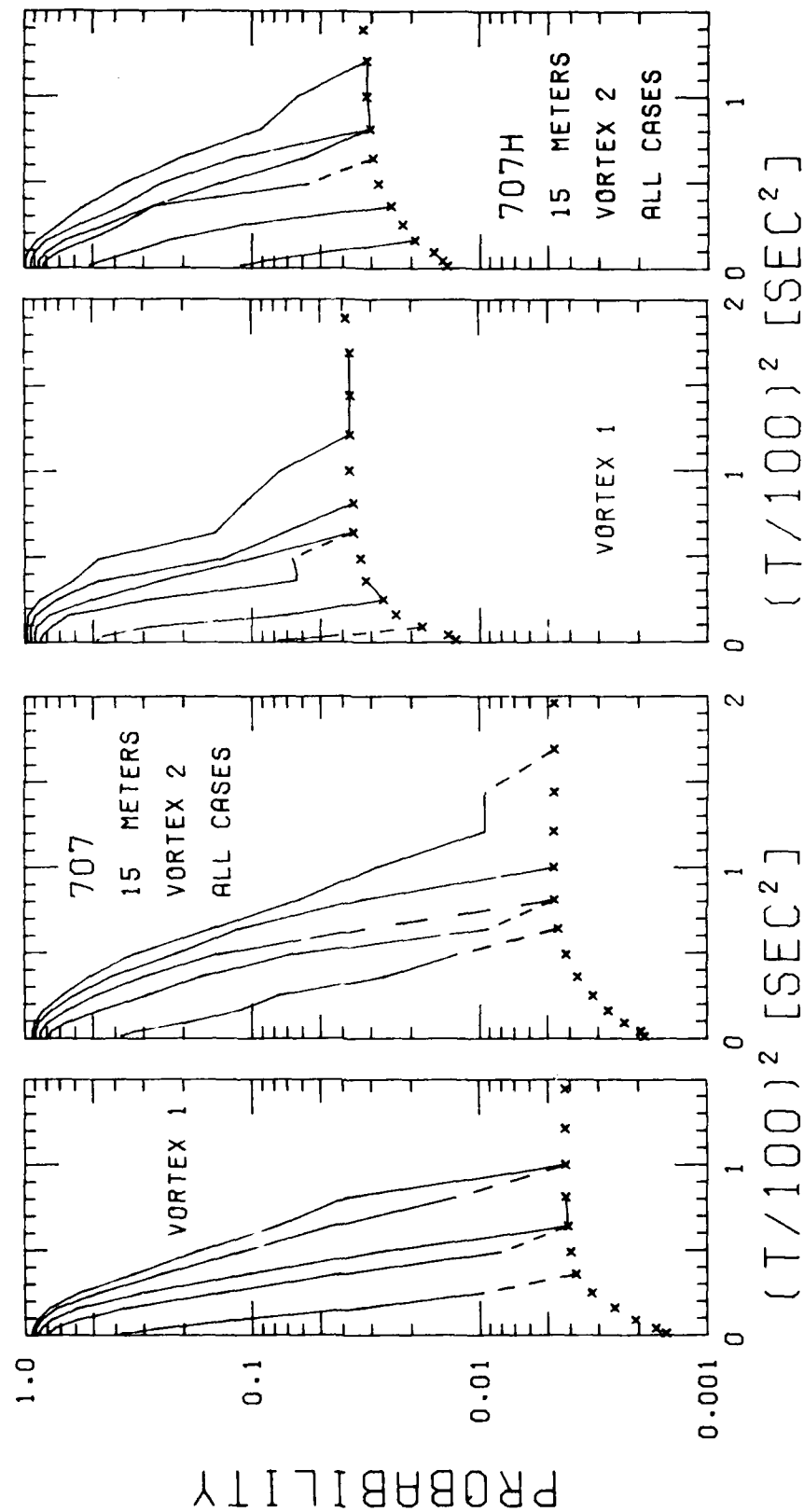


FIGURE 77. PROBABILITY OF DECAY, B-707 AND B-707H, VORTEX 1 AND 2, 15-m AVERAGING RADIUS

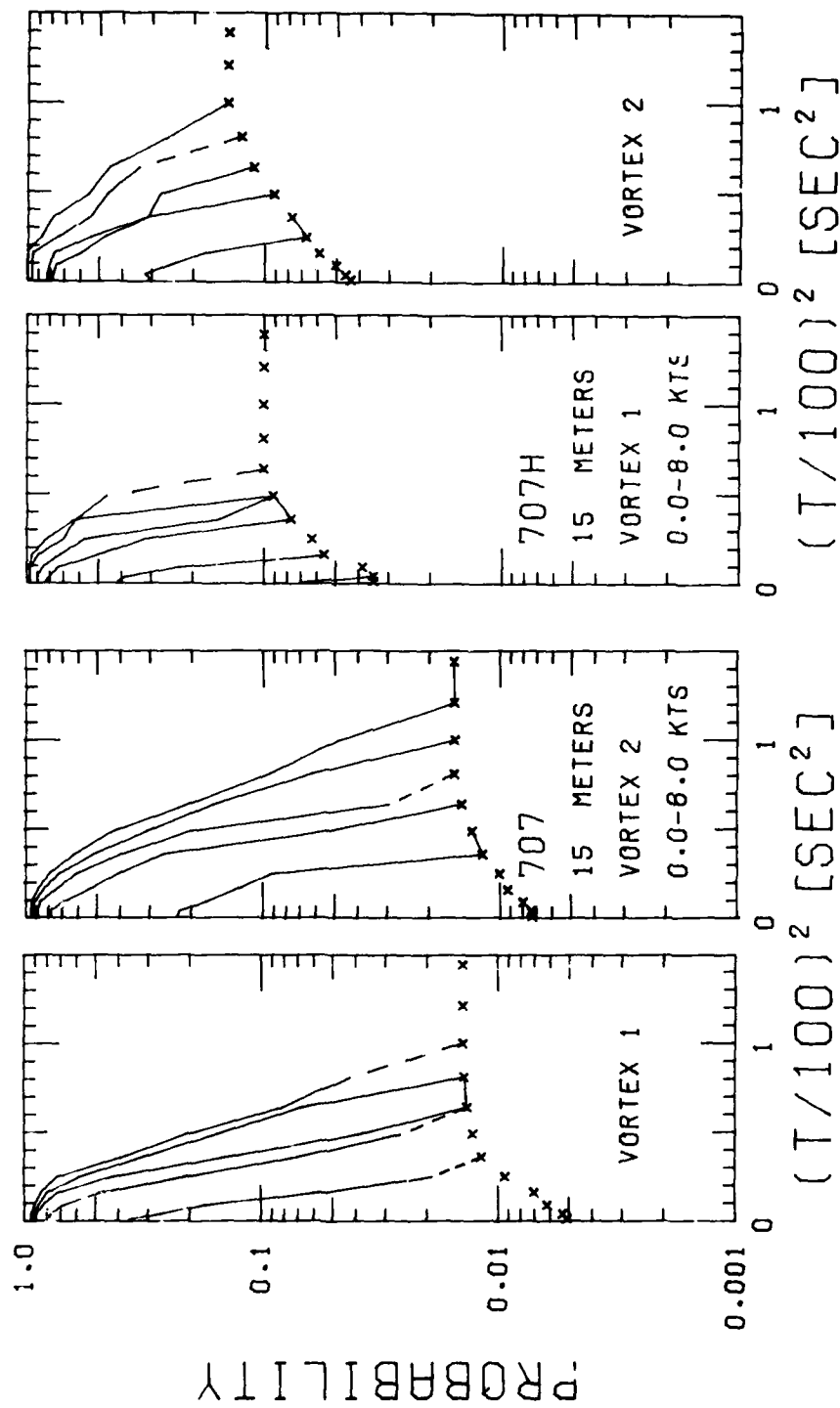


FIGURE 78. PROBABILITY OF DECAY, B-707 AND B-707H, WINDS LESS THAN 8 KNOTS, 15-m AVERAGING RADIUS

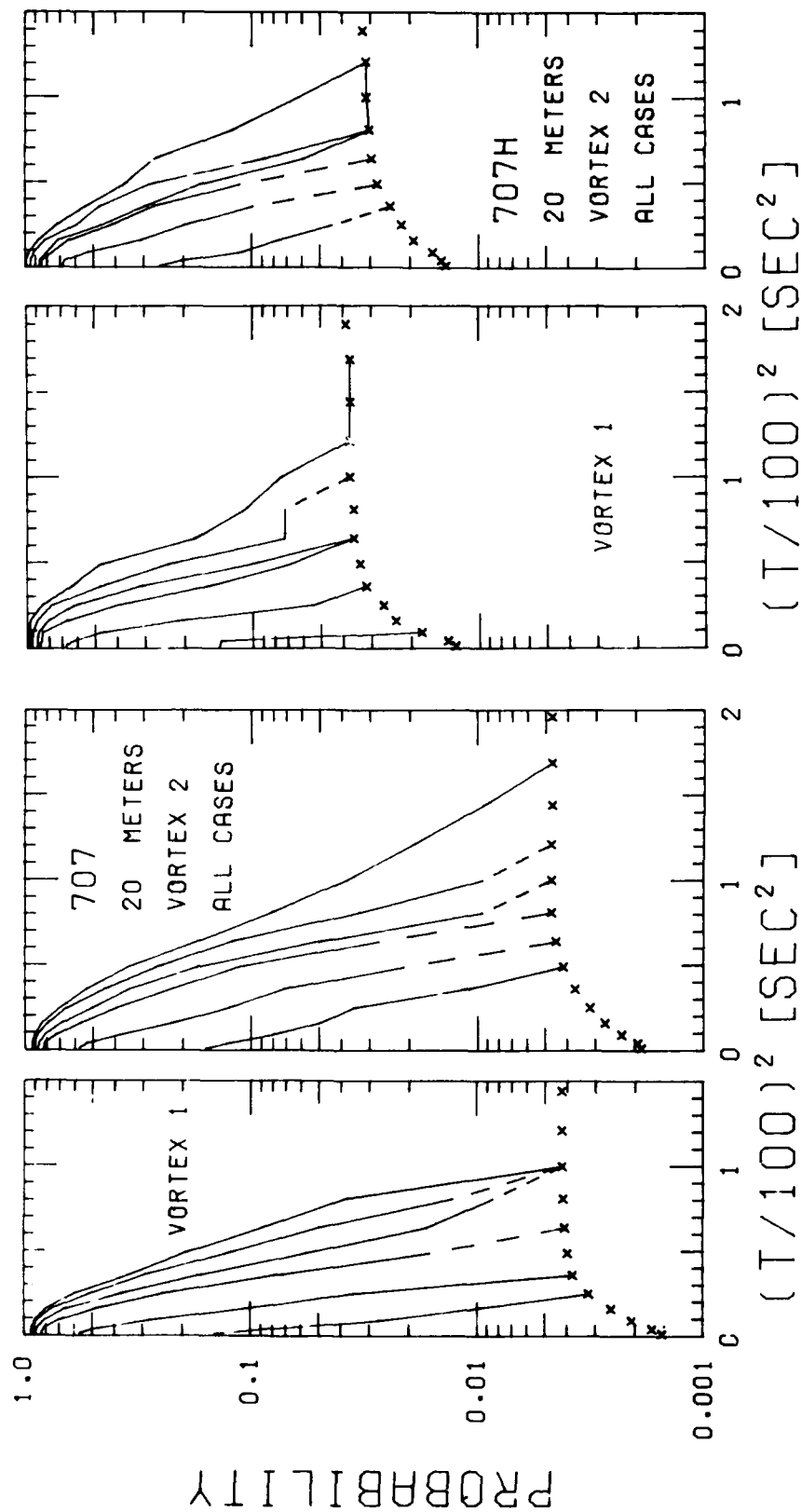


FIGURE 79. PROBABILITY OF DECAY, B-707 AND B-707H, VORTEX 1 AND 2, 20-m AVERAGING RADIUS

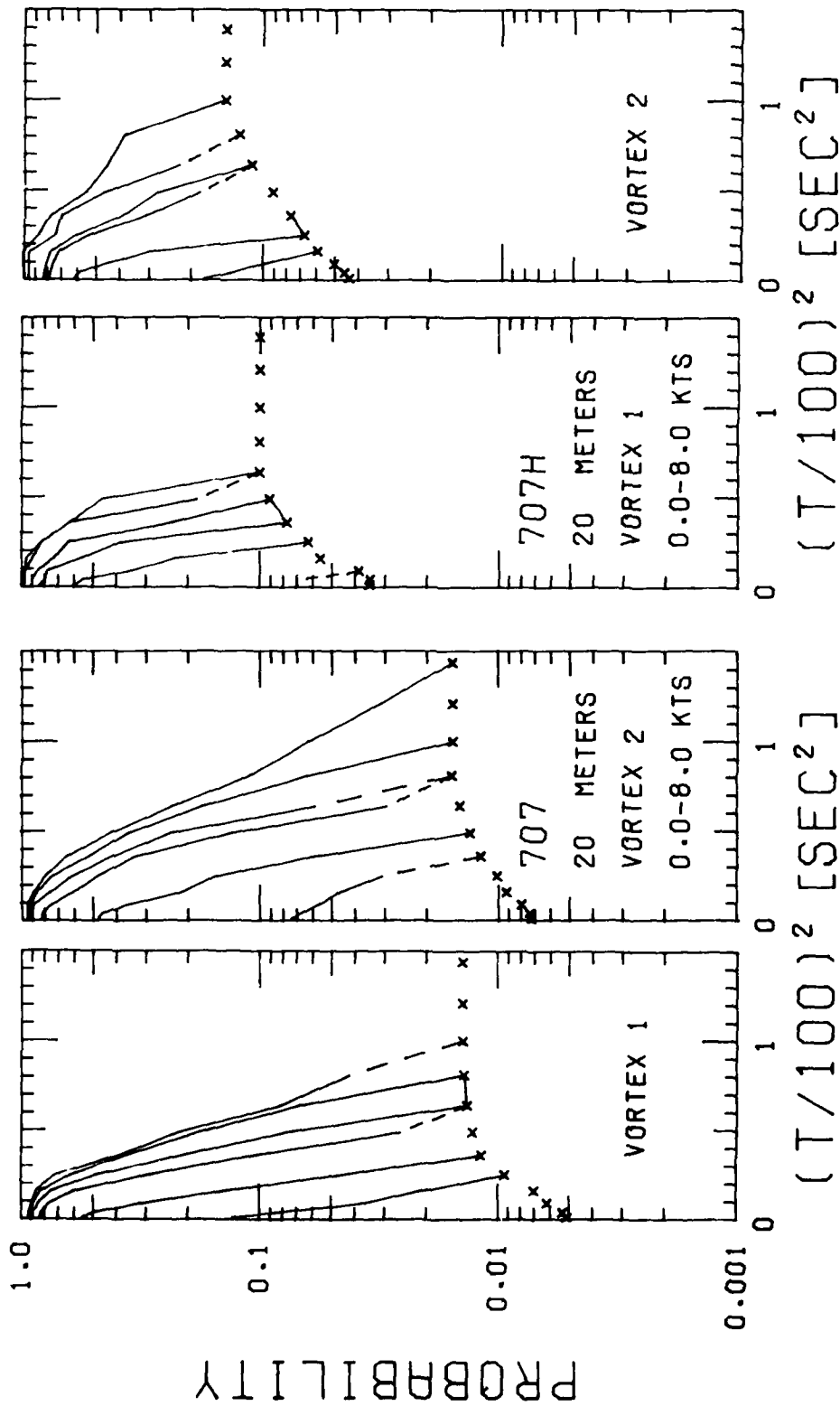


FIGURE 80. PROBABILITY OF DECAY, B-707 AND B-707H, WINDS LESS THAN 8 KNOTS, 20-m AVERAGING RADIUS

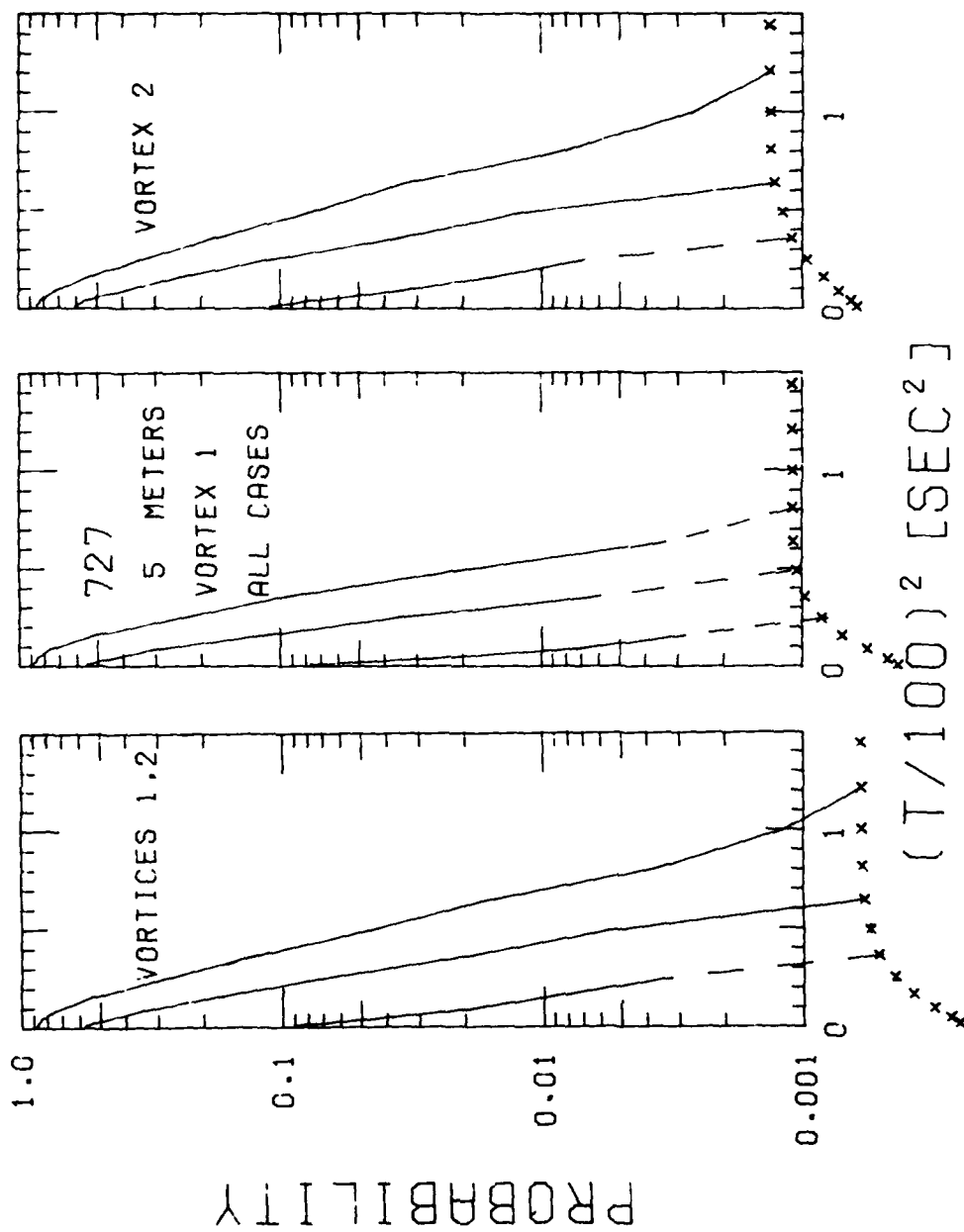


FIGURE 81. PROBABILITY OF DECAY, B-727, VORTEX 1 AND 2, 5-m AVERAGING RADIUS

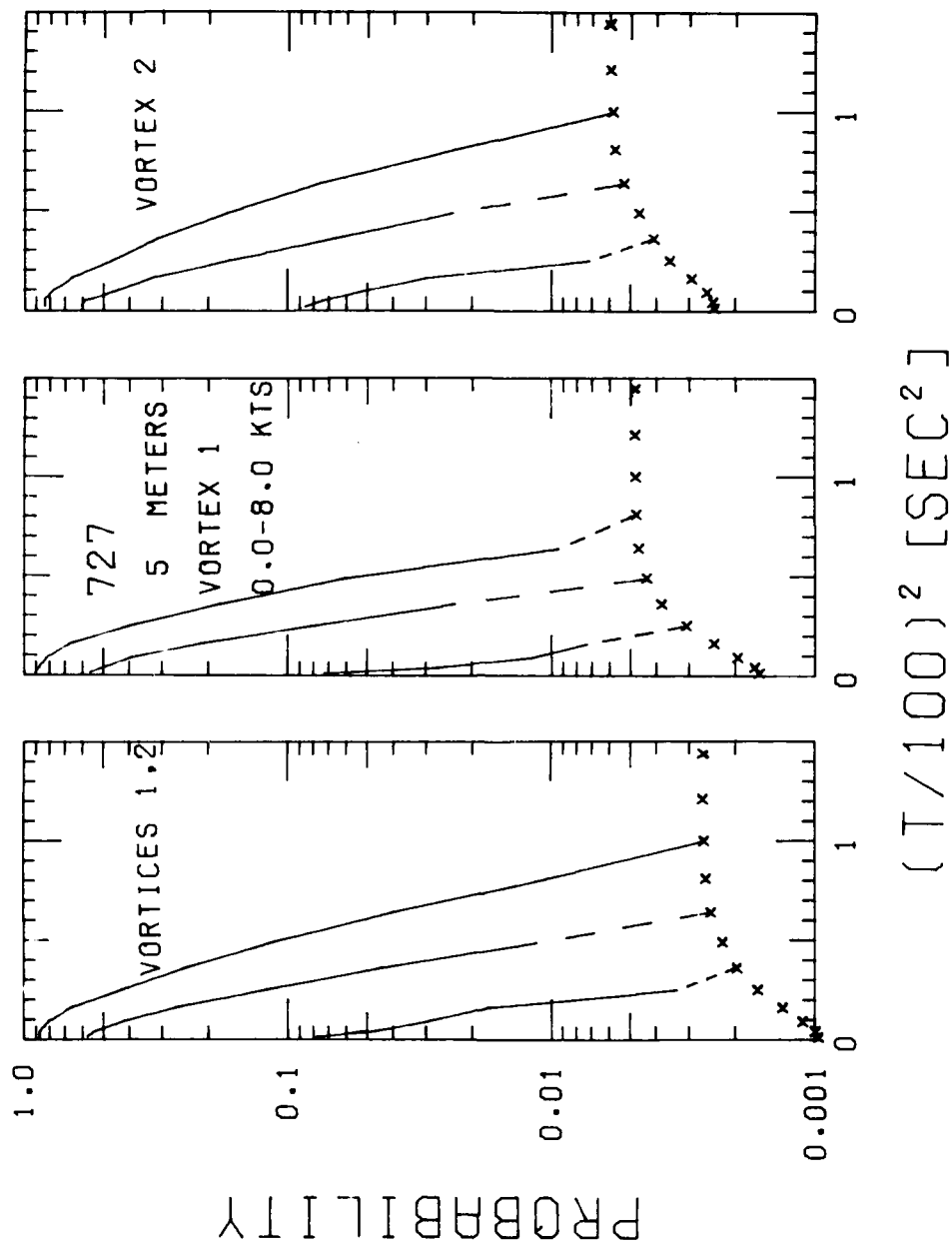


FIGURE 82. PROBABILITY OF DECAY, B-727, WINDS LESS THAN 8 KNOTS, 5-m AVERAGING RADIUS

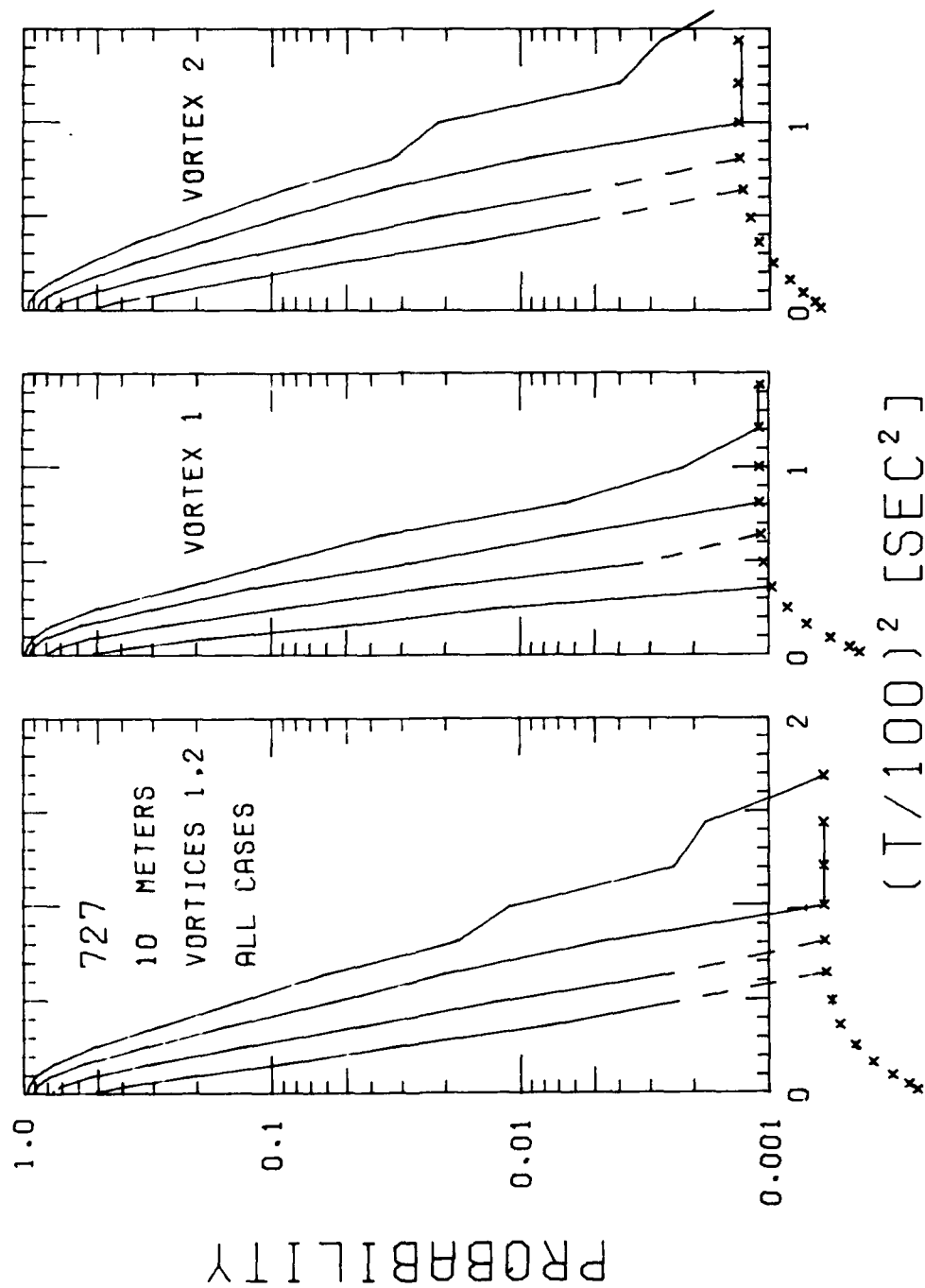


FIGURE 83. PROBABILITY OF DECAY, B-727, VORTEX 1 AND 2, 10-m AVERAGING RADIUS

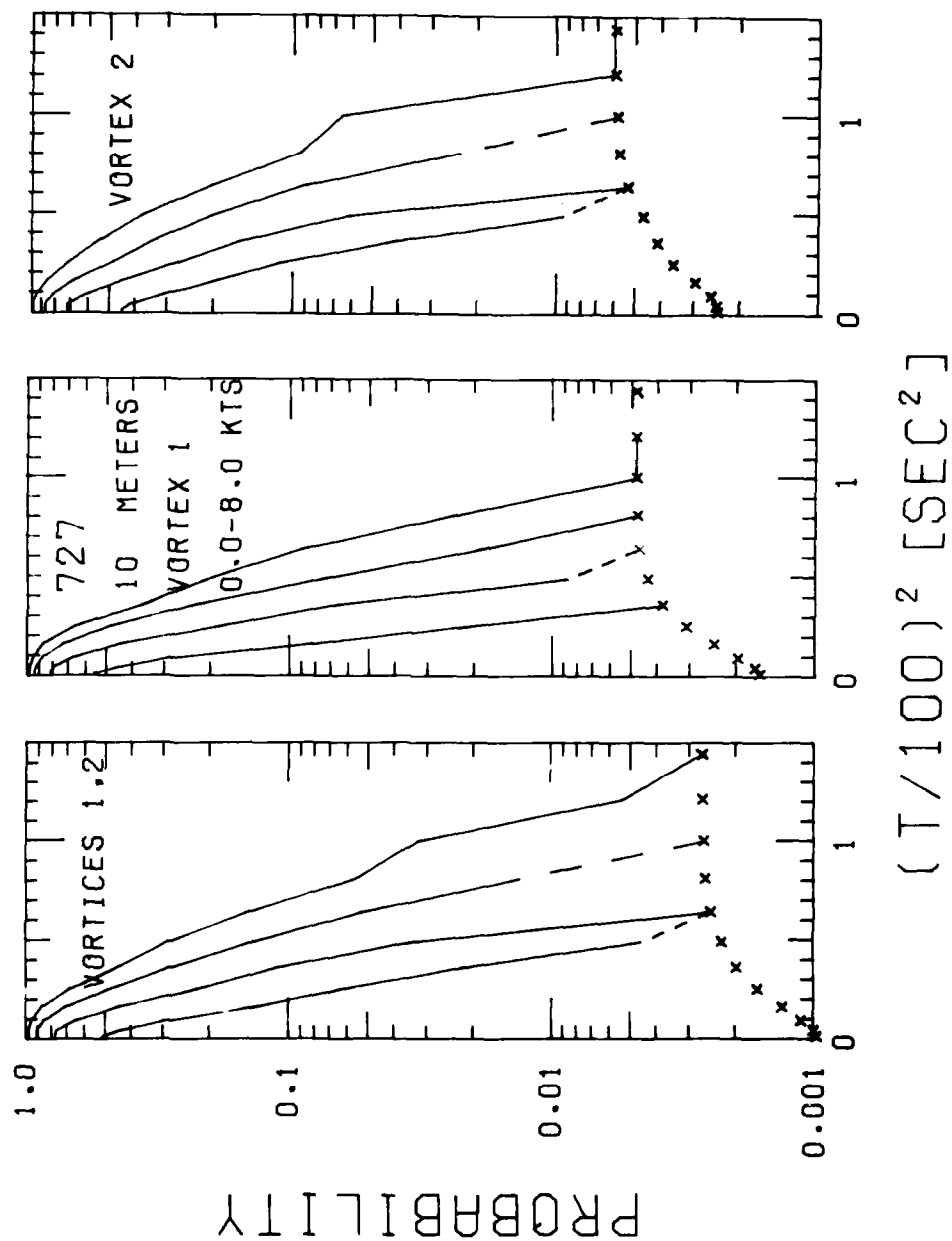


FIGURE 84. PROBABILITY OF DECAY, B-727, WINDS LESS THAN 8 KNOTS, 10-m AVERAGING RADIUS

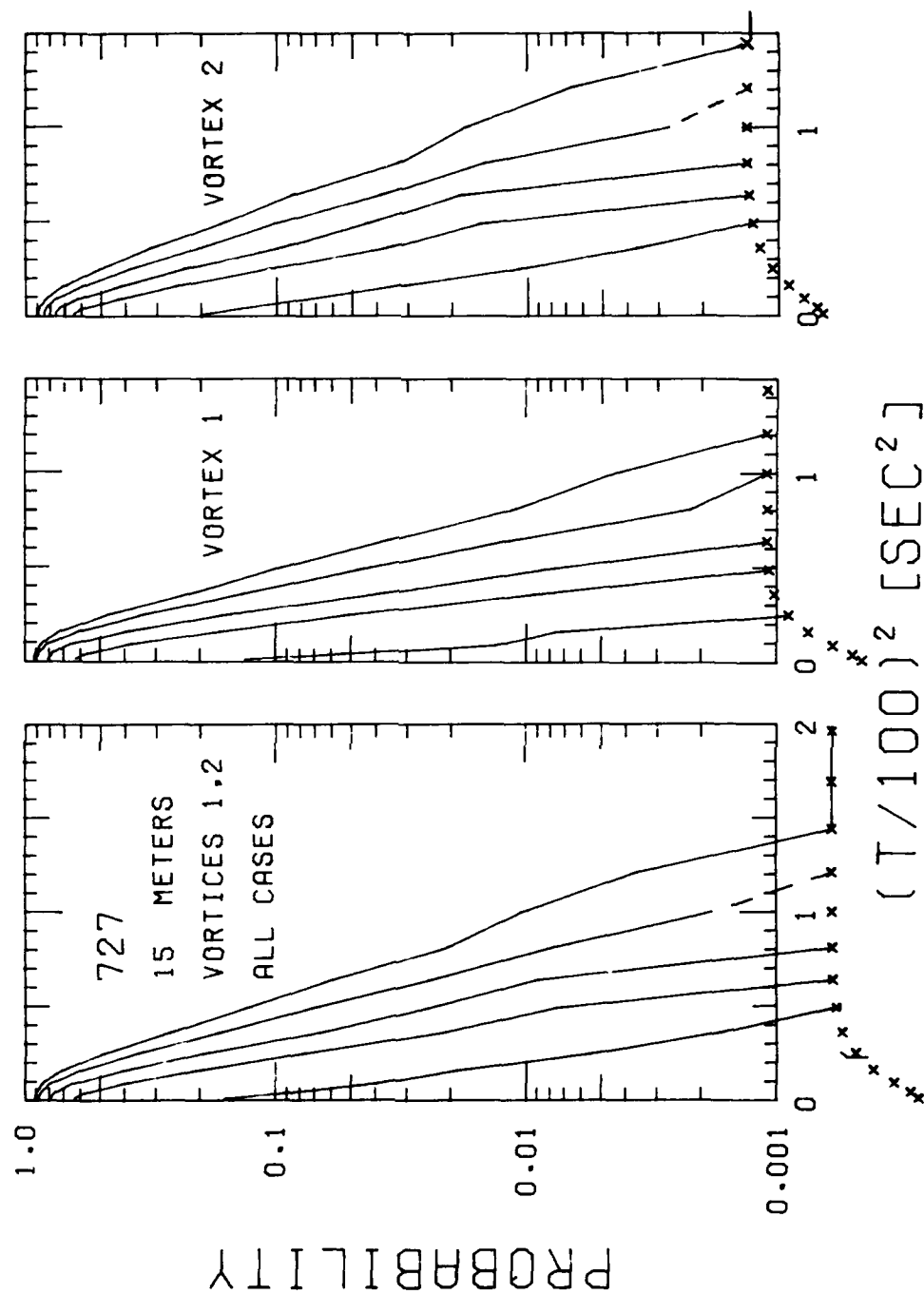


FIGURE 85. PROBABILITY OF DECAY, B-727, VORTEX 1 AND 2, 15-m AVERAGING RADIUS

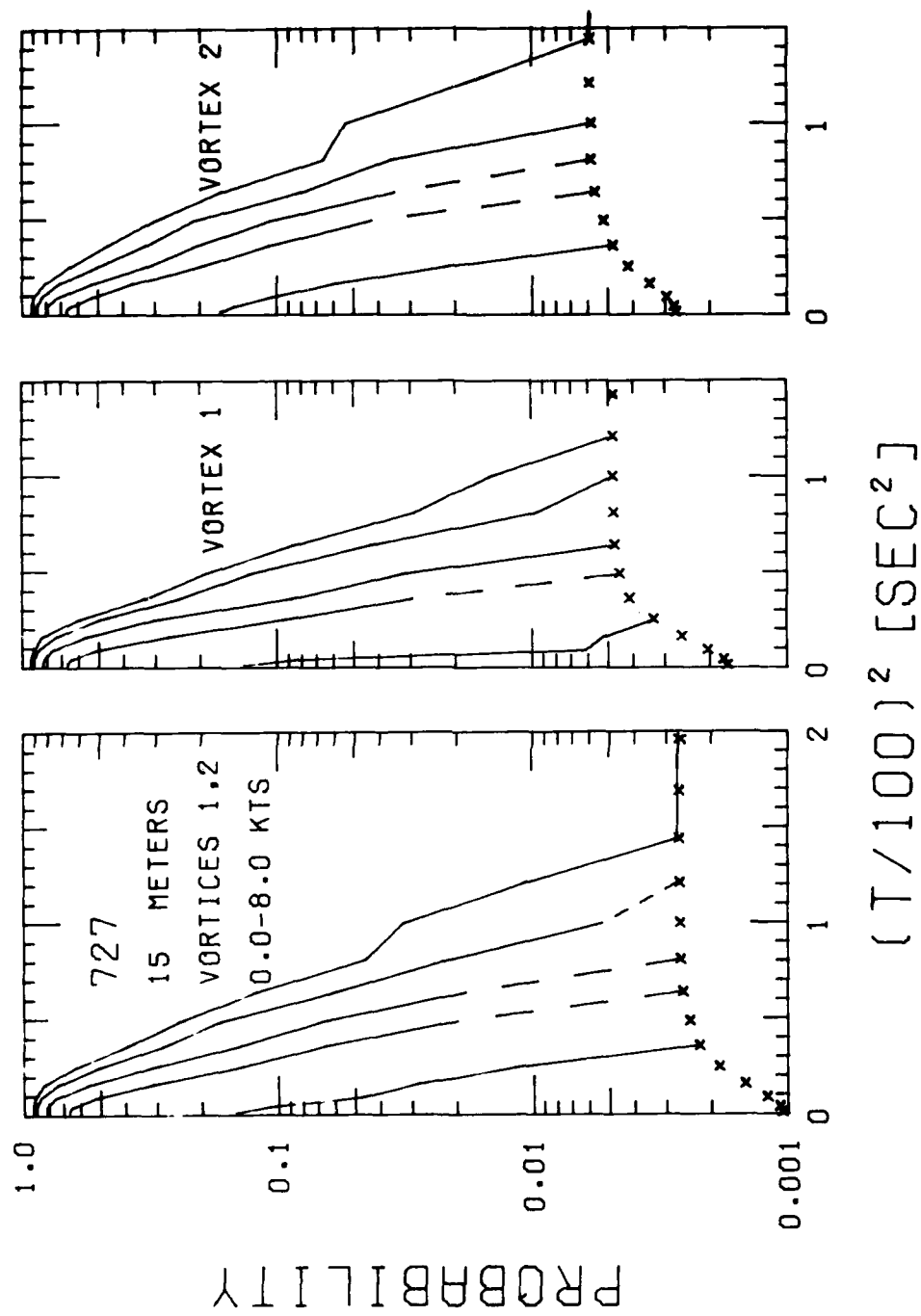


FIGURE 86. PROBABILITY OF DECAY, B-727, WINDS LESS THAN 8 KNOTS, 15-m AVERAGING RADIUS

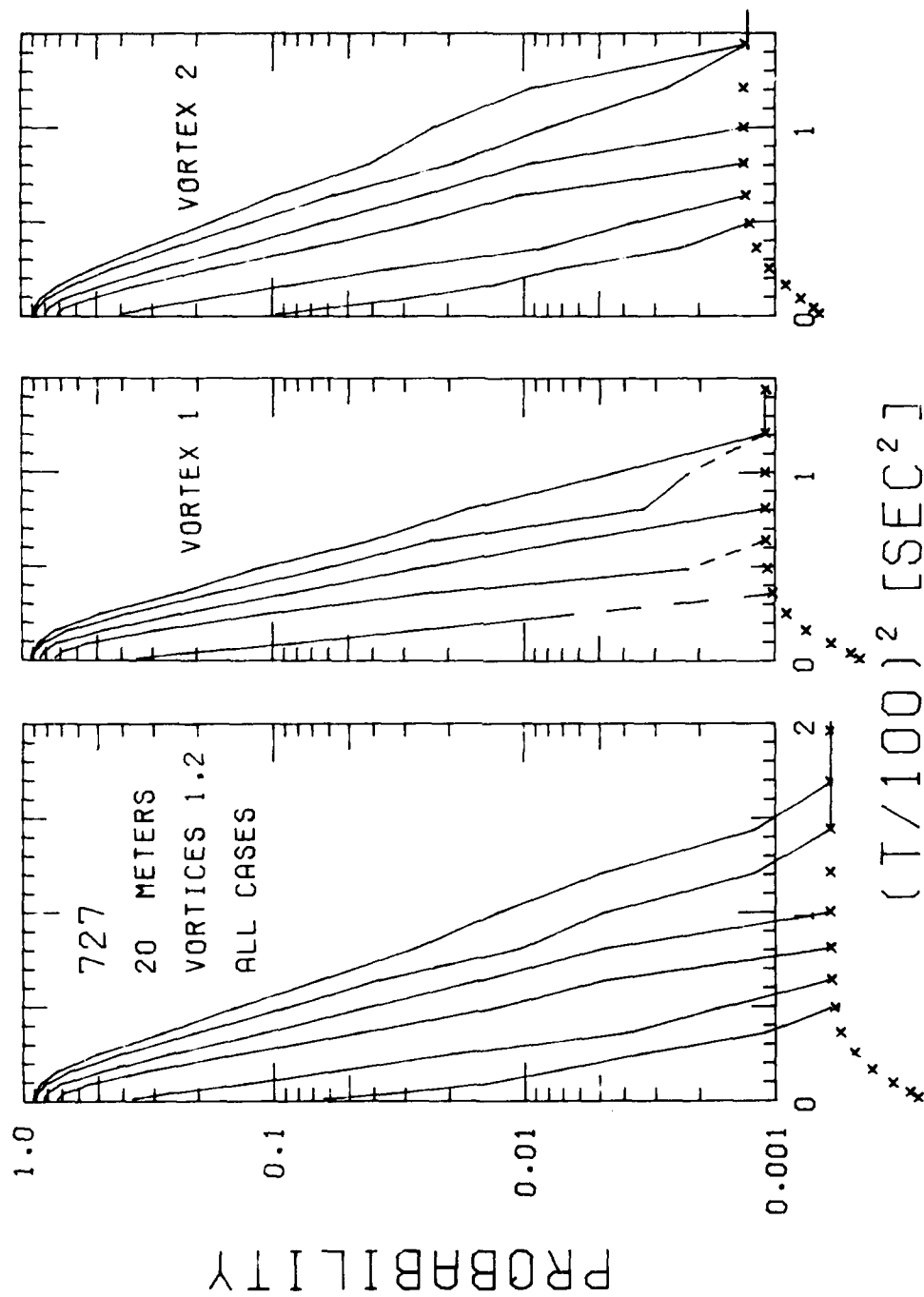


FIGURE 87. PROBABILITY OF DECAY, B-727, VORTEX 1 AND 2, 20-m AVERAGING RADIUS

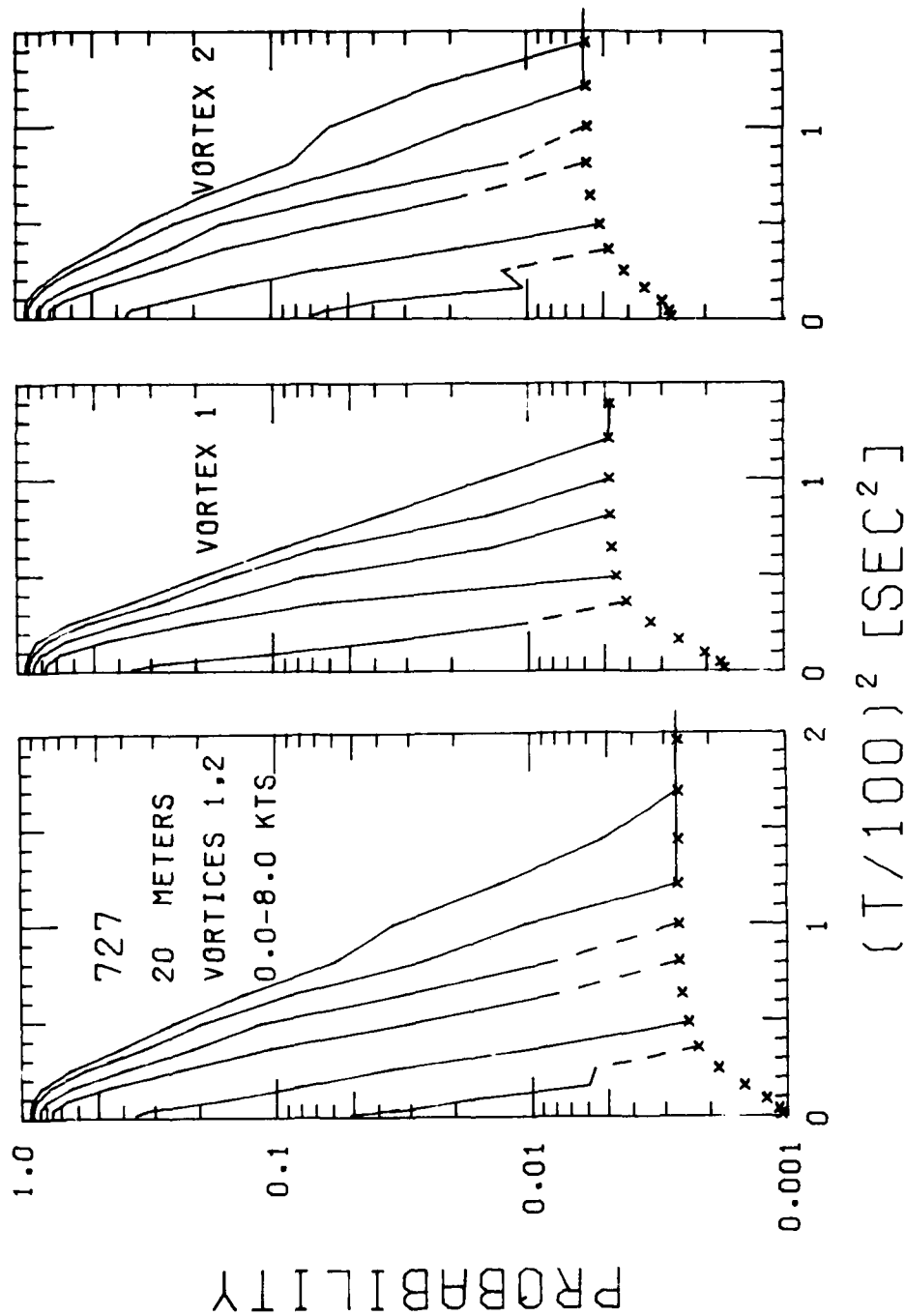


FIGURE 88. PROBABILITY OF DECAY, B-727, WINDS LESS THAN 8 KNOTS, 20-m AVERAGING RADIUS

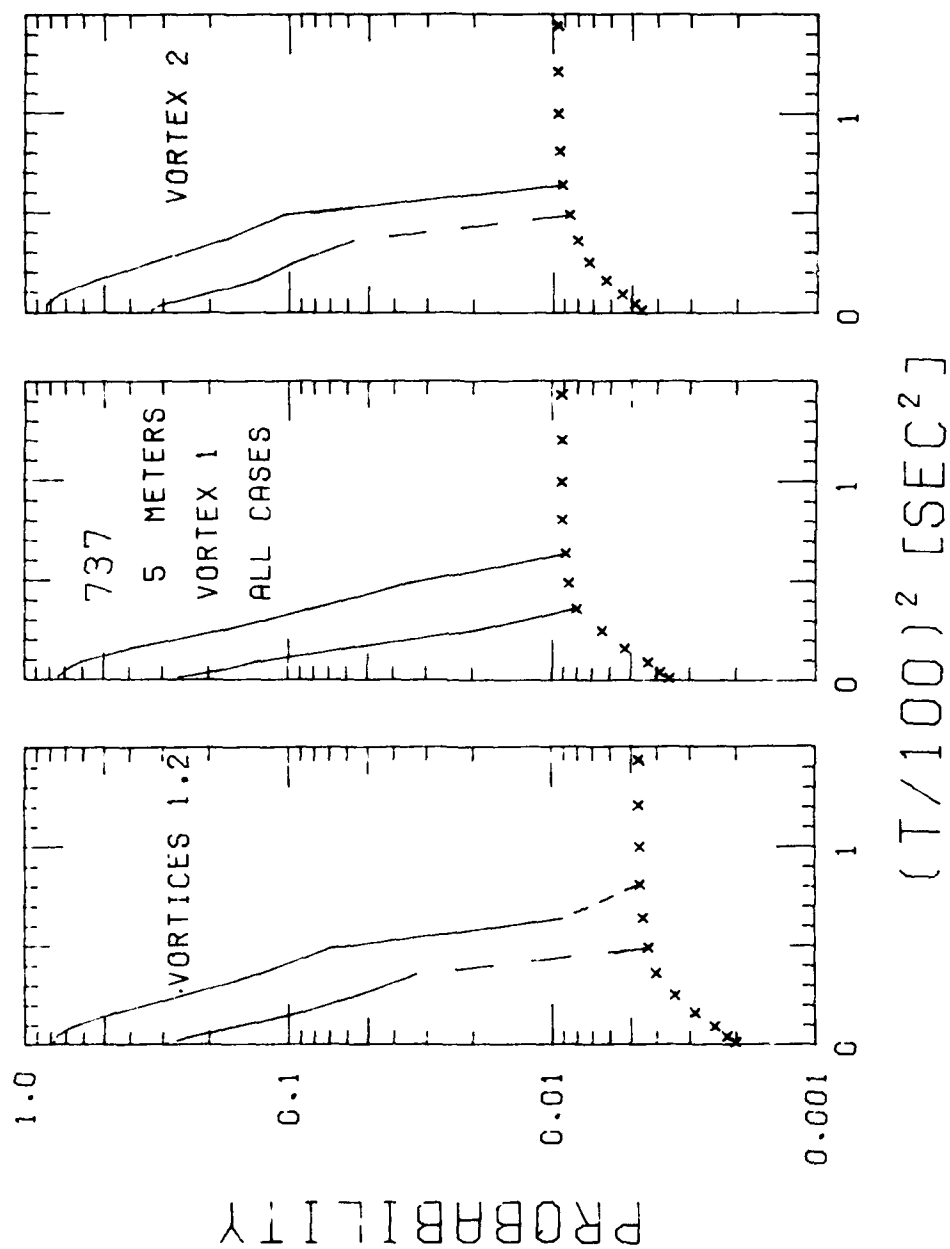


FIGURE 89. PROBABILITY OF DECAY, B-737, VORTEX 1 AND 2, 5-m AVERAGING RADIUS

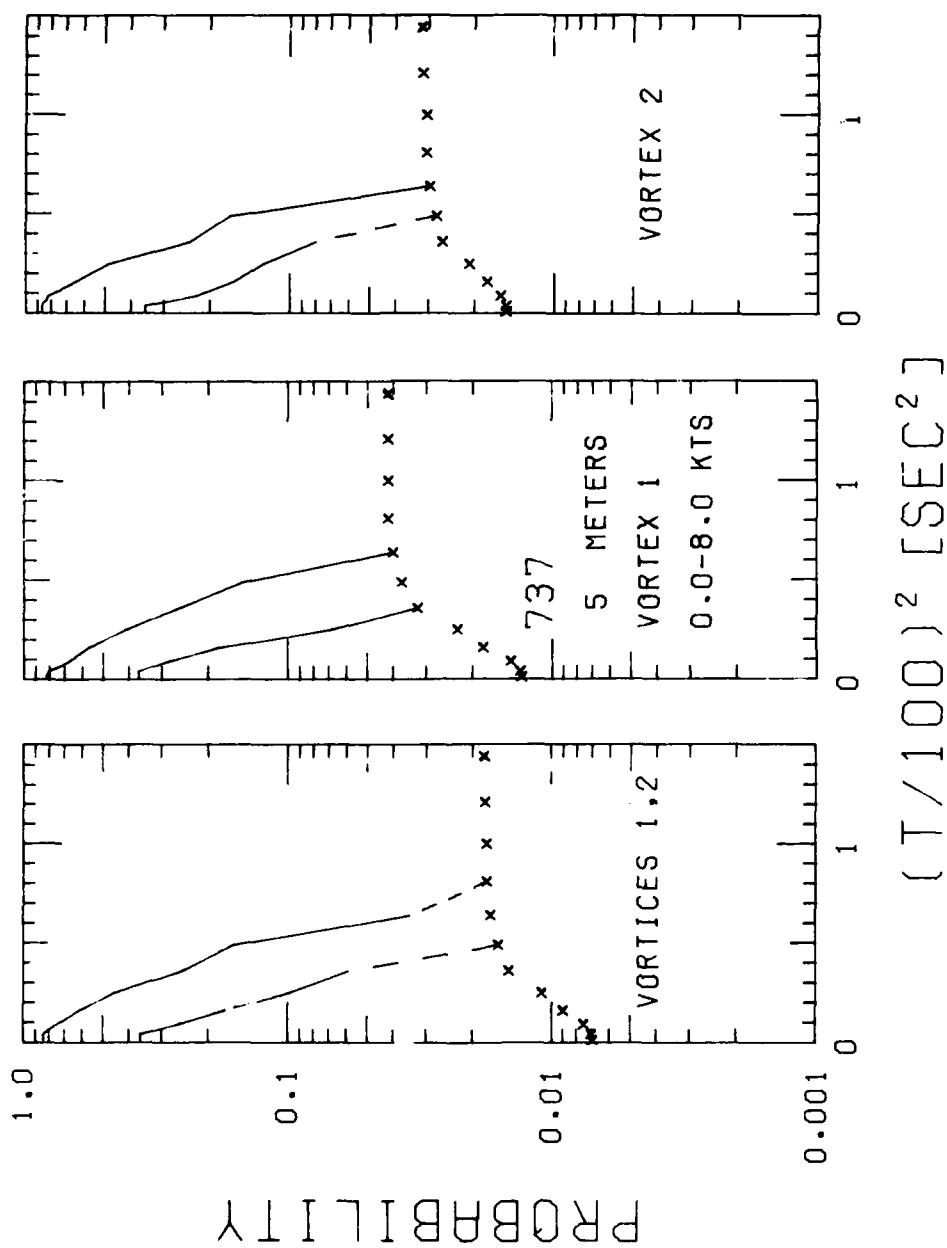


FIGURE 90. PROBABILITY OF DECAY, B-737, WINDS LESS THAN 8 KNOTS, 5-m AVERAGING RADIUS

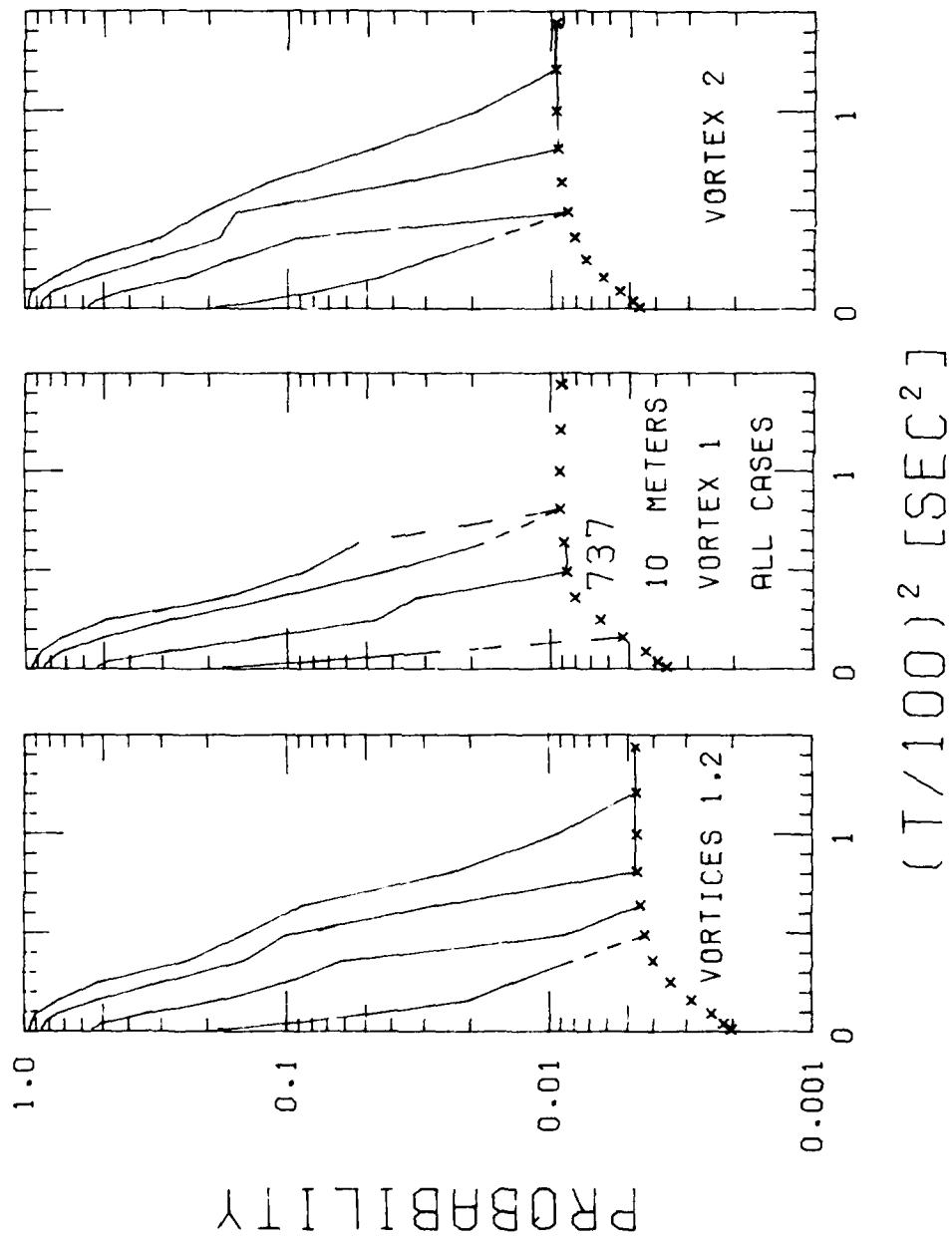


FIGURE 91. PROBABILITY OF DECAY, B-737, VORTEX 1 AND 2, 10-m AVERAGING RADIUS

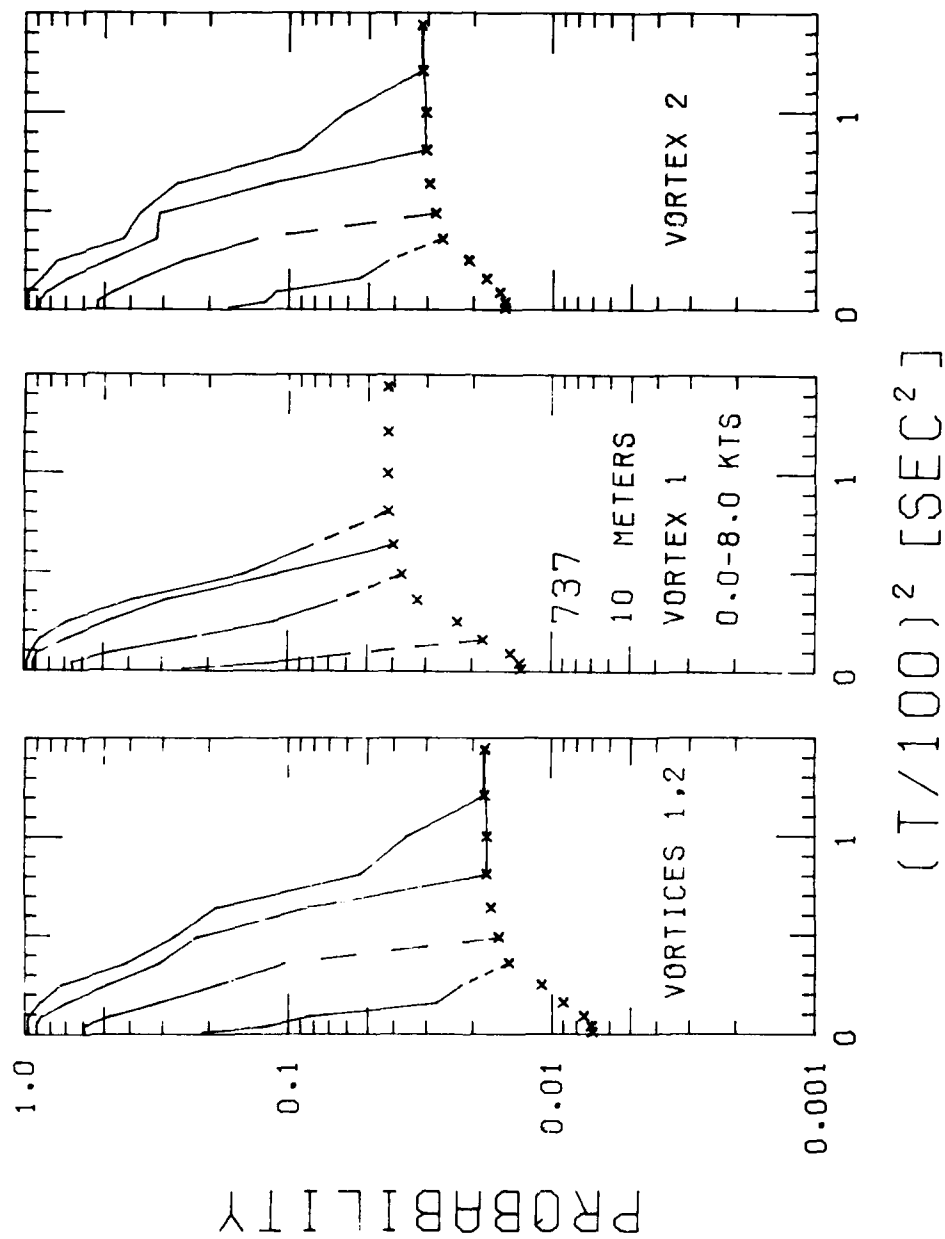


FIGURE 92. PROBABILITY OF DECAY, B-737, WINDS LESS THAN 8 KNOTS, 10-m AVERAGING RADIUS

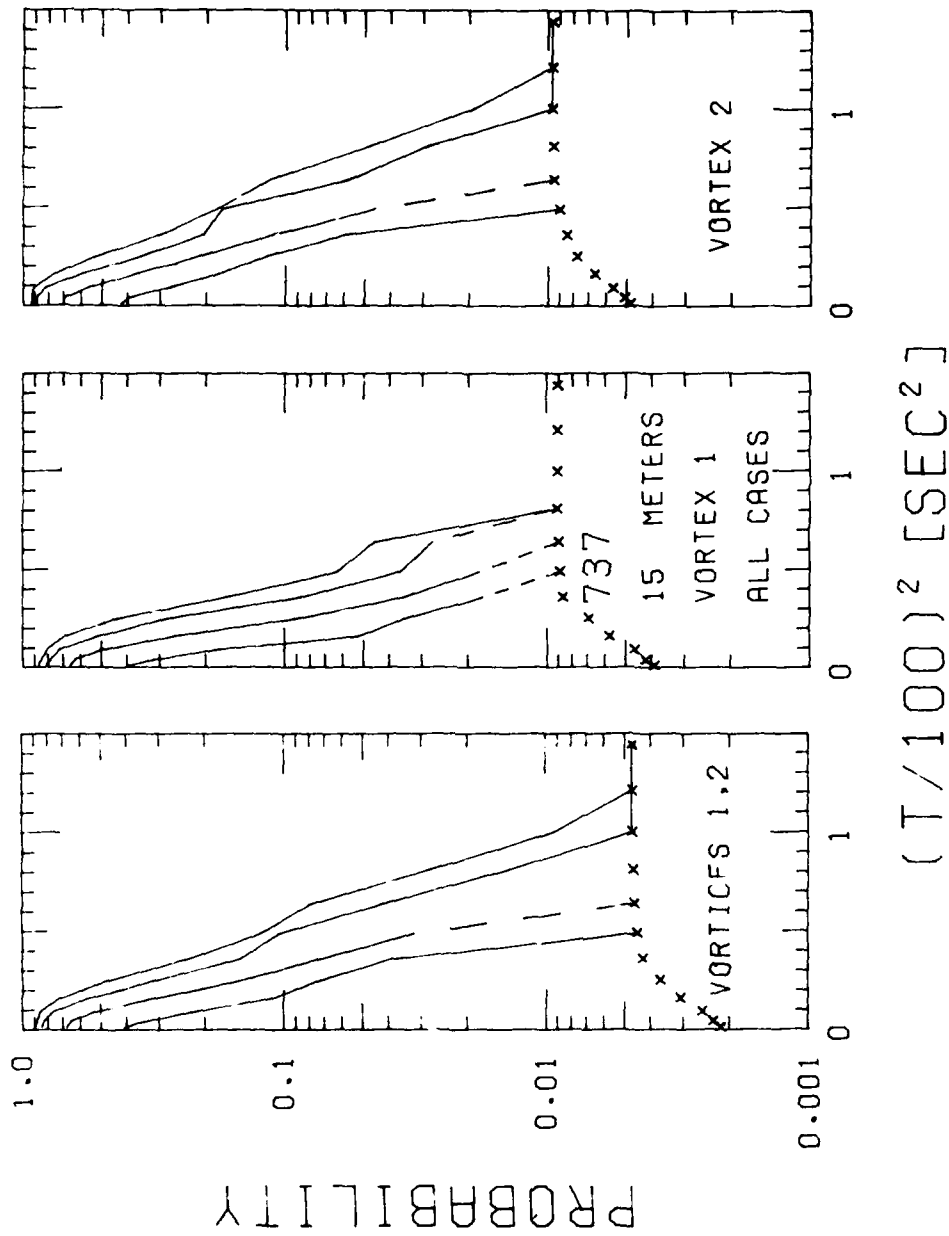


FIGURE 93. PROBABILITY OF DECAY, B-737, VORTEX 1 AND 2, 15-m AVERAGING RADIUS

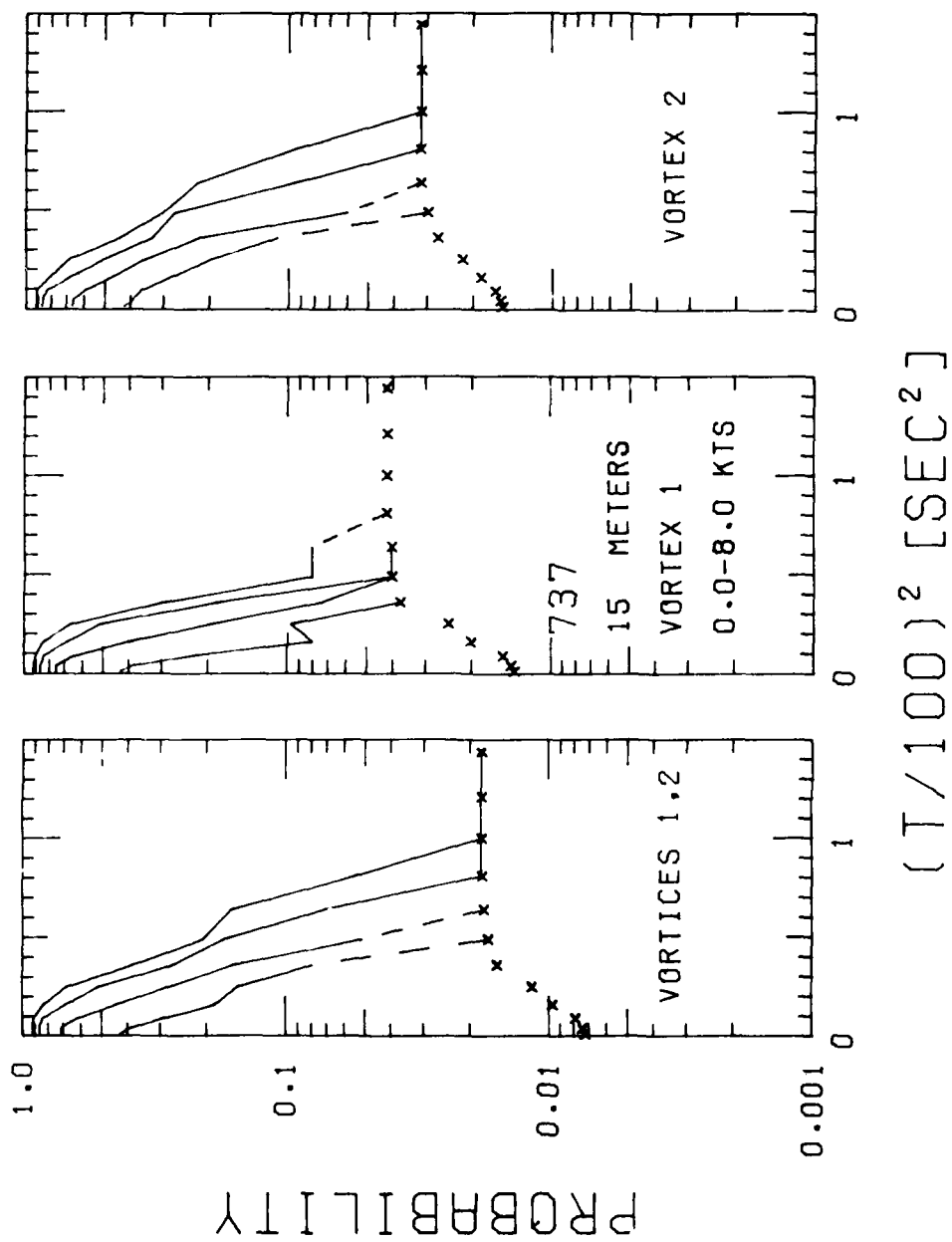


FIGURE 94. PROBABILITY OF DECAY, B-737, WINDS LESS THAN 8 KNOTS, 15-m AVERAGING RADIUS

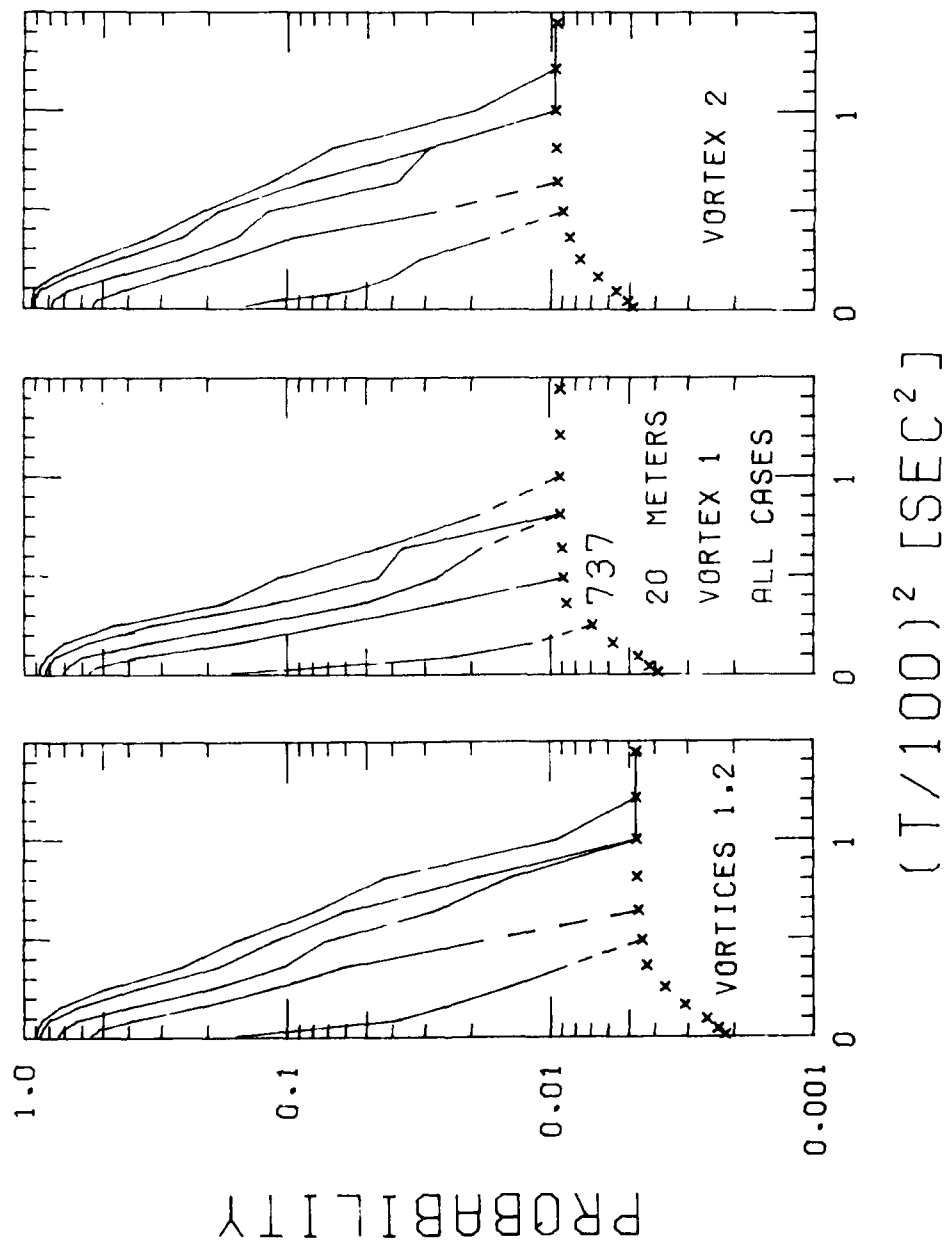


FIGURE 95. PROBABILITY OF DECAY, B-737, VORTEX 1 AND 2, 20-m AVERAGING RADIUS

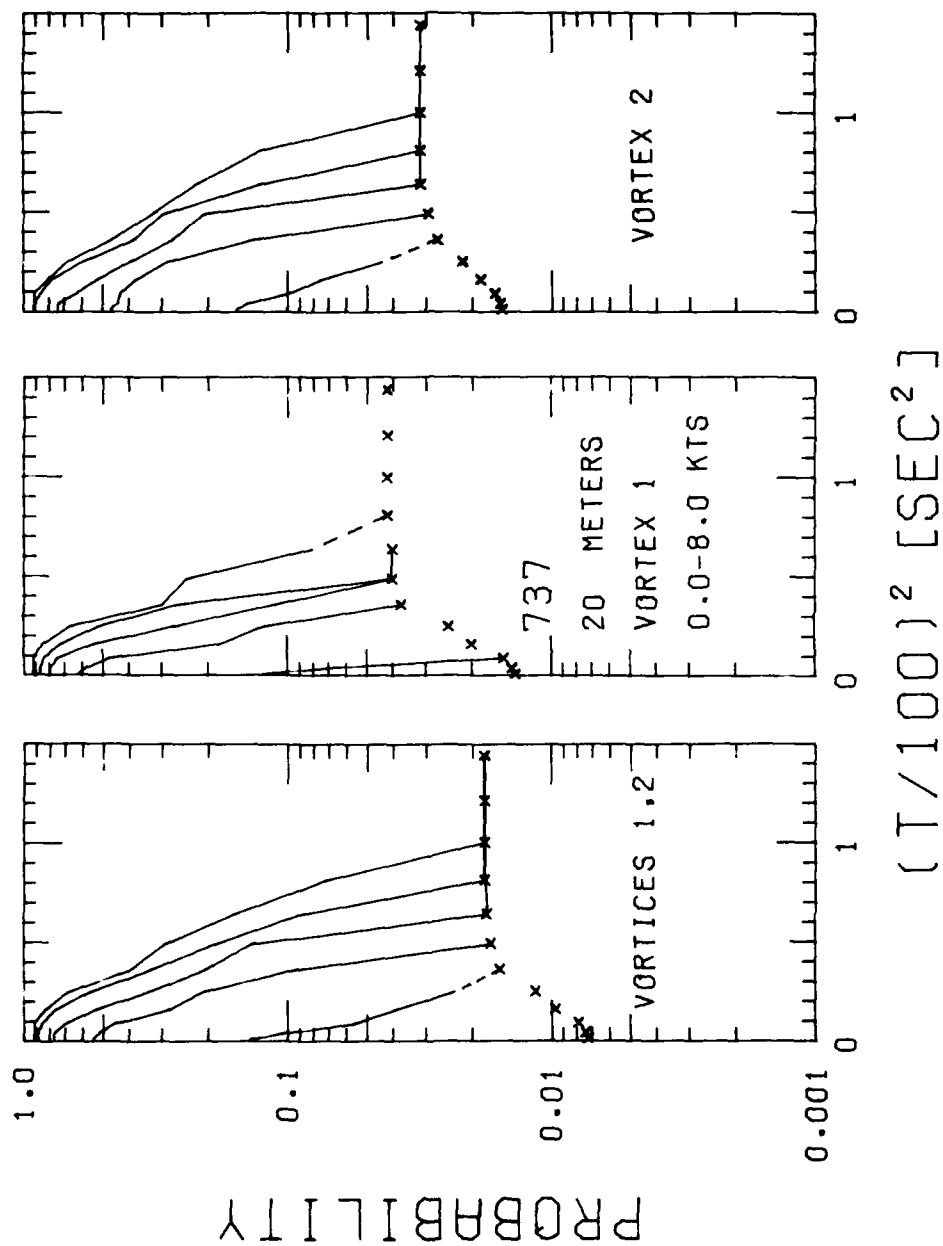


FIGURE 96. PROBABILITY OF DECAY, B-737, WINDS LESS THAN 8 KNOTS, 20-m AVERAGING RADIUS

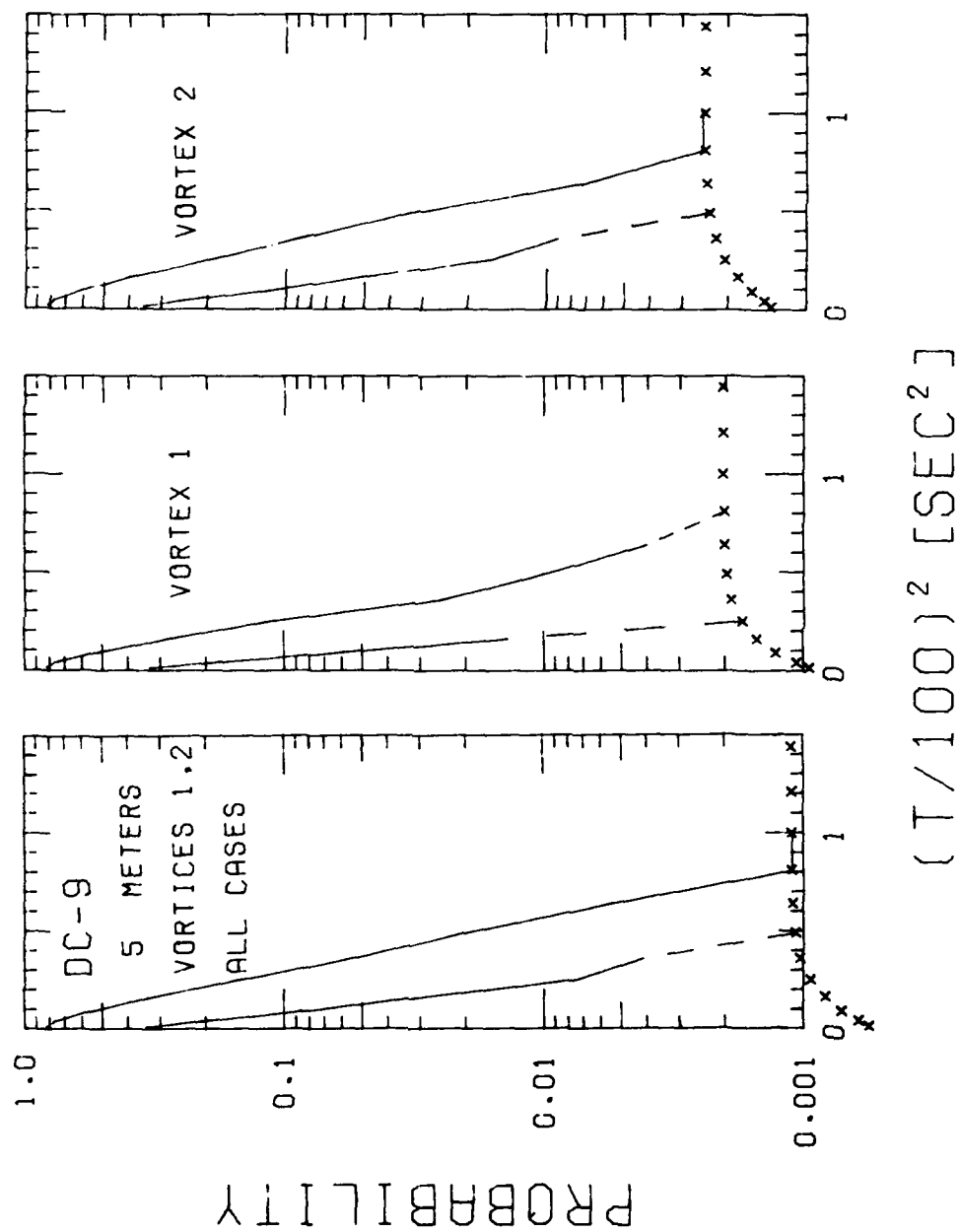


FIGURE 97. PROBABILITY OF DECAY, DC-9, VORTEX 1 AND 2, 5-m AVERAGING RADIUS

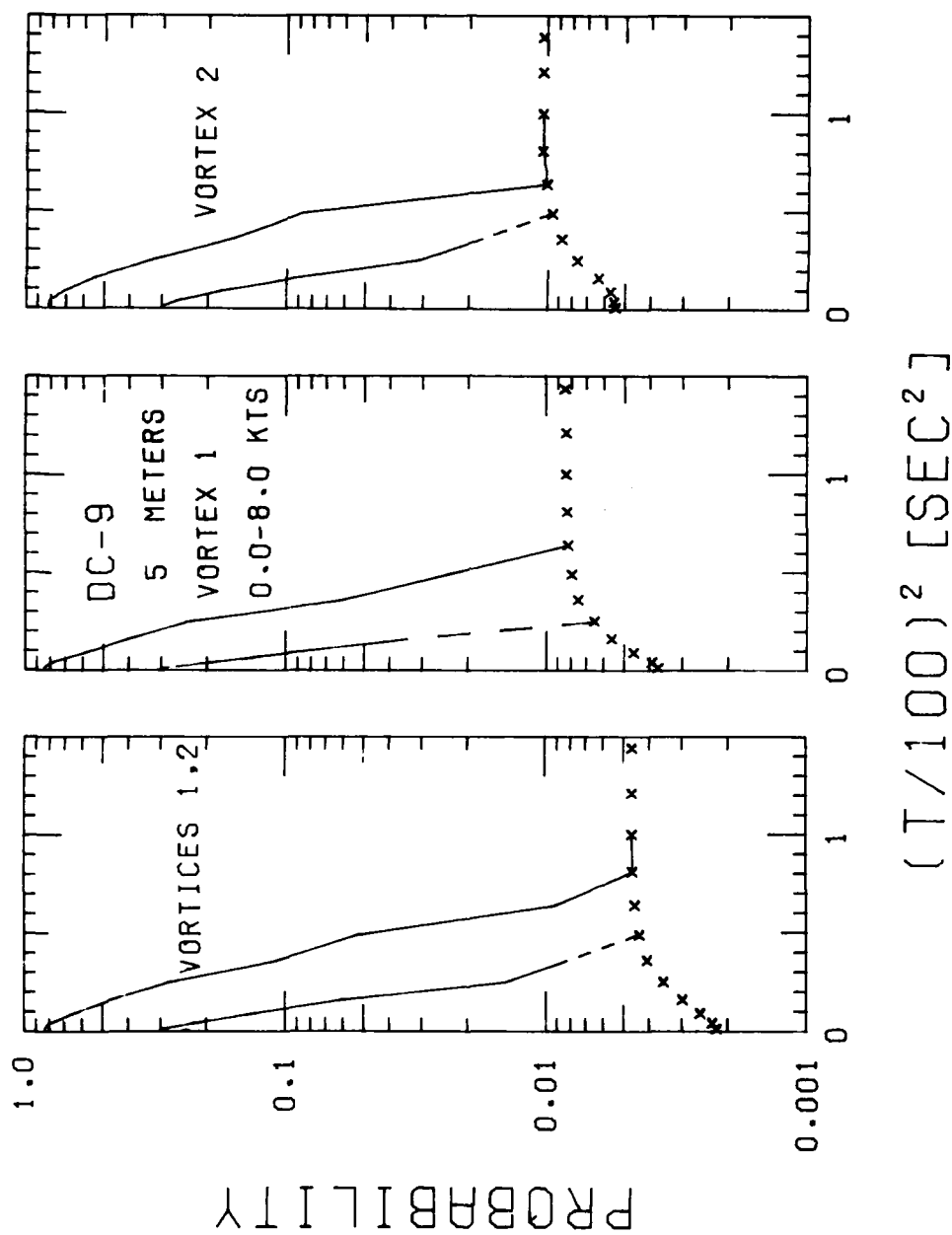


FIGURE 98. PROBABILITY OF DECAY, DC-9, WINDS LESS THAN 8 KNOTS, 5-m AVERAGING RADIUS

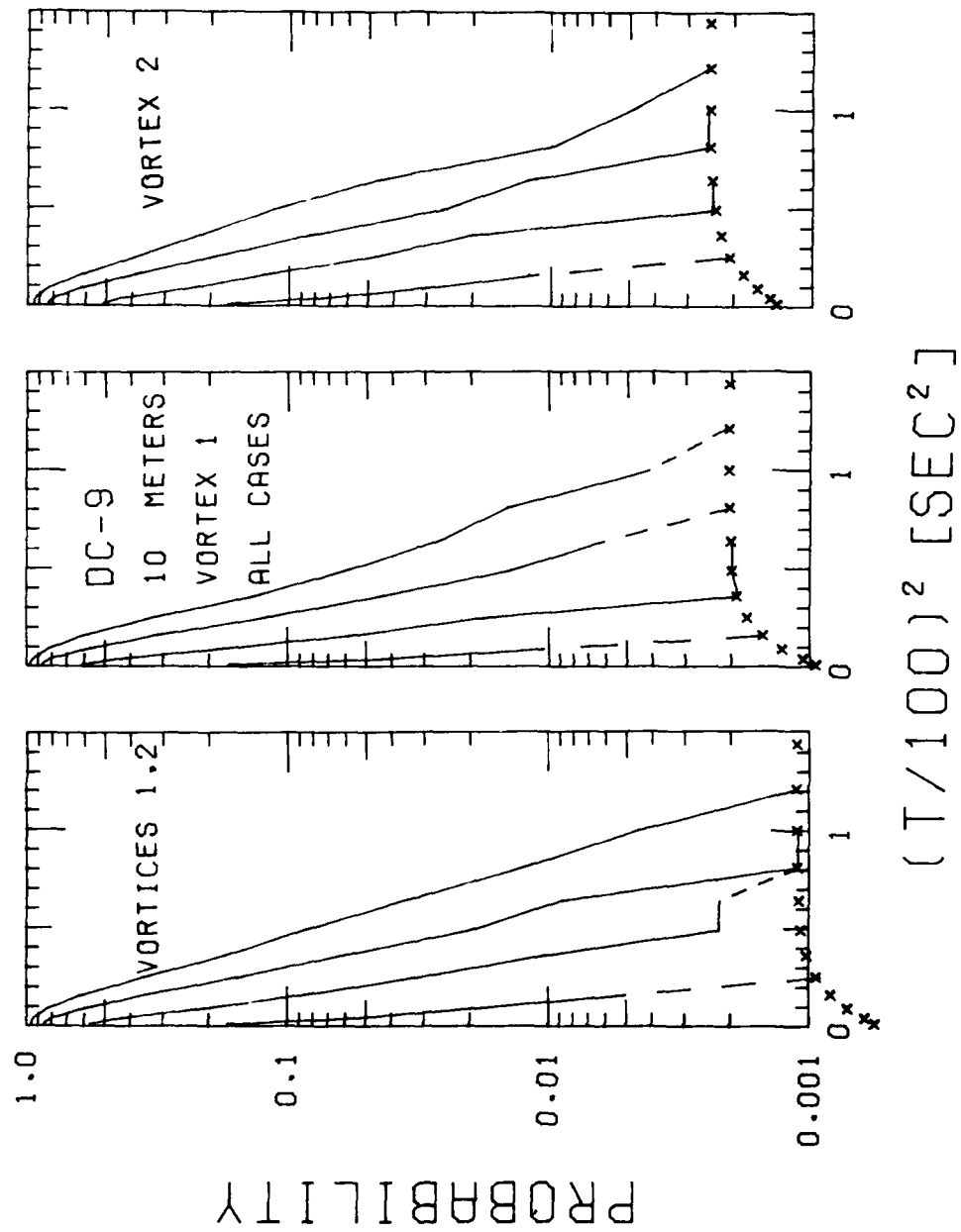


FIGURE 99. PROBABILITY OF DECAY, DC-9, VORTEX 1 AND 2, 10-m AVERAGING RADIUS

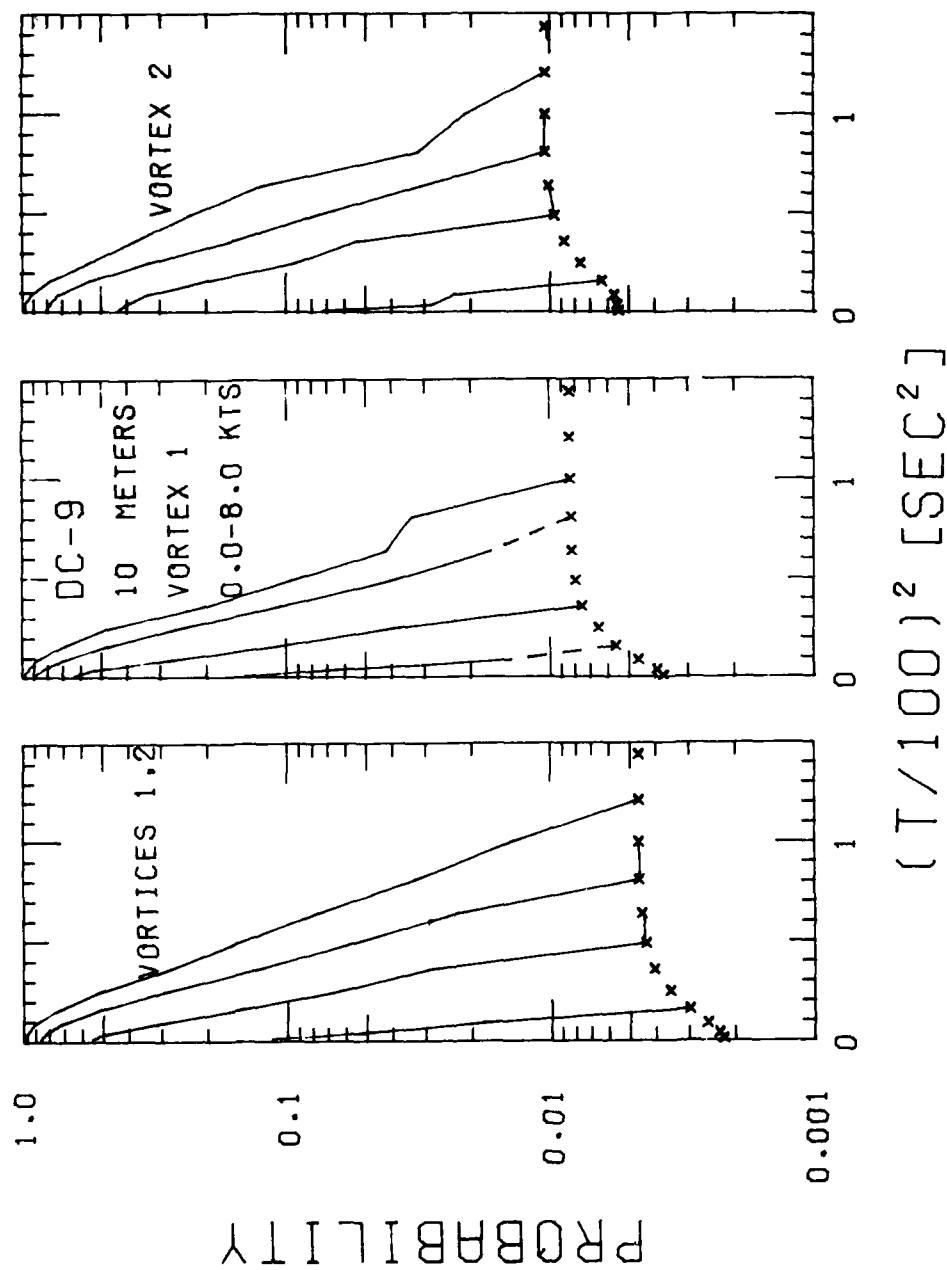


FIGURE 100. PROBABILITY OF DECAY, DC-9, WINDS LESS THAN 8 KNOTS, 10-m AVERAGING RADIUS

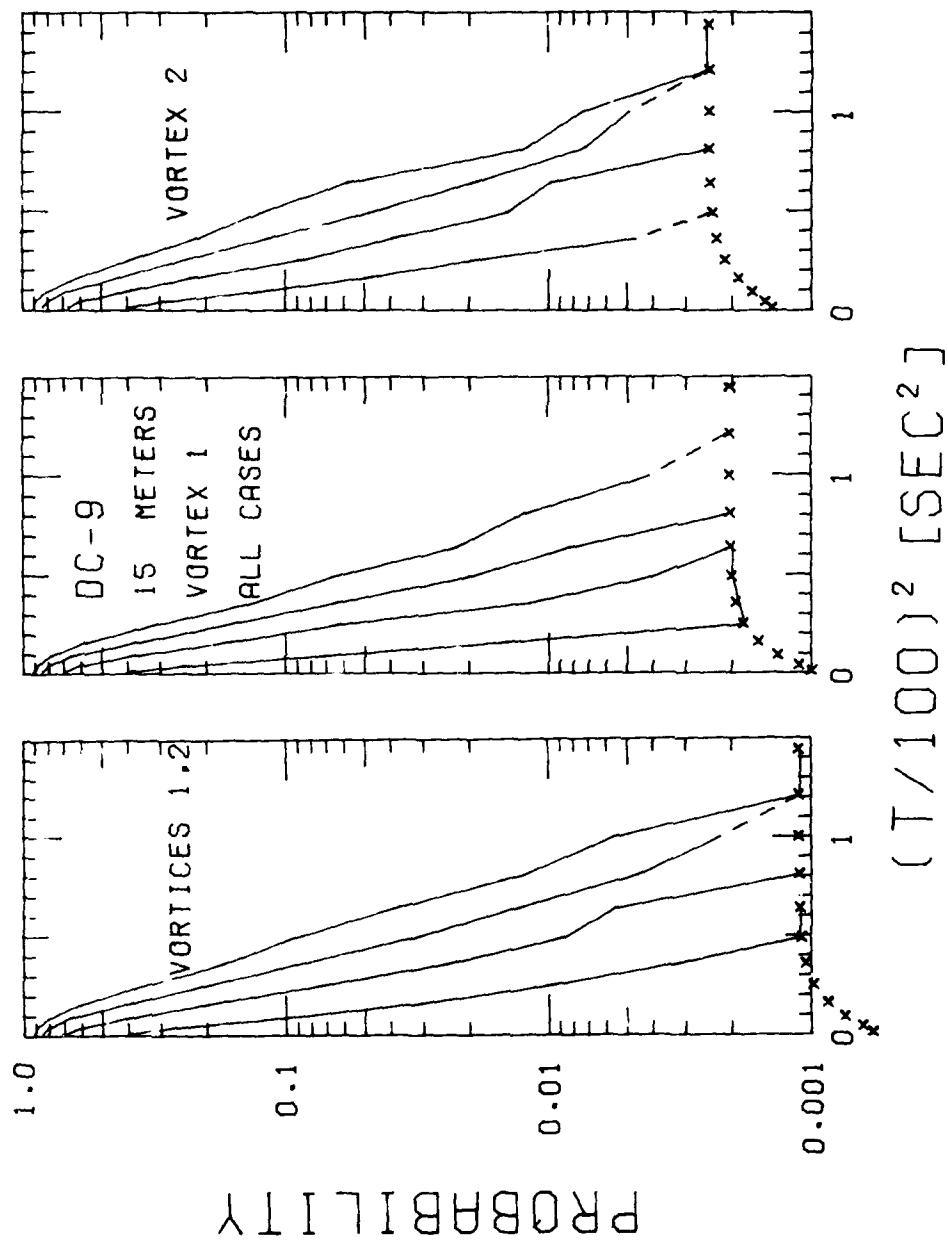


FIGURE 101. PROBABILITY OF DECAY, DC-9, VORTEX 1 AND 2, 15-m AVERAGING RADIUS

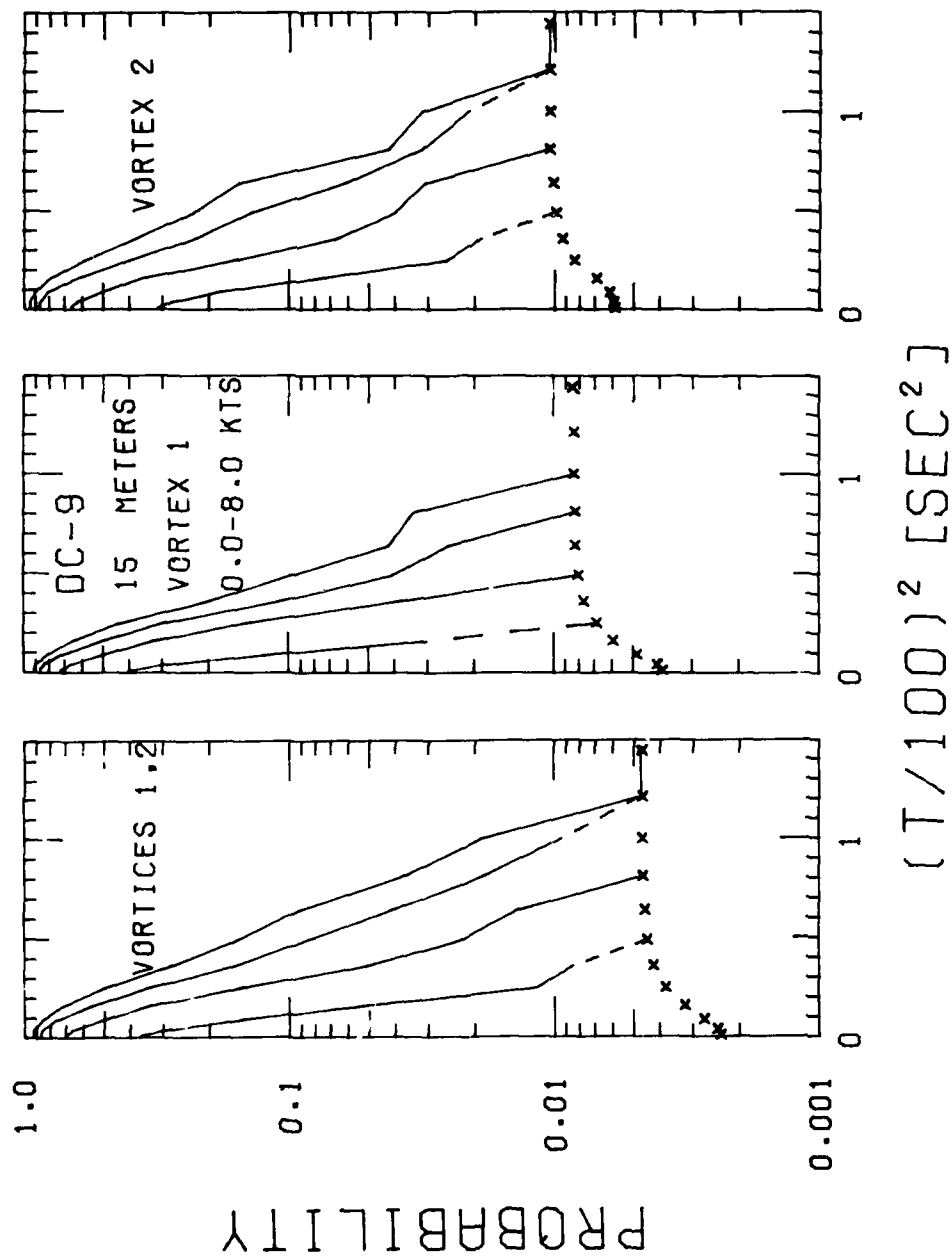


FIGURE 102. PROBABILITY OF DECAY, DC-9, WINDS LESS THAN 8 KNOTS, 15-m AVERAGING RADIUS

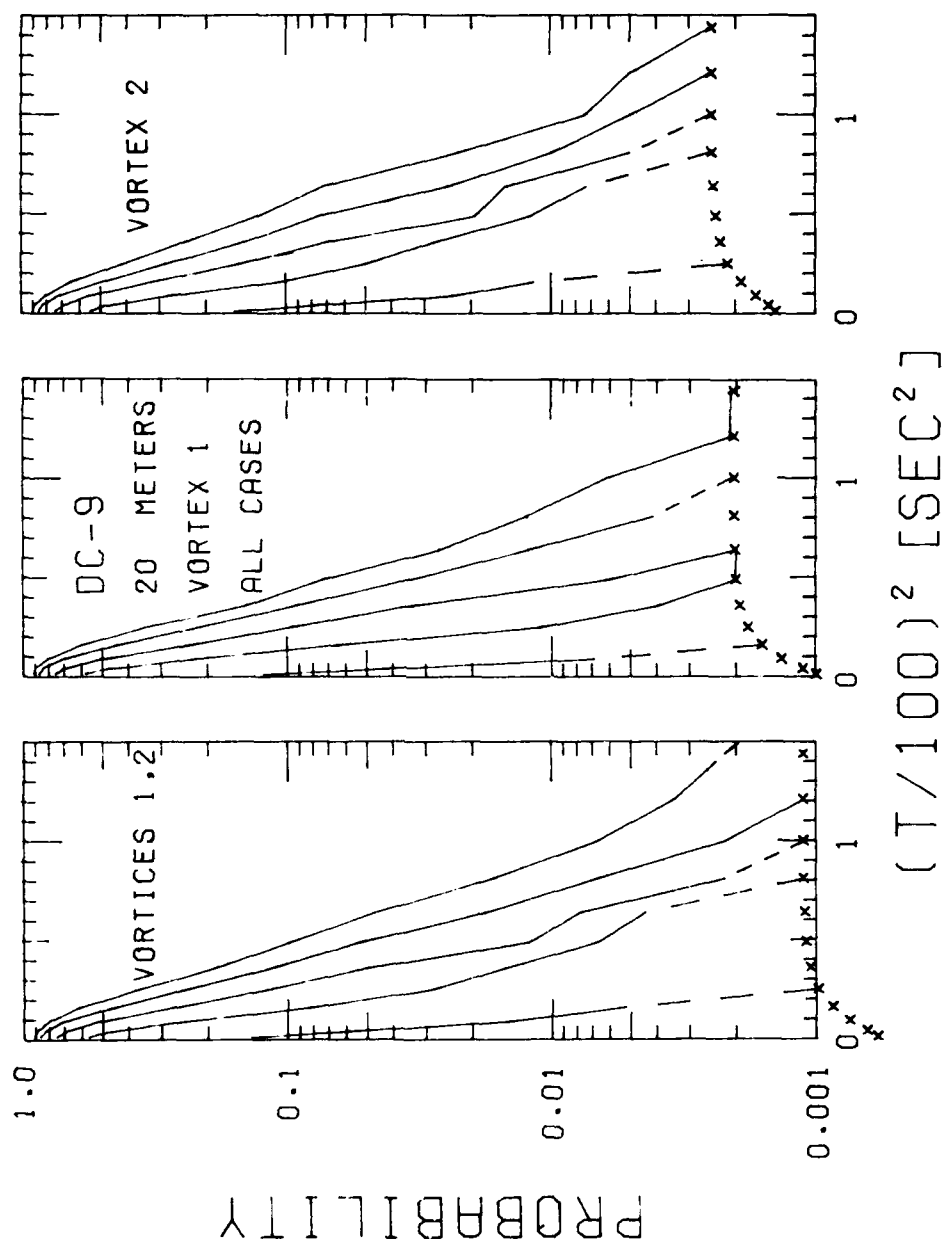


FIGURE 103. PROBABILITY OF DECAY, DC-9, VORTEX 1 AND 2, 20-m AVERAGING RADIUS

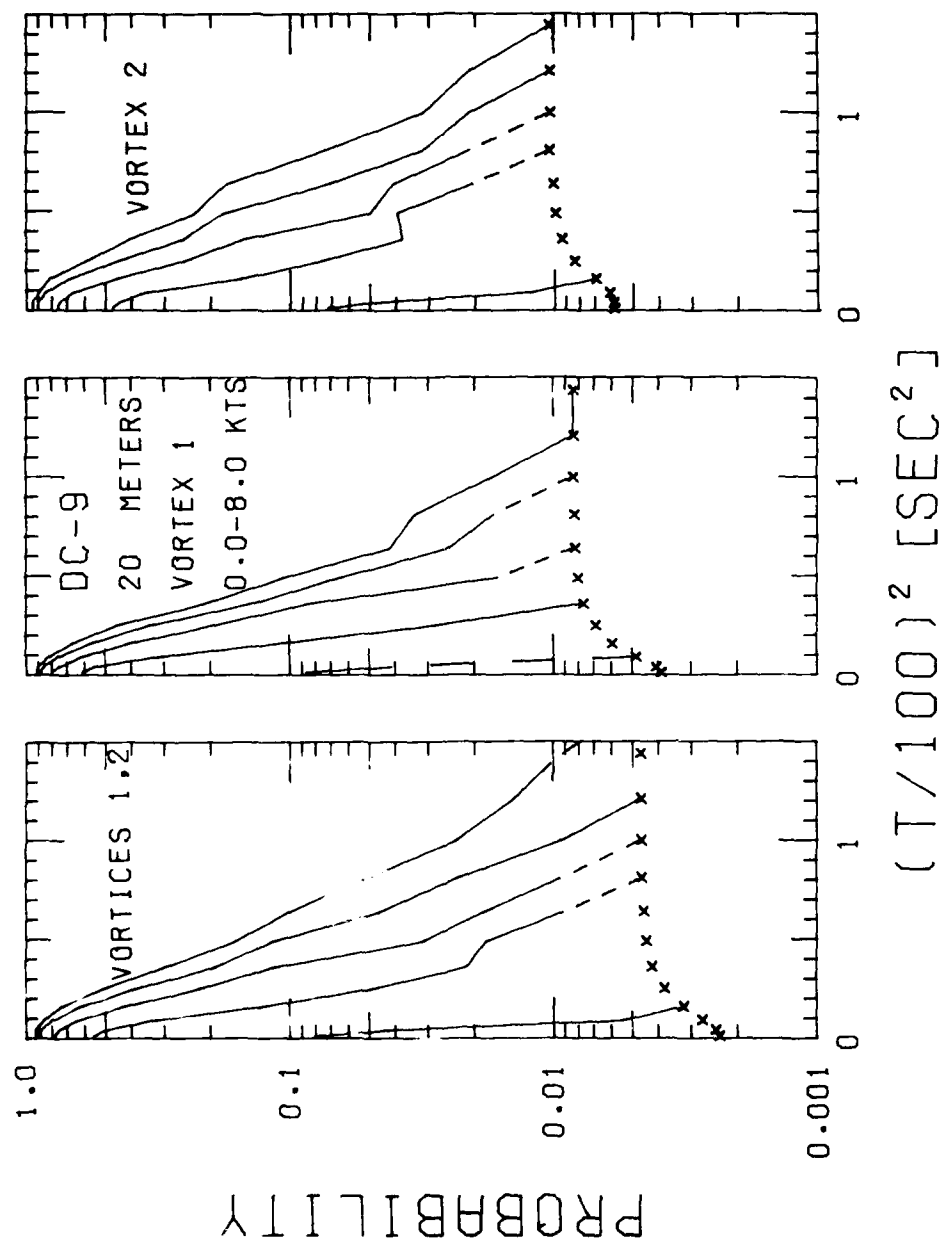


FIGURE 104. PROBABILITY OF DECAY, DC-9, WINDS LESS THAN 8 KNOTS, 20-m AVERAGING RADIUS

APPENDIX D
DECAY OF AVERAGE VORTEX STRENGTH

Figures 105 through 111 show the decay of average vortex strength for the DC-10, L-1011, DC-8H, B-707H, B-727, B-737, and DC-9, respectively. The plots for the B-747, B-707, and DC-8 are in the main text, Figures 11 to 13, respectively.

AB-A120 081

TRANSPORTATION SYSTEMS CENTER CAMBRIDGE MA
CHICAGO MONOSTATIC ACOUSTIC VORTEX SENSING SYSTEM. VOLUME IV. W--ETC(U)
JUL 82 D C BURNHAM, J N HALLOCK

F/G 20/4

UNCLASSIFIED

DOT-TSC-FAA-79-18-4

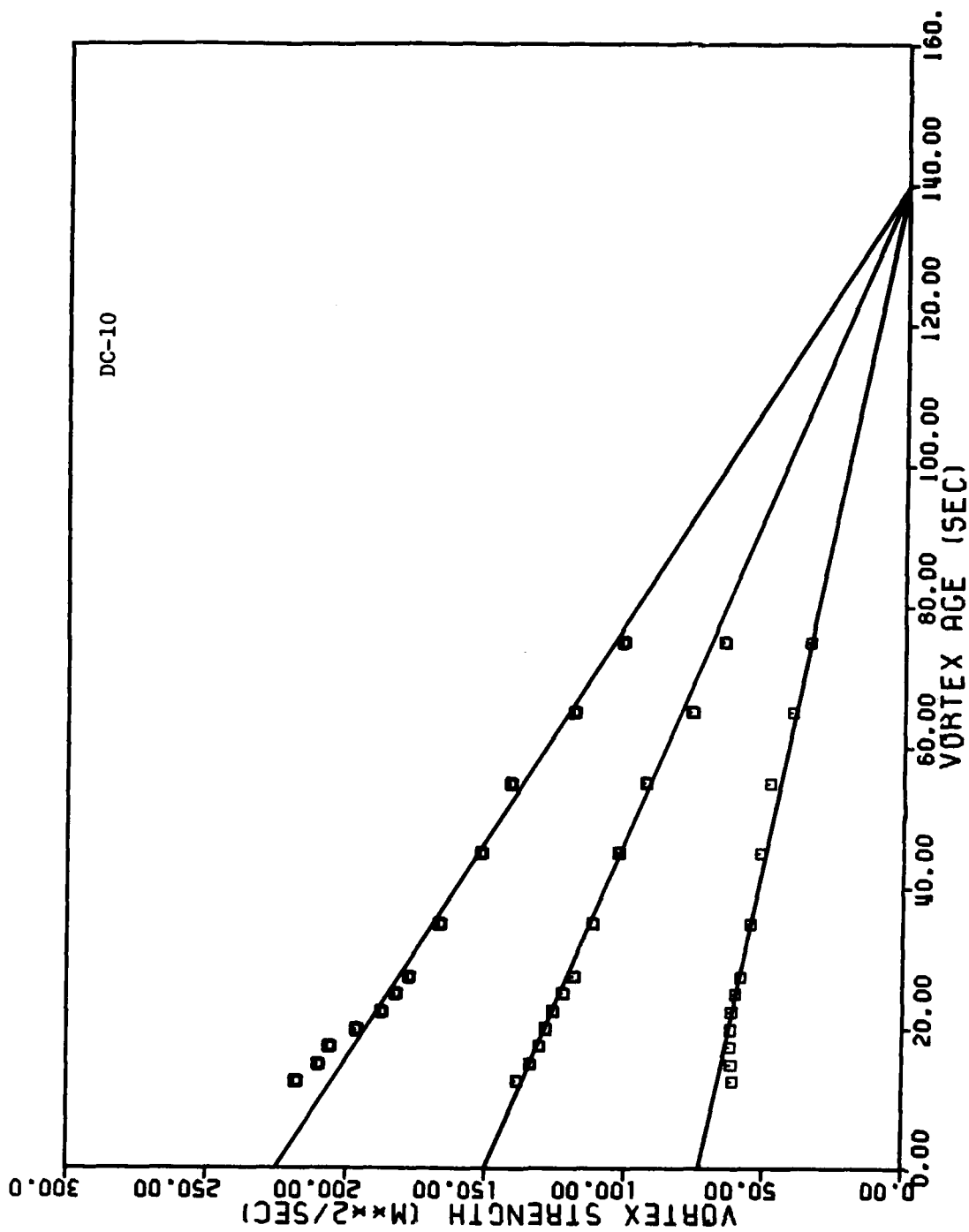
DOT/FAA/RD-79-103-VOL-4

NL

3
2-0004

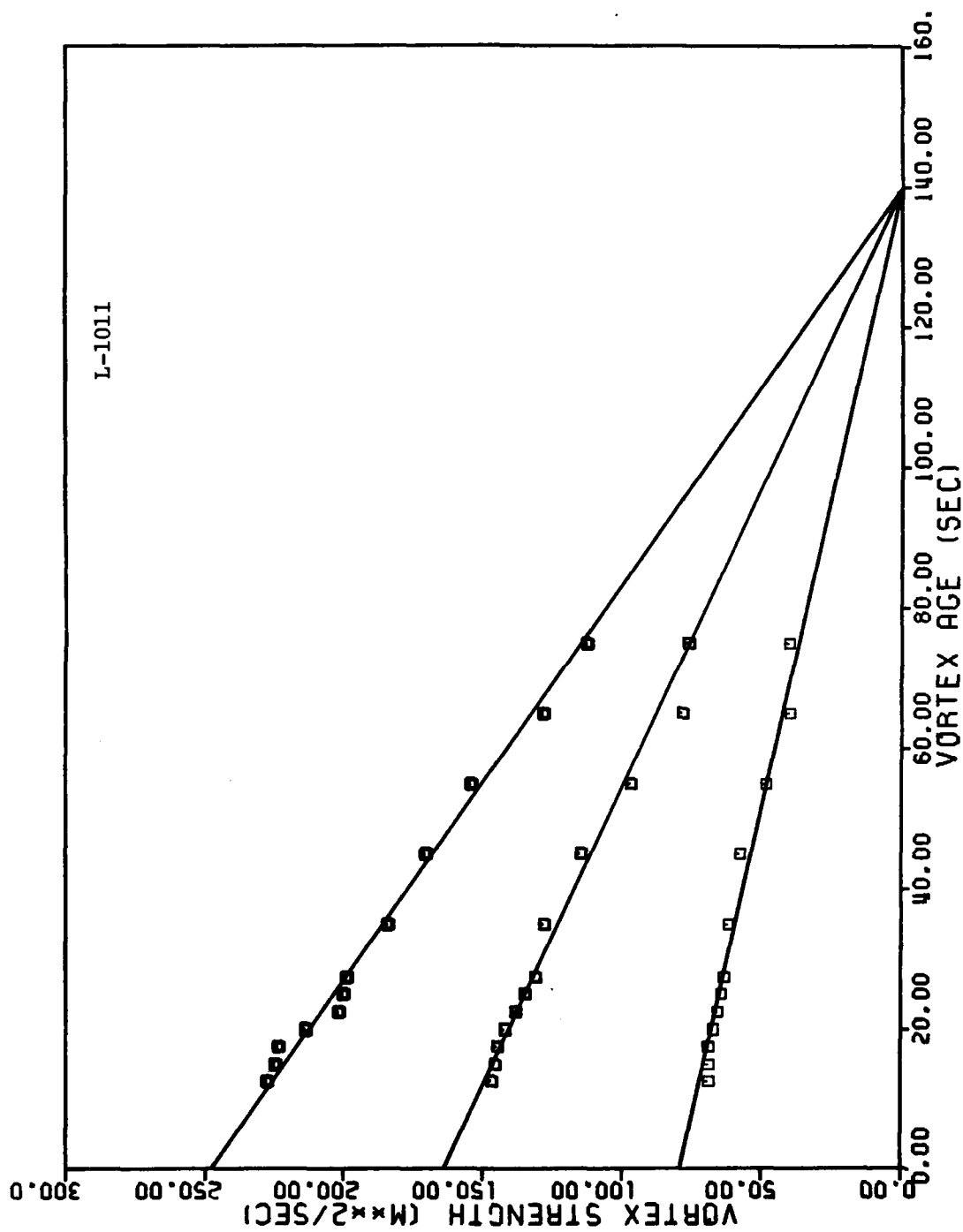


END
DATE
FILED
11-82
DTIC



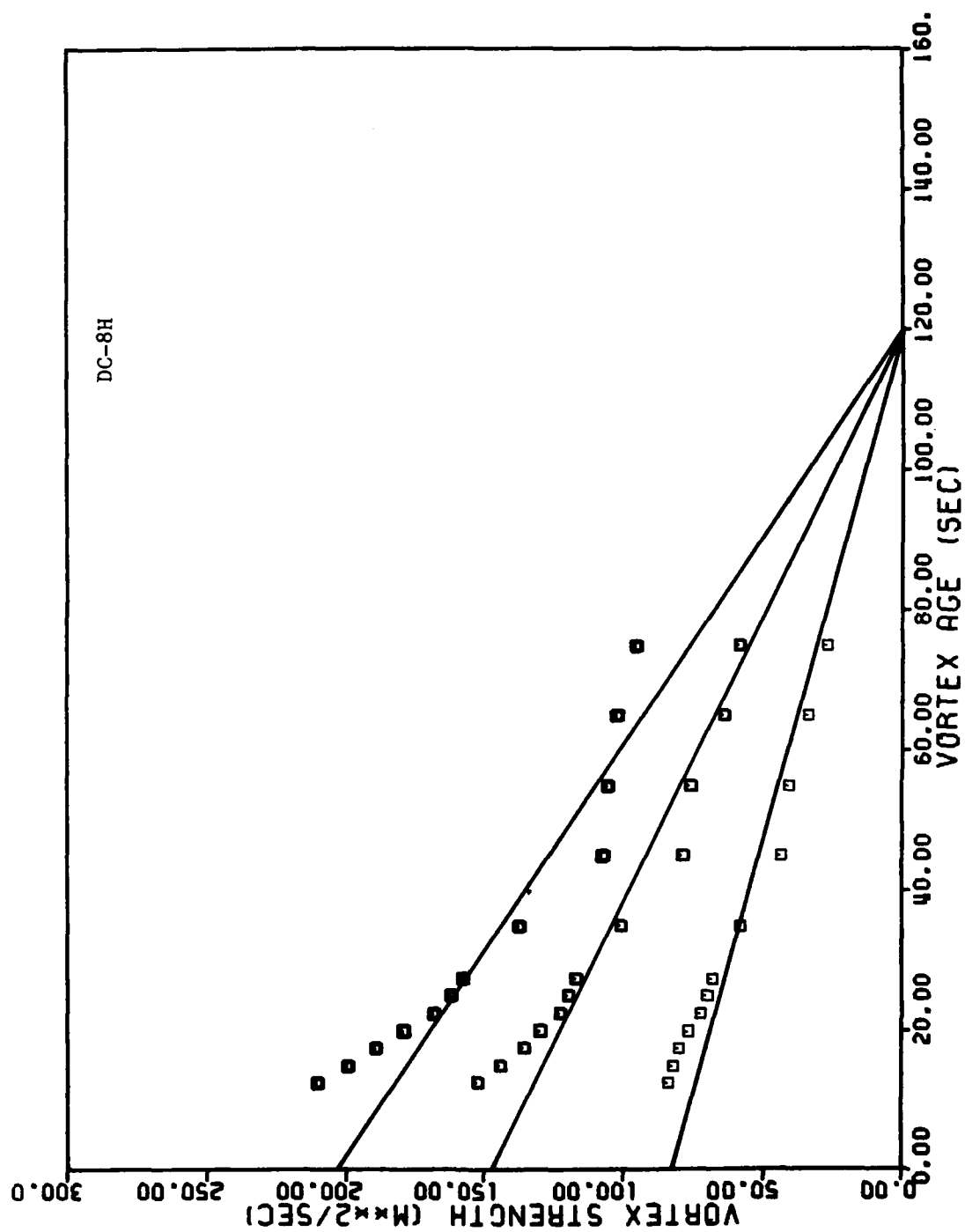
NOTE: Averaging Radius = 5 m (lower line), 10 m (middle line), and 20 m (upper line)

FIGURE 105. DECAY OF AVERAGE VORTEX STRENGTH FOR ALL DC-10 DETECTED VORTICES



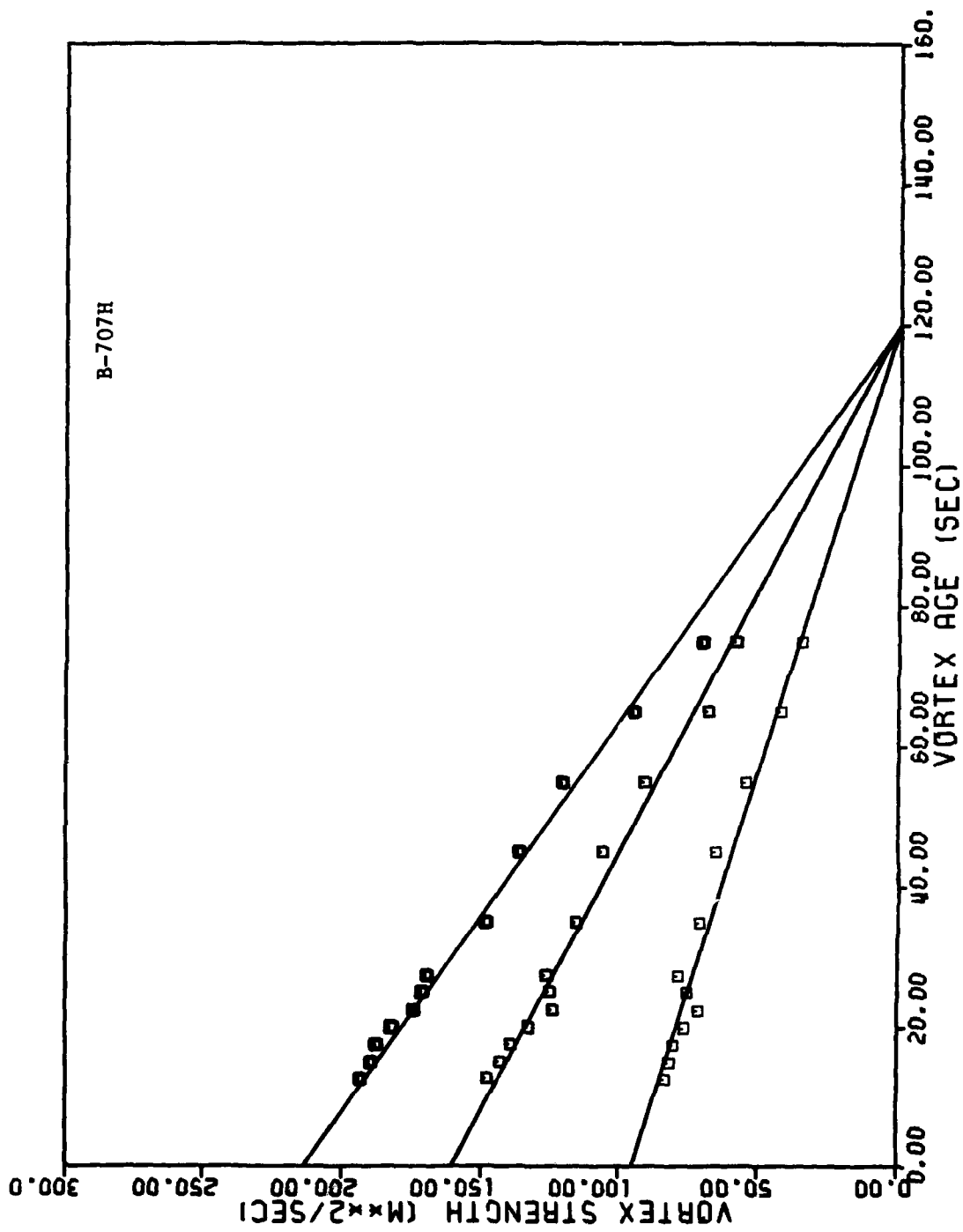
NOTE: Averaging Radius = 5 m (lower line), 10 m (middle line), and 20 m (upper line)

FIGURE 106. DECAY OF AVERAGE VORTEX STRENGTH FOR ALL L-1011 DETECTED VORTICES



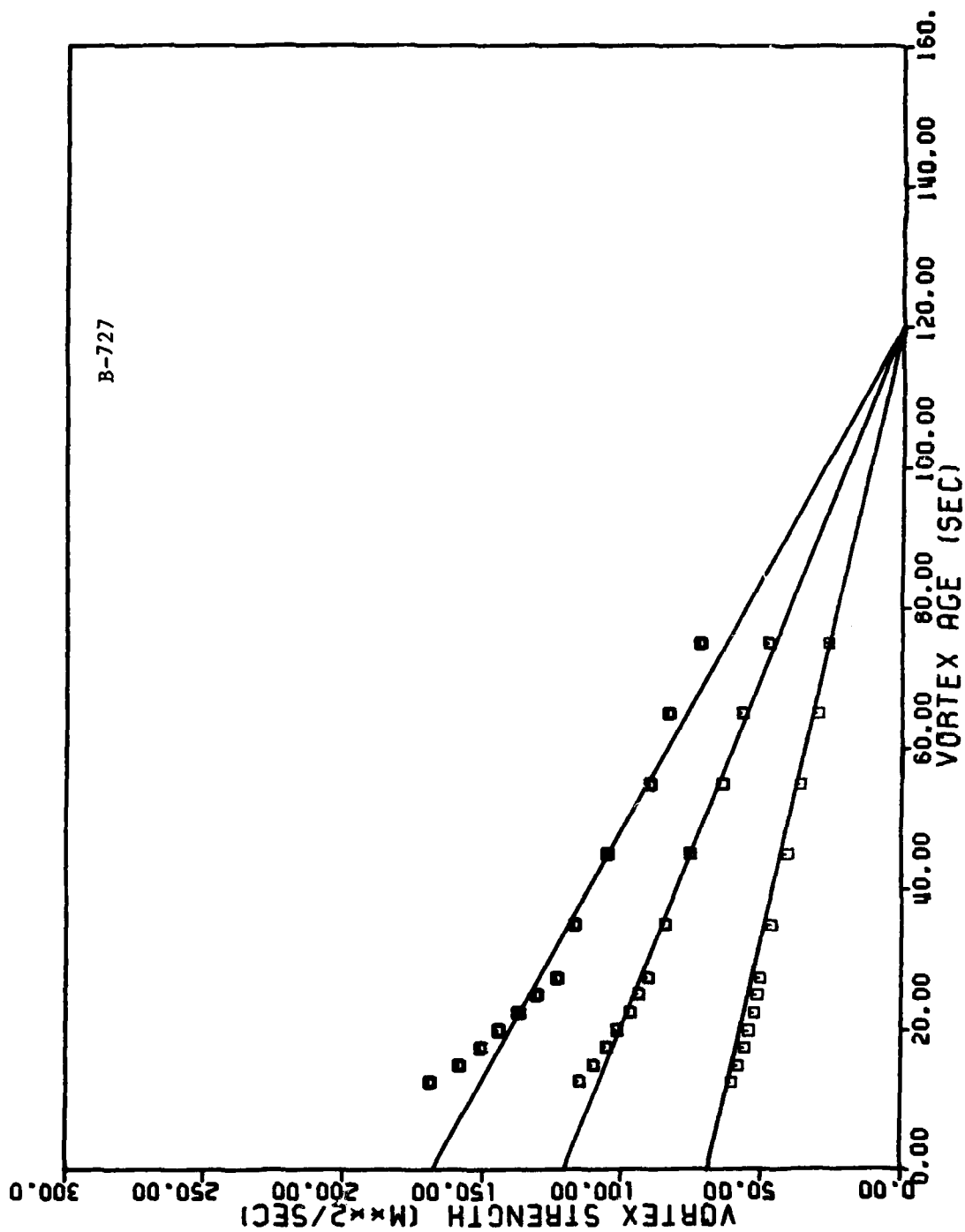
NOTE: Averaging Radius = 5 m (lower line), 10 m (middle line), and 20 m (upper line)

FIGURE 107. DECAY OF AVERAGE VORTEX STRENGTH FOR ALL DC-8H DETECTED VORTICES



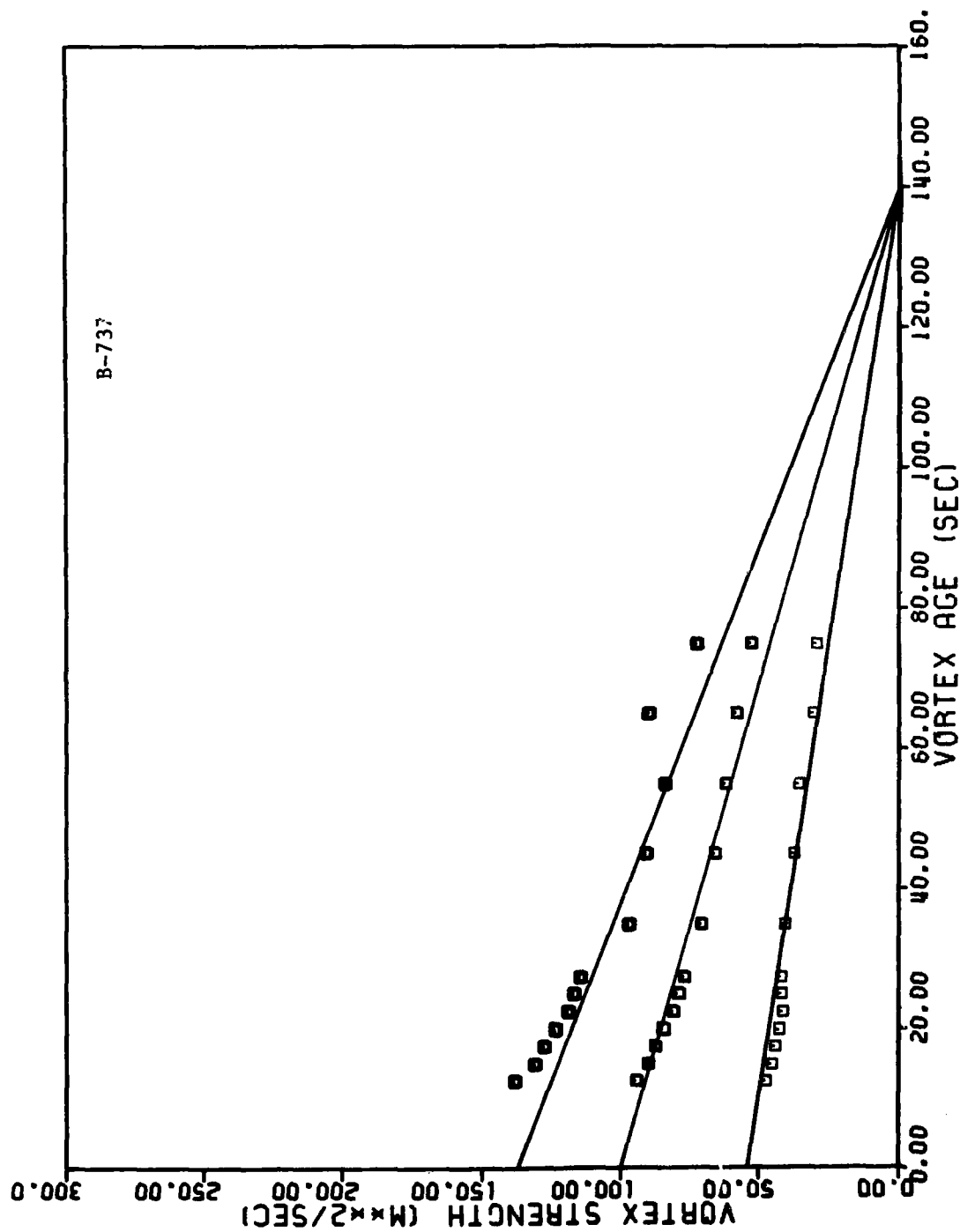
NOTE: Averaging Radius = 5 m (lower line), 10 m (middle line), and 20 m (upper line)

FIGURE 108. DECAY OF AVERAGE VORTEX STRENGTH FOR ALL B-707H DETECTED VORTICES



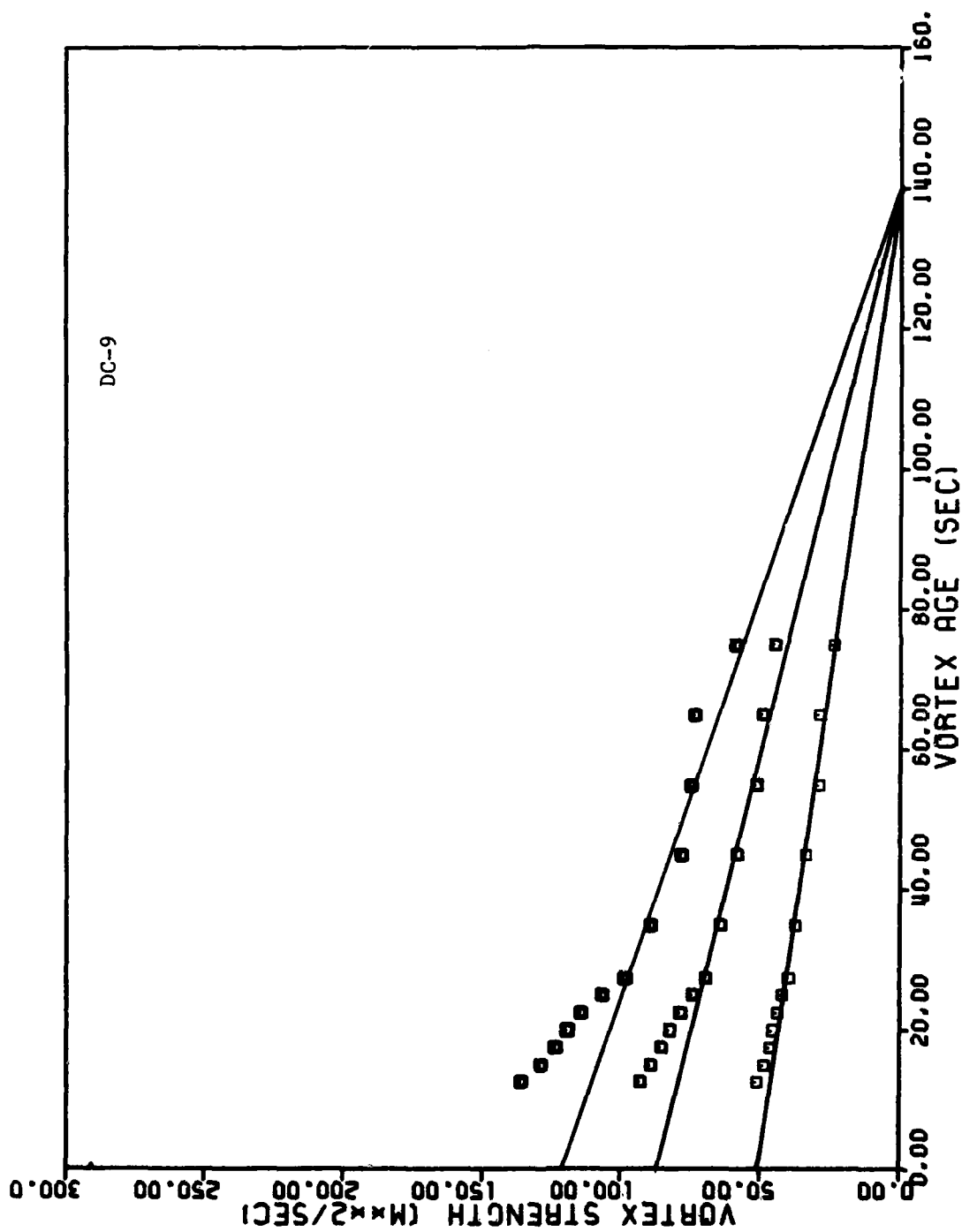
NOTE: Averaging Radius = 5 m (lower line), 10 m (middle line), and 20 m (upper line)

FIGURE 109. DECAY OF AVERAGE VORTEX STRENGTH FOR ALL B-727 DETECTED VORTICES



NOTE: Averaging Radius = 5 m (lower line), 10 m (middle line), and 20 m (upper line)

FIGURE 110. DECAY OF AVERAGE VORTEX STRENGTH FOR ALL B-737 DETECTED VORTICES



NOTE: Averaging Radius = 5 m (lower line), 10 m (middle line), and 20 m (upper line)

FIGURE 111. DECAY OF AVERAGE VORTEX STRENGTH FOR ALL DC-9 DETECTED VORTICES

APPENDIX E
REFERENCES

1. Burnham, D.C., "Chicago Monostatic Acoustic Vortex Sensing System, Volume I: Data Collection and Reduction," FAA-RD-79-103,I, Oct. 1979, DOT Transportation Systems Center, Cambridge, MA.
2. Burnham, D.C. and Hallock, J.N., "Chicago Monostatic Vortex Sensing System, Volume II: Decay of B-707 and DC-8 Vortices," FAA-RD-79-103,II, Sept. 1981, DOT Transportation Systems Center, Cambridge, MA.
3. Burnham, D.C. and Hallock, J.N., "Chicago Monostatic Acoustic Sensing System, Volume III: Executive Summary," FAA-RD-79-103,III, Jan. 1982, DOT Transportation Systems Center, Cambridge, MA.
4. Sullivan, T.E., Hallock, J.N., Winston, B.P., McWilliams, I.G., and Burnham, D.C., "Aircraft Wake Vortex Takeoff Tests at Toronto International Airport," FAA-RD-78-143, Feb. 1975, DOT Transportation Systems Center, Cambridge, MA.
5. Burnham, D.C., "B-747 Vortex Alleviation Flight Tests: Ground-Based Sensor Measurements," FAA-RD-81-99, Sept. 1981, DOT Transportation Systems Systems Center, Cambridge, MA.
6. Crow, S.C. and Bate, E.R., "Lifespan of Trailing Vortices in a Turbulent Atmosphere," J. Aircraft, Vol. 13, No. 7, July 1976, pp. 476-482.
7. Tombach, I.H., Lissaman, P.B.S., Mullen, J.B., and Barker, S.J., "Aircraft Vortex Wake Decay Near the Ground," FAA-RD-77-46, Mar. 1977, AeroVironment, Inc., Pasadena, CA.
8. Etkin, B., Dynamics of Atmospheric Flight, John Wiley & Sons, New York, 1972, p. 433.
9. Anon., Aviation Week & Space Technology, 12 March 1979, p. 129.

10. Tietjens, O.G., Applied Hydro- and Aeromechanics, Dover, New York, 1957, pp. 158-163.
11. Hallock, J.N., "Vortex Advisory System Safety Analysis, Vol. I: Analytical Model," FAA-RD-78-68,I, Sept. 1978, DOT Transportation Systems Center, Cambridge, MA.
12. Stability and Control Group, "Estimated Stability and Control Characteristics Model DC-9-30 Jet Transport," LB-32323, Dec. 1966 (revised Oct. 1968), Douglas Aircraft Company, Long Beach, CA.
13. Burnham, D.C., Hallock, J.N., Tombach, I.H., Brashears, M.R., and Barber, M.R., "Ground-Based Measurements of the Wake Vortex Characteristics of a B-747 Aircraft in Various Configurations," FAA-RD-78-146, Dec. 1978, DOT Transportation Systems Center, Cambridge, MA.

220 copies

LMEL
-8